HOKKAIDO UNIVERSITY

| | |
|---|---|
| Title | Study on Kinematic Rheometry Utilizing Ultrasonic Velocity Profiling |
| Author(s) | 芳田, 泰基 |
| Degree Grantor | 北海道大学 |
| Degree Name | 博士(工学) |
| Dissertation Number | 甲第13994号 |
| Issue Date | 2020-03-25 |
| DOI | https://doi.org/10.14943/doctoral.k13994 |
| Doc URL | https://hdl.handle.net/2115/80690 |
| Type | doctoral thesis |
| File Information | Taiki_Yoshida.pdf |

Hokkaido University Collection of Scholarly and Academic Papers : HUSCAP

# Study on Kinematic Rheometry Utilizing Ultrasonic Velocity Profiling

A dissertation submitted to the

**HOKKAIDO UNIVERSITY**

for the degree of

**Doctor of Philosophy**

presented by

Taiki YOSHIDA

Graduate School of Engineering

born May 12th, 1992

Supervised by Ph. D Yuji TASAKA

prepared at *Laboratory for Flow Control*






Copyright © 2020 Taiki YOSHIDA
Laboratory for Flow Control
Hokkaido University
All rights reserved.

**Study on Kinematic Rheometry Utilizing Ultrasonic Velocity Profiling**

Thesis for Ph. D. (Eng.) at Hokkaido University

Advisory Committee
Assoc. Prof. Ph. D Yuji Tasaka, Hokkaido University, Chair / Chief examiner
Prof. Dr.-Eng. Yuichi Murai, Hokkaido University, Co-examiner
Prof. Dr.-Eng. Nobuyuki Oshima, Hokkaido University, Co-examiner
Prof. Dr.-Eng. Masao Watanabe, Hokkaido University, Co-examiner
Assoc. Prof. Dr.-Sci. Ikuro Sumita, Kanazawa University, Co-examiner

# Acknowledgment

I wish to express my special gratitude to supervisor **Assoc. Prof. Dr. Yuji Tasaka** for giving me the opportunities to accomplish this work. His visions, idea, and extensive devotion to fluid dynamics have given me interests in the field of engineering. He told me how to research with passions, and he gave me treasures to find a way to survive as a researcher.

I would like to thank **Prof. Dr. Yuichi Murai** for giving me chances to discuss various research subjects. His way of looking at the fluid mechanics is so respectable as to move not only me but also all of students.

I would like to thank **Assist. Prof. Dr. Hyun Jin Park** for giving me opportunities to polish my coding skills. His way of thinking for analyses is bright, and he gives us precious time and energy.

**Technician Mr. Toshiyuki Sampo**'s technical supports were invaluable, because I could not complete this work without his kindnesses and illustrious sense of fabrications.

I also would like to thank **Secretary Ms. Yui Miyazaki** for taking care of paperwork and life counseling.

I would like to express my special appreciation to **Prof. Dr. Dr. Yasushi Takeda**, and he gave me extensive supports when I was in Zürich. He gave me a lot of opportunities to gain experiences for research works at ETH Zürich.

I would like to thank **Prof. Dr. Peter Fischer** for giving me opportunities to gain experience for high-level research at ETH Zürich, and express my gratitude to his solicitude for attending my doctor defense.

I would also like to express my gratitude to **Prof. Dr. Erich J. Windhab** for accepting my stay at ETH Zürich twice, and he gave me constructive comments and warm encouragement.

I am grateful to **Assoc. Prof. Dr. Atsuko Namiki** for assistance on the experiments using standard rheometer, and I was so impressed by her attitudes toward "rheology" during the short period training at Hiroshima University.

I would like to express my gratitude to **Dr. Shingo Tanaka** for contributions to the published paper, especially in the chemical aspect understanding of clay suspension.

I would like to express my gratitude to **Dr. Damien Dufour** for assisting my internship at ETH Zürich during master's course.

I would like to express my gratitude to **Prof. Dr. Nobuyuki Oshima**, **Prof. Dr. Masao Watanabe**, and **Assoc. Prof. Dr. Ikuro Sumita** for their insightful comments on this thesis.

I would like to thank **Prof. Dr. Ichiro Kumagai**, **Dr. Takatoshi Yanagisawa**, and **Dr. Shun Nomura** for giving me essential comments on my research.

Finally, I would like to express my deepest gratitude for LFC members (especially in J-Lab.), LFPE members in ETH Zürich, friends in Switzerland, schoolfellows, my family, and my dearest.

This research work was carried out at the *Laboratory for Flow Control* (LFC), Graduate School of Engineering, Hokkaido University. The project was funded by Grant-in-Aid for the *Japan Society for the Promotion of Science* (JSPS) Fellows (Grant No. 18J20516) and the Overseas Challenge Program for Young Researchers of JSPS.

*February 16, 2020*

*Signature* 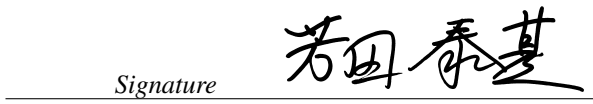

# Abstract

There exist several materials with complex flow behavior which cannot be explained even by considering the theories of classical hydrodynamics and elastodynamics through a past century. Since fluid materials having all the more complex rheological characteristics are produced in the present industry, its flow behavior cannot be controlled without a day-to-day way, that is to say, establishing an empirical rule. This problem is caused by low reliability of the commercially-supplied rheometers; the prototype of a standard rotational rheometer utilized in the various fields of both industries and academic institutes has been completed two-hundred-year ago, where the rotational torque as the mechanical response from the shaft attaching to test material can be measured, then the rheological properties are determined by the principle based on a few assumptions. Recently, a common issue regarding the commercially-supplied rheometer is that the requisite assumptions are not satisfied on the measurements for non-Newtonian fluids. The factors causing the issue are (1) slip feature between the test material and the rheometer shaft, (2) appearance of shear banding layer, (3) influence from elastic instability, (4) shear history effects causing physical property gradient in the narrow gap of rotating shaft, (5) jamming effect arising from multiphase dispersion in the gap, and more. These considerable factors are not perceived as precautions for use of the rheometer, but misunderstood as its rheological behaviors by users. When rheological evaluations are attempted without considering these influences, the obtained results will reflect the specific response as it is dealt with in the measurement device, not exposing or clarifying the true-rheological properties. Still, no fully acceptable solution for these problems is known, though extensive trials to overcome specific problems have been made, such as improvements of rheometer geometry and surface roughness, or solving mathematically the "Couette inverse problem", etc. These problems are caused by the fluid characteristics, and efforts to solve the problems have to be approached from the perspective of fluid mechanics.

In this study, a novel methodology, termed "Kinematic rheometry", is presented, which is based on equation of motion to explain the fluid rheology. The rheometry is expected to quantify the rheological properties satisfying the considered equation of motion for complex fluids, and the characteristic is to install a constitutive equation (rheological model) into the equation of motion for describing the rheological behaviors. As a point of attention, the constitutive equation here does not function as the purpose in general rheological approaches such as approximations for rheological indexes. Here, the kinematic rheometry is expected to play a role of filling "a hole" in the applicable range of standard rheometer, which is arising from common problems in the standard rheometer tests. The fluids with rheological properties that have been realized assurances of measurement, such as higher viscosity $O(10^3$ Pas), lower viscosity $O(10^{-3}$ Pas), quasi-elasticity, and more, are out of applicable target of the kinematic rheometer. By utilizing ultrasonic velocity profiling technique as a velocimetry, the wide applicable range of the kinematic rheometry is realized. To promote the rheometry development and enhance the methodology to be able to contribute to raising the level of the scientific researches, the robustness and efficacy of the kinematic rheometry must be proven and received recognition from general users; the necessity can be explained by the considerable factors in the commercially-supplied rheometers being gotten overlooked from users. That is neither more nor less than that the users (researchers or engineers) are more interested in that "if the rheological evaluations are easy or not" than that "if the obtained data is physically meaningful or not". In this study, a novel rheometry that is able to contribute to research that reveals scientific findings is presented, accompanied by methodology presentation, validation and application revealing physical properties.

This thesis is constituted by 10 chapters, and the notable findings in each chapter are summarized as follows:

1. By using phase-lag analysis to evaluate the effective viscosity calculated from phase-lag gradient of momentum propagation, it is possible to clarify yield stress determining physical border between gel and sol, shear dependent viscosity of pseudo-plastic fluid, critical condition causing viscoelasticity, and effective viscosity of multiphase fluid [Chapter 2].
2. For clay dispersion with thixotropy which is merely examined as apparent yield stress and viscosity, the critical shear rates onsetting yield and shear thinning behavior are obtained utilizing the phase-lag analysis [Chapter 3].
3. An approach to evaluate rheological property in frequency domain for avoiding the influence from noise augmentation was presented [Chapter 4]; as a result of validation of this methodology, the precision and accuracy including un-ensured materials by commercially-supplied rheometers were confirmed [Chapter 5].
4. The effective viscoelasticity of non-Newtonian fluids as macro rheological characteristics are modulated by the alignment of spherical particles, further that closely relates to the relaxation time of fluid media; the reason why this finding has been an unexamined issue on the complex rheology is limitations of commercially-supplied rheometer [Chapter 6].
5. Food testing method is updated utilizing kinematic rheometery, and shear history effects of gelled foods are revealed; this finding may relate to flows in the swallowing process of complex food materials [Chapter 7].
6. Thixotropic effects on standard rheometer tests are elucidated by considering the rheological evaluations using both large amplitude oscillatory shear (LAOS) measurement in the standard rheometer and the kinematic rheometry [Chapter 8].
7. As an applicable rheometry to practical pipelines in the industry, an algorithm of the kinematic rheometry was presented to evaluate the rheological properties without creating any holes for inserting sensors [Chapter 9].

# 要旨


数世紀かけて体系化されてきた古典弾性力学や古典流体力学でさえ、その流動が予測できない物質は数多存在する。多種多様な化合物が生成される中、その流動や生成物の品質は経験則によって場当たり的に制御・管理されている。つまり、対象が未知な物性を持つような新材料の場合、新たな経験則として制御・管理方法の創出に迫られてしまう。経験則に縛られる現状は、その流動物性（レオロジー）を評価する手法（レオメトリ）の信頼性が乏しいことに起因している。産業・学理の多分野に最も広く利用される回転式トルクレオメータの原型は、二百年以上前に完成されており、ラボレベルの分析に用いられるトルク式の市販レオメータは、高い計測精度を実現している。一方、計測確度の保証にはいくつかの仮定が満たされる必要があるが、多くの非ニュートン性流体ではそれが満たされないことが多い。最たる原因として、測定対象物質と回転子壁面との間での滑りや、局所剪断層の発現、弾性的不安定性による影響などが数多く報告されている。これらはすべて「流動」に起因する物である。一般的な市販レオメータのユーザーには認知されておらず、出力結果が盲信されている現状がある。この場合、レオメータにおける幾何設計固有の応答が計測され、物性をそのもののみを反映した結果は得られない。解決策として、多くの研究開発で精力的に取り組まれているレオメータの幾何設計や表面性状の改良、クエット逆問題に対する数学的な解法等は、対処療法でしかない。非ニュートン性流体の挙動を直接計測しレオロジー物性の導出を試みる、新たな手段が求められている。

本論文では、この問題を解決する有力な手法として、速度分布計測と運動方程式に基づく運動学的レオメトリ (Kinematic Rheometry) が提案されている。これは、複雑流体のダイナミクスに対して、運動方程式を満たすようなレオロジー物性を逆算・定量化することができる。運動方程式へ各種構成方程式（レオロジーモデル）を導入し、この構成方程式は高次のレオロジー物性を記述する。流体挙動を記述する役割を担うことから、一般にレオロジー分野で用いられるようなレオロジー係数の計算を目的としたフィッティング関数の類としては、導入されていない。$O(10^3$ Pas) 以上の高粘性流体や、$O(10^{-3}$ Pas) 以下の極低粘性流体、準完全弾性体など、市販レオメータで高精度のレオロジー物性計測がすでに可能とされている対象を除いた範囲を、本レオメトリが目指す適用範囲として設定している。これにより、市販レオメータとの相補的な使用が想定される。流速計測法として、不透明流体から混相流体まで計測可能な超音波流速計測法 (UVP) を利用することで、多様な計測対象に適用可能なレオメトリが実現されている。研究者、或いはエンジニアが、“如何に計測がなされるか” よりも、“如何に容易な計測がなされるか” に重心を据えてしまうために、市販レオメータの課題は数世紀にわたって慣習的に見過ごされきた。この現状から脱却するべく、レオメトリ開発研究を推進し、科学研究の発展に貢献できる手法の提案を、本論文の到達目標とする。そのために、レオメトリの提案・確立、妥当性検証、実践的応用による知見の提示、産業プラントへ応用可能なレオメトリの提案・検証、これら一連の研究成果を段階的に論じ、本レオメトリの剛健さと有用性を証明する。

本論文は全十章で構成されており、各章の概要は以下のとおりである。第一章は序論であり、レオロジー計測の現代にまで至る潮流と、市販レオメータにおける問題、並びに本研究の背景・目的について述べている。第二章では、Tasaka *et al*., Exp. Fluids (2015) が提案した手法をより洗練させ、運動学的レオメトリの原型としての位相差粘性逆解析法が提案・検証される。本章の内容は、Yoshida *et al*., J. Rheol. (2017) において公表済みである。本章では、チキソトロピー性やシェアシニング性、粘弾性、混相実効粘性等を有する複雑流体に対し、実験計測を行い、そのレオロジー評価を試みた。強調すべき知見として、運動学的レオメトリは同一の手法・幾何設計で上記多様に分岐する流体へ適用可能であることが明らかとなった。第三章では、チキソトロピー性を有する粘土懸濁液に対し、第二章で用いられた位相差粘性逆解析法を適用した。本章の内容は、Yoshida *et al*., Appl. Clay Sci. (2018) において公表済みである。先行研究において、粘土懸濁液の降伏臨界せん断速度付近のレオロジー物性は、見かけの降伏応力や見かけの粘性としか評価されていなかった。運動学的レオメトリを用いることで、流速分布によって定義される明確な降伏応力等の評価を行った。第四章では、線形粘弾性解析手法を導入することで、非定常に変形する気泡の実効的な粘性・弾性の定量評価を行った。本章の内容は、Tasaka *et al*., Rheol. Acta (2018) において公表済みである。本手法は、第二、三章でノイズ影響の解決に有効であった周波数空間におけるデータ処理が基軸となっている。また本手法の確立により、運動学的レオメトリの計測能力がより高次な水準へ共時的に引き上げられる。第五章では、第四章で提案・確立された、運動学的レオメトリにおける線形粘弾性解析手法が、市販レオメータと比較・検証されている。本章の内容は、Yoshida *et al*., J. Rheol. (2019) において公表済みである。数種の非ニュートン性流体への比較実験の結果、市販レオメータの盲点を補い得る、運動学的レオメトリの相補的能力が証明された。第六、七章では、運動学的レオメトリを応用し、非ニュートン性流体の未解明問題解決に挑戦した。具体的な対象は、流体緩和時間に起因する粒子配列現象が実効的粘弾性に与える変調 [Yoshida *et al*., Phys. Fluids (2019a)] と、ゲル状流動食品の食べやすさとレオロジー物性の関係 [Yoshida *et al*., Phys. Fluids (2019b)] である。これらは、市販レオメータでは計測不可能なレオロジー的知見であり、本章の研究段階を経て、運動学的レオメトリが新物理の知見創出に足る能力を有することが示された。第八章では、確立された運動学的レオメトリの能力を生かし、チキソトロピー性流体が市販レオメータへ与える不可避の影響について指摘した。特筆すべき知見は、市販レオメータにおける動的粘弾性解析法の一つである LAOS (Large Amplitude Oscillatory Shear) 計測によって、運動学的レオメトリによるレオロジー評価が支持されていることである。第九章では、運動学的レオメトリを産業プラントへ応用可能な形態へ昇華させるべく、管内の非定常流に適用する [特願 2019-056493]。解析解による流速変動からレオロジー評価を逆算的に行い、解析アルゴリズムの妥当性を検証した。第十章は本論文の結言にあたる。第二から九章における重要な知見を要約するとともに、図説によって運動学的レオメトリを体系化し、産業・学理発展を目指した今後の展望を述べる。

# Contents

**Acknowledgment** i

**Abstract** iii

要旨 v

**1 Introduction** 1

1.1 Limitations in commercially-supplied rheometers . . . 1
1.2 Velocity-profiling rheometry . . . 4
1.3 Development of "Kinematic rheometry" . . . 4
1.4 Summary of structures of the thesis . . . 5
References . . . 6

**2 Rheological evaluation of complex fluids using USR in an open container** 9

2.1 Introduction . . . 10
2.2 USR . . . 11
2.2.1 Experimental arrangements . . . 11
2.2.2 Theoretical basis for USR . . . 11
2.2.3 Procedure for evaluating rheological properties . . . 13
2.3 Demonstration of the potential of spinning rheometry when applied to complex fluids . . . 14
2.3.1 Test fluids . . . 14
2.3.2 Results and discussion . . . 16
2.4 Conclusion . . . 25
References . . . 26

**3 Rheological properties of montmorillonite dispersions in dilute NaCl concentration investigated by USR** 29

3.1 Introduction . . . 30
3.1.1 Rheology of montmorillonite dispersions . . . 30
3.1.2 Ultrasonic rheometry . . . 31
3.1.3 Objective . . . 32
3.2 Material and method . . . 32
3.2.1 Conditions of test dispersions . . . 32
3.2.2 Experimental arrangement of ultrasonic spinning rheometry . . . 33
3.2.3 Analysis of effective Newtonian viscosity . . . 33
3.3 Results of rheological evaluation for Mt dispersion . . . 33
3.3.1 Velocity and phase-lag profiles . . . 33
3.3.2 Particle network recovery in the dispersion . . . 35
3.3.3 Evaluations of shear-rate-dependent viscosity . . . 37
3.3.4 Flow curve under shear banding . . . 40
3.4 Conclusion . . . 43
References . . . 43

**4 Linear viscoelastic analysis using frequency-domain algorithm on oscillating circular shear flows for bubble suspensions** **47**
4.1 Introduction . . . 48
4.2 Ultrasonic spinning rheometry . . . 49
4.2.1 Measurement configuration . . . 49
4.2.2 USR concept and procedure . . . 49
4.3 Influence of measurement error on USR . . . 50
4.3.1 Viscoelastic analysis of bubble suspensions . . . 50
4.3.2 Numerical evaluation of influence of noise . . . 51
4.4 Frequency-domain analysis . . . 53
4.4.1 Theory . . . 53
4.4.2 Viscometry . . . 54
4.4.3 Application of viscometry . . . 55
4.4.4 Linear viscoelastic analysis of bubble suspension . . . 58
4.5 Conclusion . . . 60
References . . . 60

**5 Efficacy assessments in USR: Linear viscoelastic analysis on non-Newtonian fluids** **63**
5.1 Introduction . . . 64
5.1.1 Problems in rotational shear rheometers . . . 64
5.1.2 Rheometry coupled with velocimetry . . . 64
5.2 Basic concept of USR . . . 66
5.2.1 Experimental apparatus . . . 66
5.2.2 Theoretical basis for the linear viscoelastic analysis . . . 67
5.2.3 Demonstration of the linear viscoelastic analysis on an silicone oil . . . 68
5.3 Linear viscoelastic analysis of non-Newtonian fluids . . . 70
5.3.1 Test fluid conditions and device for comparative experiment . . . 70
5.3.2 CMC solution . . . 72
5.3.3 Mt dispersion . . . 75
5.4 Efficacy of USR as a complementary technique . . . 81
5.5 Conclusion . . . 82
References . . . 82

**6 Effective viscoelasticity of non-Newtonian fluids modulated by large-spherical particles aligned under unsteady shear** **85**
6.1 Introduction . . . 86
6.2 Method: Ultrasonic spinning rheometry (USR) . . . 87
6.2.1 Experimental setup and theoretical basis . . . 87
6.2.2 Experimental conditions . . . 89
6.3 Experimental results of the linear viscoelastic analysis . . . 90
6.3.1 Rheological evaluations of test fluids without dispersed particles . . . 90
6.3.2 Rheological evaluation of silicone oil with dispersed particles . . . 91
6.3.3 Rheological evaluation of the PAM solution with dispersed particles . . . 93
6.3.4 Rheological evaluation of the CMC solution with dispersed particles . . . 94
6.4 Discussion . . . 96
6.4.1 Verification of dominant factors of the alignment using a toy model . . . 96
6.4.2 Macro-rheological characteristics modulated by alignments . . . 98
6.5 Conclusion . . . 100

References . . . 100

**7 USR test on the rheology of gelled food for making better tasting desserts 103**
7.1 Introduction . . . 104
7.2 Materials and methodology . . . 105
7.2.1 Recipe for test materials . . . 105
7.2.2 Steady rotational and oscillatory shear tests with the standard rheometer . . . 105
7.2.3 Ultrasonic spinning rheometry (USR) . . . 106
7.3 Rheological evaluations by the standard rheometer . . . 107
7.3.1 Results of the steady rotational tests . . . 107
7.3.2 Results of oscillatory tests . . . 109
7.3.3 Summary: the sources of physical inaccuracies in a standard rheometer . . . 111
7.4 USR tests of the rheology of gelled food . . . 111
7.4.1 Rheological evaluation on phase lag in velocity distributions . . . 111
7.4.2 Results of the linear viscoelastic analysis . . . 113
7.4.3 Discussion: the rheology of a better-prepared dessert . . . 116
7.5 Conclusion . . . 116
References . . . 117

**8 Thixotropic effects on a standard rheometer test, elucidated by large amplitude oscillatory shear & USR 119**
8.1 Introduction . . . 120
8.2 Materials and method . . . 121
8.2.1 Thixotropy in montmorillonite (Mt) dispersion . . . 121
8.2.2 Ultrasonic spinning rheometry (USR) . . . 122
8.2.3 Standard shear rheometer . . . 123
8.3 Rheological evaluations of Mt dispersions w/o and with NaCl . . . 124
8.3.1 Dynamic viscoelasticity examined by rotational rheometer . . . 124
8.3.2 Comparison of rotational rheometer data of LAOS and USR . . . 126
8.4 Discussion . . . 128
8.4.1 Summary of findings from LAOS/USR measurements . . . 128
8.4.2 Fourier analysis of the waves considered to result from elastic instabilities . . . 128
8.4.3 Consideration of artifacts due to thixotropy in standard rheometers . . . 130
8.5 Conclusion . . . 131
References . . . 131

**9 Development of ultrasonic in-line rheometry (UIR): Evaluation of viscosity and pressure gradient from velocity profiles of exact solution 133**
9.1 Introduction . . . 134
9.2 Theoretical basis of ultrasonic in-line rheometry (UIR) . . . 135
9.3 Algorithm validations of UIR by inverse evaluations from the exact solution . . . 136
9.3.1 Velocity profiles of exact solution with artificial noise . . . 136
9.3.2 UIR validations as a viscometry . . . 140
9.4 Conclusion . . . 146
References . . . 147

**10 Concluding remarks 149**

**A Inner structure visualization of fresh fruits utilizing ultrasonic velocity profiler** **153**
A.1 Introduction . . . 154
A.2 Ultrasonic Doppler–echo visualization . . . 155
A.2.1 System configuration . . . 155
A.2.2 Procedure of ultrasonic Doppler–echo visualization . . . 155
A.2.3 Echo intensity field expected from numerical simulation . . . 159
A.3 Practical application to fresh fruits . . . 162
A.4 Conclusion . . . 166
References . . . 166

**B Supplemental information to upgrade USR** **169**
B.1 Noise evaluation in measured velocity . . . 169
B.1.1 Statistical calculation for obtained velocity . . . 169
B.1.2 Production of artificial random noises with normal distribution . . . 170
B.2 Accuracy and precision assessments . . . 170
B.2.1 Phase lag averaging with short time DFT . . . 170
B.2.2 Spectral subtraction method utilizing periodic functionalized algorithm . . . 171
B.3 Influence from radial gradient of viscosity profile in phase-lag analysis . . . 172
B.4 Summary . . . 174
References . . . 175

**C Rheological evaluation of non-Newtonian effects on Newtonian fluid with localized bubble dispersions** **177**
C.1 Introduction . . . 177
C.2 Experimental setup . . . 177
C.3 Statistics of viscoelastic analysis in the region of localized bubble dispersions . . . 178
C.4 Summary . . . 179
References . . . 180

**Curriculum Vitae** **181**

**List of Publications** **183**

Chapter 1

# Introduction

## Contents


1.1 Limitations in commercially-supplied rheometers . . . . . 1
1.2 Velocity-profiling rheometry . . . . . 4
1.3 Development of "Kinematic rheometry" . . . . . 4
1.4 Summary of structures of the thesis . . . . . 5
References . . . . . 6


## 1.1 Limitations in commercially-supplied rheometers

In the engineering field of new material development, conventional fluid mechanics cannot always explain behaviors of the materials. This common perception has been regarded as an significant issue in the industry utilizing materials with atypical characteristics. In recent years, the demand to develop a tool to comprehend thermofluid dynamics is arising from the existence of various physical properties, e.g. highly-functional liquid crystal, high-value added liquid food, micro-bubble suspension, etc. However, performing empirical trials and tribulations is still regarded as the main tool to control such thermofluid behaviors with complexity, because understanding "rheology" explaining complex fluid dynamics is still at a developing stage.

The origin of experimental evaluation of elastic properties was established by Robert Hooke in 1678, as "True Theory of Elasticity". He studied classical elasticity that spring stress is in the same proportion with the deformation, and the mechanical relation is given by

$$\tau = G\gamma, \tag{1.1}$$

where $\tau$, $G$, and $\gamma$ denote shear stress, modulus, and strain.

After that, in 1687, Isaac Newton established the following important principle based on fluid dynamics such that "The resistance which arises from the lack of slipperiness of the parts of the liquid, other things being equal, is proportional to the velocity with which the parts of the liquid are separated from one another". In this sentence, "the lack of slipperiness" is better known as viscosity of fluids in the present. The relationship can be described as

$$\tau = \mu\dot{\gamma}, \tag{1.2}$$

where fluids obeying this law are categorized as Newtonian fluids.

It has been trusted that properties of all materials can be dealt with Hooke's law or Newton's law for two centuries. Imaginably, however, these linear equations must not be applied to complex materials, which concerns are well-known and pointed out in uncounted previous reports. At the beginning of the twentieth century, non-linearity between stress and deformation has attracted the attention of researchers, and further works are still undergoing with increasing doubts about the applicability of those linear equations.

To understand such complex fluid behaviors (e.g. printing inks, polymer, detergents, oils, biological materials, food processing, etc) that cannot be assumed by the linear functional laws, Hooke's and Newton's law, "Rheology" has developed as a broad-based study between deformations and flows. The term, rheology, was coined by Eugene C. Bingham in 1920, and several tools have been developed to evaluate rheological properties of complex fluids. The tool measuring rheological properties is here termed "Rheometer", and the methodology is called "Rheometry" in the present. The goal of rheometry development is to fully comprehend the rheology of all soft materials, and this leads to ensuring the quality of manufactured materials and the optimization of systems in industries. It will raise the quality level of various components in the following industries, such as in polymer producing, biological and food processing, and multiphase dispersion controlling.

To satisfy rheological evaluations with high accuracy and precision, we must choose an appropriate geometry although there exist not a few kind of geometries to quantify a wide variety of complex fluids. Needless to mention, each geometry has both advantages and disadvantages. Typical rheometers are depicted as the examples of systems with different geometries [see Fig. 1.1] that measure the axial torque via solid walls with a specific gap. Parallel-plate type geometry measures wide range of viscosity [Fig. 1.1(a)]. The gap between the solid wall is adjustable, however, in this gap there is a radial distribution of the applied shear strain/rate. Cone plate type geometry keeps the applied shear strain/rate constant though the minimum gap is fixed to the certain distance $O(0.01 - 0.1$ mm) [Fig. 1.1(b)]. Taylor–Couette type geometry ensures the rheological evaluation even as small torque values because of its large-contact area to test materials [Fig. 1.1(c)]. The fundamental concept for the geometry of Fig. 1.1(d) is improvement of the contact area from Fig. 1.1(c). However, influences of flow instabilities, e.g. Taylor vortex, elastic instability and more, should be regarded for ensuring accuracy of measurements using such Couette geometry. Recent representative measurement methods that have been developed int the past decade are the twin-drive [Fig. 1.1(e)] and ball measuring [Fig. 1.1(f)] method. The twin-drive type measures the torque and rotational angle by both upper and lower plates; the geometry of the twin-drive type is basically same with that of Fig. 1.1(a). This applies twice as much shear amplitudes against test fluids compared to that of Fig. 1.1(a). The ball-measuring type is applicable to test material with large-dispersions by measuring the rheological resistance from the attached sphere, since it does not require a narrow gap shown in the geometries of Fig. 1.1(a)–(e). However, a strong assumption such as ideal laminar velocity around the sphere is required even in the case where the fluid includes large dispersions, because the Stokes law must be satisfied to ensure the accuracy of the methodology. Not only deformation-based but also flow-based rheometers in commercially-supplied systems have limitations. As examples of flow-based rheometers, there are cap-type, spread-type, bubble-type, falling-ball, and capillary rheometer as shown in Fig. 1.1(g)–(k). These rheometers measure Newtonian viscosity with high accuracy, but the application to non-Newtonian fluids is difficult as the approximations of flow behavior are theoretically based on Newtonian fluids; there is no proper solution against unexpected behaviors arising from complex fluids. This is why the torque/rotation-angle-based rheometers are generally used in the present industries and scientific researches.

Several rheometers with different geometries have been proposed to be applicable to evaluate the complex rheology, and most of the rheometers are based on axial torque measurement consistently, in other words, little efforts have been made to establish other methods instead of torque/rotation-angle measurement due to the origin of rheology. As mentioned at the beginning, there are significant differences in the two different roots in the experimental approach for rheological understanding, whether “the deformation” or “the flow” is regarded to understand rheology. Torque/rotation-angle-based rheometers originate “the deformation”, and these rheometers have already been established. Improving the sensitivity of torque measurement can ensure high precision of rheological evaluations, however, at the same time, rheometers encounter other serious difficulties, such as shear history effects [1–4], wall-slip [5–7], shear banding [8–13], elastic instability [14–16], and more, in the evaluation of complex materials. Especially at critical-shear conditions where the stress approaches the yield stress, such problems of torque/rotation-angle-based rheometer measurements become prominent;

Wolthers *et al.* [2] explored the shear history dependence of viscosity in aggregated-colloidal dispersions and concluded that the observed rheological behavior depends on the specific geometry of the shear rheometers due to effects of thixotropy and sedimentation. Nechyporchuk *et al.* [5] applied the cone-plate geometry and reported that wall-slip was detected at low shear rates for fluids with gel-like and shear thinning properties. From these experimental observations, they concluded that the obtained values include unavoidable measurement errors when wall-slip occurs. Fardin *et al*. [15] investigated the elastic instability arisen from the unstable shear banding, when shear stress in flow curves exhibits plateau with respect to shear rate. Further, this phenomenon indicates unsteady feature, that is, there is a significant difficulty in elimination of the influence even with the improvement of the torque meter. Thus, such improvement on the torque sensitivity does not always contribute to the assurance of accuracy of the standard rheometers.

Several attempts have been made to prevent occurrences of the measurement difficulties in standard rheometers by improving the post processing or geometry; to solve problems arising from non-ideal flow condition, semi analytical techniques, which solve the inverse problem to estimate original velocity profiles in wider-gap Couette rheometry, was proposed, termed as the “Couette inverse problem” [17, 18]. As examples of another trials, improvement of surface texture on the solid wall exposed the test material [19, 20]. These efforts may “modify” the influences of wall-slip or rheological inhomogeneity of test material. Unfortunately, these efforts cannot be a universal solution to avoid the unexpected phenomena (e.g. shear banding and elastic instability) arising from characteristics of the non-Newtonian fluid, because the considerable problems may not be caused by the surface texture, etc.

To be brief, though there are many approaches for rheological evaluations of non-Newtonian fluids, most are limited treatments solving the problem for specific test fluids. Recent years, several approaches [21, 22] have been explored to attain rheological indexes by applying functional approximation to flow curves obtained from the standard rheometer. However, obtained indexes should be considered because of the existence of unpredictable/unforeseen phenomena and limitations of

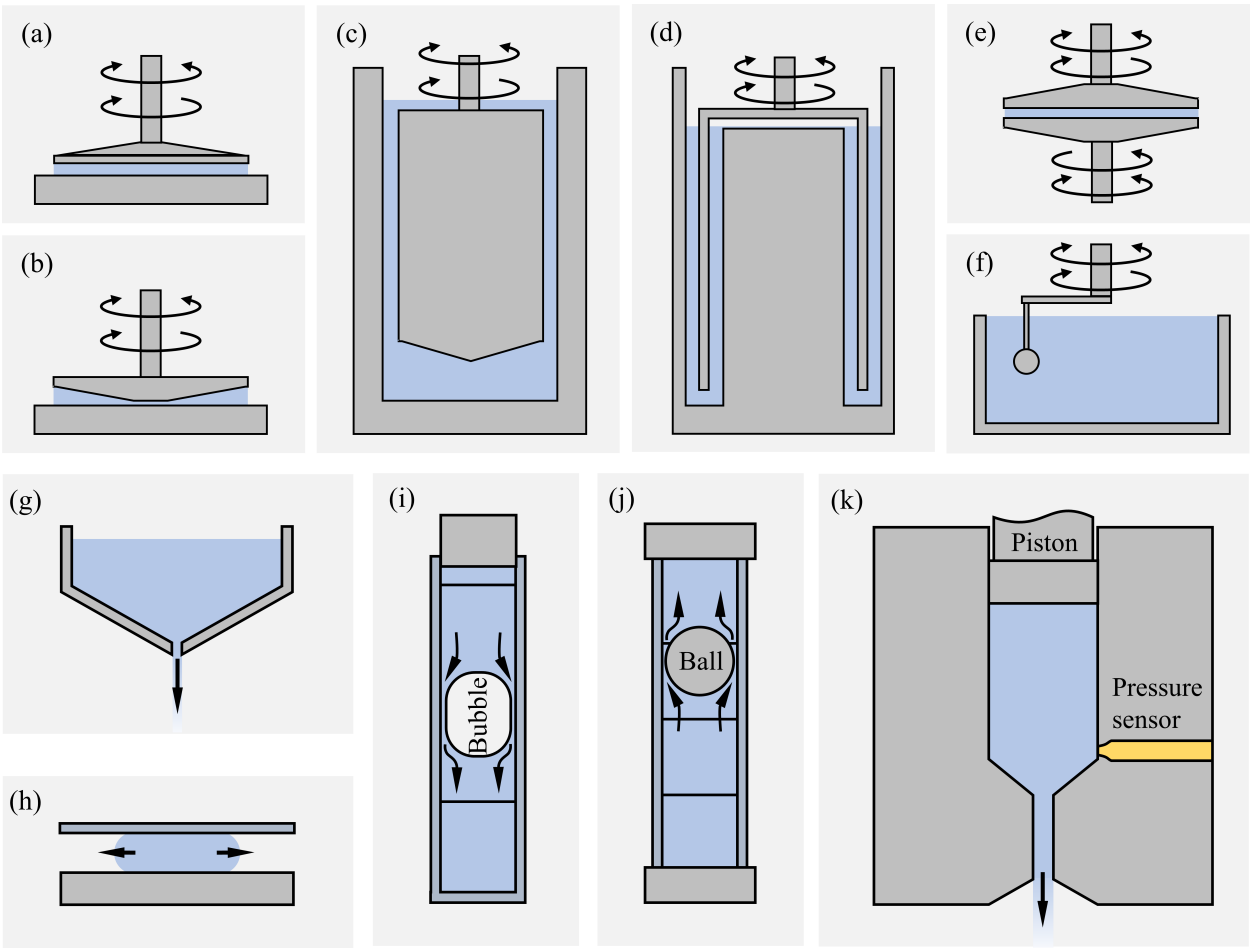


Figure 1.1: Schematics of commercially-supplied rheometers; (a) parallel-plate type, (b)cone plate type, (c) Taylor–Couette type, (d) modified Taylor–Couette type, (e) twin-drive parallel-plate type, (f) ball-measuring type, (g) cup type, (h) spread-plate type, (i) bubble type, (j) falling-ball type, and (k) capillary type.

methodology as mentioned above. Fitting constitutive equations for the measured torque data, which may include artifacts arising from geometry, is also not an appropriate way to evaluate true-rheological property. Therefore, rheological indexes obtained from rheometers have the possibility of including unexpected artifacts and thus, it is easily imaginable that numerical simulations done using these indexes will include errors and will also be incorrect.

## 1.2 Velocity-profiling rheometry

To fully understand the true-rheology of such complex materials, the "flow" must be taken account. Though we did not know the appropriate way to directly measure the flow velocity before two centuries, we have now established various techniques to quantify the velocity information. By measuring spatiotemporal velocity distributions, we can utilize the information of fluid flows that has the potential to reflect all rheological information, and finally, its establishment will lead to overcoming the common problem originated from non-ideal, unknown velocity profiles; we call it "velocity-profiling rheometry".

For velocity-profiling rheometries, various velocimetries have been applied, e.g. ultrasonic velocity profiling (UVP) [24–27], ultrasonic echo-imaging [28, 29], ultrasonic imaging velocimetry (UIV) [30, 31], particle imaging velocimetry (PIV) [32–34], magnetic resonance imaging (MRI) velocimetry [35, 36], and laser Doppler velocimetry (LDV) [37, 38]. As examples of rheometry with optical velocimetry, Marín-Santibáñez *et al*. [32] examined rheological evaluations by utilizing a combined method of rheometry and PIV. Also, Serrano-Aguilera *et al*. performed rheological evaluation by conventional rotational rheometer with wide gap Couette flow, adapting PIV measurement. With PIV and LDV, only transparent fluids are applicable, whereas most complex fluids, such as dense suspensions, colloid dispersions, multiphase fluids, or similar, are all opaque. The MRI velocimetry can perform visualizations of opaque and multiphase fluids, however, it requires very large measurement facilities, and monitoring is handicapped to low temporal resolutions due to fluid flow.

Ultrasonic measurement techniques have advantages, such as offering ease of handling and the option of employing opaque fluids. Ouriev and Windhab [26] proposed a combined technique of UVP measurements and pressure difference measurements, which is termed UVP-PD in-line rheometry. This is used as a practical tool in the food processing industry [27], since it has the advantages of in-line measurements from outside of steel pipe walls. Derakhshandeh *et al*. [25] performed measurements of transient behaviors of thixotropic fluids using a Couette rheometer with a wide gap and UVP. This can detect yielding regions of the fluid from quasisteady velocity profiles, although the torque measurements may be influenced by wall-slip, which will lead to errors in evaluations of the rheological characteristics. Later, the coupling of the conventional rheometer and ultrasonic imaging technique, and the spatiotemporal analyses were developed. As one of the examples, Gallot *et al*. [28] proposed a technique that reveals the unstable shear-banded flow of non-Newtonian fluids. As a recent development of ultrasonic rheometry, Gurung *et al* [30] reported a novel rheometry that combines an ultrasonic scanning technique and PIV (UIV or echo-PIV), and they performed real-time measurement of opaque fluid flows with complex rheology in particle-laden fluids. Originally, this technique has mainly been used to measure flow behaviors in blood vessels in the field of medical engineering. Previous research has dealt with only time averaged velocity profile that was limited to steady flow states. Since one of the non-Newtonian characteristics involves both shear-rate-dependence in the rheological properties and time-dependence, the techniques must be able to attain detailed time-dependent properties.

## 1.3 Development of "Kinematic rheometry"

For the past several years, our group has progressively presented velocity-profiling rheometry, termed "ultrasonic spinning rheometry" (USR). Sakurai *et al*. [39] examined ultrasonic velocity profiling to reveal the rheology of transient bubble deformations. Spatio-temporal velocity information was here utilized with equation of motion, although noise augmentations could be found due to differential calculation in the equation. After that, Shiratori *et al*. [40] visualized the shear rate and strain field for non-Newtonian fluids and ensured the potential of the pilot kinematic rheometry. However, a problem of noise augmentation which arises from differential terms in the equation of motion still remains. Because of the generation of spiky noise in the measured velocity profiles by UVP, the direct differential calculations using velocity profiles would not be considered as an adequate way to satisfy the equation of motion. To overcome this limitation, Tasaka *et al*. [41] utilized the Fourier transform for velocity profiles in periodic oscillatory flows, and the analysis performs effectively to avoid the influence of noise augmentation.

A novel kinematic rheometry presented here is based on the stream of previous researches (see [42–44]), and it is expected to evaluate "true-rheological properties". The "kinematic rheometry" aims to evaluate the complex rheology by the kinematics-based idea. The basic concept of this rheometry is that velocity profiles of unsteady shear flows are substituted into the equation of motion and is solved by utilizing Fourier transformation. Although UVP can obtain one velocity component

parallel to the line of propagation of ultrasonic waves, this rheometry is accomplished by a single UVP in cases satisfying the assumption of one-directional shear flow in the azimuthal direction. Since this would make it possible to quantify shear-rate-dependent properties over a wider range of shear rates obtained from single measurements, the kinematic rheometry is expected to measure spatial profiles of local rheological properties.

Most rheologists tend to trust the obtained data injudiciously because they do not have an interest in measurement methodology but the rheological evaluation itself. That is to say, it is not important that "if the obtained data is physically meaningful or not" but that "if the rheological evaluations are easy or not". As a reason, most development research of rheometry grows stagnant after publishing and there is a little effort to prove the efficacy of rheometry regarding the potential to find a novelty in physics. In this study, a novel rheometry that is able to contribute to research that reveals scientific findings is presented, accomanied by methodology presentation, validation and application revealing physical properties. Further, to complete the kinematic rheometry for both laboratory and industry use, the methodology is also introduced to the pipeline flow measurement. By a series of these attempts, "a useful tool" in the wide fields of academic research and industrial development is completed. Emphatically, the kinematic rheometry does not aim for rheological evaluation of the fluids with higher viscosity than $O(10^3\ \mathrm{Pa \cdot s})$, lower viscosity than $O(10^{-3}\ \mathrm{Pa \cdot s})$, and perfect-elasticity, where those already could be evaluated with high-accuracy using conventional rheometers; in other words, the ultimate aim of the kinematic rheometry here is to fill "the hole" that cannot be measured by the conventional rheometers. This realization of kinematic rheometry will help to escape from the situation in rheological development that has been fallen between the cracks during the stream of time for a few centuries.

## 1.4 Summary of structures of the thesis

To realize the objective of this study, research is progressed through stages in each chapter as follows:

In Chapter 2, as the bleeding-edge state of kinematic rheometry, effective Newtonian viscosity analysis is performed by streamlining from the method presented by Tasaka *et al*. (2015) [41]. As a demonstration of the methodology, the kinematic rheometry is applied to various kinds of fluids with different rheological characteristics, and its robustness is experimentally proven. What is notable is that the complex fluid rheology can be equally evaluated without changing the geometry and analytical method, whereas at the standard shear rheometer, both the geometry and the method must be changed depending on the rheological characteristics of the test fluid. (The work in this chapter was published in [45])

In Chapter 3, the kinematic rheometry presented and established in Chapter 2 is utilized for revealing unexplained issues in clay science. The existence of characteristic viscoelasticity in montmorillonite clay dispersion showing thixotropy is highlighted and discussed. From this effort, the potential of the kinematic rheometry to reveal the physical findings is clarified. (The matter in this chapter was published in [46])

In Chapter 4, an idea of linear viscoelastic analysis is introduced to the kinematic rheometry for raising the level of capability to understand rheology. Here, evaluating the viscoelastic response from the dispersed bubbles deformed by unsteady oscillations in Newtonian fluid, the efficacy of the kinematic rheometry is discussed. The benefit arising from this idea is that the elastic characteristics that have been understood as the inclusive effect to the effective viscosity can be evaluated separately. (The work in this chapter was published in [47])

In Chapter 5, the kinematic rheometry based on the linear viscoelastic analysis that has been presented in Chapter 4 is validated by comparative experiment with a rotational shear rheometer with parallel plate geometry. The efficacy of the kinematic rheometry is proven as a novel method having the potential to play a complementary role in covering the hole that cannot be filled by results from standard rheometers. (The work in this chapter was published in [48])

In Chapter 6, the kinematic rheometry elucidates effective viscoelasticity of non-Newtonian fluids as macro rheology modulated by the alignment of spherical particles that is closely related to the relaxation time of fluid media. In addition, quantitative evaluations are performed regarding more practical parameters to deeply discuss the rheology, such as Weissenberg and Deborah numbers. This finding is one of the most significant examples for elucidating the unexplained phenomena which occurs when using a standard rheometer due to the limitation of methodology, so it is emphasized that the kinematic rheometry has great potential in finding unsolved problems in complex rheology. (The work in this chapter was published in [49])

In Chapter 7, the rheological evaluations of gelled food with complex rheological properties are examined by utilizing both the standard rheometer and kinematic rheometry. The aim of this study is to clarify the rheological properties of gelled foods that may relate to flows in the swallowing process of complex food materials. The highlighted finding here is that stability of the food materials in the unsteady shear displays great importance in understanding which rheology indicates better texture. (The work in this chapter was published in [50])

Through the study in Chapters 6 and 7, it is proven that the established kinematic rheometry has a great potential for elucidating the rheological issues which is unexplained by using standard rheometers.

In Chapter 8, by considering the rheological evaluations using both large amplitude oscillatory shear (LAOS) measurement in the standard rheometer and the kinematic rheometry, the influence causing the considerable errors in standard rheometer measurement from thixotropic characteristics is clarified.

From findings in the all of Chapters 2–8, the efficacy of kinematic rheometry for the scientific research is completely established.

In Chapter 9, by applying the theory of kinematic rheometry to unsteady flows in a circular pipe, the methodology is innovated to be used in the industry as a clamping on system. In this study, the algorithm for evaluating the rheology from the pipeline flows is presented and is validated by inverse-calculations from the velocity profiles obtained by an exact solution.

In Chapter 10, the notable findings in each chapter are summarized.

## References


[1] J. Mewis, and G. De Cleyn, "Shear history effects in the spinning of polymers," AIChE Journal, 28(6), 900–907 (1982).

[2] W. Wolthers, M. H. G. Duits, D. Van Den Ende, and J. Mellema, "Shear history dependence of the viscosity of aggregated colloidal dispersions," J. Rheol. 40, 799–811 (1996).

[3] C. Viseras, G. H. Meeten, and A. Lopez-Galindo, "Pharmaceutical grade phyllosilicate dispersions: the influence of shear history on floc structure," Int. J. Pharm.,182(1), 7–20 (1999).

[4] L. Shan, K. Chen, M. Zhou, X. Zhang, Y. Meng, and Y. Tian, "Shear history effect of magnetorheological fluids," Smart Mater. Struct. 24(10), 105030 (2015).

[5] O. Nechyporchuk, M. N. Belgacem, and F. Pignon, "Rheological properties of micro-/nanofibrillated cellulose suspensions: Wall-slip and shear banding phenomena," Carbohydr. Polym. 112, 432–439 (2014).

[6] S. Q. Wang, S. Ravindranath, and P. E. Boukany, "Homogeneous shear, wall slip, and shear banding of entangled polymeric liquids in simple-shear rheometry: A roadmap of nonlinear rheology," Macromolecules 44(2), 183–190 (2011).

[7] K. Yang, and W. Yu, "Dynamic wall slip behavior of yield stress fluids under large amplitude oscillatory shear," J. Rheol. 61(4), 627–641 (2017).

[8] M. Ito, Y. Yoshitake, and T. Takahashi, "Shear-induced structure change in shear-banding of a wormlike micellar solution in concentric cylinder flow," J. Rheol. 60, 1019–1029 (2016).

[9] C. J. Dimitriou, L. Casanellas, T. J. Ober, and G. H. Mckinley, "Rheo-PIV of a shear-banding wormlike micellar solution under large amplitude oscillatory shear," Rheol. Acta. 51, 395–411 (2012).

[10] G. Ovarlez, S. Rodts, X. Chateau, and P. Coussot, "Phenomenology and physical origin of shear localization and shear banding in complex fluids," Rheol. Acta 48, 831–844 (2009).

[11] T. Divoux, M. A. Fardin, S. Manneville, and S. Lerouge, "Shear banding of complex fluids," Annu. Rev. Fluid Mech. 48, 81–103 (2016).

[12] P. Fischer, E. K. Wheeler, and G. G. Fuller, "Shear-banding structure orientated in the vorticity direction observed for equimolar micellar solution," Rheol. Acta 41, 35–44 (2002).

[13] S. Manneville, "Recent experimental probes of shear banding," Rheol. Acta 47, 301–318 (2008).

[14] G. H. McKinley, J. A. Byars, R. A. Brown, and R. C. Armstrong, "Observations on the elastic instability in cone-and-plate and parallel-plate flows of a polyisobutylene Boger fluid," J. Non-Newton. Fluid Mech. 40, 201–229 (1991).

[15] M. A. Fardin, C. Perge, L. Casanellas, T. Hollis, N. Taberlet, J. Ortín, S. Lerouge, and S. Manneville, "Flow instabilities in large amplitude oscillatory shear: a cautionary tale," Rheol. Acta 53, 885–898 (2014).

[16] M. A. Fardin, L. Casanellas, B. Saint-Michel, S. Manneville, and S. Lerouge, "Shear-banding in wormlike micelles: Beware of elastic instabilities," J. Rheol. 60, 917–926 (2016).

[17] Y. L. Yeow, W. C. Ko, and P. P. Tang, "Solving the inverse problem of Couette viscometry by Tikhonov regulation," J. Rheol. 44, 1335–1351 (2000).

[18] C. Ancey, "Solving the Couette inverse problem using a waveletvaguelette decomposition," J. Rheol. 49, 441–460 (2005).

[19] C. Carotenuto, and M. Minale, "On the use of rough geometries in rheometry," J. Non-Newton. Fluid Mech. 198, 39–47 (2013).

[20] L. P. Paduano, T. Schweizer, C. Carotenuto, J. Vermant, and M. Minale, "Rough geometries with viscoelastic Boger fluids: Predicting the apparent wall slip with a porous medium approach," J. Rheol. 63(4), 569–582 (2019).

[21] A. Y. Malkin, I. Masalova, D. Pavlovski, and P. Slatter, "Is the choice of flow curve fitting equation crucial for the estimation of pumping characteristics?," Appl. Rheol. 14(2), 89–95 (2004).
[22] A. Potanin, "3D simulations of the flow of thixotropic fluids, in large-gap Couette and vane-cup geometries," J. Non-Newton. Fluid Mech. 165(5–6), 299–312 (2010).
[23] R. I. Dekker, M. Dinkgreve, H. de Cagny, D. J. Koeze, B. P. Tighe, and D. Bonn, "Scaling of flow curves: Comparison between experiments and simulations," J. Non-Newton. Fluid Mech. 261, 33–37 (2018).
[24] *Ultrasonic Doppler Velocity Profiler for Fluid Flow*, Springer Science, edited by Y. Takeda (Springer, Tokyo, 2012).
[25] B. Derakhshandeh, D. Viassopoulos, and S. G. Hatzikiriako, "Thixotropy, yielding and ultrasonic Doppler velocimetry in pulp fibre suspensions," Rheol. Acta 51, 201–214 (2012).
[26] B. Ouriev, and E. Windhab, "Transient flow of highly concentrated suspensions investigated using the ultrasound velocity profiler–pressure difference method," Meas. Sci. Technol. 14, 1963–1972 (2003).
[27] J. Wiklund, and M. Stading, "Application of in-line ultrasound Doppler-based UVP–PD rheometry method to concentrated model and industrial suspensions," Flow Meas. Instrum. 19, 171–179 (2008).
[28] T. Gallot, C. Perge, V. Grenard, M. A. Fardin, N. Taberlet, and S. Manneville, "Ultrafast ultrasonic imaging coupled to rheometry: Principle and illustration," Rev. Sci. Instrum. 84, 045107 (2013).
[29] C. Perge, N. Taberlet, T. Gibaud, and S. Manneville, "Time dependence in large amplitude oscillatory shear: A rheo-ultrasonic study of fatigue dynamics in a colloidal gel," J. Rheol. 58, 1331–1357 (2014).
[30] A. Gurung, J. Haverkort, S. Drost, B. Norder, J. Westerweel, C. Poelma, "Ultrasound image velocimetry for rheological measurements," Meas. Sci. Technol. 27, 094008 (2016).
[31] C. Poelma, "Ultrasound imaging velocimetry: A review," Exp. Fluids 58, 3 (2017).
[32] Marín-Santibáñez, B. M., Pérez-González, J., De Vargas, L., Rodríguez-González, F., and Huelsz, G., "Rheometry–PIV of Shear-Thickening Wormlike Micelles," Langmuir, 22(9), 4015–4026 (2006).
[33] F. Rodrigez-Gonzalez, J. Perez-Gonzalez, L. De Vargas, and B. M. Marin-Santibane, "Rheo-PIV analysis of the slip flow of a metallocene linear low density polyethylene melt," Rheol. Acta 49, 145–154 (2010).
[34] J. Perez-Gonzalez, J. J. Lopez-Duran, B. M. Marin-Santibanez, and F. Rodriguez-Gonzalez, "Rheo-PIV of a yield-stress fluid in a capillary with slip at the wall," Rheol. Acta 51, 937–946 (2012).
[35] S. Jarny, N. Roussel, S. Rodts, F. Bertrand, R. Le Roy, and P. Coussot, "Rheological behavior of cement pastes from MRI velocimetry," Cement Concrete Res. 35, 1873–1881 (2005).
[36] G. Ovarlez, F. Bertrand, and S. Rodts, "Local determination of the constitutive law of a dense suspension of noncolloidal particles through magnetic resonance imaging, " J. Rheol. 50, 259–292 (2006).
[37] L. M. Quinzani, R. C. Armstrong, and R. A. Brown, "Use of coupled birefringence and LDV studies of flow through a planar contraction to test constitutive equations for concentrated polymer solutions," J. Rheol. 39, 1201–1228 (1995).
[38] J. P. Rothstein, and H. M. Gareth, "Inhomogeneous transient uniaxial extensional rheometry," J. Rheol. 46, 1419–1443 (2002).
[39] K. Sakurai, Y. Tasaka, Y. Murai, "Modification of effective viscosity on bubbly flows due to transient bubble deformations," kikaib 79(797), 1–11 (2013) in Japanese.
[40] T. Shiratori, Y. Tasaka, Y. Murai, and Y. Takeda, "Development of ultrasonic visualizer for capturing the characteristics of viscoelastic fluids," J. Vis. 16, 275–286 (2013).
[41] Y. Tasaka, T. Kimura, and Y. Murai, "Estimating the effective viscosity of bubble suspensions in oscillatory shear flows by means of ultrasonic spinning rheometry," Exp. Fluids 56, 1867 (2015).
[42] T. Shiratori, Y. Tasaka, Y. Oishi, and Y. Murai, "Ultrasonic velocity profiling rheometry based on a widened circular Couette flow," Meas. Sci. Thechnol. 26, 085302 (2015).
[43] T. Shiratori, Y. Tasaka, and Y. Murai, "Rapid rheological characterization of viscoelastic fluid based on spatiotemporal flow velocimetry," Exp. Therm. Fluids Sci. 71, 1–13 (2016).
[44] Y. Tasaka, T. Shiratori, T. Yoshida, and Y. Murai, "Rheometry utilizing ultrasonic velocity profiler —Importance of flow measurement and propositions—," Journal of the Visualization Society of Japan 36(142), 7–11 (2016) in Japanese.
[45] T. Yoshida, Y. Tasaka, and Y. Murai, "Rheological evaluation of complex fluids using ultrasonic spinning rheometry in an open container," J. Rheol. 61, 537–549 (2017).
[46] T. Yoshida, Y. Tasaka, S. Tanaka, H. J. Park, and Y. Murai, "Rheological properties of montmorillonite dispersions in dilute NaCl concentration investigated by ultrasonic spinning rheometry," Appl. Clay Sci. 161, 513–523 (2018).
[47] Y. Tasaka, T. Yoshida, R. Rapberger, and Y. Murai, "Linear viscoelastic analysis using frequency-domain algorithm on oscillating circular shear flows for bubble suspensions," Rheol. Acta 57, 229–240 (2018).
[48] T. Yoshida, Y. Tasaka, and Y. Murai, "Efficacy assessments in ultrasonic spinning rheometry: Linear viscoelastic analysis on non-Newtonian fluids," J. Rheol. 63, 503–517 (2019).

[49] T. Yoshida, Y. Tasaka, and Y. Murai, "Effective viscoelasticity of non-Newtonian fluids modulated by large-spherical particles aligned under unsteady shear," Phys. Fluids 31(10), 103304 (2019).
[50] T. Yoshida, Y. Tasaka, and P. Fischer, "Ultrasonic spinning rheometry test on the rheology of gelled food for making better tasting desserts," Phys. Fluids 31(11), 113101 (2019).

Chapter 2

# Rheological evaluation of complex fluids using USR in an open container

## Contents


**2.1 Introduction . . . . . 10**
**2.2 USR . . . . . 11**
2.2.1 Experimental arrangements . . . . . 11
2.2.2 Theoretical basis for USR . . . . . 11
2.2.3 Procedure for evaluating rheological properties . . . . . 13
**2.3 Demonstration of the potential of spinning rheometry when applied to complex fluids . . . . . 14**
2.3.1 Test fluids . . . . . 14
2.3.2 Results and discussion . . . . . 16
**2.4 Conclusion . . . . . 25**
**References . . . . . 26**


## Preface

The aim in this chapter is to present and streamline kinematic rheometry at primary development stage with demonstrations of fluids with various rheological characteristics. Effective viscosity evaluations based on phase-lag analysis here are performed, and the potential of kinematic rheometry is stressed to realize quantitative evaluations of complex-rheological behavior. This work was published in Yoshida *et al*., J. Rheol. (2017).

## Abstract


We propose a rheometry using ultrasonic velocity profiling (UVP) that visualizes and evaluates quantitatively opaque complex fluids in a cylindrical open vessel performing unsteady rotation. The methodology termed "ultrasonic spinning rheometry (USR)" is expected to provide details of various rheological properties. In our study of USR applications, an enhancement in measuring some rheological properties was achieved for three different non-Newtonian fluids. For quantitative evaluations, we focused on momentum propagation in unsteady shear flows from an oscillating cylindrical container. In such flows, this propagation is represented in the radial profiles of the phase lag of velocity fluctuations. The phase lag information is obtained by a discrete Fourier transform of the spatio-temporal velocity distributions measured using UVP and indicates that the phase lag changes substantially as rheological properties change in a test fluid. As the primary rheological property, a local effective viscosity that is representative of the Newtonian viscosity in the bulk of a measurement volume is determined using UVP. In addition, the shear stress distribution, yield stress, spatial viscosity profile, and shear modulus are obtained as secondary rheological properties.

## 2.1 Introduction

Like two wheels of a bicycle, rheometry together and suitable rheological models have importance in evaluating rheological characteristics in the fields such as polymers, biology, food processing, and dispersion systems. Most fluid materials dealt with in these fields are non-Newtonian having shear-rate-dependent viscosities [1], exhibiting, for example, shear banding [2] and shear history effects [3]. The development of a universal rheometry that can deal with fluids having any rheological property is an ultimate goal of rheology. Conventional spinning rheometers, employing double cylinders, cone and plate, and double disks, are useful in providing details of physical properties such as the apparent viscosity and linear viscoelasticity subject to simplifying assumptions such as Couette flow in a thin test fluid layer. In practice, however, the behavior is not in accord with assumptions, with differences arising between the expected and actual velocity profiles. Measuring rheological properties, therefore, involves numerous factors associated with errors in conventional systems based on measurements of spinning shear flows and torques. This problem is known as the "Couette inverse problem" [4–6]. Furthermore, there are complexities arising from multiphase fluids that have discontinuities associated with their physical properties because the plate separation in conventional measurement systems is narrow [7, 8].

To mitigate such problems, an alternative approach to rheometry, termed velocity-profiling rheometry, which measures the velocity profiles directly, has been proposed in the last decade. Various approaches have been used such as ultrasonic velocity profiling (UVP) [9], ultrasonic imaging velocimetry [10], magnetic resonance imaging velocimetry [11, 12], particle imaging velocimetry (PIV) [2, 13, 14], and laser Doppler velocimetry (LDV) [15, 16]. Magnetic resonance imaging velocimetry is required for use in very large measurement facilities but is not suitable for unsteady fluid flows. Both PIV and LDV require transparent test fluids whereas most fluids of interest are opaque. If ultrasonic waves can propagate in the fluids, UVP measurements of opaque fluids such as concentrated suspensions are possible and some work involving UVP rheometry has been reported [17–19]. Ouriev and Windhab [18] proposed an in-line UVP-pressure difference (PD) technique, a combination of UVP measurements and PD measurements. This can be used to calculate parameters of rheological models, such as the shear-rate-dependent viscosity, the power law model, and the Herschel-Bulkley model, to give the best profiles representing the measured velocity profiles under measured pressure difference assuming steady flows. A selected rheological model that does not fit the test fluid cannot provide a useful result. Fluids including different ingredients, bubbles, or particles, are examples of this. Derakhshandeh *et al*. [19] adopted UVP for a wide-gap double-cylinder system that was combined with axial torque measurements to evaluate the rheology of fine fiber suspensions. This approach requires selecting a suitable rheology model and hence suffers from the same problems as the in-line UVP-PD method. These methodologies achieve precise estimates of the rheological properties of fluids that obey ordinary rheological models, but they are not useful in evaluating rheological properties of general complex fluids encountered in industry and nature that do not obey simple rheological models. Originally, the spatio-temporal velocity fields measured using UVP reflect all rheological properties and provide a rich source of rheological information. Adopting highly sophisticated rheological models for estimations removes the need to evaluate a precise but restricted set of rheological properties.

A rheometry using UVP for complex fluids in rotating cylindrical systems without requiring an inner cylinder to measure the axial torque was proposed. With simple, open cylindrical containers, measurements of a wide range of target properties are possible. Termed ultrasonic spinning rheometry (USR), this approach has been adopted to evaluate the effective viscosity of a bubbly liquid, corresponding to the Newtonian viscosity in the bulk of a measurement volume of UVP containing tiny bubbles [20]. In the analysis, the phase lag in the velocity fluctuations propagating from the oscillating cylinder wall to the inner part of the fluid is related to the local effective viscosity. Shiratori *et al*. [21] proposed a model-free USR for a quantitative evaluation of the shear-rate-dependent viscosity without adopting any rheological model. This was achieved through a combination of UVP and axial torque measurements in a doublecylinder system as a general circular Couette flow. This method was used to evaluate the viscoelastic properties of fluids using the oscillatory motions of the inner cylinder, and the relationship between strain, strain rate, and shear stress representing the properties as a "flow surface" similar to the flow curves representing shear-rate-dependent viscosity [22]. An ultrasonic visualizer of the rheological characteristics was developed [23]; here the spatio-temporal velocity field of test fluids in an oscillating cylinder are measured using UVP, from which the distributions of velocity, strain rate, and deformation are calculated and thereby provide in an intuitive manner features of the fluid characteristics.

Through a series of studies, our experimental arrangement has progressed toward a universal USR for general complex fluids including multiphase fluids by extracting information embedded in spatio-temporal velocity distributions measured using UVP. USR makes it possible to quantify various properties from a single measurement of the velocity distributions. The velocity distribution measurements are completed within seconds, and USR can be used to evaluate instantaneous rheological properties that can change rapidly with time. The purpose of the present study is to extend the regime of applicability of USR to general complex fluids through sophisticated signal processing. The proposed USR will provide rapid qualitative

evaluations of rheological characteristics and quantitative estimates of such properties in local bulk volumes (cylindrical measurement volume of UVP), principally the effective bulk viscosity of complex fluids. To demonstrate USR capabilities, three test fluids are chosen as examples of thixotropic fluids, shear-thinning fluids, and multiphase fluids. The apparatus, theoretical basis, and procedures of USR are detailed in §2.2. Details of the test fluids are then summarized, followed by an evaluation of the rheological properties of each test fluid.

## 2.2 USR

### 2.2.1 Experimental arrangements

Given the setup of the experimental apparatus (Fig. 2.1), the experiments were conducted in an open vertical rotating cylinder made of acrylic resin with 145-mm inner diameter ($2R$) and 65-mm high, 2-mm thick lateral wall. There is no lid on the cylinder, which is filled with the test fluid, leaving the top surface of the fluid layer free. The cylinder is mounted at the center of a 1000 mm × 1000 mm water bath to maintain a uniform temperature $T_0$ and to allow ultrasonic waves to propagate from outside the cylinder. Oscillations of the cylinder are controlled by a stepping motor set for a given oscillation angle $\Theta$ and oscillation frequency $f$. During an oscillation of the cylinder, the velocity distribution of the fluid is measured using UVP. The ultrasonic echoes obtained are processed using an UVP monitor: Model Duo (Met-Flow S.A., Switzerland) to calculate the spatio-temporal velocity distribution. The type of ultrasonic transducer influences the accuracy of the UVP measurement, and selection takes into account the attenuation of the ultrasonic waves in the test fluid media, minimization of the measurement volume, and reduction in the measurement error in accordance with the fundamental understanding of the UVP method (e.g., [9]). To obtain the azimuthal component of velocity, an ultrasonic transducer of resonance frequency 4 MHz and 5 mm effective element diameter was mounted in the chamber at a horizontal displacement $\Delta y$ from the centerline of the cylinder. The UVP measures the velocity component $u_\xi$ parallel to the measurement line n at each measurement point on the line. Assuming that the axisymmetric flow field and the velocity component in the radial direction is negligible compared to the azimuthal component, the azimuthal velocity component $u_\theta$ is

$$u_\theta = \frac{u_\xi r}{\Delta y} \tag{2.1}$$

at a radial position $r$. Installation of the transducer requires careful handling. Because the measurement volume for UVP is considerable, a much smaller $\Delta y$ creates significant error and enhances measurement errors. In contrast, larger $\Delta y$ induces an inflection in the ultrasonic wave at the inner surface of the cylinder wall as a consequence of the large curvature effect. Empirically, based on the results of previous studies [20, 23], $\Delta y = 15$ mm was selected. The distance to the wall also needs the proper setting to avoid influences of partially reflected ultrasonic waves at the outer surface of the cylinder. The distance, therefore, was adjusted by monitoring the ultrasonic echo in an oscilloscope experiment. The transducer was set at 40 mm from the bottom of the cylinder to avoid effects of shear stress caused by oscillations at the cylinder bottom plate. The bottom of the cylinder has an axisymmetric down slope running from the cylinder wall to the center (Fig. 2.1) to suppress the generation of meridional secondary circulations, which induce a considerably large radial velocity component. Suppressing the radial flow requires special attention to ensure the quality of the profiles of the azimuthal velocity component. The range of applicability of USR is determined by that of UVP, and thus cases of very viscous fluids, for example, larger than $10^6$ cSt, and highly concentrated multiphase media would be outside this range because the attenuation of ultrasonic waves in the media is appreciable.

### 2.2.2 Theoretical basis for USR

With this methodology, rheological properties, such as the local Newtonian viscosity, shear stress distribution, and shear modulus, are evaluated quantitatively by comparing the phase lag between the analytical solution and the experimental results. For a comparison of the experimental results of the characteristics of momentum propagation, Tasaka *et al.* [20] derived an analytical solution for the spatiotemporal velocity distribution of Newtonian fluids. Assuming an axisymmetric flow field and a unidirectional flow in the azimuthal direction, the conservation of angular momentum for the fluid flow is considered as

$$\frac{\partial(\rho u_\theta r)}{\partial t} = \frac{1}{r}\frac{\partial\left(r^2\tau_\theta\right)}{\partial r}, \quad \text{s.t.} \quad \tau_\theta = \mu\left(\frac{\partial u_\theta}{\partial r} - \frac{u_\theta}{r}\right). \tag{2.2}$$

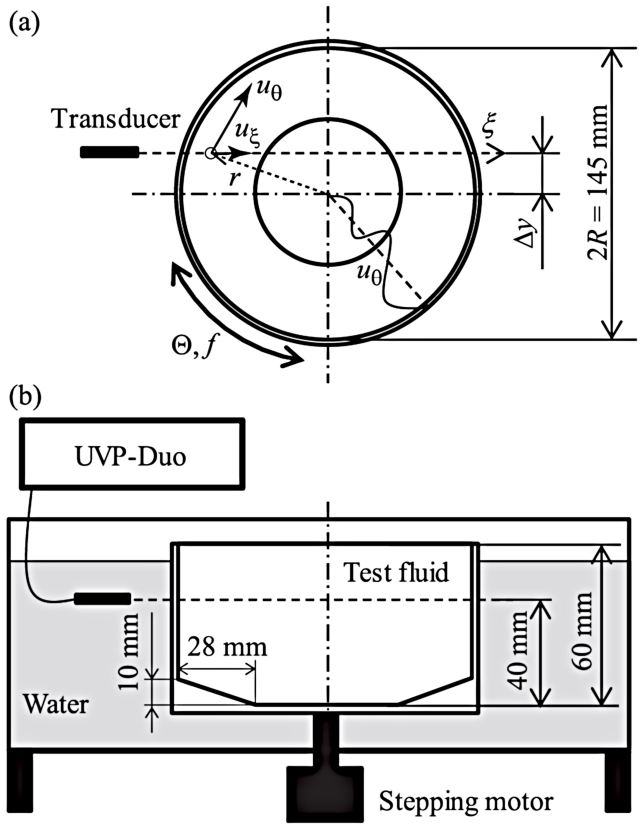


Figure 2.1: Schematics of the experimental apparatus for measuring velocity distributions of oscillating shear flows using UVP; (a) top view of the rotating cylinder without the outside container; (b) side view.

When fluid density $\rho$ and viscosity $\mu$ is regarded as constant, Eq. 2.2 for incompressible fluids is modified to

$$\frac{\partial u_\theta}{\partial t} = \nu\left(\frac{\partial^2 u_\theta}{\partial r^2} + \frac{1}{r}\frac{\partial u_\theta}{\partial r} - \frac{u_\theta}{r^2}\right), \tag{2.3}$$

where $\nu$ is the kinematic viscosity of the fluid. In Appendix B, it is discussed that the viscosity variance can be regarded as constant in Eq. 2.2. An analytical solution is solved with the initial condition; $u_\theta(r, t = 0) = 0$, and boundary conditions; $u_\theta(r = R, t) = U_{\text{wall}} \sin \omega t$ and $u_\theta(r = 0, t) = 0$, where $\omega = 2\pi f$ and the oscillation amplitude is given as $U_{\text{wall}} = 2\pi^2 f R\Theta/180$. Further details of the derivation are given in [20].

Here, to confirm the applicability of the analytical solution in the analysis of the experimental data, the azimuthal velocity distribution of silicon oil was measured; this test fluid is typical Newtonian fluids. Figure 2.2 shows a plot of the radial variation of the phase difference $\phi$ against the cylinder wall comparing the analytical solution and the experimental results for silicon oil with $\nu = 300$ mm$^2$/s, $f = 1.0$ Hz, and $\Theta = 80°$. In this figure, the radial position is normalized by the radius of the cylindrical container, $R$. The corresponding analytical solution is given as

$$u_\theta = U_{\text{wall}} A(r) \sin[\omega t + \phi(r)], \tag{2.4}$$

$$\phi(r) = \tan^{-1} \frac{\Phi_R \Psi(r) - \Phi(r)\Psi_R}{\Phi(r)\Phi_R + \Psi(r)\Psi_R}, \tag{2.5}$$

by Tasaka *et al.* [20]. The $\Phi_R$, $\Phi(r)$, $\Psi_R$, and $\Psi(r)$ terms are terms of an infinite series. The phase difference $\phi(r)$ of the experimental data is obtained from a 100 s time series of the instantaneous velocity profiles via a discrete Fourier transformation as the phase of the most dominant frequency component in the power spectrum. The experimental result is in good agreement with the analytical solution for this Newtonian fluid, therefore, the analytical solution may be adequate in describing unsteady flows in the present system. There is considerable, systematic deviation between experimental and theoretical results near the cylinder center in the range, $r/R < 0.3$. This is because the size of the flow circulation compared with the measurement volume: Near the center of the rotating cylinder, the flow changes its direction over a short distance and this influence becomes considerable compared with the measurement volume of UVP.

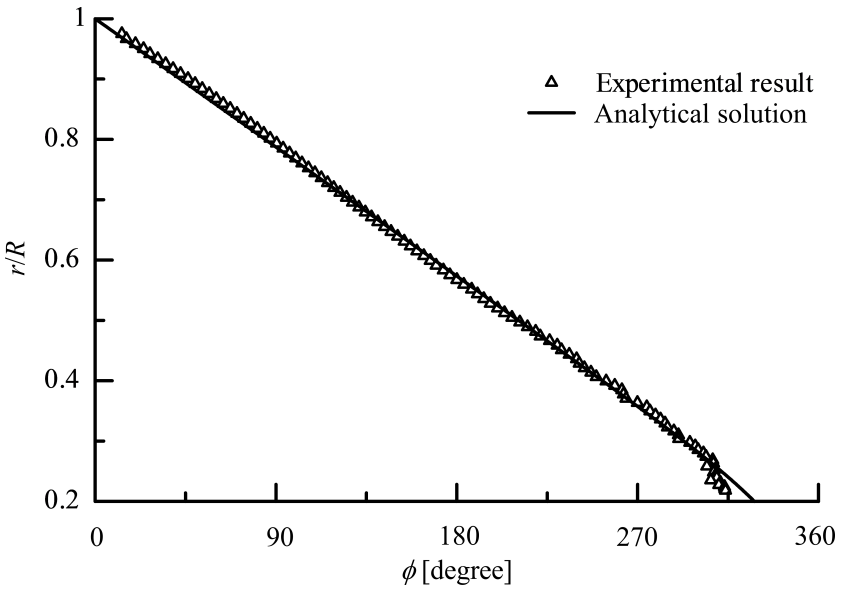


Figure 2.2: Comparison of the radial variation in phase difference along the cylinder wall between experimental for silicon oil (kinematic viscosity 300 mm$^2$/s, oscillating frequency $f_o = 1.0$ Hz, oscillation amplitude $\Theta = 80°$, temperature $T_0 = 25°$C) and the analytical solution with $\nu = 300$ mm$^2$/s.

### 2.2.3 Procedure for evaluating rheological properties

For a quantitative evaluation of general complex fluids, an algorithm for the inverse problem is established using details of the velocity fluctuations obtained in unsteady shear flows. A schematic of the procedure for distinguishing rheological properties

is summarized in Fig. 2.3. Here, we use the phase lag from the cylinder wall calculated using the discrete Fourier transform (DFT) analysis on the spatio-temporal velocity distribution of unsteady shear flows measured using UVP. This provides some advantages in the analysis as summarized below.

First, this analysis can be applied to results with an oscillation period as short as 1 s, which is typical with time resolutions of 25 ms and an oscillation frequency $f = 1.0$ Hz. It is possible to track large changes in instantaneous viscosity as for shear thinning fluids or Bingham fluids. In addition, the influence of measurement noise can be reduced using phase information calculated from the frequency analysis instead of using the spatio-temporal velocity distribution directly: Spike-like noise which is typical of UVP measurements can be removed with the Fourier transform procedure to obtain the local phase difference. Even with the phase information, long-duration measurements may be useful in ensuring a robust estimation of the viscosity of fluids that have constant or slowing-varying viscosity values under the applied shear stress. This enables adjustments in setting optimum measurement times for estimates of a wide range of fluids.

Second, the radial profile of the phase lag can be used to distinguish the rheological characteristics of test fluids: Constant phase lag regimes correspond to rigid rotation and such regimes may be regarded to occur with fluids having elastic properties or very high viscosity values. Regimes with a changing phase lag indicate fluidization areas and thereby can be regarded as fluids with viscous or viscoelastic properties. For example, radial profiles showing a discontinuous variation indicate the existence of boundaries between different regimes of a rheological property.

Finally, the analysis is able to evaluate viscosity values from the gradient of the phase lag, because phase lag represents momentum propagation reflecting viscosity values. By comparing the phase lags of the experimental results with results obtained from the analytical solution, it is possible to evaluate spatial viscosity profiles. Profiles of constant viscosity values indicate that the test fluid is a pure Newtonian viscous body, and therefore, the shear stress distributions $\tau(r)$ can be derived according to Newton's law of viscosity.

Different spatio-temporal velocity distributions contain information representing rheological characteristics other than just the phase difference. As an example of an application of such distributions, a methodology for estimating the shear modulus in elastic deformations $G$ is demonstrated below to show the potential of USR.

## 2.3 Demonstration of the potential of spinning rheometry when applied to complex fluids

In this section, we discuss the applicability of USR in evaluations of rheological properties through demonstrations of three test fluids with different rheological properties.

### 2.3.1 Test fluids

To emphasize the range of application of our method, montmorillonite suspensions, a fluid food (low methyl pectin gel: LM-pectin gel), and a curry paste containing dispersed solid ingredients were chosen as test fluids. These are, respectively, examples of thixotropic fluids, shear thinning fluids, and fluids with relatively large ingredients. This section describes in detail the rheological characteristics of each fluid.

Montmorillonite is a clay mineral; Fig. 2.4 shows a schematic of a montmorillonite particle and the structures presented by the particles in a solvent. The particles are polygonal platelets nanometer thickness extending $0.1 - 1$ $\mu$m in width. When these particles are dispersed in ionic water, the suspension is a structurally stable through by interactions that has been termed a "Card house structure," as suggested in Fig. 2.4 (right). This structure however is easily broken into smaller clusters under very weak shear stresses. If still standing in suspension, the structure restores itself with a recovery time trec. Hence, this complex behavior of the suspension, specifically, time-dependent gelling and high-shear thinning [24] in termed thixotropy. As yet, no measurement system has been established to quantitatively evaluate these behaviors of such suspensions. However, they have been estimated from results attained in various previous investigations [25–27]. In particular, montmorillonite suspensions undergo significant changes in rheological behavior through unsteady shear stresses like those occurring in Bingham fluids, including time-dependent recovery. This describes the qualitative characteristic of the fluid behavior as complex characteristics in determining the rheological properties. Establishment of quantitative details of the rheology of this thixotropic fluid demonstrates the robustness in using USR here. A montmorillonite suspension was prepared by adding 4.0 wt.% powder to 0.01 mol/L NaCl aqueous solutions. (The rheological properties of the suspensions strongly depend on this added volume in addition to the powder concentration.) For full swelling of the particles, the suspension was left for one day before measurements were taken. After filling the cylinder, the suspension was stirred vigorously to eliminate any shear stress history.

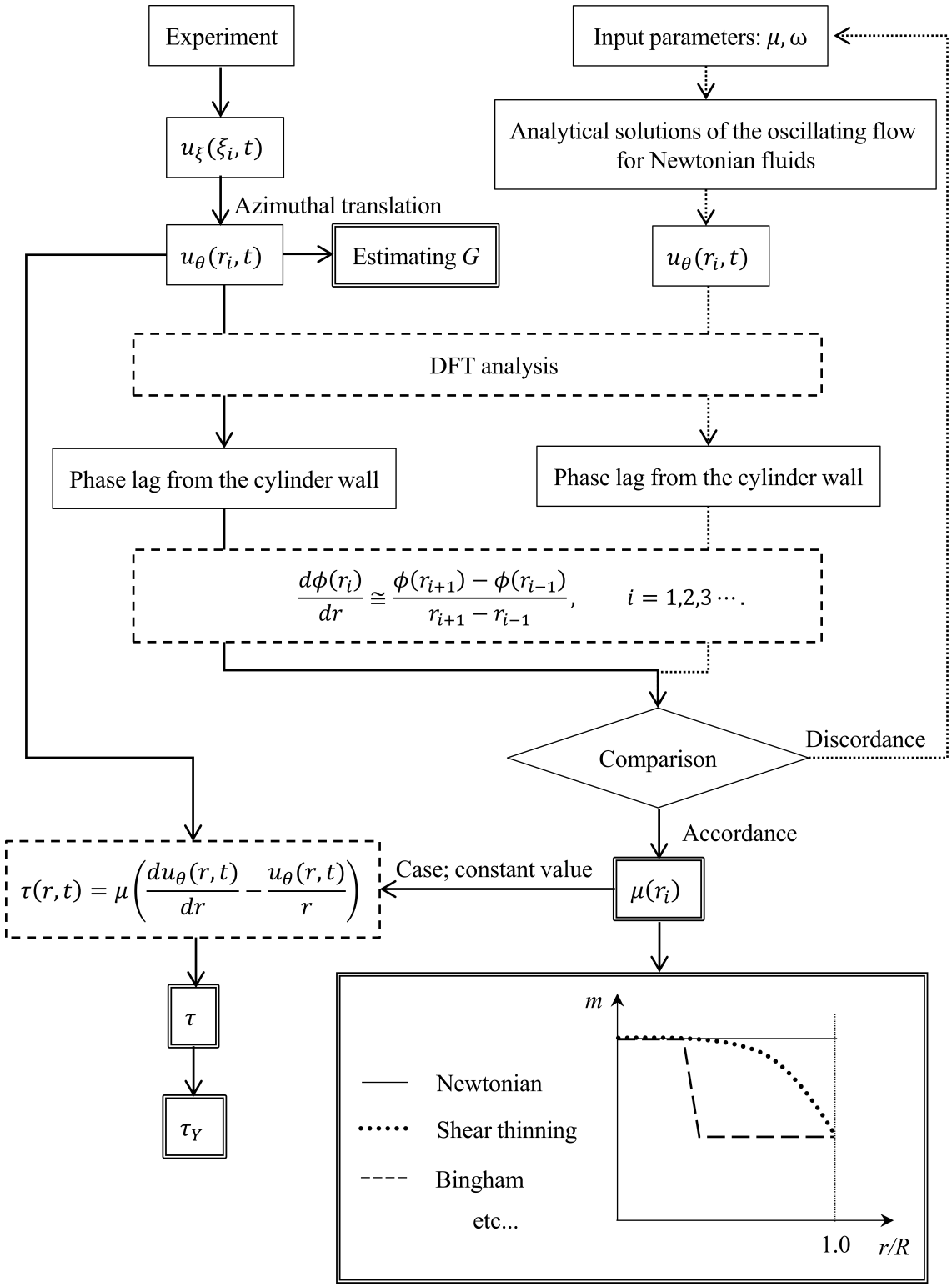


Figure 2.3: Schematic outline of the analysis process of USR to evaluate the "local" Newtonian viscosity.

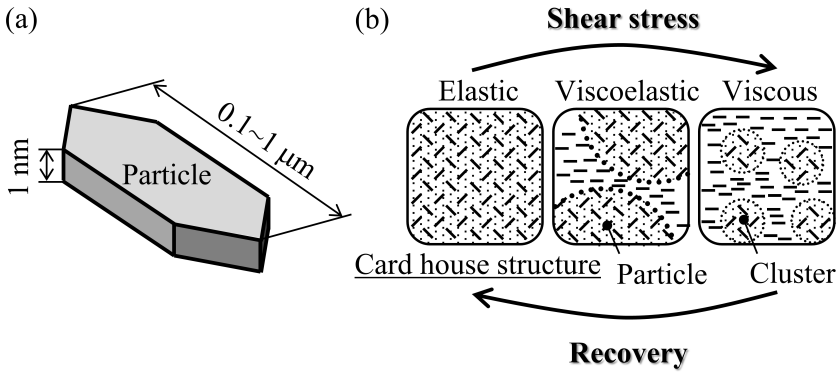


Figure 2.4: Schematics of a montmorillonite particle and the breakdown process of its thixotropic structures.

The second test fluid, LM pectin gel is a dessert base (Fruiche, House Foods Group, Inc.). This has a gelling action arising from the interaction between $Ca^{2+}$ inside the milk and the chain structure of the LM-pectin polymers. In the food industry, this interaction has been used to thicken fluid foods forming complicated entangling clusters causing an egg-carton-shaped structure (Fig. 2.5). An exerted momentum, for example, from shear stress, reduces the cluster size caused by suppressing the interactions between polymers. Thus, the LM-pectin mixture exhibits a shear thinning [28]. Such fluid foods display a stronger viscoelastic behavior than montmorillonite suspensions. When the fluid food propagates a momentumlike shear stress or by stirring, it exhibits both springlike and dashpotlike characteristics. In this experiment, we prepared the fluid food following a published recipe (House Foods Group Inc. recipe): (200 mL milk for each 50 mg of powder; the specifications of the milk used are 85 mg Na, 227 mg Ca, and 6.5 g protein in 200 mL). This fluid includes a lot of fruit pulp, which has formless shape and deforms under shear stress. Thus, this fluid features boundaries in its distributions in physical properties arising from shear deformation.

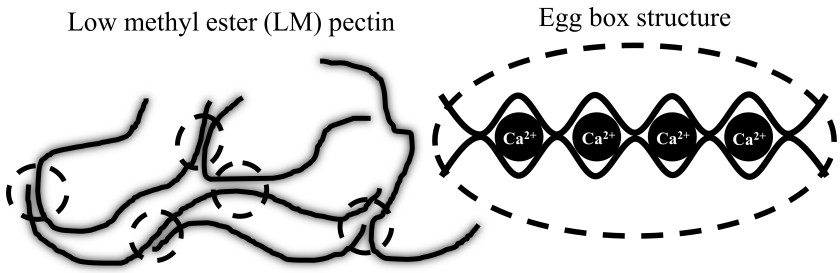


Figure 2.5: Schematics of LM-pectin cluster and the egg-carton structure.

The third test fluid is a curry paste, which is a commonly consumed fluid food containing relatively large pieces of ingredients. An ordinary retort-pouched curry paste (Bon curry, Otsuka Foods Co.) was chosen. Figure 2.6 shows that some of the ingredients, such as lumps of fat and spices, are non-uniformly dispersed in the curry paste. In addition, the shapes and sizes of the ingredients are nonuniform. Thus, being highly complex, details of its rheological properties or indeed other liquids containing such ingredients are difficult to obtain. The curry paste includes beef tallow and butter made from milk. The melting point of the beef tallow is around 40°C and that of the butter 30 – 40°C. With low melting points, these fluids result in a decrease in viscosity with increasing temperature. Here, we want to evaluate essentially the effective viscosity of this complex suspension using the proposed rheometry.

### 2.3.2 Results and discussion

The spatio-temporal velocity distributions measured by UVP reflect the rheology of the test fluids, and based on this a qualitative evaluation of the rheology can be obtained from these distributions. Rheological properties were measured and analyzed according to the procedure summarized in Fig. 2.3. From the analysis, the applicability of the present method to the various types was assessed using the measurement resolutions of the UVP, as specified in Table 2.1. The spatial resolutions specified in the table were determined theoretically from the number of cycles of ultrasonic wave and the speed of sound in the test media. The actual number of waves in a single emission of ultrasonic waves changes depending on the damping




Figure 2.6: Photo of curry paste containing dispersed ingredients [https://boncurry.jp/, Feb. 16 2020].

quality of the piezoelectric elements in ultrasonic transducers, and usually increases. There is, however, no considerable spatial averaging effect due to larger measurement volume at least in the experiments in this study; for example, see Fig. 2.1.

Table 2.1: Experimental parameters of different test fluids.

| Test fluid | Time [ms] | Velocity [mm/s] | Spatial resolution [mm] |
|---|---|---|---|
| Montmorillonite suspension | 25 | 1.304 | 0.74 |
| LM-pectin gel | 25 | 1.368 | 0.75 |
| Curry paste | 24 | 1.563 | 0.78 |
| Silicon oil (300 $mm^2/s$) | 30 | 0.664 | 0.62 |

#### 2.3.2.1 Montmorillonite suspension

With the montmorillonite suspension, assuming axisymmetry and unidirectional flow in the azimuthal direction, the spatio-temporal velocity map obtained by the UVP can be converted into a radial-temporal distribution of the azimuthal velocity component. Figure 2.7 shows the distribution obtained at different elapsed oscillation times with $f_o = 1.0$ Hz in the oscillation frequency and $\Theta = 90°$ in amplitude; here the vertical and horizontal axes indicate the radial positions normalized by the radius of the cylindrical container, $R$, and the spin-cycle time. The gray scale contours represent the azimuthal velocity normalized by the maximum azimuthal velocity at the cylinder wall, $U_{wall}(= 2\pi^2 f R\Theta/180)$. From these distributions, the oscillation of the azimuthal velocity propagates as a damped wave from the wall to the center of the cylinder. From Figs. 2.7(a)-2.7(e), the phase lag from the cylinder wall to the inner parts of the fluid develops into the inner region of the fluid layer with time. Because the phase lag represents local rheological properties as explained in §2.2.3, this development typifies the thixotropic behaviors of the suspension as the viscosity decreases with applied shear stress. There is a constant phase-lag regime in the inner region of the cylinder, which can be assumed to be an unyielded region maintaining the gel state. The boundary between the yielded and unyielded regions moves gradually toward the center, cycle-by-cycle, and reaches an equilibrium state around $t = 1800 - 1900$ s [Fig. 2.7(e)]. To quantify the phase lag, the velocity distributions were analyzed by time-directional DFT for 1 s periods. Figure 2.8 shows the radial profiles of the phase lag based on the cylinder wall oscillation at each time interval section (a)–(e) indicated in Fig. 2.7.

The phase lag profiles assume almost constant values except near the cylinder wall at the beginning. With increasing oscillation time $t$, the phase lag becomes larger and the regime with phase lag widens progressively. This indicates that the viscosity of the suspension in the cylinder is decreased by the applied shear stress from the oscillating cylinder. Eventually, the development of the phase lag profiles converges at time section (e), $t = 3600$ s from the start of the oscillation of the cylinder. There are two clearly separated yielded and unyielded (fluidized or unfluidized) regions illustrated in Fig. 2.8 (right). The discontinuity in the curve at which the profiles show a change in the variation (see Fig. 2.8) indicates the boundary between the yielded and unyielded regions.

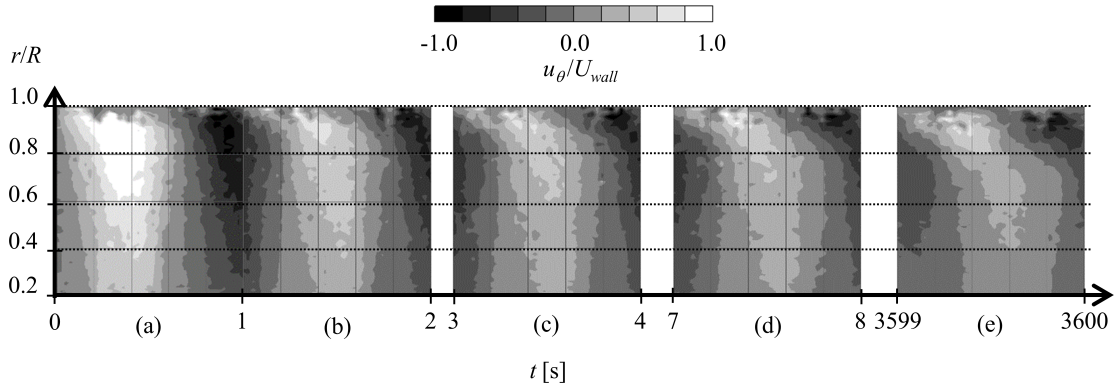


Figure 2.7: Azimuthal velocity distributions of the montmorillonite suspension (4.0 wt.% powder to a 0.01 mol/L NaCl aqueous solution) at different elapsed oscillating time, where the oscillation frequency, amplitude, temperature, and recovery time are $f_o$ = 1.0 Hz, $\Theta$ = 90°, $T_0$ = 20°C, and $t_{rec}$ = 100 min, respectively; $U_{wall}$ = 715.5 mm/s.

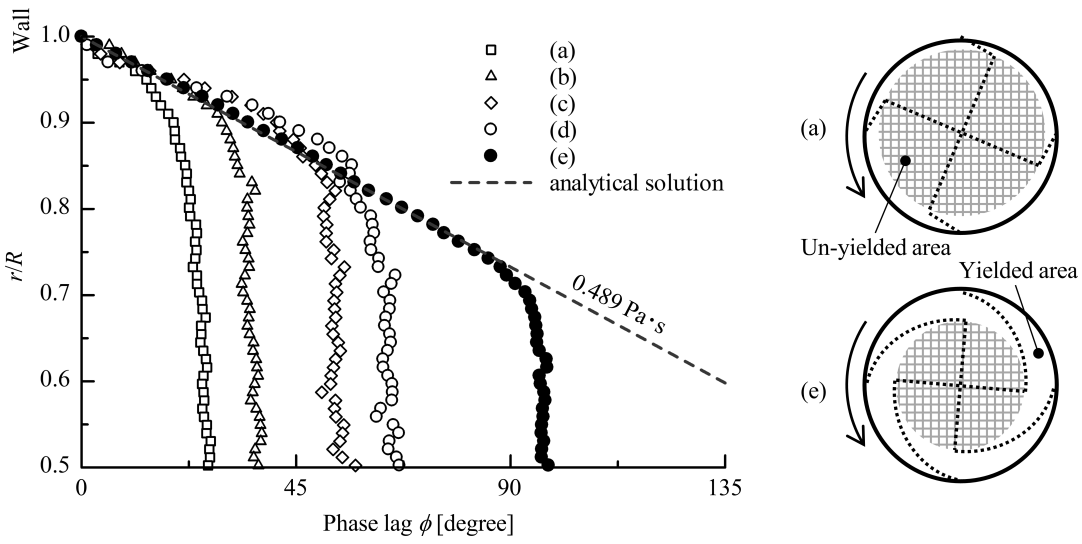


Figure 2.8: Phase lag of the local velocity fluctuations from the cylinder wall at each time step (a)–(e) indicated in Fig. 2.7, and schematic of phase lag.

In the yielded region for each time step in Fig. 2.8, the gradient of the phase lag profile remains largely unchanged. This suggests that the fluids in the yielded region have assumed distinct rheological properties. In the figure, the dashed inclined line indicates the phase lag profile obtained from the analytical solution for Newtonian fluids given in Eq. (2.5). The profile corresponds closely to that at time step (e) within the range $0.75 < r/R < 1.0$, and therefore, the suspension in the yielded region can be assumed to behave as a Newtonian fluid similar to Bingham fluids, which has a yield stress and no viscoelasticity. The least-squares approximation representing the best representation of the experimental profile in the $0.8 < r/R < 1.0$ range provides a corresponding Newtonian viscosity $\mu = 0.489$ Pa · s. In a previous study [29], the value of montmorillonite suspensions with the same NaCl percentage as in the present suspension was estimated as 0.528 Pa · s using a conventional rheometer. The conventional rheometer has measurement uncertainties in addition to random measurement errors, deriving from the influence of shear banding, slipping at the wall, and other phenomena, whereas the present measurement evaluated the value in the pure Newtonian regime. Considering measurement uncertainties, these values achieve good agreement. Additionally, this shows that the present rheometry using UVP is able to monitor the evolution of yielding from the cylinder wall to the inner region as a typical rheological behavior of the suspension.

Assuming that the suspension in the yielded region is a Newtonian fluid makes it possible to estimate the local shear stress using Newton's law of viscosity

$$\tau(r,t) = \mu\left[\frac{du_\theta(r,t)}{dr} - \frac{u_\theta}{r}\right]. \tag{2.6}$$

Substituting the analytical solution of Eq. (2.4) into Eq. (2.6) provides the shear stress distribution in the yielded region. The maximum value among the radii in the time series is shown in Fig. 2.9 as a dashed curve. Also, plotted for comparison are the shear stress values calculated from the experimental results with the numerical derivatives of Eq. (2.6) obtained using the secondary central difference method. The plots show rather large deviations from the analytical solution near the wall, but further away from the wall the variation follows the analytical solution. For the present experimental conditions, the boundary between the yielded and unyielded regions is around $r/R = 0.7$; Fig. 2.9 implies that the shear stress value at $r/R = 0.7$ is suggestive of a yield stress value $\tau_Y = 4.57$ Pa for the suspension. It is often difficult to evaluate the yield stress value by rheometry using only velocity information, and this result highlights the advantage of the present rheometry.

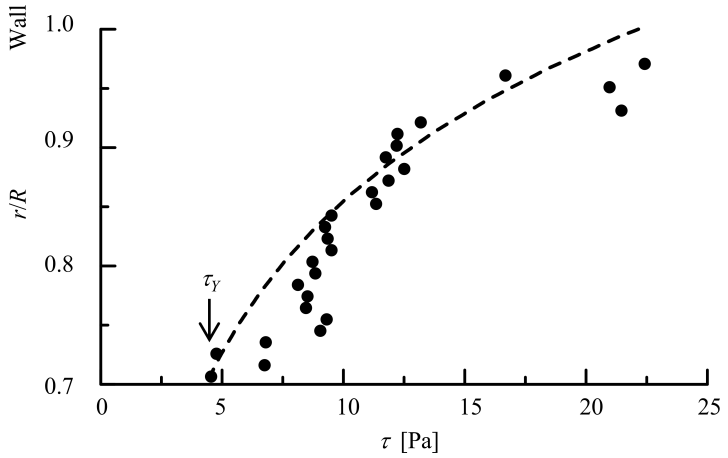


Figure 2.9: Radial profile of the local maximum shear stress; the dashed line represents the values calculated from the analytical solution with an estimated viscosity and the data points are from the spatio-temporal velocity distribution shown in Fig. 2.12(e) using numerical derivatives.

The original spatio-temporal velocity distributions measured by UVP in the present system provide more information of the rheology than the phase difference extracted from the distributions, whereas the phase difference still provides robust estimates of the viscosity via the analytical solution. As an example of further analysis that is possible from the rheology with the velocity distribution, we next focus on variations in the velocity distribution immediately after the start of the oscillation. In Fig. 2.8(a), the inner fluid flow is stationary, and the fluid exhibits elastic properties. Immediately after the oscillation starts, there is an elastic wave propagating with velocity $v_e$. From the elastic-wave theory [30], $v_e$ is given by

$$v_e = \sqrt{\frac{G}{\rho}}, \tag{2.7}$$

where $G$ and $\rho$ denote shear modulus and density, respectively, with $\rho$ a constant value. As $v_e$ varies proportionally to $G^{1/2}$, this makes it possible to estimate the shear modulus from the azimuthal velocity distributions obtained by UVP. Here, the fluid density can be regarded as constant with respect to relaxation time because the speed of sound kept constant with changing the relaxation time. Figure 2.10 shows the instantaneous radial velocity profiles immediately after the oscillation begins. Here, an initial damped wave propagates from the cylinder wall; its speed can be estimated from the velocity distribution. The front edge of the wave can be estimated by introducing a threshold, in the present case $u_\theta/U_{\text{wall}} = 0.1$ was chosen. The speed of the damping wave ve is obtained from $v_e = \Delta r/\Delta t$ (see Fig. 2.10).

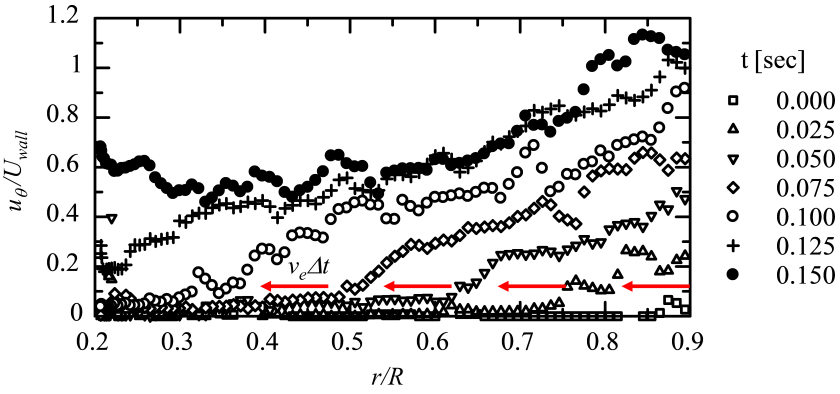


Figure 2.10: Initial development of the radial velocity profiles with time increment of 0.025 s for various staring times of the cylinder oscillation extracted from the results for the montmorillonite suspension given in Fig. 2.7.

The propagation speed $v_e$ and Eq. (2.7) provide the shear moduli, $G$, for different recovery times after stirring, $t_{\text{rec}}$. The logarithmic plot of $G$ versus $t_{\text{rec}}$ in Fig. 2.11 gives the dependence of the shear modulus on recovery time. Rand *et al.* [31] proposed an empirical formula of the recovery time dependence on the shear modulus $G$ given by

$$G = G_0 \left( \frac{t_{\text{rec}}}{t_0} \right)^{\alpha}, t_0 = 1 \text{ s}. \tag{2.8}$$

Here, $G_0$ and $\alpha$ are the zero shear modulus and a constant exponent, respectively. The results obtained obey this formula and using a least-squares fit on the plot (Fig. 2.11) provides values of $G_0 = 19.73$ Pa and $\alpha = 0.22$, respectively. These values seem quite reasonable in comparison with the time-dependence of the rheological properties such as the thixotropic behavior.

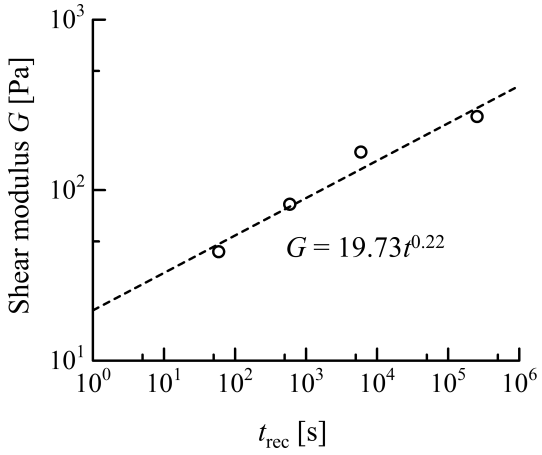


Figure 2.11: Shear modulus versus recovery time after stirring.

#### 2.3.2.2 LM-pectin gel

For the LM-pectin gel, Fig. 2.12 shows the azimuthal velocity distributions of the LM-pectin layer at various elapsed oscillation times measured using UVP. The measurements were performed after leaving the gel at rest for 100 min after mixing.

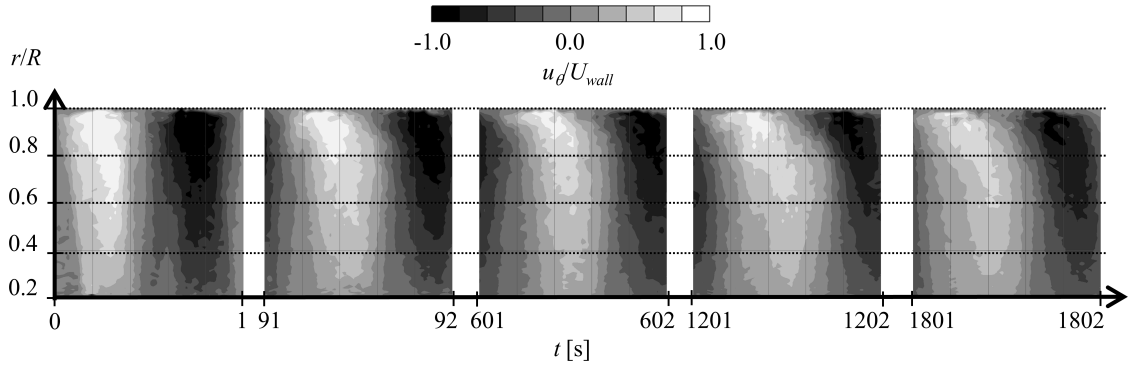


Figure 2.12: Azimuthal velocity distributions at each elapsed oscillating time measured using UVP in LM-pectin gel, where the oscillation frequency, amplitude, and temperature are $f_o$ = 1.0 Hz, $\Theta$ = 60°, and $T_0$ = 15°C, respectively; $U_{wall}$ = 477.0 mm/s.

As unidirectional flow can be realized, the parameters of the oscillation were set at $f_o$ = 1.0 Hz and $\Theta$ = 60° in each of the measurements in the test fluids. The oscillation in the azimuthal velocity propagates from the wall to the center of the cylinder as a damped wave. The time development of the velocity distributions is similar to that in the montmorillonite suspension, specifically, the region near the wall with radial variations in the phase lag widens and the boundary of the region has a constant phase lag that moves toward the center. However, the development of the velocity distribution appears to be slower than the montmorillonite suspension. To quantify the development of the phase lag profiles, the phase lags of the velocity distribution were obtained from the DFT analysis detailed in §2.2.3. To obtain a smooth curve for the phase lag, velocity distributions of longer periods of 100 s were used for the analysis. Figure 2.13 shows examples of the radial phase lag variations obtained at periods, $t$ = 0 − 100 s, $t$ = 600 − 700 s, and $t$ = 1800 − 1900 s.

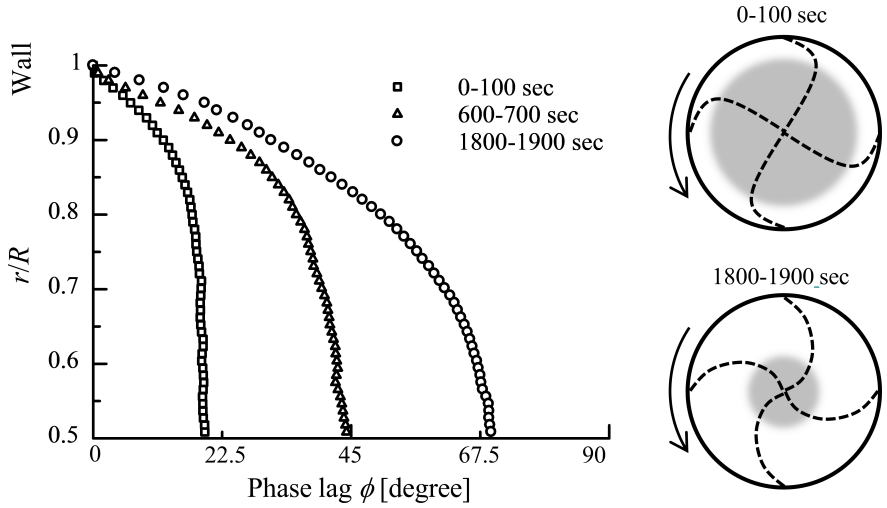


Figure 2.13: Phase lag of the local velocity fluctuations from a cylinder wall for different 100 s waiting-time intervals, and schematic of phase lag.

In the initial period ($t$ = 0 − 100 s), the phase lag has a plateau region at the inner part, and with increasing oscillation time, the curve of the phase lag changes progressively and orderly. In comparison with the results for the montmorillonite suspension (Fig. 2.8), the phase lag in the profiles in Fig. 2.13 shows a smoother variation from the cylinder wall to the center of the container, and there is no clear boundary between yielded and unyielded regions. This can be ascribed to changes in the polymer structure in the gel. Polymerization and gelation of fluids provide a shear-dependent viscosity and elastic properties, and the relaxation of the polymer structure and storage of shear stress by elastic effects make the boundary diffuse. Also, the slope of the curve in the yielded region is not constant, but increases over time. This suggests that the rheological properties are not constant in the yielded region and that the effective viscosity decreases with time. The curve plots of the phase lag indicate qualitatively rheological properties like the Herschel-Bulkley viscous suspensions unlike the viscous properties of Bingham plastic such as the montmorillonite suspension. The shape of the profiles does not change from that shown in

Fig. 2.13 at $t = 1800 - 1900$ s, and it may be assumed that the modification of the polymer structure reaches a terminal state in relation to the shear conditions.

Assuming a fluid of very large viscosity, momentum propagation for unsteady shear flows in a fluid reaches very large speeds. The resultant phase lag has a constant value at each radial position as in rigid rotation. Paradoxically, the resultant phase lags were strongly dependent on the viscosity value of the test gel fluids because the information obtained of the phase lags indicates momentum propagation from the wall to the center. In other words, a decrease in the viscosity value of the test fluid causes an increase in the phase lag. In Fig. 2.13, changes in the phase lag for different elapsed cycle numbers are indicative of viscosity decreases from the shear stress induced by the oscillation. The gradient of the phase lag profile changes continuously in the radial direction, and this suggests a radial variation in viscosity. Here, the gradient is estimated using the discrete equation of the secondary central difference method,

$$\frac{d\phi(r_i)}{dr} \cong \frac{\phi(r_{i+1}) - \phi(r_{i-1})}{r_{i+1} - r_{i-1}}, i = 1,\ 2,\ 3, \cdots . \tag{2.9}$$

Figure 2.14 displays plots of the gradients in the phase lags of the spatio-temporal velocity distribution taken from the LM-pectin gel measurements; that for the montmorillonite suspension is shown in Fig. 2.8(e). The dashed lines represent the gradient profiles calculated from the analytical solutions using the Newtonian viscosity for various kinematic viscosities, and these form contour lines of viscosity. The profiles of the gradients show clear tendencies despite deviations arising from higher measurement noise appearing because of the numerical calculation of the derivatives. For the LMpectin gel, the data points in the first period ($t = 0 - 100$ s) yield the largest fluctuations among all the data. This is because the viscosity of the test fluid changes considerably immediately after the start of the oscillation from shear thinning effects. The gradient profile for montmorillonite maintains a nearly constant value for $r/R > 0.7$, suggesting that it behaves like a Newtonian fluid in this region. The following sharp drop in the gradient around $r/R = 0.7$ indicates that there is a buffer region between the Newtonian-like fluid and the unyielded regions as noted in §2.3.2.1. The local gradient of the phase lag has a corresponding Newtonian viscosity, and therefore, it is possible to determine local effective viscosities which reflect all of the viscoelastic effects as Newtonian viscosity. The effective viscosity is determined from the local crossing points of the gradient profiles with the contour lines of the corresponding viscosities.

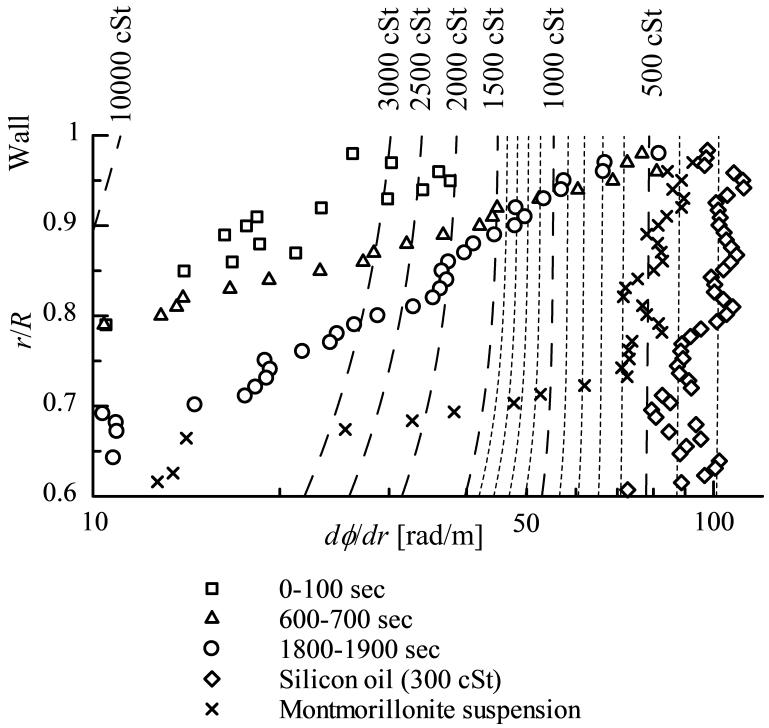


Figure 2.14: Gradient of the radial profiles of the phase lag for different elapsed time, where contour lines represent results from the analytical solution for various kinematic viscosities.

Figure 2.15 shows results of the spatial viscosity analysis for each profile of the phase gradient (shown in Fig. 2.14); only the $0.8 < r/R < 0.95$ range is shown for clarity. These plots for the first period of the LM-pectin ($t = 0 - 100$ s) have larger

viscosities at all radial positions than at the following periods, $t = 600 - 700$ s and $t = 1800 - 1900$ s. In the second period, the viscosity is small near the cylinder wall and increases toward the inside of the cylinder. The plot of the third period ($t = 1800 - 1900$ s) shows a more gradual increase in the viscosity than at earlier periods and takes similar values as the second period near the cylinder wall: Here, the viscosity appears to converge to the lower limit of the viscosity. Decreases in the viscosity are caused by fragmentation of the clusters in the LM-pectin gel, and therefore, the smallest viscosity around 1000 $mm^2/s$ may correspond to the limit of the breakup because of the applied shear stress at the wall. Different from the LMpectin gel, the plots for the montmorillonite suspension assume an almost constant viscosity around 470 $mm^2/s$ (corresponding to 0.489 Pa · s) at all radial positions. This result indicates that the particle clusters in the suspension are fully fragmented in this radial range, and hence the suspension may be considered to behave as a pure (uniform) viscous fluid. In addition to these results, the kinematic viscosity of silicon oil (300 $mm^2/s$ at 25°C; see corresponding phase-lag profile in Fig. 2.2), which is a Newtonian fluid, was evaluated to be near 300 $mm^2/s$. This provides supporting evidence of the measurement precision of the present estimation procedure; within 5% accuracy assuming 300 $mm^2/s$ is the true value with no deviation.

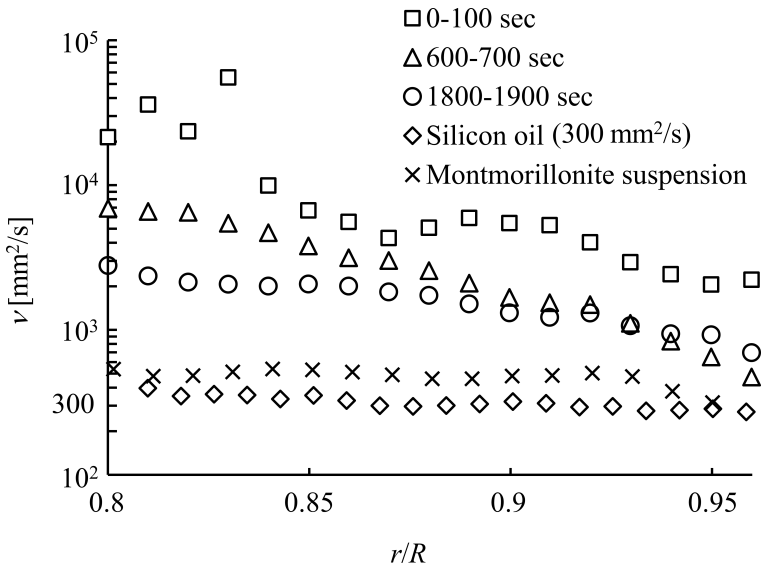


Figure 2.15: Local effective viscosity distributions of LM-pectin gel at each elapsed time and the distributions of montmorillonite suspension and 300 $mm^2/s$ silicone oil.

#### 2.3.2.3 Curry paste with dispersed ingredients

Figure 2.16 shows the azimuthal velocity distributions of curry paste in cylindrical unsteady shear flow with an oscillation frequency $f = 2.0$ Hz and amplitude $\Theta = 45°$ obtained for two temperatures $T_0 = 35$°C (upper panels) and 40°C (lower panels). Comparing these figures indicates that the spatial velocity distributions are considerably different at $20 < t < 21$ s; the distributions for $T_0 = 40$°C also change more considerably. To evaluate this change quantitatively, the phase lags of the fluctuation were calculated in a DFT analysis, as in §2.3.2.1. To capture the time development of the phase lag, a 1 s period was chosen for the DFT analysis.

From the time variations in the phase lag profiles for the two preset temperatures (Fig. 2.17), the phase lag increases with time for the lower temperature, and the variation is more pronounced near the wall as indicated by the distortion in the phase-lag profile. This result arises most likely because of the shear thinning viscous behavior in rheological properties of curry paste due to the solid clusters of beef tallow and other ingredients. For the higher temperature, the phase-lag variation is more gradual. Generally, the viscosity of fluids decreases with increasing temperature. However, this result indicates the contrary, with an increase in viscosity with temperature. This phenomenon occurs because of dilatant behavior from a concentration of ingredients in curry paste. At the lower temperature, the viscous resistance and centrifugal forces on ingredients are balanced. However, because the viscosity of beef tallow decreases with increasing temperature, centrifugal forces exceed the viscous resistance, and this allows the ingredients to move more freely. A slight radial motion of the ingredients may increase momentum propagation from the wall that is reflected in a widening of the area with phase lag. This phenomenon is correlated with the melting point of beef tallow (almost 40°C) and butter (30 – 40°C) in curry paste.

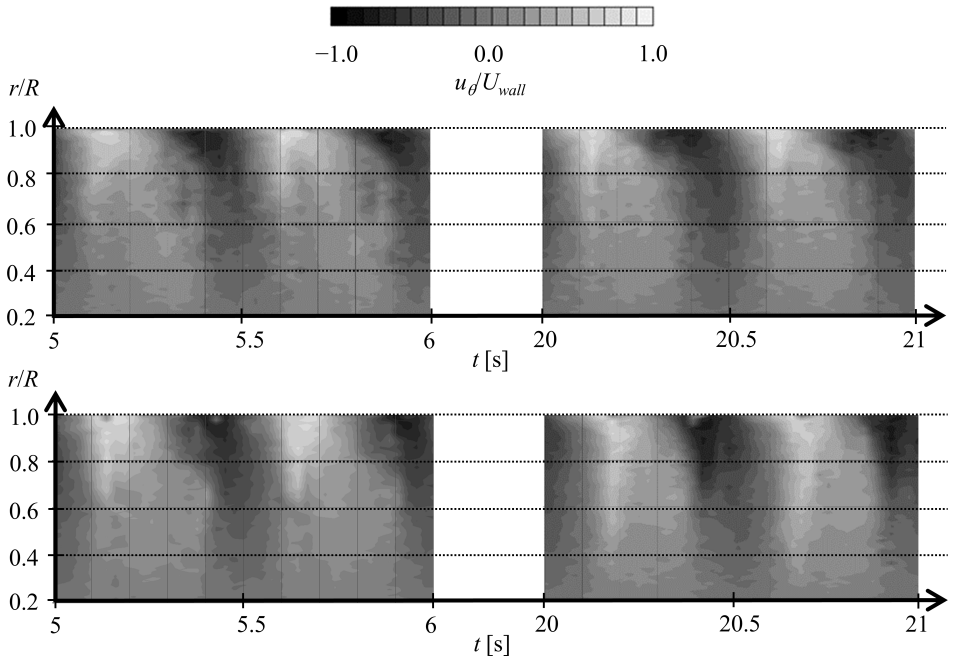


Figure 2.16: Azimuthal velocity distributions of the curry paste at each elapsed oscillating time, where the oscillation frequency and amplitude are $f_o$ = 2.0 Hz and $\Theta$ = 45°, respectively, setting temperatures are; (upper) $T_0$ = 35°C, and (lower) $T_0$ = 40°C; $U_{wall}$ = 715.5 mm/s.

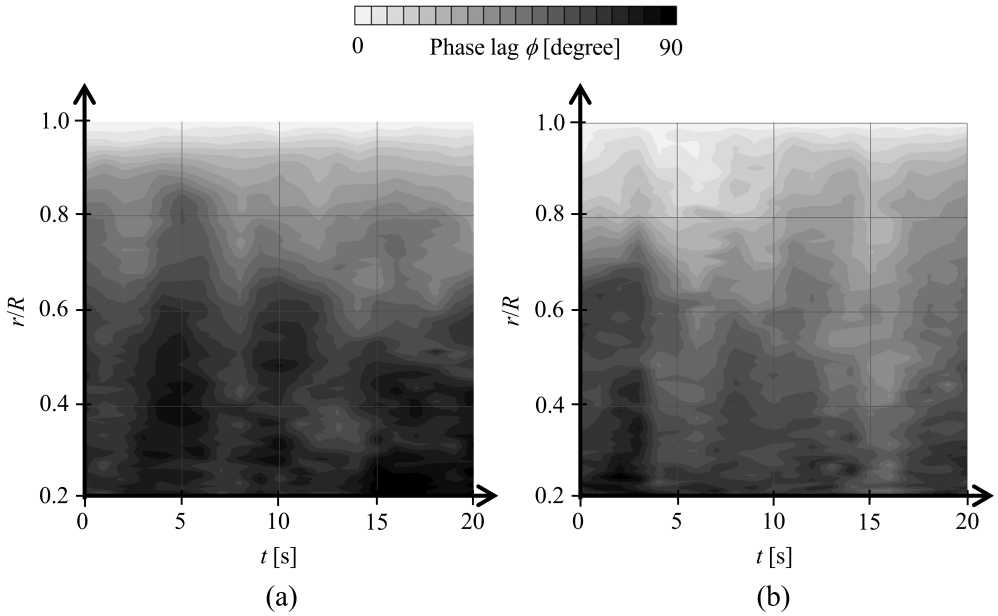


Figure 2.17: Radial-time distribution of phase lag in the local velocity fluctuations from a cylinder wall for curry paste at fixed temperatures (a) $T_0$ = 35°C, (b) $T_0$ = 40°C.

To determine quantitative differences in the rheological characteristics between two set temperatures, phase lag profiles (Fig. 2.18) were obtained from an analysis of all the time profiles (25 s) using the DFT analysis. From their trend of phase-lag profiles, evaluating the effective viscosity is difficult as it is influenced by the dispersed multiphase properties in curry paste. By averaging the gradients of the phase lag at each radial position, estimates of the viscosity in the bulk volume can be obtained. From these averaged gradients in the radial range, $r/R = 0.8 - 1.0$, the values estimated for the viscosity were 3022 mm$^2$/s for $T_0 = 35°$C and 6479 mm$^2$/s for $T_0 = 40°$C. These values are effective bulk viscosities for the test fluids plus ingredients, estimated from momentum transfer from the cylinder wall. In brief, the viscosity of beef tallow decreases with increasing temperature that simultaneously allows the ingredients to move more freely in the radial direction. This increases the effective bulk viscosity in the solution estimated with the present USR.

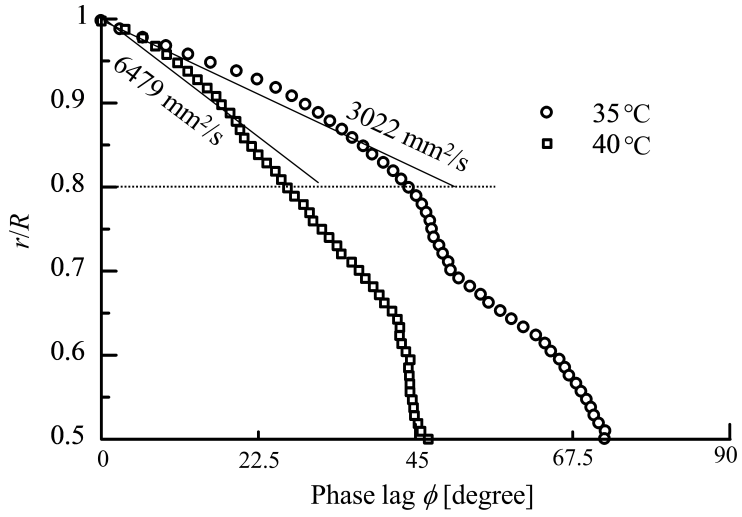


Figure 2.18: Phase lag of the local velocity fluctuations from a cylinder wall for curry paste at two fixed temperatures.

## 2.4 Conclusion

To provide a visualization and quantitative evaluation of opaque and complex fluids, which are commonly encountered in industry and nature, we have proposed a rheometry using UVP, termed USR, which permit measurements to be taken of fluids in an open cylindrical vessel undergoing unsteady rotation. The USR approach provides a qualitative evaluation of rheological characteristics and a quantitative estimate of rheological properties in the local bulk volume. The principle property is the effective bulk viscosity of general complex fluids using phase-lag information extracted from spatio-temporal velocity data measured by UVP.

Three fluids, montmorillonite suspension, LM-pectin gel, and curry paste, with different complex behaviors were used as test fluids to demonstrate the utility of USR. These test fluids are typical examples of thixotropic fluids, pseudo plastic fluids, and fluids containing large semisolid ingredients. For the montmorillonite suspension, the phase lag appears as its time-dependent viscosity decreases in the suspension through unsteady shear stress induced by oscillations at the cylinder wall. In the yielded region, the radial profile of the phase lag closely follows the analytic solutions for a Newtonian fluid; the corresponding Newtonian viscosity was found to be $\mu = 0.489$ Pa $\cdot$ s along with a yield stress of $\tau_Y = 4.57$ Pa. The local gradients of the phase-lag profiles lead to corresponding viscosities, and this makes it possible to obtain local effective viscosities, which reflect all viscoelastic effects as an effective Newtonian viscosity. The effective viscosity is determined from the local crossing point of the gradient profile with the contour of the corresponding viscosity. For LM-pectin gel, a decrease in the viscosity occurs through the fragmentation of large gel clusters into smaller ones, and the smallest viscosity recorded, of around 1000 mm$^2$/s, may correspond to the limit at which clusters break up near the container wall under the applied shear stress. In the determination of the viscosity of curry paste, the viscosity values were estimated at 3022 mm$^2$/s for $T_0 = 35°$C and 6479 mm$^2$/s at $T_0 = 40°$C. These values are effective bulk viscosities of curry paste plus ingredients, estimated from momentum transfer from the cylinder wall.

In summary, USR provides useful rheometry determining instantaneous rheological properties in the local bulk volume (corresponding to the cylindrical measurement volume used for UVP). The measurement of the velocity profiles is completed within seconds and USR is able to capture rheological properties in a run-time manner. Postprocessing to extract useful

rheological information offers excellent potential for obtaining details of other rheological properties. Further developments of USR could establish a method for evaluating not only the viscosity but also the elasticity from velocity information something that appears highly attractive. Other options may include methods for measuring viscoelasticity through linear analysis using a rheology model such as the Maxwell model for complex fluids. In performing linear viscoelastic analysis with velocity information only, measurement noise will be a considerable problem to overcome. The development of UVP technology and ultrasonic velocimetry in general also has been progressing. Ultrasonic measurements of velocity fields still have a large potential in resolving and expanding on current information [32–34]. These developments will improve the capability of USR procedures.

## References


[1] L. Nicodemo, L. Nicolais, and R. F. Landel, "Shear rate dependent viscosity of suspensions in Newtonian and non-Newtonian liquids," Chem. Eng. Sci. 29, 729–735 (1974).

[2] C. J. Dimitriou, L. Casanellas, T. J. Ober, and G. H. Mckinley, "Rheo-PIV of a shear-banding wormlike micellar solution under large amplitude oscillatory shear," Rheol. Acta. 51, 395–411 (2012).

[3] W. Wolthers, M. H. G. Duits, D. Van Den Ende, and J. Mellema, "Shear history dependence of the viscosity of aggregated colloidal dispersions," J. Rheol. 40, 799–811 (1996).

[4] C. Ancey, "Solving the Couette inverse problem using a waveletvaguelette decomposition," J. Rheol. 49, 441–460 (2005).

[5] Y. L. Yeow, W. C. Ko, and P. P. Tang, "Solving the inverse problem of Couette viscometry by Tikhonov regulation," J. Rheol. 44, 1335–1351 (2000).

[6] G. Heirman, R. Hendrickx, L. Vandewalle, D. Van Gemert, D. Feys, G. De Schutter, B. Desmet, and J. Vantomme, "Integration approach of the Couette inverse problem of powder type self-compacting concrete in a wide-gap concentric cylinder rheometer," J. Non-Newton. Fluid Mech. 150, 93–103 (2008).

[7] J. J. Stickel, and R. L. Powell, "Fluid mechanics and rheology of dense suspensions," Ann. Rev. Fluid Mech. 37, 129–149 (2005).

[8] M. Doi, and T. Ohta, "Dynamics and rheology of complex interfaces," J. Chem. Phys. 95, 1242–1247 (1991).

[9] *Ultrasonic Doppler Velocity Profiler for Fluid Flow*, Springer Science, edited by Y. Takeda (Springer, Tokyo, 2012).

[10] A. Gurung, J. W. Haverkort, S. Drost, B. Norder, J. Westerweel, and C. Poelma, "Ultrasound image velocimetry for rheological measurements," Meas. Sci. Technol. 27, 094008 (2016).

[11] G. Ovarlez, F. Bertrand, and S. Rodts, "Local determination of the constitutive law of a dense suspension of noncolloidal particles through magnetic resonance imaging, " J. Rheol. 50, 259–292 (2006).

[12] S. Jarny, N. Roussel, S. Rodts, F. Bertrand, R. Le Roy, and P. Coussot, "Rheological behavior of cement pastes from MRI velocimetry," Cement Concrete Res. 35, 1873–1881 (2005).

[13] F. Rodrigez-Gonzalez, J. Perez-Gonzalez, L. De Vargas, and B. M. Marin-Santibane, "Rheo-PIV analysis of the slip flow of a metallocene linear low density polyethylene melt," Rheol. Acta 49, 145–154 (2010).

[14] J. Perez-Gonzalez, J. J. Lopez-Duran, B. M. Marin-Santibanez, and F. Rodriguez-Gonzalez, "Rheo-PIV of a yield-stress fluid in a capillary with slip at the wall," Rheol. Acta 51, 937–946 (2012).

[15] L. M. Quinzani, R. C. Armstrong, and R. A. Brown, "Use of coupled birefringence and LDV studies of flow through a planar contraction to test constitutive equations for concentrated polymer solutions," J. Rheol. 39, 1201–1228 (1995).

[16] J. P. Rothstein, and H. M. Gareth, "Inhomogeneous transient uniaxial extensional rheometry," J. Rheol. 46, 1419–1443 (2002).

[17] T. Gallot, C. Perge, V. Grenard, M. A. Fardin, N. Taberlet, and S. Manneville, "Ultrafast ultrasonic imaging coupled to rheometry: Principle and illustration," Rev. Sci. Instrum. 84, 045107 (2013).

[18] B. Ouriev, and E. J. Windhab, "Rheological study of concentrated suspensions in pressure-driven shear flow using novel in-line ultrasound Doppler method," Exp. Fluids 32, 204–211 (2002).

[19] B. Derakhshandeh, D. Viassopoulos, and S. G. Hatzikiriako, "Thixotropy, yielding and ultrasonic Doppler velocimetry in pulp fibre suspensions," Rheol. Acta 51, 201–214 (2012).

[20] Y. Tasaka, T. Kimura, and Y. Murai, "Estimating the effective viscosity of bubble suspensions in oscillatory shear flows by means of ultrasonic spinning rheometry," Exp. Fluids 56, 1867 (2015).

[21] T. Shiratori, Y. Tasaka, Y. Oishi, and Y. Murai, "Ultrasonic velocity profiling rheometry based on a widened circular Couette flow," Meas. Sci. Thechnol. 26, 085302 (2015).

[22] T. Shiratori, Y. Tasaka, and Y. Murai, "Rapid rheological characterization of viscoelastic fluid based on spatiotemporal flow velocimetry," Exp. Therm. Fluids Sci. 71, 1–13 (2016).

[23] T. Shiratori, Y. Tasaka, Y. Murai, and Y. Takeda, "Development of ultrasonic visualizer for capturing the characteristics of viscoelastic fluids," J. Vis. 16, 275–286 (2013).
[24] H. A. Barnes, "Thixotropy—A review," J. Non-Newton. Fluids Mech. 70, 1–33 (1997).
[25] R. Goh, Y.-K. Leong, and B. Lehane, "Bentonite slurries - zeta potential, yield stress, adsorbed additive and time-dependent behaviour," Rheol. Acta 50, 29–38 (2011).
[26] G. Lagaly, and S. Ziesmer, "Colloid chemistry of clay minerals: The coagulation of montmorillonite dispersions," Adv. Colloid Interface Sci. 100, 105–128 (2003).
[27] V. C. Kelessidis, and R. Maglione, "Yield stress of water-bentonite dispersions," Colloids Surf. A: Physicochem. Eng. 318, 217–226 (2008).
[28] J. T. Fu, and M. A. Rao, "Rheology and structure development during gelation of low-methoxyl pectin gels: The effect of sucrose," Food Hydrocolloid 15, 93–100 (2001).
[29] K. Suzuki, T. Yoneda, and H. Enoto, "Factors affecting to the viscosity of montmorillonite/water suspension," Clay Sci. 50, 162–174 (2012) in Japanese.
[30] J. Achenbach, *Wave Propagation in Elastic Solids* (Elsevier, Amsterdam, 2012).
[31] B. Rand, E. Pekenc, J. W. Goodwin, and R. W. Smith, "Investigation into the existence of edge-face coagulated structures in Na-montmorillonite suspensions," J. Chem. Soc., Faraday Trans. 1 76, 225–235 (1980).
[32] C. Poelma, "Ultrasound imaging velocimetry: A review," Exp. Fluids 58, 3 (2017).
[33] V. Meacci, S. Ricci, J. Wiklund, B. Birkhofer, and R. Kotze, "Flow-Viz—An integrated digital in-line fluid characterization system for industrial applications," in IEEE Sensors Applications Symposium (SAS) (2016), pp. 1–6.
[34] S. Fischer, P. Schmitt, D. Ensminger, F. Abda, and A. Pallares, "A new velocity estimation method using spectral identification of noise," Flow Meas. Instrum. 19, 197–203 (2008).

Chapter 3

# Rheological properties of montmorillonite dispersions in dilute NaCl concentration investigated by USR

## Contents


**3.1 Introduction** . . . . . **30**
3.1.1 Rheology of montmorillonite dispersions . . . . . 30
3.1.2 Ultrasonic rheometry . . . . . 31
3.1.3 Objective . . . . . 32
**3.2 Material and method** . . . . . **32**
3.2.1 Conditions of test dispersions . . . . . 32
3.2.2 Experimental arrangement of ultrasonic spinning rheometry . . . . . 33
3.2.3 Analysis of effective Newtonian viscosity . . . . . 33
**3.3 Results of rheological evaluation for Mt dispersion** . . . . . **33**
3.3.1 Velocity and phase-lag profiles . . . . . 33
3.3.2 Particle network recovery in the dispersion . . . . . 35
3.3.3 Evaluations of shear-rate-dependent viscosity . . . . . 37
3.3.4 Flow curve under shear banding . . . . . 40
**3.4 Conclusion** . . . . . **43**
**References** . . . . . **43**


## Preface

The aim is to prove that the kinematic rheometry presented in Chapter 2 can reveal the capability to clarify the unexplained phenomena as practical methodology. The kinematic rheometry using phase-lag analysis here shows promise for the application of elucidations of unexamined phenomena in clay rheology. This work was already in Yoshida *et al.*, Appl. Clay Sci. (2018).

## Abstract


Rheological changes of gelled montmorillonite dispersions with different NaCl concentrations and alkali conditions were evaluated by ultrasonic spinning rheometry. It uses velocity-profile information that is obtained in an open-cylindrical container under periodic oscillations. The measurement was conducted with a focus on the rheological behavior at a low shear rate $O(1\ \mathrm{s}^{-1})$, which is difficult to measure because of shear banding. The rheometry represents the coexistence of gel and sol conditions in dispersions as profiles of the phase lag of oscillations that are propagated from the cylinder wall. The critical shear rate at a yielding point and the onset of shear-thinning behavior was quantified, which has been regarded as only an apparent or speculated value by many previous researchers. Viscoelasticity from particle networks in the dispersion was observed, and the networks deform like a spring, without breaking the structure under low-shear-rate conditions.

# 3.1 Introduction

## 3.1.1 Rheology of montmorillonite dispersions

Particles of montmorillonite (Mt), which is a type of smectite, are polygonal platelets with a $O$(nm) thickness and a 0.1- to 1- $\mu$m planiform size. When Mt powder swells in ionic solvents, the dispersions provide typical rheological characteristics arising from networks of Mt particles that are termed thixotropic characteristics [1, 2], as summarized in the review by [3]. These characteristics have been utilized in field such as agriculture, civil engineering, and nuclear engineering, as drilling muds, adsorbents, and nanocomposites. In these applications, the networks must be understood, which are structuralized passively with a time-dependence and with physical bonding forces. An anomalous viscosity or viscoelasticity of the dispersion is given by structuring networks, which are affected by particle aggregation or flocculation as a result of particle attractive or forces. Three main factors influence the structuring: Van der Waals attraction, electrostatic repulsion, and Coulomb attraction forces [4, 5].

According to [6], the particle networks in Mt dispersions vary according to solvent pH and ionic strength as summarized in Fig. 3.1. The particle has electrocharacteristics of a large permanent negative face charge that arise from isomorphic substitution within the particle structure, and a pH-dependent edge charge at the end of the structure. The negative charge is compensated by exchangeable cations. The electrostatic interaction between the particles can change easily by pH and cation concentration in the solution. These electrical characteristics promote the structuring of stable networks at microscopic scales, and therefore, the dispersions result in an anomalous viscosity or viscoelasticity in the macroscopic rheological properties [7].

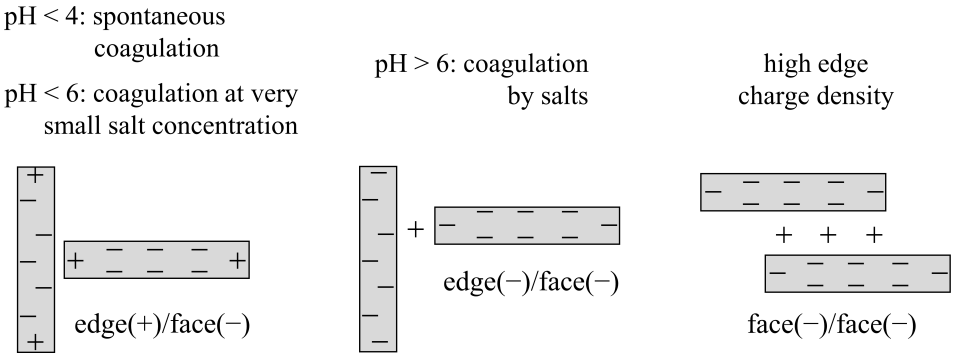


Figure 3.1: The different modes of coagulation of swelling Mt particles [6].

Particle networks in the dispersion have various microscopic structures, which are classified into two types, namely, house-of-cards and band-type structure. The former is a stable structure with edge/face bonding, and is only formed in acidic media for edges that are positively charged, or in slightly alkaline media above the critical salt concentration [6]. If the concentration increases gradually beyond a critical value, the structure changes from the house-of-cards to the band-type structure [7]. This occurs because the ionic strength shifts from an edge/face to a face/face network, which causes high densities of edge charges from an increase in salt concentration as shown in Fig. 3.1.

To understand the rheological properties of different structural networks, some factors have been investigated through experimental and theoretical research at microscopic scales [8–10]. When structural transitions occur, the structure type and attractive force between each particle changes as expected from DLVO theory [5, 11], which describes the forces between charged surfaces that interact through a liquid medium. Macroscopic responses result from these microstructures, the strength of interactions in each particle increases with respect to the salt concentration [12]. Brandenburg *et al.* [4] indicated that the viscosity changes significantly depending on the solvent, pH, fluid temperature, Mt powder density and sodium salt concentration, when they aimed to understand the electrical interactions between each particle.

At pH $<$ 6 (isoelectric point), when particle networks are broken by a shear force, they can reconstruct instantly and spontaneously because of positive edge charges. This reconstruction is a key factor of thixotropy. In contrast, at pH $>$ 6, the particles disperse homogeneously because of negative edge charges. However, salt addition allows each particle to structure networks because attractive forces exist through the cations. The thixotropy is also developed in this situation, and the thixotropic properties change with an increase in salt concentration unless the particles completely aggregate in fluid media.

A typical transition map at pH $>$ 6 with changes in salt concentrations is deduced from some experimental investigations by using torque rheometry and microscopy [4, 13–16] as summarized in Fig. 3.2. Each structure can be broken and the particles are dispersed by shear forces, and are reconstructed by leaving them at rest. The strength of particle networks

indicates that this map is divided into three phases from the rheological observations, namely, a viscous, a viscoelastic, and an elastic phases. These represent totally dispersed, flocculated, and aggregated conditions, respectively.

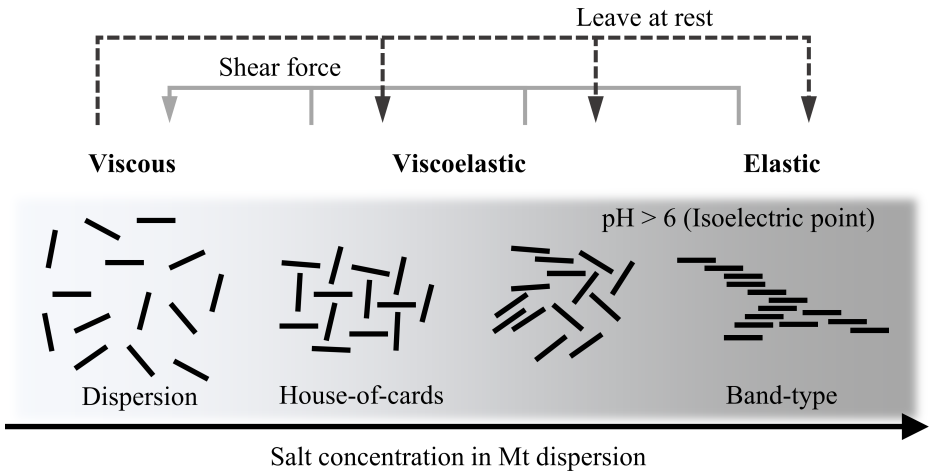


Figure 3.2: Regime map of particle networks in the Mt dispersion with changes in salt concentration, shear force and leave at rest, deduced from previous studies [4, 13 –16].

Many investigations have been performed to reveal the quantitative mechanical response of dispersions and to control dynamic fluid behaviors. Experimental approaches are divided into two main types; an assumption of the microstructural network from a macrorheological response [17–19], and an assumption of the macro-rheological response from microscopy [20, 21]. Because no measurement systems exist that enable us to obtain microscopic structural deformations directly, recent research is still focused mainly on only the macro-mechanical response under high-shear-rate conditions by using torque rheometers. Minimal research exists on the macro-rheological response by using torque rheometry.

This has occurred because of limitations and problems from shear banding [22–24] and wall slip [25] for applications to Bingham or Herschel–Bulkley fluids under low-shear-rate conditions, such as a co-existing gel and sol media. Few experimental investigations exist on thixotropic fluids with unsteady shearing, because torque rheometers can evaluate only macro-rheological properties, including influences from the problems mentioned above. The properties are defined as an apparent viscosity or plastic viscosity, are the most significant sources of ambiguity for conventional torque rheometers, and are termed the “Couette inverse problem” [26–28].

### 3.1.2 Ultrasonic rheometry

To overcome these limitations and to reveal the rheological characteristics of dispersions with thixotropic behaviors, another rheometry approach was proposed recently in which ultrasonic waves are used [29–32]. A rheometry using ultrasonic velocity profiling (UVP) [33] was proposed; UVP can measure instantaneous velocity profiles along propagation lines of ultrasonic waves.

We proposed a rheometry using UVP for complex fluids in rotating cylindrical system without requiring an inner cylinder to measure the axial torque, termed ultrasonic spinning rheometry (USR) [34–37]. This technique can be applied even for opaque liquids and for complex fluids.

With simple, open cylindrical containers, measurements of a wide range of target properties are possible. Different simple shear conditions are realized as spatial distributions by setting the oscillation frequency $f$ and the amplitude $\Theta$ to different values. Shiratori *et al*. [35] proposed a model-free USR for the quantitative evaluation of a shear-rate-dependent viscosity without using any rheological models. A supplemental axial torque measurement was used to satisfy the boundary conditions to solve the equations of motion.

Tasaka *et al*. [37] used USR to evaluate the effective viscosity of a liquid with tiny bubbles as a corresponding Newtonian viscosity in a UVP measurement volume under strong oscillatory shear flows. In an analysis of this approach, the phase lag of velocity fluctuations that propagated from the oscillating cylinder wall to the inner part of the fluid is related to the local effective viscosity. Here, the viscosity is determined from local information on the phase lag, and thus the method can provide spatial viscosity distributions. As an advanced USR analysis mentioned in Chapter 2, the method was established for general complex fluids, such as strong viscoelastic fluids and fluids with dispersed $O$(10 mm) solid materials. Spatial effective viscosity profiles, yield stresses, and elastic moduli of Mt dispersions were evaluated by analyzing only the instantaneous

velocity profiles. From these branches of applicability in previous reports, USR system raises the possibility of evaluating rheological properties in complex fluids in more robust methodology than conventional rheometry, such as rotational torque rheometry.

### 3.1.3 Objective

In this paper, unexamined rheological properties of Mt dispersions are evaluated by using USR. The rheological responses of the dispersion show great differences, especially under relatively low-shear-rate conditions in unsteady shear flows. USR is applicable to the existence of shear banding, which have been dealt with by using an empirical valuation because of the limitations mentioned above. USR can provide proof of critical shear rates to achieve particle-network breakdown as summarized in Fig. 3.2. The changes in critical shear rates with NaCl concentration for cases where sols and gels co-exist are explored to understand shear-rate-dependent viscosity and shear-banding effects.

## 3.2 Material and method

### 3.2.1 Conditions of test dispersions

Kunipia-F (Kunimine Industries Co., Ltd.) was used as the test material. According to [38], its structural formula calculated from chemical analysis is $Na_{0.84}Ca_{0.05}K_{0.01}[Si_{7.82}Al_{0.18}][Al_{3.19}Fe_{0.21}Mg_{0.52}]O_{20}(OH)_4$. Kunipia-F comprised 99 wt.% of Mt with other accessory minerals including quartz (chalcedony), feldspar, and calcite [39]. Exchangeable cations were composed of Na: 108, Ca: 9.18, K: 1.19, and Mg: 0.11 cmol(+)/kg tachi2014integrated. The material included $Na_2SO_4$: $4.17 \times 10^5$ mol/g and NaCl: $1.54 \times 10^5$ mol/g. To prepare fully swelled and homogeneous dispersions with 4.0 wt.% Mt, 40 g Kunipia-F was swelled in 0.5 L of pure water for two days (48 h). Then, the dispersion was stirred for 30 min and was kept for a day (24 h). After ensuring that the dispersion was fully swelled, $c_x$ mol/L NaCl aqueous solution (0.5 L) was added. Before the experiments, the dispersion was kept for two additional days to ensure that it had reached equilibrium.

The speed of sound is an important property in ultrasonic measurements. The speed of sound in the dispersion is almost equal to that of water (1480 m/s). Here, the dispersion density is $\rho = 1040$ kg/m$^3$. The pH in some prepared dispersions was measured by using a pH meter (TOA DKK Co., HM-30G) as shown in Table 3.1. The pH was almost constant under the alkali experimental conditions.

Table 3.1: pH values in each $c_x$ of Mt dispersion.

| $c_x$[mol/L] | 0.01 | 0.02 | 0.04 | 0.08 |
|---|---|---|---|---|
| pH | 8.98 | 9.03 | 9.06 | 8.64 |

To achieve the shear-rate measurement range, 1 – 100 s$^{-1}$, the oscillation amplitude was set at different $\Theta = \pi/8,\ \pi/4,\ \pi/2,\ 3\pi/4$ rad with a fixed oscillation frequency, $f = 1.0$ Hz. To approach gel/sol transitions of the Mt dispersion as determined by NaCl concentration, especially under low-shear-rate conditions, concentrations were set to $c_x = 0.001 - 0.05$ mol/L according to [3, 16, ]. The experimental parameters are summarized in Table 3.2. The test fluid temperature was kept constant at $T_0 = 20$°C. After filling the cylinder with the dispersion, the dispersion was stirred vigorously to eliminate the influence of shear history [3]. For the velocity profile measurements, the UVP requires tracer particles to be dispersed uniformly in test fluids. Mt dispersions do not require any additional tracer particles for the measurements.

Table 3.2: Experimental NaCl concentration ($c_x$) and oscillating amplitude ($\Theta$), where the oscillating frequency, $f$, was 1 Hz in these experimental parameters.

| # | $c_x$[mol/L] | $\Theta$[rad] | # | $c_x$[mol/L] | $\Theta$[rad] |
|---|---|---|---|---|---|
| 1 | 0.001 | $\pi/4$ | 8 | 0.02 | $3\pi/4$ |
| 2 | 0.001 | $\pi/2$ | 9 | 0.025 | $\pi/2$ |
| 3 | 0.01 | $\pi/8$ | 10 | 0.03 | $\pi/2$ |
| 4 | 0.01 | $\pi/2$ | 11 | 0.04 | $\pi/2$ |
| 5 | 0.01 | $3\pi/4$ | 12 | 0.04 | $3\pi/4$ |
| 6 | 0.02 | $\pi/4$ | 13 | 0.05 | $3\pi/4$ |
| 7 | 0.02 | $\pi/2$ | | | |

### 3.2.2 Experimental arrangement of ultrasonic spinning rheometry

An open vertical rotating cylinder made from acrylic resin with a 145-mm inner diameter ($2R$) and 65-mm-high, 2-mm-thick lateral wall, was used as the test container. The cylinder was mounted at the center of a 1000 mm × 1000 mm water bath to maintain a uniform temperature $T_0$ and to allow ultrasonic waves to propagate from outside the cylinder. Cylinder oscillations were controlled at a setting oscillation angle $\Theta$ and oscillation frequency $f$. Instantaneous velocity profiles of the fluids in regular oscillations were measured by using UVP. These parameters determine the maximum and minimum input shear strength for the test fluids, and should be selected carefully to achieve suitable conditions. For large fluctuations of the maximum shear flow, the flow condition could not maintain unidirectional shear flow because of the non-negligible meridional circulations.

To process captured echo signals and to calculate spatio-temporal velocity distributions, UVP-model Duo (Met-Flow S.A., Switzerland) was selected as the velocity measurement system. To obtain the azimuthal velocity component, an ultrasonic transducer of resonance frequency 4 MHz and 5 mm effective element diameter was mounted in the bath at a horizontal displacement, $\Delta y$, which is set in the off-axis from the cylinder center to obtain an azimuthal velocity component. $\Delta y$ = 15 mm was selected from empirical considerations based on the results of previous study [37] and Chapter 2. Assuming that an axisymmetric flow field and the velocity component in the radial direction are negligible compared with the azimuthal component, the azimuthal velocity component $u_\theta$ is

$$u_\theta = \frac{u_\xi r}{\Delta y} \tag{3.1}$$

at a radial position $r$. Typical measurement resolutions in time and space are 25 ms and 0.74 mm in the measurement direction $\xi$, respectively. The radial position in $r/R < \Delta y/R \approx 0.2$ cannot be measured due to the off-axis displacement of transducer. Further details of the configurations are given in previous study [37].

### 3.2.3 Analysis of effective Newtonian viscosity

To evaluate rheological properties, phase-lag analysis was used, and details of the procedure are summarized in Appendix. If the parameter, $\Theta$ or $f$, changes, the measurable range of the shear rate profiles also changes. In terms of parameter settings, it is very important to satisfy unidirectional flow in the cylindrical container. To expand the measurable range of shear rate, the oscillation amplitude, $\Theta$, was changed. Here, silicone oil (KF-96 300 cSt, Shin-Etsu silicone, Shin-Etsu Chemical Co. Ltd., Japan) of which its kinematic viscosity precisely is given as 300 mm$^2$/s under low shear rates, $\dot{\gamma} < O(10^3\ \mathrm{s}^{-1})$, is used to validate the precision of rheological evaluation. The oil temperature was kept constant at $T_0$ = 25°C by using a thermostatic bath.

Four oscillation amplitudes, $\Theta = \pi/8,\ \pi/4,\ \pi/2,\ 3\pi/4$ rad, were examined and the results of the rheological evaluation are shown in Fig. 3.3. The vertical and horizontal axes indicate the effective Newtonian kinematic viscosity $\nu$ and shear rate $\dot{\gamma}_{\mathrm{eff}}$ that were obtained from measured velocity profiles (see Appendix). Here, the dashed line shows $\nu$ = 300 mm$^2$/s, which is an ideal kinematic viscosity in silicon oil (300 cSt) at 25°C.

Results at $\Theta = \pi/8,\ \pi/4$ rad are almost equal to the index value in each shear rate profile. Irrespective of the oscillating amplitudes, $\Theta$, the viscosity results are close to a true value (300 mm$^2$/s). This provides supporting evidence of the measurement precision, especially in the range of $10^0 < \gamma_{\mathrm{eff}} < 10^2\ \mathrm{s}^{-1}$. However, deviations from the value in low $\dot{\gamma}_{\mathrm{eff}}$ regions, such as near the center of the cylinder, become larger than any other region. This occurs because, when the velocity fluctuations are small near the center of the cylinder, quantifications of phase-lag profiles can be influenced strongly by measurement noises. In addition, relative differences in ultrasonic measurement volume at each radial position influence the results. From these reasons, the regions to evaluate the viscosity are limited to $r/R < 0.6$ in this report, although it is possible to widen the regions by enhance the noise filtering methods.

## 3.3 Results of rheological evaluation for Mt dispersion

### 3.3.1 Velocity and phase-lag profiles

The azimuthal velocity, $u_\theta$, were obtained instantaneously by substituting velocity obtained using UVP, $u_\xi$, to Eq. (3.1), where the schematic of positional relations between spatial displacement of the ultrasonic beam emitted from transducer and radial position in the oscillating cylindrical container [Fig. 3.4(a)]. The oscillation was controlled by sine functional angular velocity, $u_{\mathrm{wall}}(t) = 2\pi^2 f R\Theta/180 \sin 2\pi f t\ \ (= U_{\mathrm{wall}} \sin 2\pi f t)$ [Fig. 3.4(b)]. Thus, velocity in the test fluid is propagated as unsteady shear flows [Fig. 3.4(c)], where the measured velocity is at case of $c_x$ = 0.001 (Table 3.2: # = 2). From these velocity profiles, the shear wave propagates inside from the cylinder wall, where the highest shear rate is applied near the

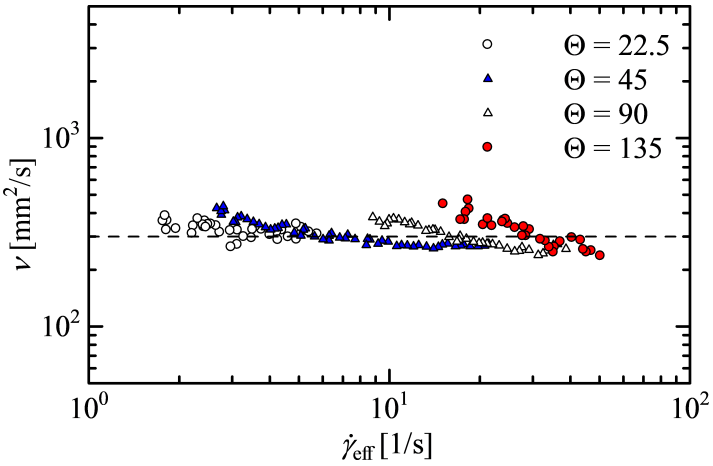


Figure 3.3: Measurement results in limited radial range ($0.6 < r/R$) of shear rate and kinematic viscosity in silicon oil (300 mm$^2$/s), where each symbol indicates a different oscillating amplitude, $\Theta = \pi/8,\ \pi/4,\ \pi/2,\ 3\pi/4$ rad.

cylinder wall. UVP with high temporal resolutions $O$(10 ms) can measure the test fluid motions as spatio-temporal velocity profiles. Moreover, noises in instantaneous velocity profiles are eliminated by averaging in 100 periods of oscillation (100 s).

With the assumption of axisymmetric and unidirectional flow in the azimuthal direction, the spatio-temporal velocity map obtained by the UVP can be converted into a radial-temporal distribution of the azimuthal velocity component. The phase-averaged velocity profiles $u_\theta(r,\ t)$ in 100 periods of oscillation (100 s) is shown in Fig. 3.5, measured at $f = 1.0$ Hz, $\Theta = \pi/2$ rad, and $c_x = 0.001,\ 0.01,\ 0.02,\ 0.03,\ 0.04$ (Table 3.2: # = 2, 4, 7, 10, 11). The vertical and horizontal axes indicate the radial positions normalized by the radius of the cylindrical container, $R$, and the spin-cycle time. The gray-scale contours represent the azimuthal velocity normalized by the maximum azimuthal velocity at the cylinder wall, $U_{\rm wall}$. Here, analyzing the instantaneous velocity profiles shown in Fig. 3.4(c) in parallel, the gray-scale contour of Fig. 3.5(a) was obtained.

Phase lags in the velocity fluctuations result from the oscillating cylinder wall, and these behaviors change with increases in NaCl concentration. In Fig. 3.5(a), for the lowest case of $c_x$, the phase lags propagate from the wall to inside the fluid media. A comparison between Fig. 3.5(a) and (b) shows little difference between the velocity distribution near the central region in $r/R < 0.6$. This difference shows a change in momentum propagation because of the transition in rheological properties. Moreover, this region with a constant phase lag developed gradually for $r/R < 0.8 - 0.9$ with an increase in NaCl concentration. As shown for $c_x = 0.04$ mol/L, the region reaches $r/R = 0.85$.

To quantify these phase lags in the velocity fluctuation, a discrete Fourier transform (DFT) was applied. The oscillation in this system was kept at a constant frequency ($f_{\rm o} = 1.0$ Hz), so the response of fluid motion appears at this dominant frequency. Radial profiles of the phase lags calculated from the velocity distributions shown in Fig. 3.5 are summarized in Fig. 3.6(a). The vertical and horizontal axes show the radial position normalized by the radius of the cylindrical container and the phase lag that is propagated from the wall, and each symbol represents different NaCl concentrations.

For an easy and intuitive understanding of the entire outline of the plots, illustrations drawn from the relationships between the $\phi$ and $r/R$ in Fig. 3.6(b)–(d) were reconstructed. At $c_x = 0.001$ mol/L, the phase-lag profile maintains an almost constant gradient in each radial position. The gradient reflects the momentum propagation that is observed in the velocity fluctuation as mentioned in Fig. 3.5. For $c_x$ (= 0.01 mol/L) that is ten-times larger, a bending point in the profile appears near $r/R = 0.6$. The point shifts gradually to the wall with an increase in $c_x$.

At the inner side of the point, the profile plateaus with no significant change in phase lag. The plateau indicates that a rigid-body medium exists and thus the dispersion is in a gel condition. In contrast, the region with a slope implies that the test material flows with phase-lag profiles, and thus it is regarded as existing in the viscous or viscoelastic state, such as a sol or a quasi-sol. The phase lag at $c_x = 0.01$ mol/L plateaus for $r/R \leqq 0.6$. For $c_x = 0.02$ mol/L, the plateau expands to $r/R = 0.75$. At $c_x = 0.03$ mol/L, the region reaches $r/R = 0.8$. At $c_x = 0.04$ mol/L, an interface exists between the phase-lag profiles with gradients and that with plateaus becomes sharper than other conditions. From previous research, the gel strength and salt concentration of Mt dispersions are correlated positively in $c_x \leq 0.1$ [7]. The interface can be seen clearly because of the increase in gel strength.

Restorative forces exist at the interface between the gel and the sol, and thus the profiles with bending include viscoelasticity. If gels do not possess any viscoelastic characteristics around the interface, the gel regions could not be oscillated

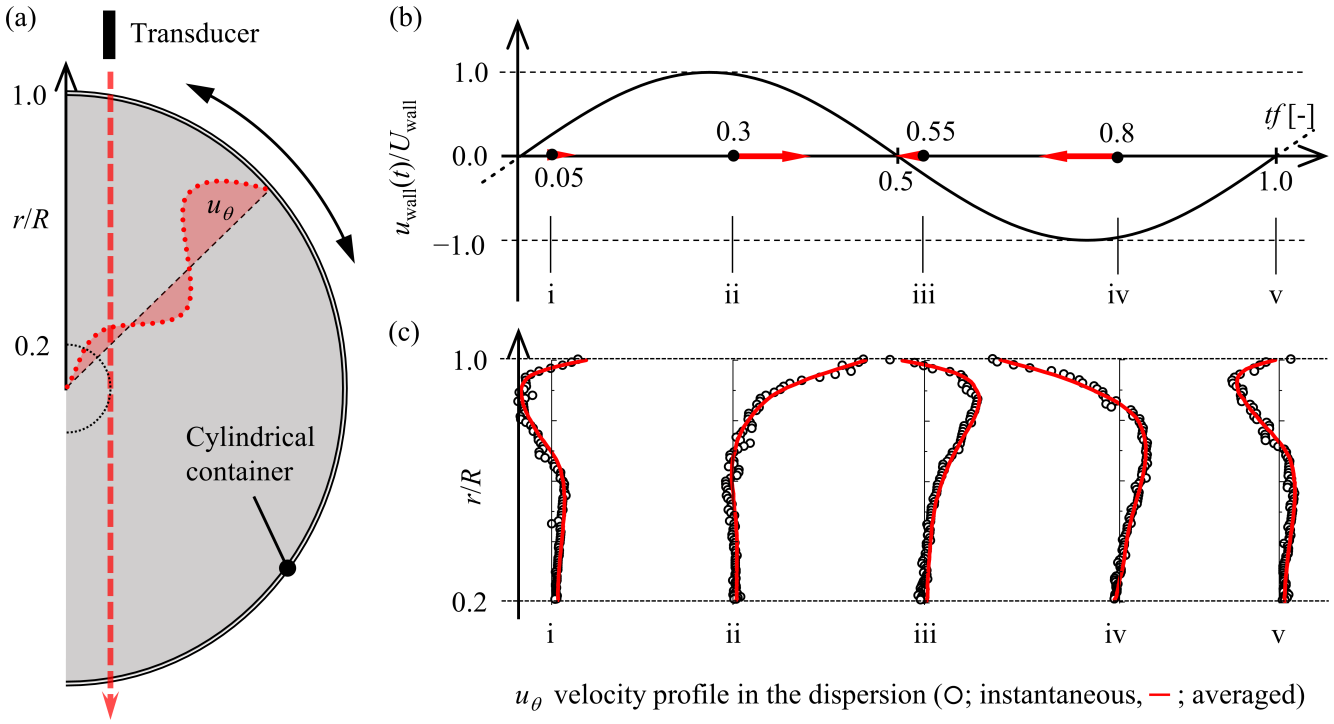


Figure 3.4: (a) Schematic of oscillating cylindrical container and transducer displacement, (b) oscillation angular velocity fluctuation of cylinder wall $u_{wall}(t)/U_{wall}$, (c) instantaneous and averaged azimuthal velocity profiles $u_\theta$ at each spin-cycle $tf_o$ (i–v) at case of $c_x$ = 0.001 mol/L (Table 3.2: # = 2).

followed by an unsteady shear force from the viscous regions. For stably structured dispersions of strong particle networks, strong repulsive or attractive forces exist because of the high response to deformations. Hence, at the gel/sol interface, a curvature of the phase-lag profiles may relate to a viscoelasticity in the Mt dispersions.

### 3.3.2 Particle network recovery in the dispersion

Ionic strength enhances not only the gel strength but also recovery time scale of the particle network in thixotropic fluids. But actually, measurements using a torque rheometer to obtain the recovery time scale have to take many repeated trials of high and low amplitude shearing. USR system can reveal instantaneous response placed important information in thixotropy, such as a time dependence. By utilizing real time monitoring in the advantage of USR, behaviors of the time dependence in Mt dispersion can be captured quantitatively.

The ionic strength enhances the gel strength and the recovery time scale of the particle network in thixotropic fluids. However, measurements to obtain the recovery time scales require many repeated trials of high- and low-amplitude shearing. A USR system can reveal an instantaneous response, which indicates the importance of thixotropy, such as time dependence. An advantage of USR is the use of real-time monitoring, in which the time-dependent behavior of the Mt dispersion can be captured quantitatively.

To evaluate the recovery speed at different $c_x$, Mt dispersions at two NaCl concentrations (Table 3.2: # = 8, 12) were prepared. After filling the cylindrical container with dispersion and stirring it sufficiently to break down the particle networks, velocity measurements were conducted for 1500 s. To quantify the change in phase lag with time, DFT analysis was conducted every four cycles ($tf$ = 4). Time variations of the phase lag are shown in Fig. 3.7, where the vertical and horizontal axes indicate the radial position that is normalized by the cylinder radius and the periodic cycles. The gray scale indicates phase lags from the cylindrical container wall, where different scales are provided for each distribution for better visibility.

In Fig. 3.7(a), the phase lag for $c_x$ = 0.02 shows an almost linear slope in the entire radial position immediately after the measurement started and is shown in Fig. 3.7(c)–i as an instantaneous profile. According to the relationship between the profile shape and the rheological properties mentioned above, the dispersion is a quasi-Newtonian sol state in the entire cylinder. As the oscillation periods increase, $tf$, the profiles converge gradually to a certain shape at $tf \sim 1400$. This result means that the profiles reach the terminal equilibrium state under the set oscillation conditions. The profiles at $tf$ = 1400 as

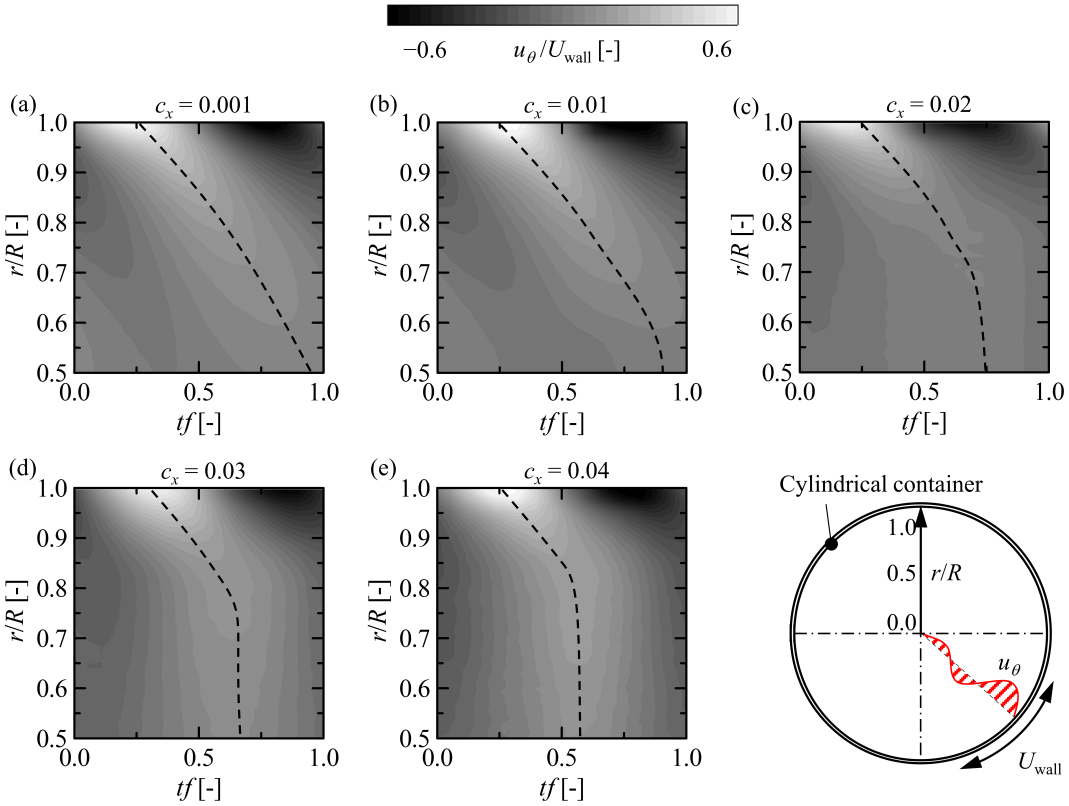


Figure 3.5: Radial-temporal distributions of azimuthal velocity of the Mt dispersion in 4.0 wt.% powder in different NaCl aqueous solutions, $c_x$ = (a) 0.001, (b) 0.01, (c) 0.02, (d) 0.03, (e) 0.04 mol/L, where the oscillation frequency, amplitude, maximum angular velocity, temperature, and recovery time are $f_o$ = 1.0 Hz, $\Theta = \pi/2$ rad, $U_{\mathrm{wall}}$ = 715.5 mm/s, $T_0$ = 20°C, and 100 min, respectively.

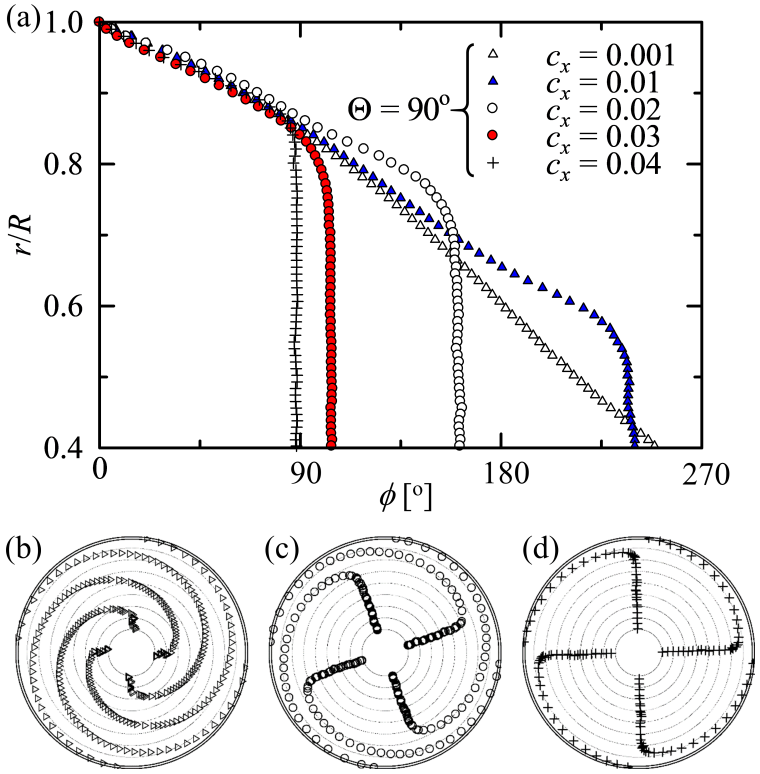


Figure 3.6: (a) Radial profiles of phase lag of local velocity fluctuations from the cylinder wall at each NaCl concentration in Fig. 3.5, and reconstructed schematics of phase-lag profiles at (b) $c_x = 0.001$, (c) 0.02, and (d) 0.04 mol/L.

shown in Fig. 3.7(d)–ii are different from that at $tf = 50$ [Fig. 3.7(c)–i]. The profile bends at around $r/R = 0.6$, which means that the dispersion layer restores the network structures as the gel region ($r/R \leq 0.6$) inside the quasi-Newtonian sol region ($r/R \geq 0.6$).

The profiles for $c_x = 0.04$ in Fig. 3.7(b) change significantly more than those for $c_x = 0.02$ with the convergence time being approximately $tf = 380$. Immediately after the measurement starts [Fig. 3.7(b)], the profiles as extracted in Fig. 3.7(c)–iii show a more gradual variation than those of Fig. 3.7(c)–i. The profile of Fig. 3.7(c)–i has an almost linear shape, whereas that of Fig. 3.7(c)–iii has a round and a plateau region. In Chapter 2, the shape of Fig. 3.7(c)–iii is similar to that of polymer solutions with viscoelastic characteristics, thus the dispersion in $c_x = 0.04$ immediately after stirring behaves like a viscoelastic body. Here, the viscoelastic characteristics result from microscopic structures that are maintained by the particle networks even after strong stirring. After reaching terminal equilibrium states, although the profiles of Fig. 3.7(d)–ii and iv have similar shapes, considerable differences exist. The profile of Fig. 3.7(d)–iv has a wider plateau region, which indicates a wider gel region than that in Fig. 3.7(d)–ii. The profile of Fig. 3.7(d)–ii shows a sharper bending than that of Fig. 3.7(d)–iv. Both differences may be explained by a dependence of the robustness of the particle networks on the NaCl concentration. At lower concentrations, weaker particle networks cannot sustain the microscopic structures. The viscoelasticity and stronger gelling do not manifest under an applied periodic shear stress, whereas the solution with a larger concentration achieves such properties. These results mean that the recovery speed of particle networks and the viscoelastic response of the networks are influenced strongly by changes in NaCl concentration.

### 3.3.3 Evaluations of shear-rate-dependent viscosity

In §3.3.1 and 3.3.2, the phase-lag profiles that are obtained from velocity distributions provide key information to approach the rheological properties under conditions with the co-existence of a gel and sol response. To evaluate the shear-rate-dependent viscosity of the Mt dispersions, we have explained the basic concepts and validations in §3.2.3, and some data processing will be described in Appendix. Experiments were conducted with parameters as summarized in Table 3.2.

The results of kinematic viscosity measurements with different oscillation amplitudes to widen the range of exerted shear rates are summarized in Fig. 3.8(a). The measurement conditions are specified in Table 3.2 (# = 1, 2, 3, 5, 6, 8, 9, 10, 13). The vertical and horizontal axes show a kinematic viscosity and effective shear rate, respectively. Here, in previous report [37]

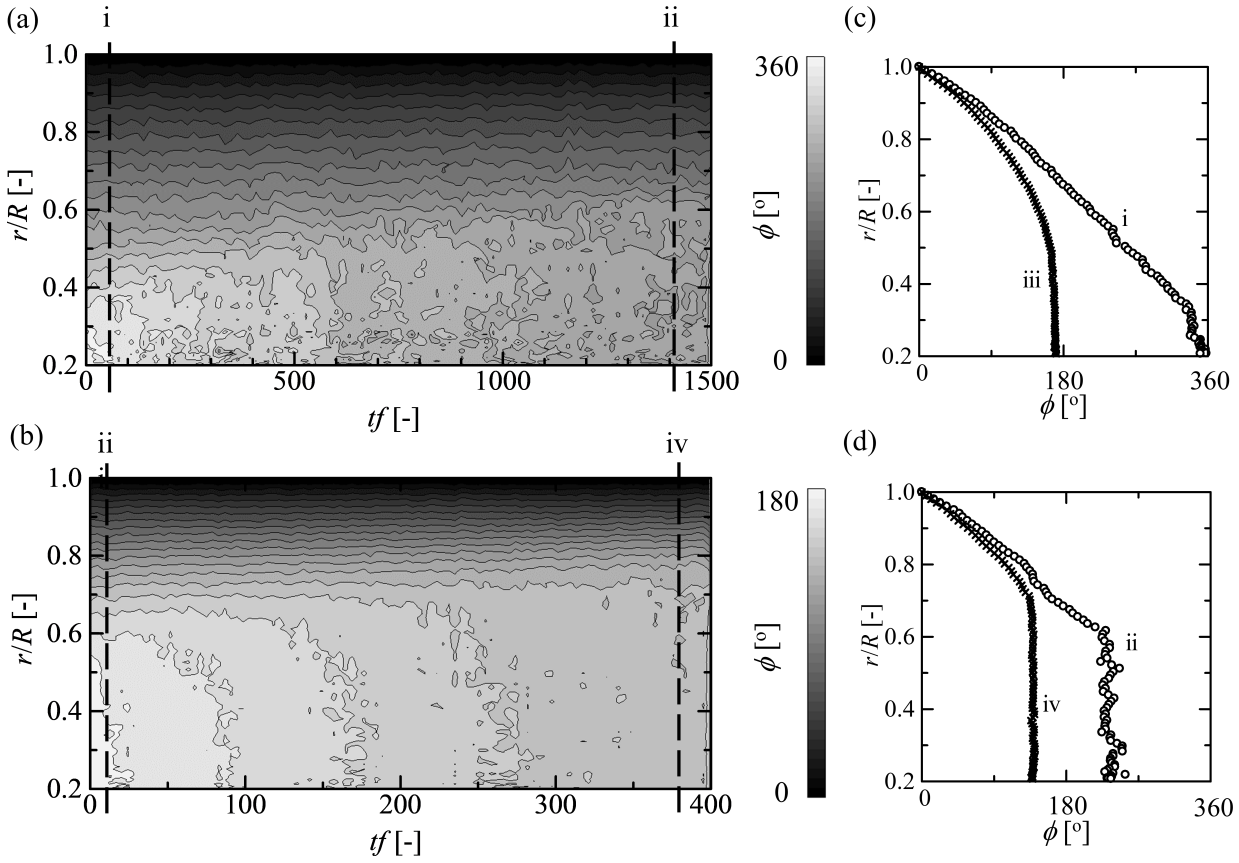


Figure 3.7: Radial-time distribution of phase lag in local velocity fluctuations from a cylinder wall for Mt dispersion at (a) $c_x$ = 0.02 mol/L and (b) $c_x$ = 0.04 mol/L immediately after stirring, where the oscillation frequency, amplitude, and temperature are $f_o$ = 1.0 Hz, $\Theta = 3\pi/4$ rad, and $T_0$ = 20°C, respectively, and (c) and (d) are the extracted phase-lag profiles from (a) and (b) at i: $tf_o$ = 50, ii: $tf_o$ = 1400, iii: $tf_o$ = 10, iv: $tf_o$ = 380.

and Chapter 2, the obtained viscosity was calculated by assuming that all non-Newtonian effects, such as the viscoelasticity and shear-thinning viscosity, can be reflected into an effective Newtonian viscosity.

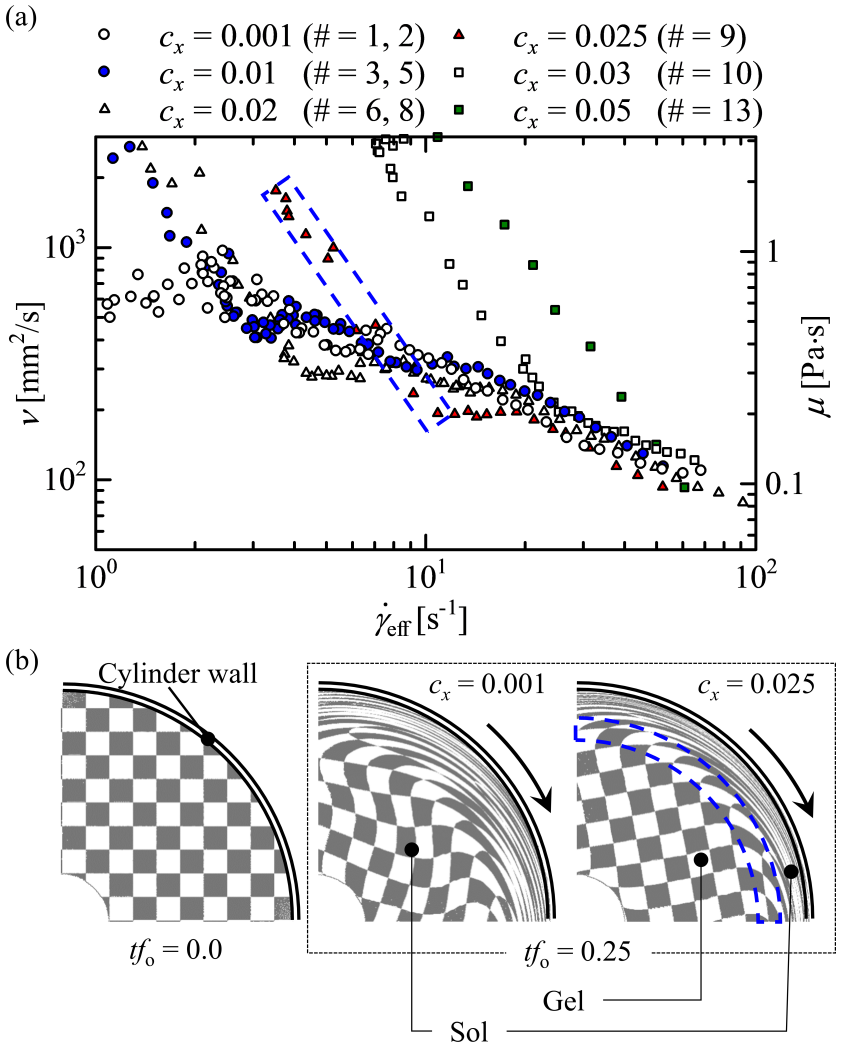


Figure 3.8: (a) Measurements of shear rate and kinematic viscosity in Mt dispersion, where each symbol indicates oscillation amplitude Θ and NaCl concentration $c_x$, (b) visualized images of deformation obtained from velocity profiles in $tf_o = 0.25$ at cases of $c_x = 0.001$, and 0.025.

For $c_x = 0.001$, as indicated by open circle symbols, plateau regions exist with deviations in $1.0 < \dot{\gamma}_{\rm eff} < 3.0$ s$^{-1}$. The tendency changes gradually to a monotonic decrease for $\dot{\gamma}_{\rm eff} > 3.0$ s$^{-1}$, where Mt dispersion has a sol condition. It may exhibit homogeneous dispersed behaviors, which is regarded as viscous fluids. Thus, the velocity fluctuations propagated constantly with viscous damping from the cylinder wall to the center. At the turning point of the tendency between the plateau and the monotonic decrease, a critical shear rate exists, which is able to achieve a shear-thinning behavior. One of the reasons why this occurs is that plate-like particles could be aligned in the circumferential direction.

The result for $c_x = 0.01$ exhibits a large difference from that for $c_x = 0.001$, especially for $\dot{\gamma}_{\rm eff} < 2.0$ s$^{-1}$, where the kinematic viscosity decreases significantly as the shear rate increases. This occurs because a certain critical shear amplitude exists at $\dot{\gamma}_{\rm eff} \approx 2.0$ s$^{-1}$ between a gel and a sol states. The constant-viscosity state appears in $2.0 < \dot{\gamma}_{\rm eff} < 5.0$ s$^{-1}$. From the state at a higher shear rate than 5.0 s$^{-1}$, the viscosity decreases with an almost constant gradient at $c_x = 0.01$.

For larger concentration cases at $c_x = 0.02$ and 0.025, the tendency in variation is almost the same as the case for $c_x = 0.01$, but the critical shear rate increases. For $c_x = 0.03$, the kinematic viscosity decreases monotonically and the range for the constant viscosity disappears [Fig. 3.8(a)]. The profile for $c_x = 0.05$ appears as a parallel shift of the profiles for $c_x = 0.03$ to the larger $\dot{\gamma}_{\rm eff}$ side. According to previous research [8, 40, 10], a dispersion gel strength increases as the cation concentration increases because of aggregation or flocculation, which is a consequence of enhancements in electrical attractive effects.

Here, actual deformations of Mt dispersions (# = 2, 9) in unsteady oscillations were visualized using measured $u_\theta$ to be

compared with the viscosity measurement results. From visualized images [Fig. 3.8(b)], the square grids were deformed at all radial positions when $c_x = 0.001$ and $tf = 0.25$. On the other hand, when $c_x = 0.025$ and $tf = 0.25$, the grids kept its shape inside of the cylinder wall from dash-enclosed region. In comparison of the anomalous viscosity regions (dash-enclosed line as shown in Fig. 3.8 and deformation visualized by azimuthal velocity profiles, the regions placed in intermediate between gel and sol.

When Mt dispersion in stable gel state deforms, responses from the deformation appear as restorative and repulsive forces. Typical responses in viscoelastic media are similar to the mechanical characteristics of a spring. So, the viscoelastic effects appear as an effective Newtonian viscosity in the negative slope, shown in Fig. 3.8(a) (dash-enclosed line). Furthermore, the viscoelastic response changes at a critical shear rate because of the breakdown of stable particle networks.

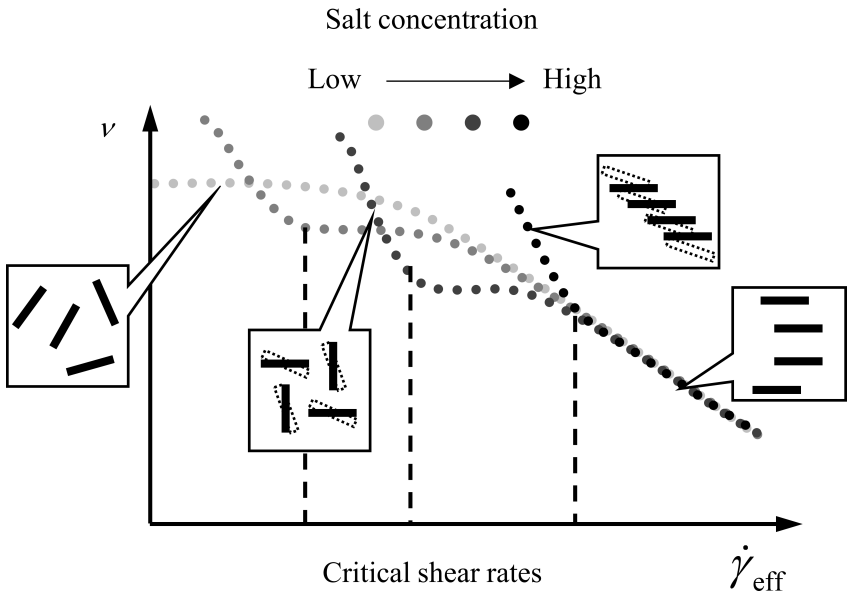


Figure 3.9: Schematic of relationship between different NaCl concentrations, shear rate, and kinematic viscosity, considering experimental results of Mt dispersion shown in Fig. 3.8; e.g., the left region of the critical shear rate shows a viscoelastic response, and the right is a Newtonian (plateau region) and shear-thinning (inclination region) viscous response.

The relations of the effective Newtonian viscosity, the NaCl concentration, and inferable particle networks are schematically considered in Fig. 3.9. These schematics of the inferable particle networks are based on previous researches [6, 13]. If the particle networks change from the house-of-cards to the band-type structure with increases in salt concentration, the rheological response in different types of particle networks shows a clear difference in viscoelasticity. The experimental results indicate anomalous viscosity conditions that are caused by the house-of-cards structures at low salt concentrations occur at a lower shear rate compared with the band-type structures at high salt concentrations. This means that the viscoelasticity changes with structural transitions that are caused by salt concentrations. The rheological response of the band-type structure, therefore, shows a relatively stronger viscoelasticity than that of the house-of-cards.

### 3.3.4 Flow curve under shear banding

To produce flow curves from the experimental results, the shear stress, $\tau(r)$, can be calculated from $\nu(r)$ and $\dot{\gamma}_{\mathrm{eff}}(r)$ by Newton's law of viscosity as:

$$\tau(r) = \mu(r)\dot{\gamma}_{\mathrm{eff}}(r) = \rho\nu(r)\dot{\gamma}_{\mathrm{eff}}(r) \tag{3.2}$$

where $\tau$ and $\rho$ denote the shear stress and density of the test fluid, respectively. From this equation, it is assumed that $\nu(r)$ accommodates with $\dot{\gamma}_{\mathrm{eff}}(r)$ at each "local" radial position, where the shear stress profiles are obtained without torque measurement. The flow curve is a rheological expression, which can represent the fluid characteristics from relations between the shear rate and the shear stress, and especially the shear-rate-dependent viscosity.

Flow curves from these experiments are provided in Table 3.2 (# = 2, 4, 7, 9, 10) and are shown in Fig. 3.10. The vertical and horizontal axes indicate the shear stress $\tau$ and effective shear rate $\dot{\gamma}_{\mathrm{eff}}$, respectively. To compare the difference between Newtonian and non-Newtonian fluids, experimental results of the silicon oil (300 $\mathrm{mm}^2/\mathrm{s}$) mentioned in §3.2.3 were

also plotted on the same graph. The silicon oil flow curve has an almost constant gradient for each effective shear rate, $\dot{\gamma}_{\mathrm{eff}}$. Thus, the flow curve that is obtained in this study is identical to that obtained by empirical knowledge.

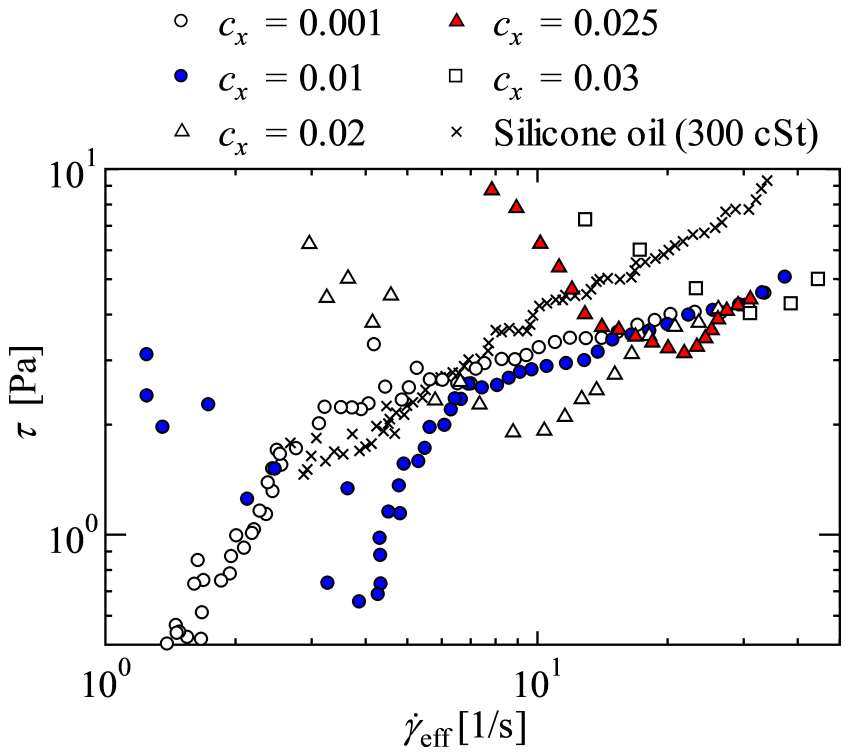


Figure 3.10: Flow curves of Mt dispersion with different NaCl concentrations (Table 3.2: # = 2, 4, 7, 9, 10) and silicon oil (300 mm$^2$/s, $T_0 = 25°$C, $\Theta = \pi/2$ rad).

For $c_x = 0.001$, the shear stress increases monotonically with respect to the effective shear rate, but its slope changes at $\dot{\gamma}_{\mathrm{eff}} \approx 3$ s$^{-1}$. For $c_x = 0.01$, for $\dot{\gamma}_{\mathrm{eff}}$ close to 1 s$^{-1}$, the shear stress is larger than that at $c_x = 0.001$. It decreases significantly with an increase in $\dot{\gamma}_{\mathrm{eff}}$, and reaches a minimum at $\dot{\gamma}_{\mathrm{eff}} \approx 4$ s$^{-1}$. Beyond this shear rate, the shear stress increases linearly and its slope changes at $\dot{\gamma}_{\mathrm{eff}} \approx 7$ s$^{-1}$, which is similar to the behavior for $c_x = 0.001$. For larger $c_x$, the flow curves shift to a higher shear rate and maintain their shape, and thus the shear stresses increase at each turning point, where the slope of the curves changes.

According to previous research using a rotational torque rheometer [5], flow curves under similar conditions to the Mt dispersions was estimated. The flow curves, however, are unclear in evaluations of rheological characteristics especially under the condition of $\dot{\gamma} < O(1\ \mathrm{s}^{-1})$ due to limitations on the rotational torque rheometry. Thus, plastic or apparent viscosity has been used to express the rheological properties. The flow curves of Mt dispersion in this report have a negative slope below the critical shear rate. Møller *et al.* [41] have already proofed by two different types of measurement that flow curves of yield stress fluid have a negative slope below the critical shear rate, which was used gel formed from an aqueous suspension of charged colloidal particles. The fact of this previous report offers evidence that the flow curves revealed rheological properties of Mt dispersions in lower shear rate. It cannot be evaluated directly using rotational torque rheometry due to influences of shear banding.

In the rotational torque measurements, shear banding phenomena is an unavoidable problem especially when low shear rates are applied to yield stress fluids. According to [42], flow curves at a lower shear rate than at critical shear rates are difficult to obtain because of instabilities in flow behaviors. In that case, shear banding is somewhat trivially observed when the yield stress of the fluid under scrutiny lies between the maximum and minimum local stresses [24]. Then, the shear stresses obtained from torque measurements were outputted as broad stress plateaus in the flow curves. Since the shear banding has variety of expressions and definitions and changes depending on rheological approaches what is focusing on, we consider that shear banding is what the flow curve behaves as typical multiple functions (e.g. Fig. 4 in [24]).

Based on the results, the flow curves are explained as shown in Fig. 3.11; critical shear rates and stresses lead to changes in rheological properties. Here, $\tau_{\mathrm{y}}$, $\tau_{\mathrm{s}}$, $\dot{\gamma}_{\mathrm{y}}$, and $\dot{\gamma}_{\mathrm{s}}$ indicate the yield stress, critical shear stress at the onset of shear thinning, critical shear rate at the yield stress, and critical shear rate at the onset of shear thinning, respectively. Assuming that the flow curves follow this tendency, the critical values are estimated as summarized in Table 3.3.

Table 3.3: Estimated results of critical values in shear stress and shear rate.

| $c_x$[mol/L] | 0.001 | 0.01 | 0.02 | 0.025 | 0.03 | 0.04 |
|---|---|---|---|---|---|---|
| $\dot{\gamma}_y$[1/s] | – | 3.88 | 8.78 | 22.83 | 31.20 | 42.15 |
| $\tau_y$[Pa] | – | 0.65 | 1.91 | 2.80 | 4.01 | 5.04 |
| $\dot{\gamma}_s$[1/s] | 2.55 | 7.47 | 18.13 | 27.41 | – | – |
| $\tau_s$[Pa] | 1.65 | 2.51 | 3.50 | 4.10 | – | – |

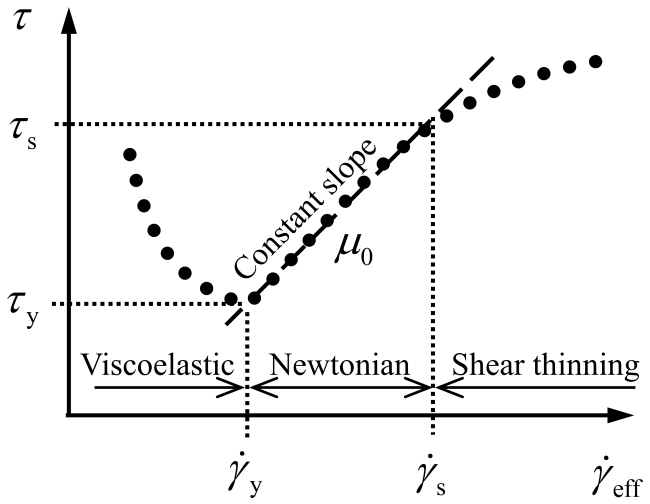


Figure 3.11: Schematic of flow curve in gelled Mt dispersion divided into three regions, where $\tau_y$, $\tau_s$, $\dot{\gamma}_y$, and $\dot{\gamma}_s$ indicate the yield stress, critical shear stress at the onset of shear thinning, the critical shear rate at the yield stress, and the critical shear rate at the start of shear thinning, respectively.

Viscoelastic effects appear in the results for $\dot{\gamma}_{eff} < \dot{\gamma}_y$ as shown in Fig. 3.11; the shear stress profiles decrease significantly with an increasing $\dot{\gamma}_{eff}$ because of sharp changes in kinematic viscosity shown at the left of the critical shear rate in Fig. 3.9. In these rheometry measurements, the kinematic viscosity is obtained as a local effective viscosity, which reflects all viscoelastic effects and represents a Newtonian viscosity. Thus, these significant changes on the flow curves at a lower effective shear rate than $\dot{\gamma}_y$ reflect viscoelastic responses.

Important findings in this section are summarized as follows; (1) the rheological properties of the Mt dispersion with a dilute NaCl concentration are a Newtonian and shear-thinning viscosity; (2) the yield stress, $\tau_y$, appears for NaCl concentrations larger than the critical value ($c_x > 0.01$ mol/L in this paper), where $\tau_y$ and $\dot{\gamma}_y$ increase with an increase in $c_x$; (3) shear-thinning behaviors occur at the critical shear stress and shear rate, $\tau_s$ and $\dot{\gamma}_s$, respectively, which increase with an increasing $c_x$. Considering changes in the flow curves with an increase in NaCl concentration, three important findings are caused by attractive forces of particle networks, which can affect the rheological responses under low-shear-rate conditions; (4) states of Newtonian viscosity are not observed for $c_x > 0.03$ in the studied range of $\dot{\gamma}_{eff}$.

Critical values that were estimated at different $c_x$ are arranged in Fig. 3.12, which indicates that the Newtonian viscosity state shrinks with an increasing $c_x$. Viscoelasticity magnifications result because particle networks are considered to deform flexibly like springs above critical salt concentrations without breaking. If this viscoelastic effect is dominant in connections between the particles, states of Newtonian viscosity may disappear. Then, $\dot{\gamma}_s$ becomes unclear for $c_x > 0.03$.

Fluids in which particles are dispersed homogeneously can indicate a Newtonian viscosity. Attractive forces in the particle network increase with an increase in $c_x$, so homogeneous particle dispersions may be difficult to maintain. Instead, particles maintain networks under unsteady shearing and responses against the shear force emerge as a viscoelasticity. The Newtonian viscosity region shrinks with an increase in $c_x$ as shown in Fig. 3.12. Hence, a sudden yielding and shear-thinning response against shear forces is observed at $c_x \approx 0.04$. The particle networks can be shifted from the house-of-cards to the band-type structure with an increase in $c_x$. This occurs because, at $c_x \approx 0.04$, the particle networks of the band-type structure can deform more easily than the house-of-cards structure because of sliding in the shearing direction. A higher critical shear stress results than for the house-of-cards because of increases in the bonding force between particles.

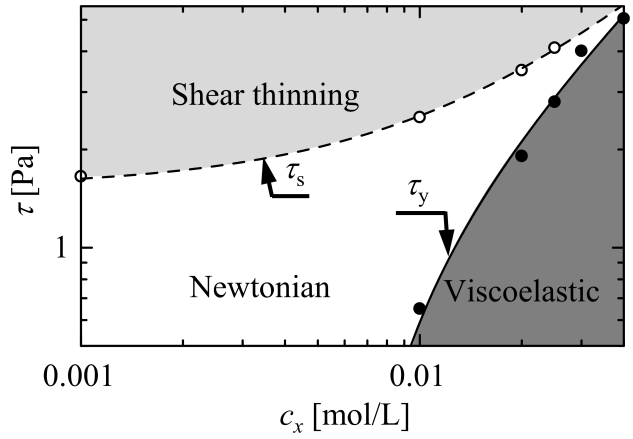


Figure 3.12: Critical values ($\tau_y$, $\tau_s$) and NaCl concentration.

## 3.4 Conclusion

Ultrasonic spinning rheometry (USR) was adopted to study the rheological properties of gelled Mt dispersions under low shear rates, which has been difficult to be measured by conventional torque rheometries because of the instability of thixotropic fluid flows and the appearance of shear banding. Significant findings in these experimental results for Mt dispersions at different NaCl concentration are as follows:

1. Mt dispersion with a dilute NaCl concentration exhibit a Newtonian and shear-thinning response, depending on shear rate.
2. Recovery speed of the particle networks changes with respect to the ionic strength of the dispersion.
3. Critical shear rate and stress at the yielding and shear-thinning point increases with an increase in NaCl concentration.
4. Viscoelastic effects are dominant above a critical NaCl concentration because of the high attractive force in each particle.

The viscoelastic effects are enhanced with an increase in NaCl concentration. At a low shear rate $O(1 - 10\ \mathrm{s}^{-1})$, the Mt particle networks, which have different structures based on the NaCl concentration, can maintain their structure and exhibit stretching behaviors such as that of a spring. For NaCl concentrations that exceed a certain critical value, the state of Newtonian viscosity may disappear because of the viscoelastic effects in connections of each particle. Thus, we speculate that changes in viscoelasticity with changes in NaCl concentrations imply structural transitions from the house-of-cards to the band-type networks.

Because the rheological responses dramatically shift with a change in the microscopic-particle networks, an alternative approach is strongly desired instead of the conventional torque rheometry. USR has a large potential in resolving unexamined issues and completely understanding in the rheological characteristics of Mt dispersions.

## References

[1] H. Vali, L. Bachmann, "Ultrastructure and flow behavior of colloidal smectite dispersions. J. Colloid Interface Sci. 126, 278–291 (1988).
[2] B. Velde (Ed.), "*Origin and Mineralogy of Clays: Clays and the Environment*," Springer (2013).
[3] H. A. Barnes, "Thixotropy–a review," J. Non-Newtonian. Fluid Mech. 70, 1–33 (1997).
[4] U. Brandenburg, G. Lagaly, "Rheological properties of sodium montmorillonite dispersions," Appl. Clay Sci. 3, 263–279 (1988).
[5] E. Tombácz, M. Szekeres, "Colloidal behavior of aqueous montmorillonite suspensions: the specific role of pH in the presence of indifferent electrolytes," Appl. Clay Sci. 27, 75–94 (2004).
[6] G. Lagaly, S. Ziesmer, "Colloid chemistry of clay minerals: the coagulation of montmorillonite dispersions," Adv. Colloid Interf. Sci. 100, 105–128 (2003).
[7] S. Abend, G. Lagaly, "Sol–gel transitions of sodium montmorillonite dispersions," Appl. Clay Sci. 16, 201–227 (2000).
[8] B. Rand, E. Pekenć, J. W. Goodwin, R. W. Smith, "Investigation into the existence of edge–face coagulated structures in Na-montmorillonite suspensions," J. Chem. Soc. Faraday Trans. 76, 225–235 (1980).

[9] K. Bekkour, M. Leyama, A. Benchabane, O. Scrivener, "Time-dependent rheological behavior of bentonite suspensions: An experimental study," J. Rheol. 49, 1329–1345 (2005).
[10] R. Goh, Y. K. Leong, B. Lehane, "Bentonite slurries–zeta potential, yield stress, adsorbed additive and time-dependent behaviour," Rheol. Acta 50, 29–38 (2011).
[11] T. Missana, A. Adell, "On the applicability of DLVO theory to the prediction of clay colloids stability," J. Colloid Interface Sci. 230, 150–156 (2000).
[12] M. Morvan, D. Espinat, J. Lambard, T. Zemb, "Ultrasmall-and small-angle X-ray scattering of smectite clay suspensions," Colloid Surf. A 82, 193–203 (1994).
[13] G. Lagaly, "Colloid clay science," In: F. Bergaya, B. K. G. Theng, G. Lagaly (Eds.), *Handbook of Clay Science*, Elsevier, New York, pp. 141–245 (2006).
[14] E. Paineau, L. J. Michot, I. Bihannic, C. Baravian, "Aqueous suspensions of natural swelling clay minerals. 2. Rheological characterization," Langmuir 27, 7806–7819 (2011).
[15] L. J. Michot, I. Bihannic, F. Thomas, B. S. Lartiges, Y. Waldvogel, C. Caillet, J. Thieme, S. S. Funari, P. Levitz, "Coagulation of Na-montmorillonite by inorganic cations at neutral pH. A combined transmission X-ray microscopy, small angle and wide angle X-ray scattering study," Langmuir 29, 3500–3510 (2013).
[16] N. Cruz, Y. Peng, "Rheology measurements for flotation slurries with high clay contents–A critical review," Miner. Eng. 98, 137–150 (2016).
[17] H. A. Barnes, J. O. Carnali, "The vane-in-cup as a novel rheometer geometry for shear thinning and thixotropic materials," J. Rheol. 34, 841–866 (1990).
[18] K. Nakaishi, "Flow characteristic of dilute Na montmorillonite suspension," Appl. Clay Sci. 12, 377–386 (1997).
[19] G. Zhuang, H. Zhang, H. Wu, Z. Zhang, L. Liao, "Influence of the surfactants' nature on the structure and rheology of organo-montmorillonite in oil-based drilling fluids," Appl. Clay Sci. 135, 244–252 (2017).
[20] H. L. Zhang, H. C. Wang, J. Y. Yu, "Effect of aging on morphology of organo-montmorillonite modified bitumen by atomic force microscopy," J. Microsc. 242, 37–45 (2011).
[21] J. Mouzon, I. U. Bhuiyan, J. Hedlund, "The structure of montmorillonite gels revealed by sequential cryo-XHR-SEM imaging," J. Colloid Interface Sci. 465, 58–66 (2016).
[22] S. Manneville, "Recent experimental probes of shear banding," Rheol. Acta 47, 301–318 (2008).
[23] P. D. Olmsted, "Perspectives on shear banding in complex fluids," Rheol. Acta 47, 283–300 (2008).
[24] T. Divoux, M. A. Fardin, S. Manneville, S. Lerouge, "Shear banding of complex fluids," Annu. Rev. Fluid Mech. 48, 81–103 (2016).
[25] N. Dogan, M. McCarthy, R. Powell, "In-line measurement of rheological parameters and modeling of apparent wall slip in diced tomato suspensions using ultrasonics," J. Food Sci. 67, 2235–2240 (2002).
[26] Y. T. Nguyen, T. D. Vu, H. K. Wong, Y. L. Yeow, "Solving the inverse problem of capillary viscometry by tikhonov regularisation," J. Non-Newtonian Fluid Mech. 87, 103–116 (1999).
[27] C. Ancey, "Solving the Couette inverse problem using a wavelet-vaguelette decomposition," J. Rheol. 49, 441–460 (2005).
[28] G. Heirman, L. Vandewalle, D. Van Gemert, O. Wallevik, "Integration approach of the Couette inverse problem of powder type self-compacting concrete in a wide-gap concentric cylinder rheometer," J. Non-Newtonian Fluid Mech. 150, 93–103 (2008).
[29] B. Ouriev, E. Windhab, "Transient flow of highly concentrated suspensions investigated using the ultrasound velocity profiler–pressure difference method," Meas. Sci. Technol. 14, (1963).
[30] B. Derakhshandeh, D. Vlassopoulos, S. G. Hatzikiriakos, "Thixotropy, yielding and ultrasonic Doppler velocimetry in pulp fibre suspensions," Rheol. Acta 51, 201–214 (2012).
[31] A. Gurung, J. Haverkort, S. Drost, B. Norder, J. Westerweel, C. Poelma, "Ultrasound image velocimetry for rheological measurements," Meas. Sci. Technol. 27, 094008 (2016).
[32] C. Poelma, "Ultrasound imaging velocimetry: A review," Exp. Fluids 58, 3 (2017).
[33] Y. Takeda (Ed.), "*Ultrasonic Doppler Velocity Profiler for Fluid Flow*," vol. 101, Springer, Japan (2012).
[34] T. Shiratori, Y. Tasaka, Y. Murai, Y. Takeda, "Development of ultrasonic visualizer for capturing the characteristics of viscoelastic fluids," J. Vis. 16, 275–286 (2013).
[35] T. Shiratori, Y. Tasaka, Y. Oishi, Y. Murai, "Ultrasonic velocity profiling rheometry based on a widened circular Couette flow," Meas. Sci. Technol. 26, 085302 (2015).
[36] T. Shiratori, Y. Tasaka, Y. Murai, "Rapid rheological characterization of a viscoelastic fluid based on spatiotemporal flow velocimetry," Exp. Thermal Fluid Sci. 71, 1–13 (2016).
[37] Y. Tasaka, T. Kimura, Y. Murai, "Estimating the effective viscosity of bubble suspensions in oscillatory shear flows by

means of ultrasonic spinning rheometry," Exp. Fluids 56, 1867 (2015).
[38] J. Hrachová, I. Chodák, P. Komadel, "Modification and characterization of montmorillonite fillers used in composites with vulcanized natural rubber," Chem. Pap. 63, 55–61 (2009).
[39] Y. Tachi, K. Yotsuji, T. Suyama, M. Ochs, "Integrated sorption and diffusion model for bentonite. Part 2: porewater chemistry, sorption and diffusion modeling in compacted systems," J. Nucl. Sci. Technol. 51, 1191–1204 (2014).
[40] "*An Introduction to Rheology*," H. A. Barnes, J. F. Hutton, K. Walters, vol. 3 Elsevier, Amsterdam (1989).
[41] P. C. F. Møller, S. Rodts, M. A. J. Michels, D. Bonn, "Shear banding and yield stress in soft glassy materials," Phys. Rev. E 77, 041507 (2008).
[42] P. C. F. Møller, J. Mewis, D. Bonn, "Yield stress and thixotropy: on the difficulty of measuring yield stresses in practice," Soft Matter 2, 274–283 (2006).

Chapter 4

# Linear viscoelastic analysis using frequency-domain algorithm on oscillating circular shear flows for bubble suspensions

## Contents


**4.1 Introduction** . . . . . **48**
**4.2 Ultrasonic spinning rheometry** . . . . . **49**
4.2.1 Measurement configuration . . . . . 49
4.2.2 USR concept and procedure . . . . . 49
**4.3 Influence of measurement error on USR** . . . . . **50**
4.3.1 Viscoelastic analysis of bubble suspensions . . . . . 50
4.3.2 Numerical evaluation of influence of noise . . . . . 51
**4.4 Frequency-domain analysis** . . . . . **53**
4.4.1 Theory . . . . . 53
4.4.2 Viscometry . . . . . 54
4.4.3 Application of viscometry . . . . . 55
4.4.4 Linear viscoelastic analysis of bubble suspension . . . . . 58
**4.5 Conclusion** . . . . . **60**
**References** . . . . . **60**


## Preface

The aim in this chapter is to present the linear viscoelastic analysis of kinematic rheometry that can quantitatively divide the rheological property into viscosity and elasticity. This establishment leads to raising the level of kinematic rheometry to understand the more detailed rheology of complex fluids. The work was published in Tasaka *et al*., Rheol. Acta (2018).

## Abstract


To achieve a stable evaluation of the linear viscoelasticity of bubble suspensions, which have difficulties for conventional rheometers from spatial distributions of rheological properties with bubble deformations, we proposed a novel rheometry based on spatio-temporal velocity data obtained by ultrasonic velocity profiling (UVP). A frequency-domain algorithm was adopted to overcome a critical influence of measurement noise on the rheological assessment, which is inferred from error propagation characteristics through the equations of motion in discretized form. Applicability and advantage of the present rheometry with the frequency-domain algorithm were verified by two kinds of fluids: high viscous oil as a Newtonian fluid and polyacrylamide aqueous solution as a shear thinning, viscoelastic fluid. The rheometry was finally adopted for bubble suspensions subject to high oscillatory shear, and it could validly extract elasticity-originated momentum transfer as a function of space.

## 4.1 Introduction

Regarding aspects such as quality control of products, safety issues, and more efficient processing in any industrial field, details of rheological properties of fluid media are required. The development of highly precise torque meters has made it possible to provide good estimations of such details. Along with rheological models that are constitutive equations describing the stress response in materials, rotational rheometry has provided details of properties using only a small number of characteristic constants. Nevertheless, rotational rheometry assumes simple Couette flows produced in a narrow gap between the stator and rotor connected to torque meters. However, dispersed multiphase media, which are not seen as a continuum even at the macroscopic scale, are difficult to measure. Non-ideal conditions run counter to the assumption of Couette flows required to solve the "Couette inverse problem" to obtain the original rheological properties (e.g., [1–3]). Furthermore, in measurements of multiphase media, additional complexities arise for example from the presence of interfaces in gap size (e.g., [4, 5]).

A focus of our studies on the rheology of multiphase media is bubble suspensions for understanding the mechanisms underpinning drag reduction from injected bubbles (e.g., [6, 7]). Bubbles accumulated in flow elements, strong shear layers, and vortices create locally different rheological properties in conditions of unsteady shear flow in turbulence. Beginning with the appearance of the classical theory on dilute spherical suspensions (assuming that surface tension is strong enough to sustain the spherical shape) in [8, 9], the study of suspension rheology has a century long history. By considering capillary number, the theory was extended to deformable bubbles in simple steady shear flows [10], and its applicability was validated by experiments [11]. Choi and Schowalter [12] provided a more sophisticated equation that considered higher orders in the volume fraction to extend the theory to larger volume fractions. Despite the progress made over the century, there remain aspects to be explained about the elastic response attributed to surface tension effect in unsteady shear flows [13–15].

For a rheological evaluation of multiphase media, there are two issues to be solved: (1) the narrow-gap problem and (2) the inverse Couette problem. The Stokes-type rheometry, for instance, the falling sphere rheometry (bubble suspensions; e.g., see [16]) and commercial turning sphere rheometry (BMS, Anton Paar GmbH), can avoid the issues arising from Couette-type rheometry. However, the rheological properties evaluated using these methods correspond to aggregated rheological properties because of the multidimensional, multicomponent flows dealt with. Thus, the rheological properties obtained are difficult to interpret along standard approaches in rheology.

In solving the issues in regard to Couette-type rheometry, a combination of a wide-gap cylinder system and velocimetry has been tried; spatial profiling of velocity measured in a wider gap using different kinds of velocimetry can reveal deviations to ideal Couette flow that arises from complex rheological properties, for example, shear banding (e.g., [17]). Supplementing the data by torque measurements to give an integrated boundary condition on a rotor in the system has supported evaluation of complex rheological properties. The kinds of velocimetry adopted include particle image velocimetry (PIV), specially named "Rheo-PIV" [17–20], magnetic resonance imaging velocimetry [21, 22], laser Doppler velocimetry [23, 24], and ultrasonic imaging velocimetry [25].

In contrast to these types of velocimetry, ultrasonic Doppler velocimetry or ultrasonic velocity profiling (UVP) [26] offers ease of handling and access to opaque fluids. Also, UVP is being further developed in both hardware and software [27–29], and we can expect in the near future greater sophistication in its methodology. Moreover, recent progress in combining it with Doppler optical coherent tomography has overcome several disadvantages of UVP in near-wall measurements of the velocity field [30]. UVP was applied to a circular Couette system [31, 32] and also to pipe flow with measurements of the pressure drop along the pipe [33, 34]. The latter technique has been termed the in-line UVP-PD method and has been recognized as a semi-standard evaluation tool in food rheology [35] as ultrasonic velocimetry has been applied avidly in the food processing industry.

Because of its spatio-temporal velocity profiling, UVP has also been explored in visualizing rheological behaviors [36]. Our group has been developing ultrasonic spinning rheometry (USR) that uses such data to evaluate rheological properties modeled by equations of motion of fluid media and has extended its applicability to viscoelastic analyses of multiphase media including bubble suspensions.

This study evaluates the applicability of USR in linear viscoelastic analysis in general and bubble suspensions in particular. We investigate the influence of measurement noise on spatio-temporal velocity data measured by UVP that is required for a viscoelastic analysis. We propose a novel algorithm for USR applying the Fourier transform theory to the velocity data to achieve more stable analysis. The structure of this paper is as follows: USR including theory and fundamental measurement configuration is briefly summarized in §4.2. The applicability of the USR and the numerical experiments in investigating the influence of the measurement noise on USR are presented in §4.3. The theory of "frequency-domain analysis" is described. Its applicability to viscosity analysis is evaluated in numerical experiments and on actual velocity data obtained from viscous oil treated as a Newtonian fluid. Then, linear viscoelasticity analysis using the algorithm on bubble suspension is performed

in §4.4. Finally, concluding remarks are presented in §4.5.

## 4.2 Ultrasonic spinning rheometry

### 4.2.1 Measurement configuration

The USR process involves two main steps: the measurements of the velocity profile of test fluids placed in a cylindrical vessel and the post-processing of the velocity data to evaluate rheological properties. In preparation for explaining the post-processing, a brief explanation of the measuring of velocity profiles is given here. The basic configuration of the measurement [Fig. 4.1(a)] comprises an open-type cylindrical vessel of radius $R$ filled with a test fluid rotating under set conditions. Measurements of the velocity are performed using an ultrasonic transducer (TDX) mounted on the outside of the cylinder. The measurement line for UVP (e.g., [26]) is set parallel to the centerline of the cylinder with a certain displacement of $\Delta y$ to measure the azimuthal component of velocity $u_\theta$; UVP measures the on-axis velocity component $u_\xi$ along the measurement line $\xi$ , and thus, the azimuthal velocity component is given as $u_\theta = u_\xi r/\Delta y$ when the radial velocity component is negligibly small. Test fluids are required to be seeded where there are no ingredients that can scatter ultrasonic waves. Further details of individual measurements are described elsewhere [15] and Chapter 2.

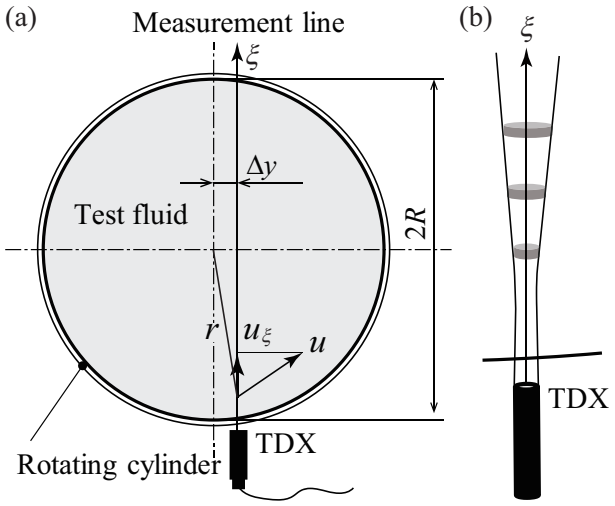


Figure 4.1: Schematics of (a) the experimental setup showing the rotating cylinder and the measurement line for ultrasonic velocity profiling (UVP) and (b) the measurement volume of UVP.

In measurements by UVP, representative velocities in the disk-shaped volume of the test sample are captured as on-axis velocity components at each radial position along the measurement line [Fig. 4.1(b)]. The diameter and width of the measurement volume are determined from the size of the piezo-element in the transducers and the wavelength of the ultrasonic wave in the test fluids; typically, these are around 5 and 1 mm, respectively. Velocities $u(r, t)$ calculated from the on-axis velocity component measured in UVP at each volume are processed. They reflect flow behaviors determined by the local characteristics of the test fluids responding to cylinder motions. These characteristics include rheological characteristics, for example, shear-rate-dependent viscosity, viscoelasticity, and non-uniformity of ingredients and local structures. USR extracts from $u(r, t)$ the local characteristics with post-processing, which shall be summarized below.

### 4.2.2 USR concept and procedure

USR is concerned with deriving rheological characteristics from spatio-temporal velocity distributions measured by UVP.

Here we summarize the post-processing procedure used in USR. The rheological characteristics of fluids are reflected in the spatio-temporal velocity distributions which are governed by the equation of motions and the constitutive equations (in rheological modeling) describing the relationships between stress $\tau$, strain $\gamma$ , and strain rate $\dot{\gamma}$ . To simplify the model, we assume just two-dimensional one-directional flows in the azimuthal direction that can be realized in the setup mentioned in

the last section. The corresponding equation of motion, Cauchy's equation, is

$$\rho\frac{\partial u_\theta}{\partial t} = \frac{\partial \tau}{\partial r} + \frac{2\tau}{r}, \tag{4.1}$$

where $\rho$ is the density of the fluid. To determine the rheological properties, Murai [31] proposed minimizing a cost function expressed by the least-squares approximation,

$$F(A, B, C, \cdots) = \left(\rho\frac{\partial u_\theta}{\partial t} - \frac{\partial \tau}{\partial r} - \frac{2\tau}{r}\right)^2, \tag{4.2}$$

where the parameters, $A, B, C, \cdots$, denote constants in rheological models representing rheological properties. In the equation above, $u_\theta(r,t)$ is given as measurement data in circular shear flows measured by UVP, and $\tau$ is also calculated from $u_\theta(r,t)$ through a rheological model adopted.

## 4.3 Influence of measurement error on USR

### 4.3.1 Viscoelastic analysis of bubble suspensions

We performed an analysis using the above equations of motion to evaluate viscoelasticity of bubble suspensions, having examined their effective Newtonian viscosity in a previous paper [15]. Experiments measuring velocity profiles were performed with a cylinder of inner diameter $2R = 145$ mm filled with 1000 mm$^2$/s silicone oil to a depth of 330 mm. Small bubbles of around 1 mm diameter were dispersed in the fluid layer to a volume fraction of about 2%. The cylinder underwent sinusoidal oscillations of frequency $f_o = 1$ Hz and angular amplitude $\Theta = 90°$. The spatio-temporal velocity profiles were captured in ultrasonic velocimetry at a spatial resolution of 0.99 mm along the measurement axis and a time resolution of 30 ms.

We recall Cauchy's equation of motion, Eq. (4.1), and adopt Maxwell's spring-dashpot model in describing viscoelastic fluids,

$$\tau + \frac{\mu}{E}\frac{\partial \tau}{\partial t} = \mu\left(\frac{\partial u_\theta}{\partial r} - \frac{u_\theta}{r}\right), \tag{4.3}$$

in establishing the simplest model to describe linear viscoelasticity, which is evaluated by first determining viscosity $\mu$ and elasticity $E$ from measurement data of $u_\theta(r,t)$. A suitable set of $\mu$ and $E$ that satisfy these equations is derived as a constraint condition on $\tau$ . Mathematically, the calculation is

$$F(\mu, E; r) = \min_{\tau,\,\mu,\,E} \int_r \int_t \left[\tau + \frac{\mu}{E}\frac{\partial \tau}{\partial t} - \mu\left(\frac{\partial u_\theta}{\partial r} - \frac{u_\theta}{r}\right)\right]^2 dtdr,$$

$$\text{s.t. } \rho\frac{\partial u_\theta}{\partial t} = \frac{\partial \tau}{\partial r} + \frac{2\tau}{r}. \tag{4.4}$$

In terms of difference expressions for $u_\theta(r,t)$ and $\tau(r,t)$, these become

$$F(\mu, E; r) = \min_{\tau,\,\mu,\,E} \sum_r \sum_t \left[\tau_{i,j} + \frac{\mu}{E}\frac{\tau_{i+1,j} - \tau_{i,j}}{\Delta t} - \mu\left(\frac{u_{i,j+1} - u_{i,j}}{\Delta r} - \frac{u_{i,j}}{r_j}\right)\right]^2,$$

$$\text{s.t. } \rho\frac{u_{i+1,j} - u_{i,j}}{\Delta t} = \frac{\tau_{i,j+1} - \tau_{i,j}}{\Delta r} + \frac{\tau_{i,j}}{r_j}. \tag{4.5}$$

where $\Delta t$ and $\Delta r$ correspond to the spatial and radial resolutions, respectively, of the velocity profile measurements. More precisely, the radial positions are calculated from the positions on the measurement line with $\xi$ and $\Delta r$ varying depending on radial positions.

The calculations described above are performed after applying a filter to $u_\theta(r,t)$ to suppress the influence of measurement noise. Here we adopt a Savitzky-Golay FIR smoothing filter [37] with various filter sizes in time and space to examine the influence of the filter. As radial variations of the viscoelasticity are expected, a narrow radial range of velocity profiles in $r/R = 0.86 - 0.96$ are analyzed over a period of 4 s. The evaluation results for viscosity $\mu$ and elasticity $E$ under different filter sizes are summarized in Table 4.1. The phase difference in linear viscoelasticity $\Delta$ is defined as the fraction of storage

modulus to loss modulus and has the following relation with elasticity and viscosity in the Maxwell model:

$$\tan\delta = \frac{G''}{G'} = \frac{E}{2\pi f_0 \mu}. \tag{4.6}$$

Phase values of around 90° mean that a fluid is close to a pure viscous body and smaller values indicate larger elastic contributions to stress in the fluids.

Table 4.1: Evaluation results of viscosity $\mu$ and elasticity$E$, with phase difference in linear viscoelasticity $\delta$ for the differently filtered data of $u(r,t)$ for measurements ranging from $r/R = 0.86$ to $r/R = 0.96$ over a period of 4 s; $N_t$ and $N_s$ correspond to the number of time and space points used in filtering, respectively.

| # | $N_t$ | $N_s$ | $\mu$ [Pa · s] | $E$ [Pa] | $\delta$ [°] | # | $N_t$ | $N_s$ | $\mu$ [Pa · s] | $E$ [Pa] | $\delta$ [°] |
|---|---|---|---|---|---|---|---|---|---|---|---|
| 1 | 15 | 19 | 1.05 | 69.6 | 84.57 | 5 | 15 | 11 | 0.70 | 46.2 | 84.54 |
| 2 | 15 | 17 | 0.99 | 64.8 | 84.55 | 6 | 15 | 9 | 0.58 | 37.9 | 84.54 |
| 3 | 15 | 15 | 0.91 | 60.3 | 84.56 | 7 | 35 | 15 | 0.02 | 1.2 | 84.49 |
| 4 | 15 | 13 | 0.82 | 53.6 | 84.54 | 8 | 27 | 15 | 0.39 | 125.9 | 84.52 |

From the various analyses with different filter sizes, designated by the serial number in Table 4.1, the evaluation results of $\mu$ and $E$ are widely scattered. Taking similar values for different analyses, the phase difference $\delta$, however, is stable against the variation in filter size. This trend may arise from two factors: one is that $\mu$ and $E$ appear as a fraction (or product) in the equation to be analyzed, and the other is that the influence of measurement error and noise on $u_\theta(r,t)$ including the influence of filtering buries local minima on the surface of the cost function, Eq. (4.5), in parameter space. We therefore evaluated the influence of noise in determining the local minima of the cost function.

### 4.3.2 Numerical evaluation of influence of noise

For this purpose, we reduce the problem to a Newtonian viscosity analysis. For Newtonian fluids, the equation of motion in Eq. (4.1) becomes

$$\frac{\partial u_\theta}{\partial t} = \nu\left(\frac{\partial^2 u_\theta}{\partial r^2} + \frac{1}{r}\frac{\partial u_\theta}{\partial r} - \frac{u_\theta}{r^2}\right) = \nu D_r u_\theta, \tag{4.7}$$

where $\nu$ is the kinematic viscosity and $D_r$ is a differential operator with respect to $r$ defined as

$$D_r = \frac{\partial^2}{\partial r^2} + \frac{1}{r}\frac{\partial}{\partial r} - \frac{1}{r^2}. \tag{4.8}$$

This can be reduced into the cylindrical Bessel differential equation by separation of variables about $t$ and $r$. Then, it can be solved by inserting the infinite series

$$u_\theta(r,t) = \frac{U_{\text{wall}}}{\Phi_R^2 + \Psi_R^2}\left[(\Phi\Phi_R + \Psi\Psi_R)\sin\omega t + (\Phi_R\Psi - \Phi\Psi_R)\cos\omega t\right], \tag{4.9}$$

where $U_{\text{wall}}$ is the angular velocity of the side wall, and

$$\Phi(r) = \sum_{m=0}^{\infty}\phi_m(r), \quad \Phi_R = \sum_{m=0}^{\infty}\phi_m(r=R),$$
$$\Psi(r) = \sum_{m=0}^{\infty}\psi_m(r), \quad \Psi_R = \sum_{m=0}^{\infty}\psi_m(r=R),$$

and

$$\phi_m(r) = \frac{2^m}{m!(m+1)!}\left(\frac{kr}{2}\right)^{2m+1} f_m,\ k = \sqrt{\frac{\omega}{2\nu}},\ f_m = \begin{cases}(-1)^{(m+2)/2} & m = \text{evennumber}\\ (-1)^{(m+1)/2} & m = \text{oddnumber},\end{cases}$$
$$\psi_m(r) = \frac{2^m}{m!(m+1)!}\left(\frac{kr}{2}\right)^{2m+1} g_m,\ k = \sqrt{\frac{\omega}{2\nu}},\ g_m = \begin{cases}(-1)^{m/2} & m = \text{evennumber}\\ (-1)^{(m+1)/2} & m = \text{oddnumber}.\end{cases}$$

Details of the derivation are described in [15]. We performed numerical experiments to evaluate the influence of measurement noise using this exact solution, Eq. (4.9), with a sufficiently large number of terms and $f_o = \omega_o/(2\pi) = 1$ Hz.

To represent measurement noise, and in particular the typical spikey noise seen in UVP measurements, the Mersenne twister method [38] was used to artificially generate the random noise by modifying the standard deviation $\sigma_N$ in regard to the noise level. The cost function to be minimized is derived from Eq. (4.7) in differential form,

$$F(\nu) = \sum_{r,t} \left[ \frac{u_{i+1,j} - u_{u,j}}{\Delta t} - \nu \left( \frac{u_{i,j+1} - 2u_{i,j} + u_{i,j-1}}{\Delta r^2} + \frac{u_{i,j+1} - u_{i,j}}{2r_j \Delta r} - \frac{u_{i,j}}{r_j^2} \right) \right]^2 . \tag{4.10}$$

The correct value for the kinematic viscosity is set at $\nu_o = 1000$ mm$^2$/s, and the cost function is calculated over the range $\nu = 800 - 1200$ mm$^2$/s in increments of $\Delta\nu = 4$ mm$^2$/s over the radial range $r/R = 0.95 - 0.98$. The dependence of the cost function on $\nu$ (Fig. 4.2) is calculated from the exact solution without noise using Eq. (4.10); note that $F(\nu)$ has been normalized by the number of velocity data, $N_{\text{total}}$, used for the calculation. In the range explored for $\nu$, the cost function has a unique minimum corresponding to $\nu_0$, signifying that the methodology to evaluate $\nu$ from spatio-temporal velocity distributions works well in instances without noise.

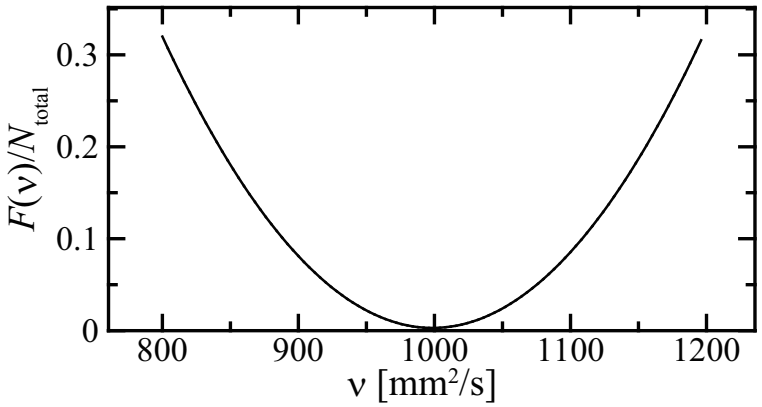


Figure 4.2: Variation of the cost function with $\nu$ around minimum setting value of $\nu_0 = 1000$ mm$^2$/s.

In assessing the influence of noise on the evaluation of $\nu$, the variation of the cost function is investigated near where it takes a minimum value. Here, Gaussian noise of zero-mean is generated at every data point of $u_\theta(r,t)$ and is added to the velocity data. Noise level $\sigma_N$ is given as the fraction normalized by the local maximum velocity $U_{\max}(r)$. The actual noise level on $u_\theta(r,t)$ measured by UVP is at least larger than 0.1% ($\sigma_N/U_{\max}(r) > 10^{-3}$). The results obtained from the velocity data calculated from the exact solution in Eq. (4.9 with different time resolutions, $\Delta t$, $f_o\Delta t = 0.03$ and 0.005, are plotted in Fig. 4.3. Here, fitted parabolic curves, obtained using the least-squares method, have been superimposed on the plots. The viscosities evaluated decrease monotonically with respect to $-\sigma_N^2$ for both time resolutions and have large deviations even at relatively small noise levels of around 0.01% in $\sigma_N/U_{\max}(r)$. For larger $\Delta t$, there is less influence from the added noise because enhancements of noise contributed by the numerical differentials are smaller.

The monotonic decrease of $\nu$ may be explained as larger noise amplification in the radial derivatives in Eq. (4.7), especially the second-order derivative (the other two terms produce no strong impact on noise transfer). The radial derivative term in Eq. (4.10) always has a larger deviation from the correct values without noise than the time derivative term, because of the second-order derivative in the radial term. To satisfy the balance of equation, the estimated $\nu$ must be smaller. By simplifying the equation for the cost function, Eq. (4.10), this is modeled simply as

$$F(\Delta\nu, \varepsilon) = \sum \left[ A - (\nu_0 + \Delta\nu) B\varepsilon \right]^2 , \tag{4.11}$$

where $A$ and $B$ are values of the differential calculations in condition without noise, so that $A \approx \nu_0 B$, and $\Delta\nu$ and $\varepsilon$ are the deviations from $\nu$ and the noise amplification rate, $\varepsilon > 1$. The local minimum of the cost function is found to be $\nu_0 + \Delta\nu$ satisfying the relation

$$\frac{\partial F}{\partial \Delta\nu} = -2 \sum AB\varepsilon + 2(\nu_0 + \Delta\nu) \sum B^2\varepsilon^2 = 0. \tag{4.12}$$

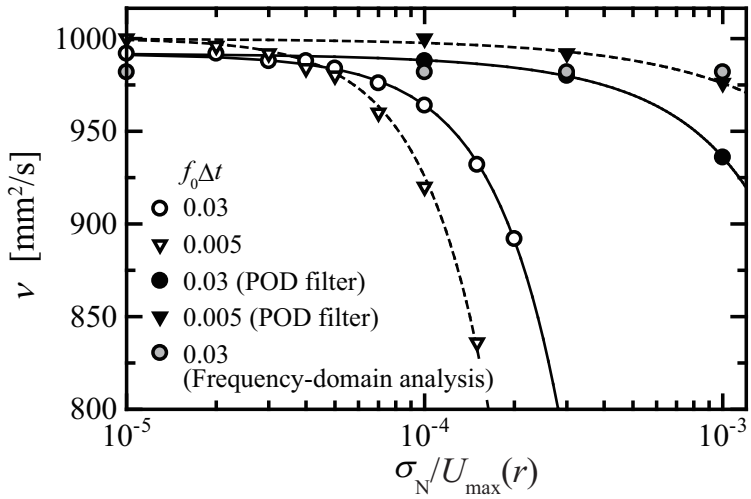


Figure 4.3: Estimated values of $\nu$ for different noise levels $\sigma N$ obtained using two different sampling times, without POD filtering and frequency-domain analysis; the solid and dashed lines represent fitted parabolic curves of the plots obtained using the least-squares approximation.

Assuming $A = \nu_0 B$, the estimated value from the preceding condition is a fraction of the correct value of $\nu$, $\nu_0$, specifically

$$\frac{\nu_0 + \Delta\nu}{\nu_0} = \frac{\sum B^2\varepsilon}{\sum B^2\varepsilon^2}. \tag{4.13}$$

This fraction is always smaller than unity. That is, the monotonic decreasing trend in $\nu$ stems from the enhancement in noise from the second-order derivative in the radial direction.

From Fig. 4.3, the influence of measurement noise on the evaluation of $\nu$ is significant and non-negligible, and therefore, eliminating noise from the velocity data is required. From the standard treatment of measured UVP data, filtering based on the (snapshot) proper orthogonal decomposition (POD) [39] provides an effective solution in achieving this purpose [40–42]. POD is good and objective at extracting organized flow structures. In the present configuration, the flows are well-organized structures and unorganized components are filtered out as noise. From Fig. 4.3, the present POD filtering can suppress the influence of noise, but there is still a certain influence of noise remaining in the evaluation. Here we remark that, after the filtering, data with a fine time resolution provides much better results than rougher ones. This is because the enhancement of noise by taking numerical differentials is reduced by POD filtering, and the fine time resolution now can provide better estimation of the differentials.

## 4.4 Frequency-domain analysis

As examined above, the influence of noise and its enhancement using numerical differentials cannot be avoided completely by filtering the velocity data. Instead, here we propose a novel algorithm to evaluate rheological properties from the velocity data employing the equation of motion as the method of analysis in the frequency domain free of difference calculation.

### 4.4.1 Theory

Taking the Fourier transform with respect to $t$, Eq. (4.3) becomes

$$\hat{\tau} + i\omega\frac{\mu}{E}\hat{\tau} = \mu\left(\frac{\partial\hat{u_\theta}}{\partial r} - \frac{\hat{u_\theta}}{r}\right), \tag{4.14}$$

where the Fourier transform is denoted

$$\hat{\tau}(r,\omega) = \mathcal{F}\left[\tau(r,t)\right], \ \hat{u_\theta}(r,\omega) = \mathcal{F}\left[u_\theta(r,t)\right]. \tag{4.15}$$

The Fourier transform changes the differential equation into an algebraic equation that can be solved for $\hat{\tau}$,

$$\hat{\tau}(r,\omega) = \frac{\mu\left(\frac{\partial \hat{u_\theta}}{\partial r} - \frac{\hat{u_\theta}}{r}\right)\left(1 - i\omega\frac{\mu}{E}\right)}{1 + \left(\omega\frac{\mu}{E}\right)^2}. \tag{4.16}$$

Cauchy's equation of motion, Eq. (4.1), is also converted into

$$i\omega\rho\hat{u_\theta} = \left(\frac{\partial}{\partial r} + \frac{2}{r}\right)\hat{\tau}. \tag{4.17}$$

Using Eqs. (4.16) and (4.17), finding $\mu$ and $E$ become an optimization problem for the cost function,

$$F(E,\mu;r) = \int_0^\Omega \left[i\omega\rho\hat{u_\theta} - \left(\frac{\partial}{\partial r} + \frac{2}{r}\right)\hat{\tau}\right]^2 d\omega. \tag{4.18}$$

That is, $\mu$ and $E$ are determined by $\min_{\mu,E} F(E,\mu;r)$. Inside the square bracket of Eq. (4.18) is a complex function that needs to be decomposed into its real and imaginary parts for the numerical calculation. We define

$$\hat{\tau}(r,\omega) = \frac{\mu}{1 + \left(\omega\frac{\mu}{E}^2\right)}\left[R_e(r,\omega) + iI_m(r,\omega)\right], \tag{4.19}$$

where

$$R_e(r,\omega) = \partial_r\Re[\hat{u_\theta}] - \frac{1}{r}\Re[\hat{u_\theta}] + \omega\frac{\mu}{E}\left(\partial_r\Im[\hat{u_\theta}] - \frac{1}{r}\Im[\hat{u_\theta}]\right),$$
$$I_m(r,\omega) = \partial_r\Im[\hat{u_\theta}] - \frac{1}{r}\Im[\hat{u_\theta}] - \omega\frac{\mu}{E}\left(\partial_r\Re[\hat{u_\theta}] - \frac{1}{r}\Re[\hat{u_\theta}]\right).$$

Substituting these into Eq. (4.18), the integrand becomes

$$\left[i\omega\rho\hat{u_\theta} - \left(\frac{\partial}{\partial r} + \frac{2}{r}\right)\hat{\tau}\right] = \left[\omega\rho\Im[\hat{u_\theta}] + \Gamma\left(\frac{\partial}{\partial r} + \frac{2}{r}\right)R_e\right]^2 + \left[\omega\rho\Re[\hat{u_\theta}] - \Gamma\left(\frac{\partial}{\partial r} + \frac{2}{r}\right)I_m\right]^2, \tag{4.20}$$

where

$$\Gamma = \frac{\mu}{1 + \left(\omega\frac{\mu}{E}\right)^2}.$$

### 4.4.2 Viscometry

To evaluate the applicability of the frequency-domain analysis proposed in this study, we perform a viscosity analysis on both velocity data created from the exact solution in Eq. (4.10) with artificial noise and UVP measurement data.

Taking the Fourier transform of the equation for Newtonian fluids yields

$$i\omega\hat{u_\theta} = \nu D_r\hat{u_\theta},\ \hat{u_\theta} = R_u(r,\omega) + iI_u(r,\omega). \tag{4.21}$$

The cost function defined in Eq. (4.18) becomes

$$\begin{aligned} F(\nu;r) &= \int_\Omega \left[i\omega\hat{u_\theta} - \nu D_r\hat{u_\theta}\right]^2 d\omega \\ &= \int_\Omega \left[(\nu D_r R_u + \omega I_u)^2 + (\omega R_u - \nu D_r I_u)^2\right] d\omega. \end{aligned} \tag{4.22}$$

The actual flows in the USR system are time periodic and discrete Fourier transform (DFT) is applicable for the analysis. From the definition of the Fourier series expansion,

$$u_\theta(r,t) = \frac{a_0(r)}{2} + \sum_{k=1}^{N}\left[a_k(r)\cos\Delta\omega kt + b_k(r)\sin\Delta\omega kt\right], \tag{4.23}$$

where

$$\Delta\omega = 2\pi\Delta f. \tag{4.24}$$

The cost function is expressed as

$$F(\nu; r) = \sum_{k=1}^{N} \left(A_k^2 + B_k^2\right), \tag{4.25}$$

where

$$A_k(r) = \Delta\omega k b_k - \nu D_r a_k,\ B_k = \Delta\omega k a_k + \nu D_r b_k. \tag{4.26}$$

The range of frequencies (or range of $k$) for the summation above is determined from the sampling frequency on $u_\theta(r,t)$, $\Delta f$, and the number of data, $N$, from $\Delta f(k=1)$ to $N\Delta f(k=N)$. Taking a wide range of frequencies, however, would induce noise caused by measurement error that is not related to the cylinder oscillation. A narrow range, $k_1\Delta f < f_o < k_2\Delta f$, is set around the driving frequency of the cylinder oscillation $f_o$. The cost function is little modified as

$$F_{f_0}(\nu; r) = \sum_{k=k_1}^{k_2} \left(A_k^2 + B_k^2\right), \tag{4.27}$$

To avoid the propagation of measurement noise caused by the numerical differentials of $r$ included in the differential operator $D_r$, an $M$th power series approximation on $a_k(r)$ and $b_k(r)$ is introduced,

$$a_k(r) = \sum_{m=0}^{M} \alpha_m r^m,\ b_k(r) = \sum_{m=0}^{M} \beta_m r^m. \tag{4.28}$$

Substituting this into definitions of $A_k$ and $B_k$, Eq. (4.26), provides

$$A_k(r) = \Delta\omega k \sum_{m=0}^{M} \beta_m r^m - \nu \sum_{m=0}^{M} (m^2-1)\alpha_m r^{m-2}, \tag{4.29}$$

$$B_k(r) = \Delta\omega k \sum_{m=0}^{M} \alpha_m r^m + \nu \sum_{m=0}^{M} (m^2-1)\beta_m r^{m-2}. \tag{4.30}$$

We perform numerical experiment as in §4.3.2 to check the applicability of the present theory and procedure. The velocity data is processed by DFT, and $a_k$ and $b_k$ in the Fourier series are approximated by fifth-order polynomials [i.e., $M = 5$ in Eq. (4.28)]. In the power spectrum of $(a_k^2+b_k^2)^{1/2}$, there is a sharp peak corresponding to the oscillation frequency $f_o$. Because the frequency resolution, $\Delta f$, is determined by the number of data and the time resolution, the peak frequency $f_c$ does not always coincide with $f_o$ and spreads over several frequencies. In the present case, $f_c = 1.0101$ Hz and three frequencies nearby contribute more than 97% of the total fluctuation in kinetic energy. Within the frequency band, $k_1 - k_2$ in Eq. (4.27), two conditions, $f = f_c$ $f_o$ and $f = f_c \pm \Delta f$, are examined. Nevertheless, there is no quantitative difference in values of $\nu$ associated with the conditions. Hence, we adopt the condition $f = f_c$ from here on. The results of evaluation of kinematic viscosity at different noise levels are summarized in Fig. 4.3 with the original results (without noise treatment) and the POD filtered velocity data. The value of $\nu$ evaluated in the present frequency-domain analysis stays the same regardless of the noise level, whereas the others decrease with increasing the noise level. The frequency-domain analysis provides slightly smaller values than the others and the correct value, $\nu_0 = 1000$ mm$^2$/s, in relatively low noise conditions. This is mainly caused by small disagreement between $f_c$ and $f_o$ due to the sampling frequency and sampling data number of $u_\theta(r,t)$. Nevertheless, it produces the small deviation even at relatively large noise levels than expected in actual situations with UVP measurements.

### 4.4.3 Application of viscometry

The frequency-domain analysis is applied on spatiotemporal velocity measurement data obtained from silicone oil ($\nu$ = 300 mm$^2$/s at 25°C) and presented in Chapter 2 with an evaluation of its kinematic viscosity using phase information. A 145-mm-diameter acrylic cylinder filled with oil was periodically oscillated with $f_o = 1$ Hz frequency and through an 80° angular amplitude. The measurement line of the velocity profiles was set at $\Delta y = 15$ mm; the UVP was performed with a 30-ms time resolution and a 0.62-mm spatial resolution (measurement direction). Figure 4.4 shows the spatio-temporal velocity distribution over three oscillation cycles. The velocity variation appears smooth compared with typical velocity profile measurements; considerable roughness is apparent in comparison with ideal velocity profiles.

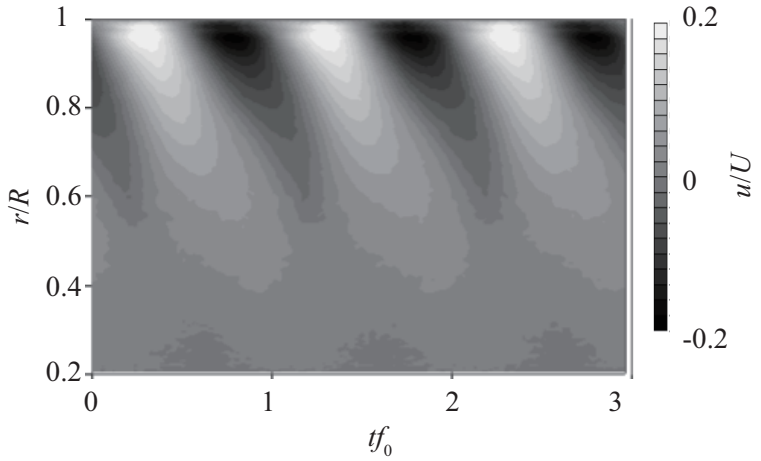


Figure 4.4: Spatio-temporal velocity distribution measured for 300 $mm^2/s$ silicone oil in a cylinder oscillating at $f_0 = 1$ Hz frequency through an 80° angular amplitude.

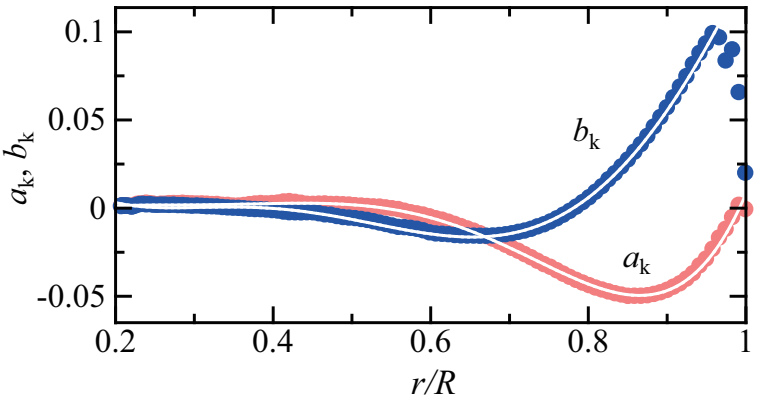


Figure 4.5: Fifth-order polynomial fittings (white curve) of the radial profiles for $a_k$ and $b_k$, where red and blue plots represent the original discrete values of $a_k$ and $b_k$, respectively.

We processed the velocity distribution using the DFT method and obtained Fourier coefficients $a_k$ and $b_k$ as radial profiles. Then, a fifth-order polynomial fitting was performed on the profiles with $f = f_c \approx f_o$ to ensure a smooth radial dependence (Fig. 4.5). An unavoidable characteristic of the UVP measurement is relatively large deviations near the boundaries around $r/R = 1$. The deviations appear mainly in $b_k(r)$, and therefore, we have omitted these points in the fitting. The fitted curves approximate the plotted data well apart from data points for $b_k$ near the cylinder wall. Following the process established in the last section, the cost function, Eq. (4.27), was calculated at each radial position in the range, $100 < \nu < 500$, and is displayed as a distribution over the $\nu - r$ plane (Fig. 4.6). The local viscosity is taken to be the local minimum of the cost function at each radial position. The radial profiles of the cost function form a "valley" with $\nu$ uniquely determined. This valley is shallower in the inner region of the cylinder because the amplitude of the velocity fluctuations is smaller and information is not sufficient for the evaluation.

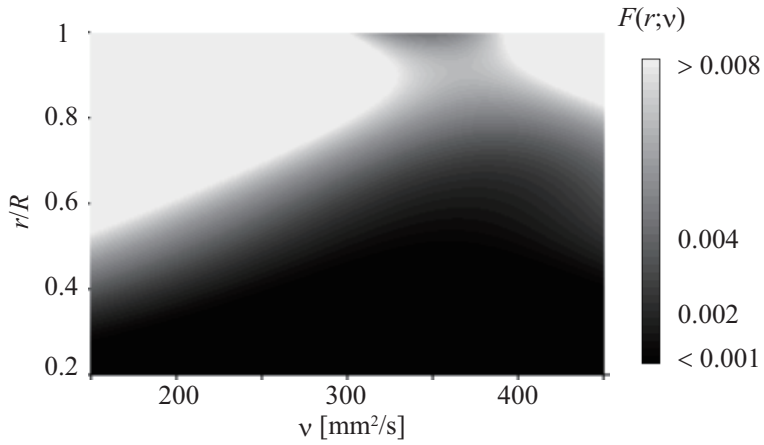


Figure 4.6: Gray-scale distribution of the cost function $F(r; \nu)$.

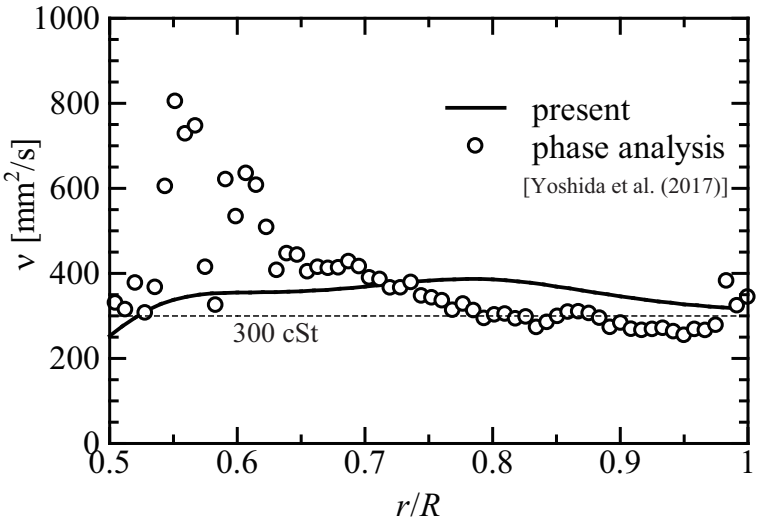


Figure 4.7: Radial profiles of the estimated kinematic viscosity from a frequency-domain analysis (solid line) and for comparison a phase profile analysis (circles) from Chapter 2.

From the frequency-domain analysis, the radial profile of $\nu$ was estimated (Fig. 4.7) using the polynomial approximation and compared with $\nu$ estimated from a phase-slope analysis on the same data given in [Chapter 2]. The local slope of the phase delay of the velocity fluctuation with respect to the cylinder oscillation reflects the local viscosity, and comparing the phase slopes obtained from the analytical solution, Eq. (4.9), and experimental data yields the local kinematic viscosity. Similar values were obtained although with deviations; $\nu$ given by the phase analysis exhibit large deviations in the interior of the cylinder, whereas those obtained from the frequency-domain analysis yield similar values. The phase analysis also employs the Fourier transform and suppresses the influence of measurement error on the velocity fluctuations. Nevertheless, the phase

information extracted from very small velocity fluctuations is not representative of the flow, and hence, calculations using numerical differentials propagate errors. In contrast, profiles of the Fourier coefficients at the main frequency retain almost all information in representing the flow, and thus, this method provides an advantage when analyzing viscometric data. Further, returning to the original purpose of the study, the frequency-domain analysis is applicable to linear viscoelastic analysis using the rheological model. We remark that the evaluation of the kinematic viscosity from the experimental data of 300 $mm^2/s$ oil using the cost function in Eq. (4.10) is unable to determine the local minimum of $\nu$ over the range $100 < \nu < 500$ even with POD filtering.

### 4.4.4 Linear viscoelastic analysis of bubble suspension

According to the same idea on the viscometry adopting Fourier series expansion of $u_\theta(r,t)$ [Eq. (4.23)] and power series approximation on the Fourier coefficients [Eq. (4.28)], the cost function for the linear viscoelastic analysis in Eq. (4.18) is modified into

$$F_{f_0}(E,\mu;r) = \sum_{k=k_1}^{k_2} \left(A_k^2 + B_k^2\right), \tag{4.31}$$

where

$$A_k(r) = \sum_{m=0}^{M} \left[-\rho\Delta\omega k\beta_m r^m + \Gamma\left(m^2-1\right)\left(\alpha_m - \Delta\omega k\mu\beta_m/E\right) r^{m-2}\right], \tag{4.32}$$

$$B_k(r) = \sum_{m=0}^{M} \left[\rho\Delta\omega k\alpha_m r^m + \Gamma\left(m^2-1\right)\left(\beta_m + \Delta\omega k\mu\alpha_m/E\right) r^{m-2}\right]. \tag{4.33}$$

The algorithm is examined on an analysis of a polyacrylamide aqueous solution (1 wt.%), which has shear-rate-dependent viscosity and elasticity, to check its applicability for more complex fluids before performing linear viscoelastic analysis of bubble suspensions. Spatio-temporal velocity information was captured in the same system of oscillating cylinder (see Fig. 4.1) that was also used in our previous study [15] and Chapter 2. The setting parameters for the oscillation are $f_o = 1$ Hz (in frequency) and $\Theta = 90°$ (in amplitude). For the analysis, the velocity data was processed by the DFT method to derive Fourier coefficients $a_k(r)$ and $b_k(r)$ in Eqs. (4.32) and (4.33) corresponding to the Fourier component of $f = f_o$. Fifth-order power series approximation is then adopted to approximate their radial profiles. In the evaluation of the cost function in Eq. (4.31) for the linear viscoelastic analysis, the phase difference in linear viscoelastic analysis $\delta$ is used as a parameter instead of $E$. Viscosity $\mu$ and $\delta$ are obtained at each radial position by the analysis as shown in Fig. 4.8; the values are plotted against the amplitude of shear-rate variations $\dot{\gamma}_0$, which is given from the Fourier coefficients and calculated using power series approximation in Eq. (4.28) as

$$\dot{\gamma}_0 = \sqrt{\left[\sum_{m=0}^{M}(m-1)\,\alpha_m r^{m-1}\right]^2 + \left[\sum_{m=0}^{M}(m-1)\,\beta_m r^{m-1}\right]^2}. \tag{4.34}$$

In the figure, the viscosity calculated by phase profile analysis [Chapter 2] from the same velocity data is also plotted for comparison. The viscosity evaluated by the linear viscoelastic analysis gradually decreases with $\dot{\gamma}_0$ and expresses shear thinning characteristics of the solution. Along the decrease of viscosity, $\delta$ approaches to 90°, meaning that the solution loses elastic property toward a pure viscous body.

We now come back to the linear viscoelastic analysis of a bubble suspension by the frequency-domain analysis established above. Fourier coefficients $a_k(r)$ and $b_k(r)$ in Eqs. (4.32) and (4.33) are given by the DFT method performed on the velocity data of the bubble suspension used in §4.3.1. Then, fifth-order power series approximation is performed on radial profiles of the coefficients corresponding to $f = f_c \approx f_o$ (1 Hz). The profiles are approximated well as shown in Fig. 4.9. In the calculation of the cost function, phase delay of the linear viscoelasticity described in Eq. (4.6) is changed as a parameter instead of $E$ in the range from 50° to 90∘ with an increment of 0.1°. Exploring the range of $\mu$ was set around the original viscosity of the base liquid of the suspension, 1000 $mm^2/s$ silicone oil, $\mu_0 = 0.97$ Pa · s, from 0.5 to 1.5 Pa · s with an increment of 0.005 Pa · s.

An example of the calculated cost function is shown in Fig. 4.10 as the distribution of $F$ on the $\delta - \mu$ plane for $r = 0.9R$. The distribution is expressed in logarithmic gray scale, and there is a single local minimum point; values of $\delta$ and $\mu$ are given as values on this point. At least in the range of $\delta$ and $\mu$ we examined, the cost function increases monotonically from the local minimum point, and the values are uniquely given. For $r/R < 0.9$, the local minimum point attaches to the boundary of $\delta = 90°$, but uniqueness of the solution is unchanged.

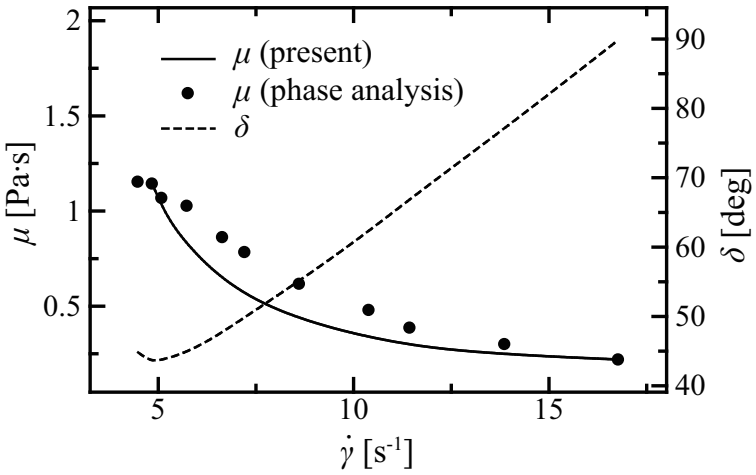


Figure 4.8: Variations of viscosity $\mu$ and phase difference in linear viscoelasticity $\delta$ with respect to shear rate $\dot{\gamma}$ for 1 wt.% polyacrylamide aqueous solution, where $\mu$ calculated by the phase profile analysis [Chapter 2] from the same velocity data is also plotted.

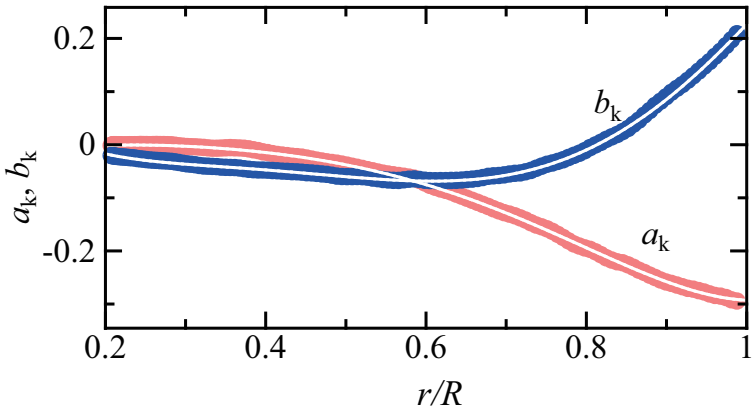


Figure 4.9: Fifth-order polynomial fittings (white curve) of the radial profiles for $a_k$ and $b_k$ obtained in the bubble suspension, where red and blue plots represent the original discrete values of $a_k$ and $b_k$, respectively.

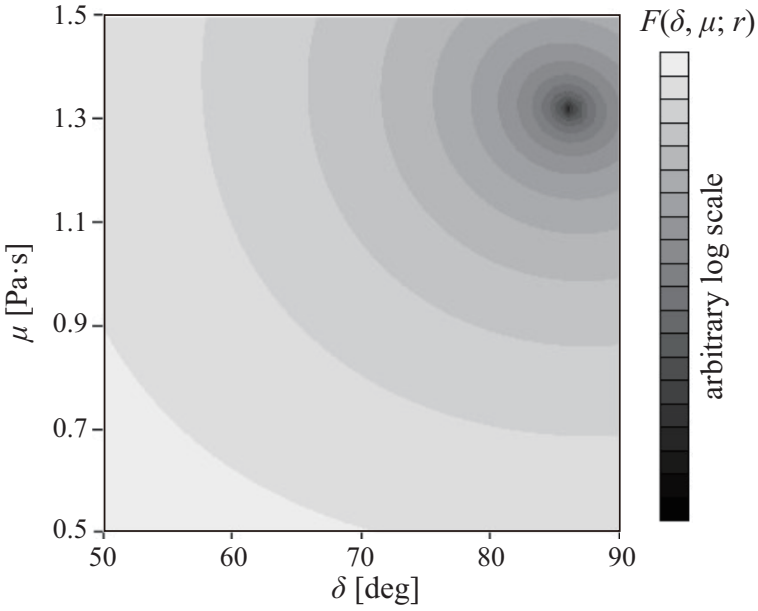


Figure 4.10: Gray-scale distribution of the cost function, $F(\mu, \delta; r = 0.9R)$, for the bubble suspension.

Results of estimations of $\delta$ and $\mu$ according to the cost function calculated at each radial position from $r/R = 0.6$ to $r/R = 0.95$ are summarized in Table 4.2. Elasticity $E$ is calculated through Eq. (4.6) with $\mu$ and $f_o$ in cases that $\delta < 90°$. $|\mu^*|$ denotes effective complex viscosity defined as

$$|\mu^*| = \frac{\mu}{\sqrt{1 + (\omega\mu/E)^2}}. \tag{4.35}$$

The linear viscoelastic analysis separated influences of unsteady bubble deformations in the oscillating shear flows on the momentum propagation into viscous and elastic contributions. In the table, $\delta$ takes 90° without a region $r/R > 0.9$, and the elastic contribution appears in the region. This is reasonable because the capillary number exceeds effectively the critical capillary number to allow bubble deformations in this range, and the deformation bubbles existing nearby the wall show considerable deformations [15]. In the oscillating shear flows, the bubbles experience periodically strong shear and relaxation. The elastic effect may be provided by restoring the original spherical shape in the relaxation. Effective viscosity normalized by original viscosity of the oil, $|\mu^*|/\mu_0$, distributes around unity within the deviation order of the volume fraction of bubbles, 2% for $r/R < 0.8$. This is in good agreement with knowledge of effective viscosity for spherical bubbles.

Table 4.2: Evaluation results of viscosity $\mu$, phase difference in linear viscoelasticity $\delta$, and elasticity $E$ calculated from $\mu$ and $\delta$ through Eq. (4.6) at different radial position $r/R$, where the amplitude of local shear-rate variation $\dot{\gamma}_0$ is calculated from the velocity data through Eq. (4.34), and $|\mu^*|$ indicates effective viscosity normalized by the original viscosity value of the oil, $\mu_0 = 0.97$ Pa · s.

| $r/R$ | $\dot{\gamma}_0$ [s$^{-1}$] | $\mu$ [Pa · s] | $\delta$ [°] | $E$ [Pa] | $\lvert\mu^*\rvert/\mu_0$ |
|---|---|---|---|---|---|
| 0.95 | 15.89 | 1.46 | 77.1 | 39.8 | 1.46 |
| 0.9 | 14.28 | 1.32 | 86.1 | 121.2 | 1.36 |
| 0.85 | 12.46 | 1.17 | 90.0 | – | 1.21 |
| 0.8 | 10.53 | 1.05 | 90.0 | – | 1.08 |
| 0.75 | 8.63 | 0.99 | 90.0 | – | 1.02 |
| 0.7 | 6.90 | 0.97 | 90.0 | – | 0.99 |
| 0.65 | 5.45 | 0.99 | 90.0 | – | 1.02 |
| 0.6 | 4.32 | 1.05 | 90.0 | – | 1.08 |

## 4.5 Conclusion

To achieve a stable evaluation of the linear viscoelasticity in bubble suspensions as complex multiphase fluids using USR, we assessed the influence of measurement noise enhancement in the evaluation of rheological properties using the equation of motion with measurement data of spatio-temporal velocity fluctuations. By avoiding calculations of numerical differential using velocity data, a frequency-domain analysis was proposed for applications in linear viscoelastic analysis. By taking the Fourier transform of the equation of motion and the constitutive equations (the rheological models), time derivatives are converted to algebraic calculations, and further, approximating the radial profiles of Fourier coefficients by finite power series enables an evaluation of the rheological properties without requiring calculation of numerical differentials. In rheology, this novel combination of techniques was scrutinized using numerical experiments by considering noise artificially generated in viscometric data. The present method provided better estimates of viscosity in comparison with dealing with raw velocity data and POD filtering. The technique was also applied to actual velocity data measured in 300 mm$^2$/s silicone oil as a Newtonian fluid, and the estimations were in reasonable agreement with previous results. The frequency-domain analysis was then extended to the linear viscoelastic analysis, and its applicability was examined on a polyacrylamide aqueous solution, which is a shear thinning, viscoelastic fluid. The analysis finally achieved separation of influences of unsteady bubble deformation into viscous and elastic contributions on the momentum propagation.

The algorithm proposed here is aptly applicable in a wider range of velocity-profiling rheometry. And, it may be able to support to evaluate, e.g., fluids taking shear banding effects and solutions with distributions of concentration.

## References

[1] Y. L. Yeow, W. C. Ko, and P. P. Tang, "Solving the inverse problem of Couette viscometry by Tikhonov regulation," J. Rheol. 44, 1335–1351 (2000).

[2] C. Ancey, "Solving the Couette inverse problem using a waveletvaguelette decomposition," J. Rheol. 49, 441–460 (2005).
[3] G. Heirman, R. Hendrickx, L. Vandewalle, D. Van Gemert, D. Feys, G. De Schutter, B. Desmet, and J. Vantomme, "Integration approach of the Couette inverse problem of powder type self-compacting concrete in a wide-gap concentric cylinder rheometer," J. Non-Newtonian Fluid Mech. 150, 93–103 (2008).
[4] M. Doi, and T. Ohta, "Dynamics and rheology of complex interfaces," J. Chem. Phys. 95, 1242–1247 (1991).
[5] J. J. Stickel, and R. L. Powell, "Fluid mechanics and rheology of dense suspensions," Ann. Rev. Fluid Mech. 37, 129–149 (2005).
[6] S. L. Ceccio, "Friction drag reduction of external flows with bubble and gas injection," Ann. Rev. Fluid Mech., 42, 183–203 (2010).
[7] Y. Murai, "Frictional drag reduction by bubble injection," Exp. Fluids, 55(7), 1773 (2014).
[8] A. Einstein, "Eine neue Bestimung der Molekuldimensionen," Ann. Phys. 19, 289–306 (1906).
[9] G. I. Taylor, "The viscosity of a fluid containing small drops of another fluid," Proceedings of the Royal Society of London. Series A, Containing Papers of a Mathematical and Physical Character, 138(834), 41–48 (1932).
[10] N. A. Frankel, and A. Acrivos, "On the viscosity of a concentrated suspension of solid spheres," Chem. Eng. Sci. 22, 847–853 (1967).
[11] A. C. Rust, and M. Manga, "Effects of bubble deformation on the viscosity of dilute suspensions," J. Non-Newton. Fluid Mech., 104(1), 53–63 (2002).
[12] S. J. Choi, and W. R. Schowalter, "Rheological properties of non-dilute suspensions of deformable particles," Phys. Fluids, 18(4), 420–427 (1975).
[13] E. W. Llewellin, H. M. Mader, and S. D. R. Wilson, "The constitutive equation and flow dynamics of bubbly magmas," Geophysical research letters, 29(24), 23-1 (2002).
[14] E. W. Llewellin, and M. Manga, "Bubble suspension rheology and implications for conduit flow," Journal of Volcanology and Geothermal Research, 143(1-3), 205–217 (2005).
[15] Y. Tasaka, T. Kimura, and Y. Murai, "Estimating the effective viscosity of bubble suspensions in oscillatory shear flows by means of ultrasonic spinning rheometry," Exp. Fluids 56, 1867 (2015).
[16] Y. Murai, and H. Oiwa, "Increase of effective viscosity in bubbly liquids from transient bubble deformation," Fluid dynamics research, 40(7–8), 565 (2008).
[17] C. J. Dimitriou, L. Casanellas, T. J. Ober, and G. H. Mckinley, "Rheo-PIV of a shear-banding wormlike micellar solution under large amplitude oscillatory shear," Rheol. Acta 51, 395–411 (2012).
[18] F. Rodrigez-Gonzalez, J. Perez-Gonzalez, L. De Vargas, and B. M. Marin-Santibane, "Rheo-PIV analysis of the slip flow of a metallocene linear low density polyethylene melt," Rheol. Acta 49, 145–154 (2010).
[19] J. Perez-Gonzalez, J. J. Lopez-Duran, B. M. Marin-Santibanez, and F. Rodriguez-Gonzalez, "Rheo-PIV of a yield-stress fluid in a capillary with slip at the wall," Rheol. Acta 51, 937–946 (2012).
[20] J. J. Serrano-Aguilera, L. Parras, C. del Pino, and F. J. Rubio-Hernandez, "Rheo-PIV of Aerosil ®R816/polypropylene glycol suspensions," J. Non-Newton. Fluid Mech., 232, 22–32 (2016).
[21] S. Jarny, N. Roussel, S. Rodts, F. Bertrand, R. Le Roy, and P. Coussot, "Rheological behavior of cement pastes from MRI velocimetry," Cement Concrete Res. 35, 1873–1881 (2005).
[22] G. Ovarlez, F. Bertrand, and S. Rodts, "Local determination of the constitutive law of a dense suspension of noncolloidal particles through magnetic resonance imaging, " J. Rheol. 50, 259–292 (2006).
[23] L. M. Quinzani, R. C. Armstrong, and R. A. Brown, "Use of coupled birefringence and LDV studies of flow through a planar contraction to test constitutive equations for concentrated polymer solutions," J. Rheol. 39, 1201–1228 (1995).
[24] J. P. Rothstein, and H. M. Gareth, "Inhomogeneous transient uniaxial extensional rheometry," J. Rheol. 46, 1419–1443 (2002).
[25] A. Gurung, J. W. Haverkort, S. Drost, B. Norder, J. Westerweel, and C. Poelma, "Ultrasound image velocimetry for rheological measurements," Meas. Sci. Technol. 27, 094008 (2016).
[26] *Ultrasonic Doppler Velocity Profiler for Fluid Flow*, Springer Science, edited by Y. Takeda (Springer, Tokyo, 2012).
[27] S. Fischer, P. Schmitt, D. Ensminger, F. Abda, and A. Pallares, "A new velocity estimation method using spectral identification of noise," Flow Meas. Instrum. 19, 197–203 (2008).
[28] V. Meacci, S. Ricci, J. Wiklund, B. Birkhofer, and R. Kotze, "Flow-Viz—An integrated digital in-line fluid characterization system for industrial applications," in IEEE Sensors Applications Symposium (SAS) (2016), pp. 1–6.
[29] E. Muramatsu, H. Murakawa, K. Sugimoto, H. Asano, N. Takenaka, and N. Furuichi "Multi-wave ultrasonic Doppler method for measuring high flow-rates using staggered pulse intervals," Meas. Sci. Technol., 27(2), 025303 (2015).
[30] J. Salmela, S. Haavisto, A. Koponen, A. Jäsberg, and M. Kataja, "Rheological characterization of micro-fibrillated

cellulose fibre suspension using multi scale velocity profile measurements," In Proceeding of 15th fundamental research symposium (2013, September).
[31] Y. Murai In: Y. Takeda (ed.) "Ultrasonic Doppler velocity profiler for fluid flow," vol 101. Springer, Tokyo, pp. 153–156 (2012).
[32] B. Derakhshandeh, D. Viassopoulos, and S. G. Hatzikiriako, "Thixotropy, yielding and ultrasonic Doppler velocimetry in pulp fibre suspensions," Rheol. Acta 51, 201–214 (2012).
[33] B. Ouriev, and E. J. Windhab, "Rheological study of concentrated suspensions in pressure-driven shear flow using novel in-line ultrasound Doppler method," Exp. Fluids 32, 204–211 (2002).
[34] J. Wiklund, and M. Stading, "Application of in-line ultrasound Doppler-based UVP–PD rheometry method to concentrated model and industrial suspensions," Flow Meas. Instrum. 19(3-4), 171–179 (2008).
[35] M. A. Rao, S. S. H. Rizvi, A. K. Datta, J. Ahmed (eds) "Engineering properties of foods," 4th edn. CRC press, Boca Raton (2014).
[36] T. Shiratori, Y. Tasaka, Y. Murai, and Y. Takeda, "Development of ultrasonic visualizer for capturing the characteristics of viscoelastic fluids," J. Vis. 16, 275–286 (2013).
[37] A. Savizky, M. J. E. Golay "Smoothing and differentiation of data by simplified least square procedures," Anal. Chem. 36:1627–1639 (1964).
[38] M. Saito, M. Matsumoto, "SIMD-oriented Fast Mersenne Twister: a 128-bit pseudorandom number generator," (2008). In: P. L'Ecuyer and A. B. Owen (eds) "Monte Carlo and quasi-Monte Carlo methods," (2006). Springer, Berlin, pp 607–622.
[39] L. Sirovich "Turbulence and the dynamics of coherent structures. Part I: coherent structures," Quart. Applied Math. 45:561–571 (1987).
[40] Y. Takeda "Quasi-periodic state and transition to turbulence in a rotating Couette system," J. Fluid Mech. 389:81–99 (1999).
[41] N. Furuichi, Y. Takeda, M. Kumada "Spatial structure of the flow through an axisymmetric sudden expansion," Exp. Fluids, 34:643–650 (2003).
[42] Y. Tasaka, K. Igaki, T. Yanagisawa, T. Vogt, T. Zuerner, and S. Eckert, "Regular flow reversals in Rayleigh-Bénard convection in a horizontal magnetic field," Phys. Rev. E 93:043109 (2016).

Chapter 5

# Efficacy assessments in USR: Linear viscoelastic analysis on non-Newtonian fluids

## Contents


**5.1 Introduction . . . 64**
5.1.1 Problems in rotational shear rheometers . . . 64
5.1.2 Rheometry coupled with velocimetry . . . 64
**5.2 Basic concept of USR . . . 66**
5.2.1 Experimental apparatus . . . 66
5.2.2 Theoretical basis for the linear viscoelastic analysis . . . 67
5.2.3 Demonstration of the linear viscoelastic analysis on an silicone oil . . . 68
**5.3 Linear viscoelastic analysis of non-Newtonian fluids . . . 70**
5.3.1 Test fluid conditions and device for comparative experiment . . . 70
5.3.2 CMC solution . . . 72
5.3.3 Mt dispersion . . . 75
**5.4 Efficacy of USR as a complementary technique . . . 81**
**5.5 Conclusion . . . 82**
**References . . . 82**


## Preface

The aim in this chapter is to stress the efficacy of the kinematic rheometry (presented in Chapter 4) as a complementary technique for conventional torque rheometers, by comparison of the rheometer with parallel plate geometry and USR. This work was already in Yoshida *et al*., J. Rheol. (2019).

## Abstract


We have progressively developed an ultrasonic spinning rheometry (USR) that has the potential to visualize complex details of rheology, such as time-dependence, coexistence of gel and sol, effective viscosity of multiphase fluids, and other particulars. This rheometry makes it possible to overcome the main issues in conventional rheometry, originating from nonideal velocity profiles in the complex fluids. The most notable advantage of USR is the ability to perform "local" rheological evaluations from only the velocity information for a short-time period by solving the equation of motion. This benefit is provided while avoiding noise augmentations by introducing a linear viscoelastic analysis in the frequency domain. Solving the equation of motion with a rheological model equation in the frequency domain, multiple rheological parameters are quantified by minimizing the cost function. In this paper, the analysis presented by USR is verified by comparative experiments using a rheometer with the typical geometry of parallel disks. As a complementary technique for conventional rheometers, the USR efficacies are shown through rheological assessments for Newtonian, shear-thinning, and thixotropic fluids.

# 5.1 Introduction

## 5.1.1 Problems in rotational shear rheometers

The goal of rheometry development is to fully understand the rheology of all soft materials. Achieving this is of great importance to ensure the quality of manufactured materials and the optimization of systems in industries. This will lead to raising the quality of various components in industry, such as in polymers, biology, food processing, and multiphase dispersions. To comprehend rheological issues in fluids with complex behaviors, there are various types of rheometers that measure "specific" rheological characteristics. The most typical rheometer is a geometric system measuring axial torque via solid walls with a specific gap [see Fig. 5.1(a) for an example of a parallel-disk-type geometry arrangement]. Different geometries to evaluate torque have been proposed; however, the fundamental concept of rheological evaluations is the same in all torque-type rheometers.

Improvements in torque meters have enabled highly accurate rheological evaluations, but rheometers encounter serious difficulties in the evaluation of complex fluids. The reasons why such difficulties arise are shear history effects [1], shear banding [2, 3], shear localization [4], and more. Rheometers can measure simple shear viscosities as an axial torque represented by the viscous resistance (the elastic response) in the fluid media. A narrow gap $O(0.1 - 1$ mm) between parallel disks is required to realize steady flows with constant shear rates $\dot{\gamma}$ (i.e., linear velocity profiles); however, the actual flows have to be treated as nonlinear profiles due to the shear-rate-dependence, viscoelastic instability, shear banding, and others. The measured results are merely apparent viscosities because of unexpected actual shear-rate profiles arising during the measurements as suggested in Fig. 5.1(b).

Particularly, at critical-shear conditions such that the stress approaches to yield stress for gelled fluids, the problems of shear rheometer measurements become prominent. There are unexpected influences from wall-slip, shear history, or shear localization when the structure of gelled fluids yields at certain critical-shear intensities; Nechyporchuk *et al*. [5] applied cone-plate geometry and reported that wall-slip was detected at low shear rates for fluids with gel-like and shear-thinning properties. From these experimental observations, they concluded that the obtained values include unavoidable measurement errors when wall-slip occurs in the measurements. Wolthers *et al*. [1] explored the shear history dependence of viscosity in aggregated-colloidal dispersions and concluded that the observed rheological behavior depends on the specific geometry of the shear rheometers due to effects of thixotropy and sedimentation.

To solve the problems arising from nonideal velocity profile, there exists a semianalytical technique with solving an inverse problem for estimating original velocity profiles in wider gap Couette rheometry, termed "Couette inverse problem" [6–8]. Also, there are many approaches for rheological evaluations of non-Newtonian fluids [9, 10], most of which are limited to treatments of the problem for specific test fluids. Wrong estimation of the original velocity profiles, however, causes measurement errors of the shear rheometry data.

The key factor to provide solutions to the problem is utilizing spatiotemporal velocity distributions of fluid motion that reflect all rheological information of the solutions that are investigated. This makes rheometries coupled with spatiotemporal velocity-profiling techniques needed for a solution to overcome the common problem originated from nonideal, unknown velocity profiles. This is termed velocity-profiling rheometry, and the techniques will be explained in detail in §5.1.2.

## 5.1.2 Rheometry coupled with velocimetry

As examples of velocity-profiling rheometries, various approaches coupled with velocimetries have been proposed, including ultrasonic velocity profiling (UVP) [11–16], ultrasonic imaging velocimetry (UIV) [17, 18], particle imaging velocimetry (PIV) [20, 19], magnetic resonance imaging (MRI) velocimetry [21, 22], and laser Doppler velocimetry (LDV) [23, 24]. With PIV and LDV, the application is limited to transparent fluids, although most complex fluids are opaque, dense suspensions, colloid dispersions, multiphase fluids, or similar. The MRI velocimetry can perform visualizations of opaque and multiphase fluids; however, it requires very large measurement facilities and monitoring is handicapped to low temporal resolutions due to fluid flow.

Ultrasonic measurement techniques have advantages, such as offering ease of handling and the option of employing them with opaque fluids. Ouriev and Windhab [13] proposed a combined technique of UVP measurements and pressure difference measurements, which is termed UVP-PD in-line rheometry, something used as a practical tool in the food processing industry [14], since it has the advantages of in-line measurements from outside of steel pipe walls. Derakhshandeh *et al*. [12] performed measurements of transient behaviors of thixotropic fluids using a Couette rheometer with a wide gap and UVP. This can detect yielding regions of the fluid from quasi-steady velocity profiles, although the torque measurements may be influenced by wall-slip and this will lead to errors in evaluations of the rheological characteristics. After then, by coupling conventional rheometer and ultrasonic imaging technique, spatiotemporal analyses were developed. As one of the examples, Gallot *et*

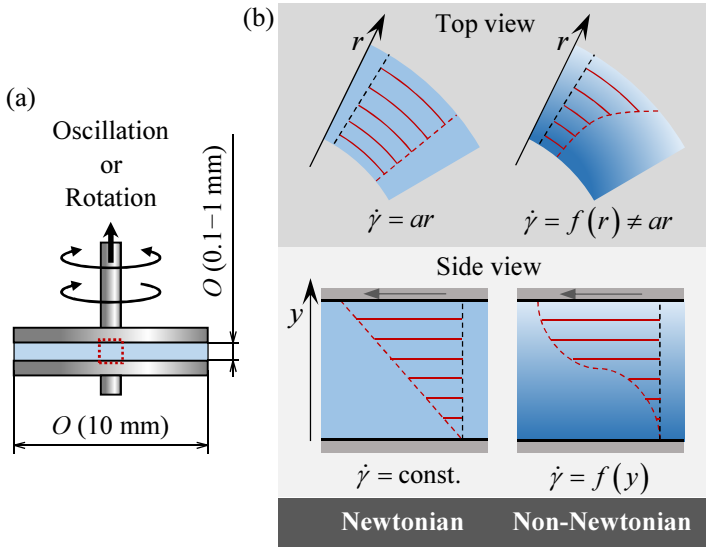


Figure 5.1: (a) Schematic of a parallel-disk rotational rheometer and (b) shear-rate profiles in test fluids between the rotating disks for Newtonian or non-Newtonian fluids.

*al*. [15] proposed a technique that reveals the unstable shear-banded flow of non-Newtonian fluids. In a recent development of ultrasonic rheometry, Gurung *et al*. [17] reported a novel rheometry with combinations of an ultrasonic scanning technique and PIV (UIV or echo-PIV), and they performed real-time measurement of opaque flows with complex rheology in particle-laden fluids. Originally, this technique has mainly been used to measure flow behaviors in blood vessels in the field of medical engineering. Researches have dealt with time-averaged velocity profiles limited to steady flow states. Since one of the non-Newtonian characteristics involves both shear-rate-dependence in the rheological properties and time-dependence, the techniques must be able to detail timedependent properties.

We have developed a novel velocity-profiling rheometry, termed ultrasonic spinning rheometry (USR) [25–28]. The basic concept of this rheometry is that velocity profiles are substituted into the equation of motion to solve it. Important characteristic compared to conventional methodology as we mentioned above is to use unsteady shear flows. Although UVP can obtain one velocity component parallel to the line of propagation of ultrasonic waves, this rheometry (USR) is accomplished by a single UVP in cases satisfying the assumption of one-directional shear flow in an azimuthal direction. Since this would make it possible to quantify shear-rate-dependent properties over a wider range of shear rates obtained from single measurements, USR is expected to be able to measure spatial profiles of local rheological properties. There is, however, a problem of noise augmentation arising from the differential terms in the equation of motion [26, 28]. Because of the nature of generating spiky noise mainly due to lack of tracer particles in UVP measurements, the differential calculations on the velocity data obtained by UVP would not be an efficient way to satisfy the equation of motion.

To avoid the influence of noise amplification of differential terms, Tasaka *et al*. [27] proposed an algorithm using phase-lag information of velocity fluctuations in unsteady shear flows. In periodically oscillating cylinders, the fluid motion has a dominant frequency corresponding to the cylinder oscillation frequency. Phase-lag information of the frequency component extracted by discrete Fourier transform (DFT) represents the momentum transfer with much less noise. The local effective Newtonian viscosity is then evaluated by comparing the phase lags between experimental results and the analytical solution. As a further development of the phase-lag analysis, the analysis was established in Chapter 2 by performing various rheological measurements: The effective Newtonian viscosity of clay dispersions with thixotropy, liquid food gelling behaviors with tiny ingredients, and curry paste containing larger ingredients. Also, observing shear localizations, the viscoelasticity of macro-rheological behaviors in clay dispersions at regions of gel and sol coexistence was speculated in Chapter 3.

We have remarked on the important advantage that Fourier components of velocity information can extract from rheological properties without the noise influence appearing in phase-lag analysis. This analysis still has limitations, in that rheological characteristics would be approximated as locally effective Newtonian viscosity. To improve on this limitation, linear viscoelastic analysis in a frequency domain was presented in Chapter 4 and suggested that the equation of motion with the rheological model can be satisfied by substituting Fourier components of velocity fluctuations. In the theory of linear viscoelastic analysis of USR, multiple rheological properties can be determined with only the velocity profile measurements. But as yet there has been little further effort to assess its applicability and efficacy for fluids with complex-rheological properties.

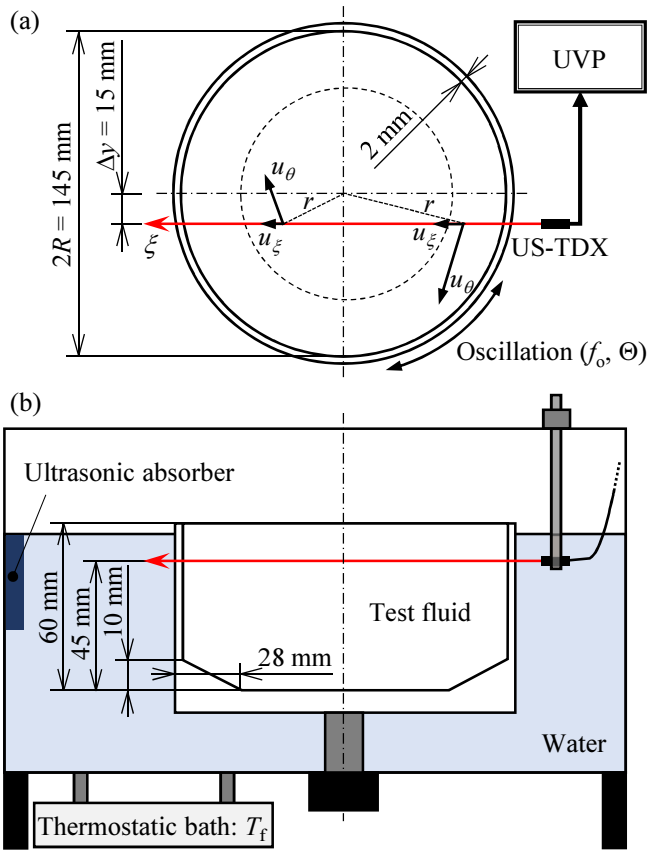


Figure 5.2: Schematic of the experimental setup for capturing oscillating shear flows coupled with an ultrasonic velocity profiler: (a) top view of the rotating cylinder and (b) side view.

The research objective of the present study is to assess the applicability and efficacy of the linear viscoelastic analysis with both Newtonian and non-Newtonian fluids. To validate that the analysis measures Newtonian viscosity correctly, the rheological evaluation of a typical Newtonian fluid was performed (§5.2.3). Carboxymethyl cellulose (CMC) solutions and montmorillonite (Mt) dispersions were selected as the objects for the non-Newtonian fluid measurements, where CMC solutions typically show shear-thinning characteristic and Mt dispersions are investigated as thixotropic fluids (see details in §5.3.1). To ensure the efficacy for the non-Newtonian fluids, comparative experiments of USR and a parallel-disk rotational rheometer as a widely used device are also examined in §5.3.1 (see details of the hypothesis in the Appendix). From the experiments, the advantages of USR with complex fluids that potentially originate unknown velocity profiles were assessed.

## 5.2 Basic concept of USR

In this section, to explain experimental apparatus and theoretical basis of linear viscoelastic analysis in USR, rheological evaluation for silicone oil is demonstrated.

### 5.2.1 Experimental apparatus

One of the main characteristics of the experimental apparatus [Fig. 5.2(a)] is an open cylindrical container made of acrylic resin. The container has 2-mm-thick side walls, 145-mm inner diameter, and is 60-mm high. To control the temperature, $T_0$, of the test fluids and to avoid any influence from co-reflected ultrasonic waves, the container was mounted at the center of a water bath [$1000 \times 1000$ mm$^2$ as shown in Fig. 5.2(b)]. Oscillation of the cylinder was controlled by a stepping motor to an oscillation angle $\Theta$ and frequency $f_o$, where the motor was attached at the bottom of the container. The oscillation was controlled by sinusoidal angular velocity, $U_{\text{wall}} \sin 2\pi f_o t$, where $U_{\text{wall}} = 2\pi f_o R\Theta$ (see Chapter 3 in detail). To avoid generating radial and axial flows during the oscillations, the bottom of the cylinder was machined with a slope near the outside wall as shown in Fig. 5.2(b).

The UVP-Model Duo (Met-Flow S.A., Switzerland) was used to measure instantaneous velocity distributions. To obtain the azimuthal velocity component, an ultrasonic transducer (resonance frequency 4 MHz and 5-mm active element diameter) was mounted with a gap $\Delta y$ from the center coordinates of the cylindrical container. Assuming that the axisymmetric flow and the radial velocity component are negligible, the azimuthal velocity $u_\theta$ is calculated from a geometric relation given as

$$u_\theta = u_\xi \frac{r}{\Delta y}. \tag{5.1}$$

Here, the radial position $r$ is calculated from the distance to the transducer $\xi$ by the geometric relation, $r^2 = \Delta y^2 + [(R^2 - \Delta y^2)^{1/2} - \xi]^2$. Considering ultrasound emissions, the ultrasonic beams become disk-like at each measurement point and may become gradually larger during propagation. Empirically, based on the results of previous study [27] and Chapter 2, $\Delta y = 15$ mm was selected, and further details of the setup for the transducer were detailed in [Chapter 3].

### 5.2.2 Theoretical basis for the linear viscoelastic analysis

Here, we will summarize the key formulae and analytical procedures derived in Chapter 4 and modify the formulae for the ease of application. Assuming that the fluid flows are one-directional and axisymmetric, Cauchy's equation of motion is given as

$$\rho \frac{\partial u_\theta}{\partial t} = \frac{\partial \tau}{\partial r} + \frac{2\tau}{r}, \tag{5.2}$$

where $\rho$ is the density of the test fluids and $\tau$ indicates the shear stress. To describe the relation of $u_\theta$ and $\tau$, Maxwell's model,

$$\tau + \frac{\mu}{E}\frac{\partial \tau}{\partial t} = \mu\left(\frac{\partial u_\theta}{\partial r} - \frac{u_\theta}{r}\right), \tag{5.3}$$

is selected as the simplest expression to represent the linear viscoelastic characteristics, where $\mu$ and $E$ indicate viscosity and elasticity of the fluid. To avoid any influence of noise amplified by the differential terms, and taking Fourier transform with respect to $t$, Eqs. (5.2) and (5.3) can be modified as

$$i\omega\rho\hat{u}_\theta = \left(\frac{\partial}{\partial r} + \frac{2}{r}\right)\hat{\tau}, \tag{5.4}$$

$$\hat{\tau} + i\omega\frac{\mu}{E}\hat{\tau} = \mu\left(\frac{\partial \hat{u}_\theta}{\partial r} - \frac{\hat{u}_\theta}{r}\right), \tag{5.5}$$

where Fourier-transformed velocity and shear stress are denoted as

$$\hat{u}_\theta(r,\omega) = \mathcal{F}[u_\theta(r,t)], \quad \hat{\tau}(r,\omega) = \mathcal{F}[\tau(r,t)], \tag{5.6}$$

with the angular frequency $\omega$. To determine $\mu$ and $E$ satisfying the optimization problem, the cost function is given as

$$F(\mu, E; r) = \left[i\omega\rho\hat{u}_\theta - \left(\frac{\partial}{\partial r} + \frac{2}{r}\right)\hat{\tau}\right]^2_{\omega=\omega_o} \quad \text{s.t. } \hat{\tau} + i\omega\frac{\mu}{E}\hat{\tau} = \mu\left(\frac{\partial \hat{u}_\theta}{\partial r} - \frac{\hat{u}_\theta}{r}\right), \tag{5.7}$$

where the spectrum was adjusted as having a single dominant frequency at the oscillation frequency $\omega = \omega_o (= 2\pi f_o)$.

Using the relation of complex viscosity from Maxwell's model, the phase difference is defined as $\tan\delta = G''/G' = E/\omega_o\mu$, where the phase values around $\pi/2$ are indicative of fluid being close to a pure viscous body and smaller values indicate larger elastic contributions to stress in the fluids [Chapter 4]. Then, substituting this, Eq. (5.5) is modified to

$$\hat{\tau}(r,\omega) = \mu \sin^2\delta\,[R_e(r,\omega) + iI_m(r,\omega)], \tag{5.8}$$

where $R_e$ and $I_m$ are given as

$$R_e(r,\omega) = \frac{\partial}{\partial r}\Re[\hat{u}_\theta] - \frac{1}{r}\Re[\hat{u}_\theta] + \left(\frac{\partial}{\partial r}\Im[\hat{u}_\theta] - \frac{1}{r}\Im[\hat{u}_\theta]\right)\cot\delta, \tag{5.9}$$

$$I_m(r,\omega) = \frac{\partial}{\partial r}\Im[\hat{u}_\theta] - \frac{1}{r}\Im[\hat{u}_\theta] - \left(\frac{\partial}{\partial r}\Re[\hat{u}_\theta] - \frac{1}{r}\Re[\hat{u}_\theta]\right)\cot\delta. \tag{5.10}$$

By Eq. (5.8), Eq. (5.7) can be expressed with real values as

$$F(\mu,\delta;r)=\left\{\omega_o\rho\Im[\hat{u}_\theta]+\mu\left(\frac{\partial}{\partial r}+\frac{2}{r}\right)R_e\sin^2\delta\right\}^2+\left\{\omega_o\rho\Re[\hat{u}_\theta]-\mu\left(\frac{\partial}{\partial r}+\frac{2}{r}\right)I_m\sin^2\delta\right\}^2. \tag{5.11}$$

Optimal values of $\mu$ and $\delta$ are determined to minimize $F$. Fourier-transformed shear rate $\hat{f}[\dot{\gamma}]$ is given as the right-hand-side term in the brackets of Eq. (5.5), and the formula can be extended as

$$\mathcal{F}[\dot{\gamma}]=\frac{\partial\hat{u}_\theta}{\partial r}-\frac{\hat{u}_\theta}{r}=\left(\frac{\partial}{\partial r}-\frac{1}{r}\right)(\Re[\hat{u}_\theta]+i\Im[\hat{u}_\theta]). \tag{5.12}$$

The effective value of the shear rate is calculated by

$$\dot{\gamma}_{\text{eff}}=\sqrt{\left\{\left(\frac{\partial}{\partial r}-\frac{1}{r}\right)\Re[\hat{u}_\theta]\right\}^2+\left\{\left(\frac{\partial}{\partial r}-\frac{1}{r}\right)\Im[\hat{u}_\theta]\right\}^2}, \tag{5.13}$$

as a root-mean-square value considering Eq. (5.12). In the same way, the effective value of the shear stress calculated from Eq. (5.8) becomes

$$\tau_{\text{eff}}=\mu\sin^2\delta\sqrt{R_e^2+I_m^2}, \tag{5.14}$$

where $\mu$ and $\delta$ are used to determine $\tau_{\text{eff}}$.

### 5.2.3 Demonstration of the linear viscoelastic analysis on an silicone oil

To validate and demonstrate the linear viscoelastic analysis step by step, a silicone oil (reported viscosity, 0.49 Pa · s at 25°C, Shin-Etsu Chemical Co., Ltd., Japan) was used; it has usually been dealt as a Newtonian fluid in a lower shear rate than the $O(10^2\ \text{s}^{-1})$. The experimental conditions and parameters are detailed in Table 5.1. The spatiotemporal velocity distributions were measured using UVP as shown in Fig. 5.3(a). The vertical and horizontal axes indicate the radial positions normalized by the radius of the container, $R$, and the spin-cycle period $tf_o$. The contours represent the azimuthal velocity normalized by the maximum azimuthal velocity at the cylinder wall ($r/R=1$), $U_{\text{wall}}(=2\pi f_o R\Theta)$. For ease of understanding the velocity profiles, Fig. 5.3(b) shows plots of instantaneous velocity profiles extracted from the spatiotemporal distribution at i-iv, indicated by dashed lines in Fig. 5.3(a). The azimuthal velocity fluctuations decrease with closeness to the center of the container since the momentum propagation is diffused by viscous damping.

Table 5.1: Parameters in USR for rheological evaluations of different test fluids. $\Delta\xi$, spatial resolution; $\Delta t$, temporal resolution; $\Delta u_\xi$, velocity resolution; $f_o$, oscillation frequency; $\Theta$, Oscillation angle; $U_{\text{wall}}$, angular velocity of cylinder wall; and $N$, a number of velocity profiles.

| Test fluid | Silicone oil 0.49 Pa · s | CMC solution 0.5 wt.% | Mt dispersion 4.0 wt.% with 0.02 mol/L NaCl | |
|---|---|---|---|---|
| Feature | Newtonian | Shear thinning | Thixotropic | |
| $\Delta\xi$ [mm] | 0.49 | 0.74 | 0.74 | 0.74 |
| $\Delta t$ [ms] | 50 | 50 | 50 | 50 |
| $\Delta u_\xi$ [mm/s] | 0.66 | 0.98 | 1.30 | 0.63 |
| $f_o$ [Hz] | 1.0 | 0.8 | 0.5 | 1.0 |
| $\Theta$ [rad] | $\pi/4$ | $5\pi/18$ | $2\pi/3$ | $\pi/4$ |
| $U_{\text{wall}}$ [mm/s] | 357.8 | 318.0 | 477.0 | 357.8 |
| $N$ [–] | 20 | 25 | 40 | 20 |
| Section # | §5.2.3 | §5.3.2.2 | §5.3.3.2 | §5.3.3.3 |

Calculating the power spectrum by the DFT, Fourier components, $\hat{u}_\theta(r,\omega)$, were clearly separated into the oscillation frequency $f_o=1.0$ Hz and others [Fig. 5.3(c)]. In this result, the ratio of the fluctuating energy between the dominant frequency and the summation of all components accounts for 97% at $r/R=0.95$, and the important information to describe the flow behavior is included in the dominant frequency component. The components of real and imaginary parts corresponding to $f_o=1.0$ Hz were shown in Fig. 5.3(d) as closed circle plots; the open circles indicate the phase-lag profile calculated by

$$\phi=\tan^{-1}\frac{\Im[\hat{u}_\theta]}{\Re[\hat{u}_\theta]}-\phi_{\text{wall}}, \tag{5.15}$$

where $\phi_{\text{wall}}$ indicates the phase lag at the cylinder wall.

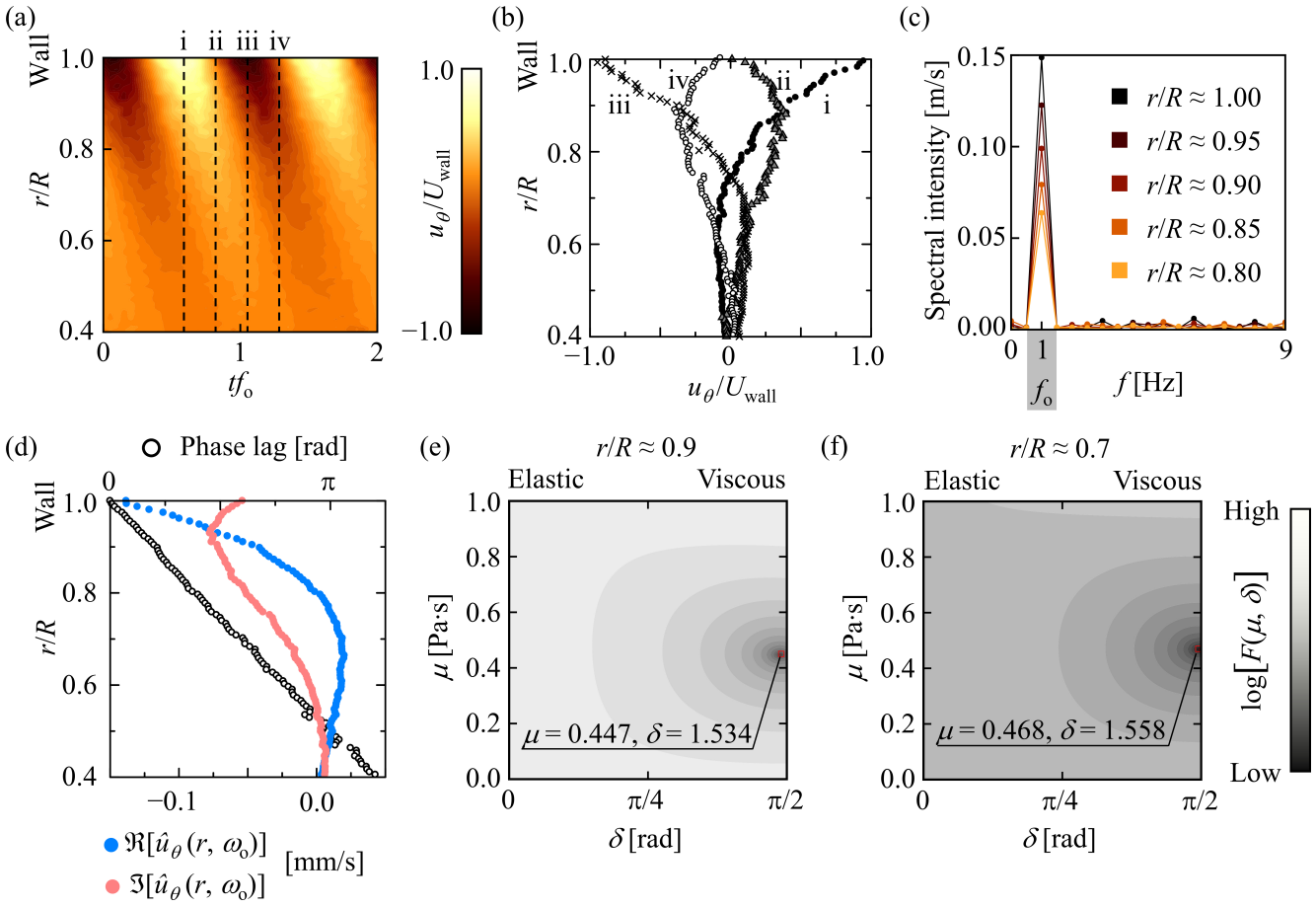


Figure 5.3: (a) Azimuthal velocity distribution of silicone oil (500 $mm^2/s$, 0.49 $Pa \cdot s$) with normalized time $tf_o$ measured by UVP; angular velocity of the cylindrical wall, $U_{wall}$ = 357.8 mm/s, (b) extracted velocity profiles from the spatiotemporal velocity of (a) indicated by dashed lines (i–iv), (c) power spectrum calculated from the velocity distribution (a) at various radial positions $r/R$, (d) magnitudes of real and imaginary components of $\hat{u}_\theta$ at the oscillation frequency $\omega = \omega_o$ ($= 2\pi f_o$) (closed circle) and phase lag calculated from the magnitudes of Fourier components as indicated in top axis (open circle), and $\mu$–$\delta$ distributions of the cost function $F$ at (e) $r/R \approx 0.9$ and (f) $r/R \approx 0.7$.

Using Eq. (5.11), the cost function $F$ is calculated as shown in Fig. 5.3(e) ($r/R \approx 0.9$) and Fig. 5.3(f) ($r/R \approx 0.7$) as examples. Contours indicate the calculated values of the cost function for changing $\mu$ and $\delta$, where the resolutions of $\Delta\mu$ and $\Delta\delta$ are approximately $10^{-3}$ Pa · s and $10^{-3}$ rad. From the results in Figs. 5.3(e) and 5.3(f), all contours show concave surfaces and singular minimal points. With $r/R \approx 0.9$ and 0.7, the minimum values were determined at $\mu = 0.447$ Pa · s, $\delta = 1.534$ rad and $\mu = 0.468$ Pa · s, $\delta = 1.558$ rad, respectively. From these results, in the rheological evaluations by calculating from single Fourier components (2-s), there exist variances within 10%. It is due to unavoidable noise arising from signal processing in velocity profiling. So, to perform secure assessments, statistical evaluation is a suitable way by counting the rheological evaluations repeatedly.

By determining optimal $\mu$ and $\delta$ values at each of the radial positions as indicating minimum values of the cost function [see Eq. (5.11)], the evaluated results ($\mu$, $\delta$, and $\tau_{\text{eff}}$) of the effective shear-rate profiles are shown in Figs. 5.4(a)–5.4(c). Each result was obtained at different cycle periods of oscillation as indicated upside of Figs. 5.4(a)–5.4(c). The coloring of the symbols is darker with longer cycle period of oscillations. In Fig. 5.4(a), the dashed line indicates the reported viscosity value of the silicone oil, $\mu = 0.49$ Pa · s at 25°C. The temperature was controlled at 25°C by the thermostatic bath, which is connected to the water bath. The measured results using the USR were very similar to 0.49 Pa · s in a wide range of shear rates, corresponding to the radial range $0.5 < r/R < 0.95$.

In Fig. 5.4(b), the dynamic viscoelastic parameter $\delta$ is obtained close to $\pi/2$ and showed some variance, suggesting that the present method does show the rheological characteristics for the silicone oil behaving as a Newtonian fluid. By substituting the obtained rheological parameters, $\mu$ and $\delta$, into Eq. (5.14), the effective shear stress profiles were calculated. Like for the effective shear rates, as mentioned above, the shear stress profiles were calculated as effective values of the periodic fluctuations [Fig. 5.4(c)]. The dotted line in Fig. 5.4(c) indicates a flow curve as assumed by Newton's law of viscosity, $\tau_{\text{eff}} = \mu\dot{\gamma}_{\text{eff}}$, where $\mu = 0.49$ Pa · s (reported viscosity), and the line passes through the origin. These results [Figs. 5.4(a)–5.4(c)] were calculated from two-cycle-data (2-s), and increasing the number of cycles in the calculations will improve the accuracy and precision.

To statistically show the accuracy and precision of the linear viscoelastic analysis of USR, we repeated the evaluations of the viscoelastic measurements 100 times in 2-s [Figs. 5.4(d)–5.4(f)]. The color scale indicates the number of samples calculated from the 100 times of measurements by counting logarithmic cells along the vertical and horizontal axes except along the $\delta$ axis shown in Fig. 5.4(e). The viscosity $\mu$ and effective shear stress $\tau_{\text{eff}}$ agree well with the theoretical values plotted as dashed lines. In these results, there exists variance with decreasing $\dot{\gamma}_{\text{eff}}$ since the measurement noise would be dominant in velocity fluctuations smaller than $O(1$ mm/s). This is because the velocity resolution, $\Delta u_\xi$, of UVP is equivalent to $O(1$ mm/s) as listed in Table 5.1. Most of the samples in $\delta$ [Fig. 5.4(e)] indicate a $\pi/2$ that reflects the viscous trend. From the results in Fig. 5.4(f), $\tau_{\text{eff}}$ is sufficiently accurate to evaluate the flow curve of the silicone oil. Also, these results show that linear viscoelastic analysis can be applied to evaluate the properties of Newtonian fluids.

## 5.3 Linear viscoelastic analysis of non-Newtonian fluids

In this section, we assess the efficacy of the linear viscoelastic analysis in USR through experiments comparing USR and a conventional torque rheometer with parallel disks in two non-Newtonian fluids with different rheological characteristics.

### 5.3.1 Test fluid conditions and device for comparative experiment

One of the test fluids is a CMC solution that is a typical non-Newtonian fluid with well-known rheological properties. The properties strongly depend on the chain length of the polymers in the fluid, and shear-thinning behavior appears for concentrations of the solution in water lower than 1.0 wt.% [30]. In the present experiment, Daicel CMC (Daicel Chemical Industries, Ltd., Japan) was used.

The second test fluid is a montmorillonite (Mt) dispersion with dissolved NaCl. Kunipia-F (Kunimine Industries Co., Ltd., Japan) was used here. When the Mt particles swell in ionic solvents, the dispersion behaves in a non-Newtonian manner due to the Mt particle networks; the dispersions gelate in nonsheared situations via a structuring by particle interactions, by van der Waals attraction, electrostatic repulsion, and Coulomb attractive forces [31]. These global particle networks are easily broken into smaller clusters with Mt concentrations of less than $O(10$ wt.%). The rheological property changes drastically even under very weak shear stresses. In simple shear cases, the local macro-rheological properties involve shear-thinning due to the alignment of the particles in parallel to the shear direction. These particle networks recover the structure with time due to the structuring by its particle interactions that have been termed "House-of-cards" or "band type" flocculating [Chapter 3]. These are structurally stable because the surface of the dispersed particles is electrically charged in particles swelling in water.

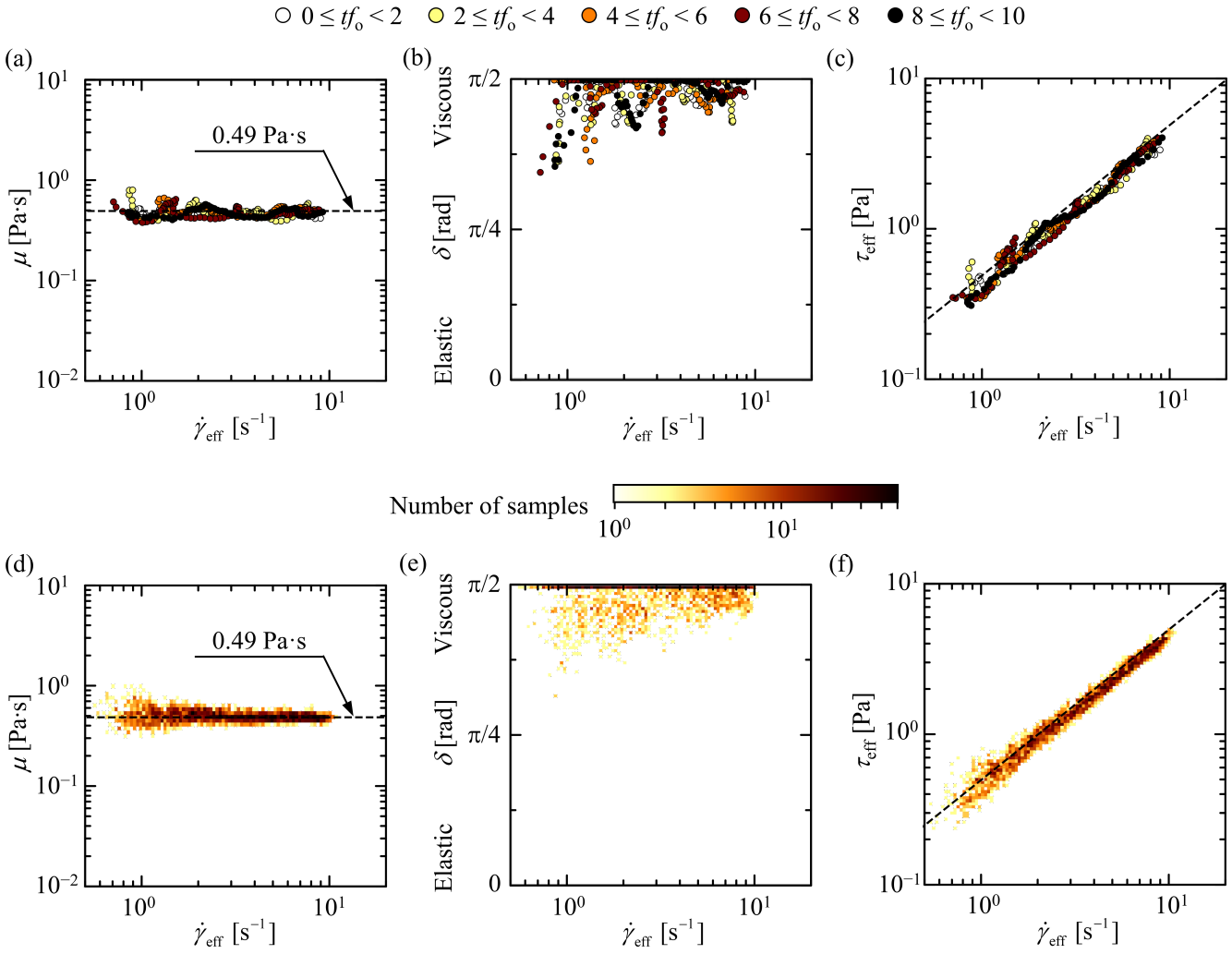


Figure 5.4: Rheological evaluations for the silicone oil from velocity profiles in short time (2-s); (a) $\mu$, (b) $\delta$, and (c) $\tau_{\mathrm{eff}}$ in the $\dot{\gamma}_{\mathrm{eff}}$ profiles obtained at different cycle period of oscillations as indicated upside, (b) 2D histograms calculated by counting all of profiles (100 times) as shown in (a)–(c); (d) $\mu$, (e) $\delta$, and (f) $\tau_{\mathrm{eff}}$ in $\dot{\gamma}_{\mathrm{eff}}$ profiles in 500 mm$^2$/s silicone oil (0.49 Pa $\cdot$ s at 25°C); $f_{\mathrm{o}}$ = 1.0 Hz, $\Theta = \pi/4$ rad, and $U_{\mathrm{wall}}$ = 357.8 mm/s.

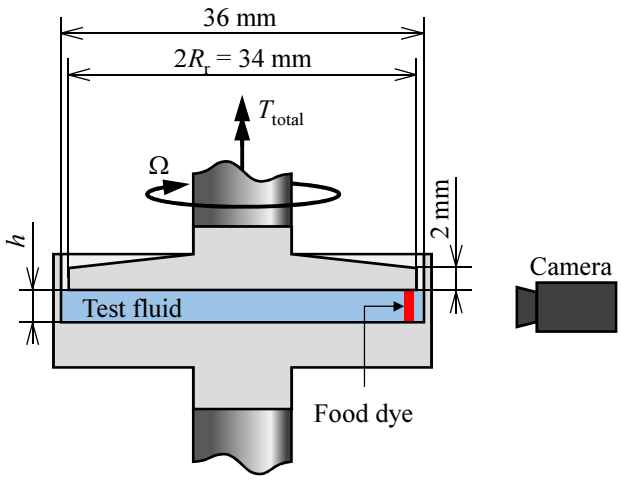


Figure 5.5: Schematic of a parallel-disk rotational rheometer used to visualize flow/deformation of test fluids.

The overall rheological characteristics are categorized as thixotropy [31–33]. The thixotropic behaviors play a critical role in the shear localization or banding as mentioned in §5.1.1.

A parallel-disk rotational rheometer (Anton Paar, MCR102) was used to compare the USR measurements of the CMC solution and the Mt dispersion. The geometric configuration of the rheometer is shown in Fig. 5.5; the test fluids are continued in the gap between the parallel disks maintained at a constant temperature ($T_0$ = 25°C). To visualize actual shear deformations of the test fluids during the measurements, the measurement section of the rheometer was made of transparent acrylic resin. Nechyporchuk *et al*. [5] investigated wall-slip and shear banding phenomena in a rotational rheometer with cone-plate geometry using ink visualization. Utilizing this, the nonlinear behaviors at the beginning of rheological measurements can be evaluated easily.

Now, to ensure understanding of important hypotheses of this rheometer in dealing with shear-strain or velocity profiles, we describe the theoretical basis and procedures of the rheometer. The required conditions are (a) one-directional flow (strain), (b) shear rate is a linear function in the axial direction, (c) non-slip conditions on the walls, and (d) homogeneity of the fluid. These conditions must be satisfied to ensure the reliability of the rheometer. In many cases, a thin layer of the test fluids is not sufficient to satisfy the assumptions (see the Appendix in detail). But in cases where the thickness is inadequate to prevent the appearance of non-Newtonian behavior, shear rate $\dot{\gamma}$ and shear stress $\tau$ must be considered as an apparent shear rate $\dot{\gamma}_{app}$ and an apparent shear stress $\tau_{app}$.

There are some empirical data correction techniques to reduce the deviation caused by insufficient satisfactions of the conditions required. But here any data correction is not performed for the comparison to highlight the essential differences between the rheometries, because such data correction is not universally applicable in general as also mentioned in the Introduction.

## 5.3.2 CMC solution

### 5.3.2.1 Rheology evaluated by the parallel-disk rotational rheometer

Measuring the viscous resistance from the CMC solution as the loaded torque during the rotation of the upper disk, flow curves of the solution were obtained by increasing and decreasing the rotation speed gradually as shown in Fig. 5.6(a). The applied shear rates were controlled with stepwise increment (or decrement) as the nested, enlarged figure in Fig. 5.6(a). To confirm whether the CMC solution has influences of the shear history and/or shear localization effect, the measurements were conducted along a pathway (i) by increasing the rotational speed from $\dot{\gamma}_{app} = 10^{-1}$ to $10^{1}$ s$^{-1}$ and (ii) by decreasing it from $\dot{\gamma}_{app} = 10^{1}$ to $10^{-1}$ s$^{-1}$ . As shown in Fig. 5.6(b), the flow curves obtained under the two rotational speed change are approximately equal.

Deformation of the CMC solution with food dye at $\dot{\gamma}_{app} = 10^{1}$ s − 1 was visualized through the transparent disks as shown in Fig. 5.6(c), and the dye distribution presented a linear strain shape between the parallel disks ($h$ = 2 mm). This indicates that shear localization or banding does not exist in rheological evaluations of the CMC solution using the rheometer. Unified flow curves [Fig. 5.6(b)] in increasing and decreasing of $\dot{\gamma}_{app}$ reflect it. These support the reliability on the rheological evaluations performed by the rheometer. In rheological evaluations for the CMC solution using the rheometer, there does

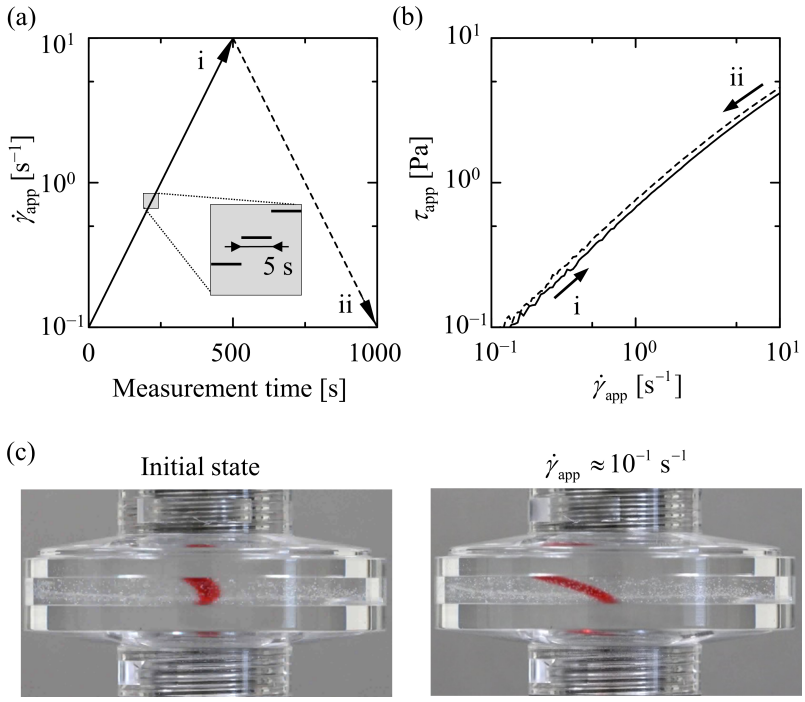


Figure 5.6: (a) Two pathways (i and ii) of the shear rate with elapsed measurement time, where the shear rates in (i) and (ii) were applied along stepwise increment or decrement, (b) flow curves (i and ii) obtained from rotational shearing, where the fluid was deformed as shown in (a) when $\dot{\gamma}_{app} = 10^{-1}$ s$^{-1}$ in (i), and (c) linear displacement of CMC solution (0.5 wt.%) under rotational shear, visualized by food dye.

not exist shear localization or banding from this visualization. Also, since flow curves shown in Fig. 5.6(b) trace the same pathway, there does not exist shear history and time-dependency. These support the reliability for the results obtained by rheometer.

#### 5.3.2.2 Rheological evaluations using USR

The distribution of $u_\theta(r,t)$ at $0 < tf_o < 2$ with $f_o = 0.5$ Hz in oscillation frequency and $\Theta = 5\pi/18$ rad in amplitude is shown in Fig. 5.7(a). Other parameters in the measurement are detailed in Table 5.1. The velocity distribution also shows periodic fluctuations with a phase lag at each radial position, the velocity amplitudes decrease with closeness to the cylinder center. The real and imaginary components of Fourier coefficients, $\Re[\hat{u}_\theta]$ and $\Im[\hat{u}_\theta]$, calculated from the velocity distributions at each radial position can be separated into the oscillation frequency fo and other factors [Fig. 5.7(b)]. Calculating phase-lag of velocity fluctuation of the CMC by Eq. (5.15), the phase-lag in Fig. 5.7(b) shows nonlinear profile compared to that of Newtonian fluid as shown in Fig. 5.3(d). According to Chapter 3, this shape of phase-lag profile is typical in polymer solutions having shear-thinning viscosity.

To evaluate the rheological parameters ($\mu$ and $\delta$), the cost function $F$ was calculated at $10^{-2} < \mu < 10^{1}$ Pa · s and $10^{-2} < \delta < \pi/2$ rad by applying the procedure to determine the minimum value of $F$ discussed in §5.2.2. The resolutions of $\Delta\mu$ and $\Delta\delta$ suggest 0.001 Pa · s and 0.001 rad, as approximate values. For instance, in the $F(\mu,\delta)$ at $r/R \approx 0.9$ and 0.7, the minimum points are apparent from the contours of $F$ [Figs. 5.7(c) and 5.7(d)]. The parameters, $\mu$ and $\delta$, are determined from the $F(\mu,\delta)$ calculated at each radial position, where the viscoelastic analysis can be achieved in a shortperiod with $O$(1 s) of velocity measurement as the shortest.

In these experiments, the 2D histograms in $\dot{\gamma}_{eff}$ and $\mu$ [Fig. 5.8(a)], $\dot{\gamma}_{eff}$ and $\delta$ [Fig. 5.8(b)], and $\dot{\gamma}_{eff}$ and $\tau_{eff}$ [Fig. 5.8(c)] were calculated from the number of samples, 200 times for the 2-s rheological measurements, where the color scale represents the number of samples. The $\dot{\gamma}_{eff}$ in Figs. 5.8(a)–5.8(c) and $\tau_{eff}$ in Fig. 5.8(c) are calculated from Eqs. (5.13) and (5.14), respectively. In Figs. 5.8(a) and 5.8(c), the solid and dashed curves show the $\mu_{app}$ and $\tau_{app}$ obtained by the rheometer as presented in §5.3.1. In Fig. 5.8(a), the variation of $\mu$ agrees well with the results of the rheometer in §5.3.1. The important feature in this result is that the viscosity $\mu$ decreases with increasing shear rate $\dot{\gamma}_{eff}$ [Fig. 5.8(a)], as the rheological characteristics of the CMC solution displays a shear-thinning behavior. From the results in Fig. 5.8(b), the phase difference $\delta$ between the viscous

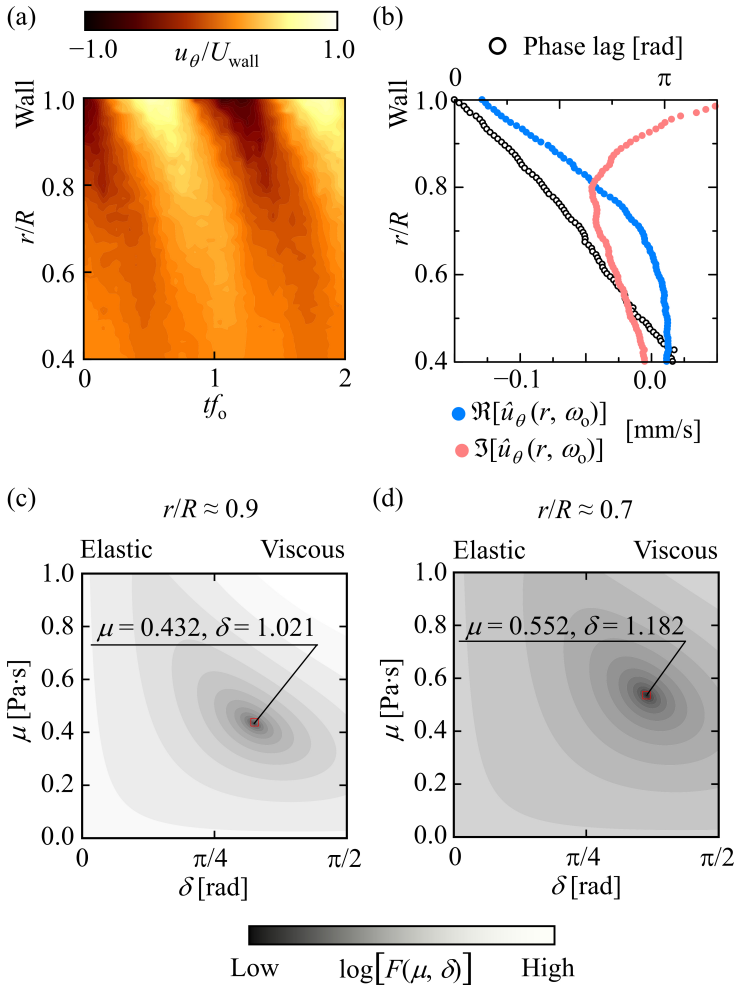


Figure 5.7: (a) Azimuthal velocity distributions with two oscillation periods tfo measured using UVP in 0.5 wt. % CMC solution, with the wall angular velocity $U_{\mathrm{wall}}$ = 318.0 mm/s, (b) magnitudes of real and imaginary components of $\hat{u}_\theta$ in the oscillation frequency $\omega = \omega_o$ (= $2\pi f_o$) (closed circle) and phase lag calculated from the magnitudes of Fourier components (open circle), and $\mu$–$\delta$ distributions of the cost function $F(\mu, \delta; r)$ at (c) $r/R$ = 0.9 and (d) 0.7.

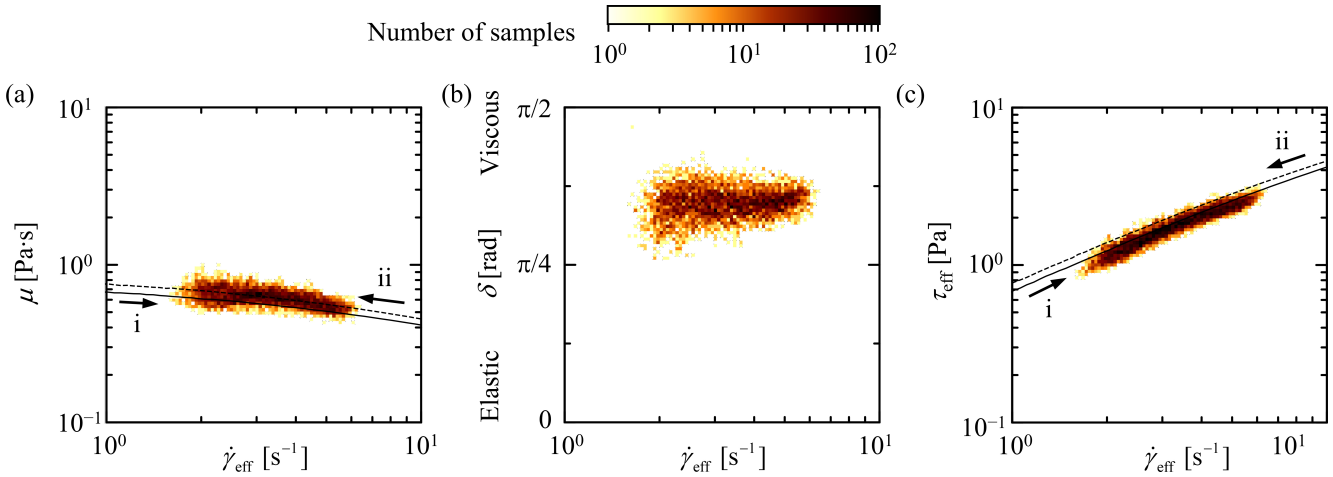


Figure 5.8: 2D histograms plotting 200 samples for the 2-s rheological measurements calculated by counting all profiles (200 times); (a) $\mu$, (b) $\delta$, and (c) $\tau_{\rm eff}$ in $\dot{\gamma}_{\rm eff}$ profiles in 0.5 wt.% CMC solution, where solid (i) and dashed (ii) curves indicate measured results using a parallel-disk rotational rheometer; $f_{\rm o} = 0.8$ Hz, $\Theta = 5\pi/18$ rad, and $U_{\rm wall} = 318.0$ mm/s.

and elastic moves closer to $\pi/2$ with increasing $\dot{\gamma}_{\rm eff}$. Considering that the CMC polymer chains are intricately intertwined, and as the chains ravel and align in the shearing direction, this agrees with the rheological behavior of the CMC solution as it changes from viscoelastic to viscous as $\dot{\gamma}_{\rm eff}$ increases. In Fig. 5.8(c), similar to the result in Fig. 5.8(a), the variations in the histogram of $\tau_{\rm eff}$ are in good agreement with the results of the rheometer.

As mentioned in §5.3.1, the dilute CMC solution is well known as a typical shear-thinning fluid without yield stress or time-dependence. The results show that here USR performance of simultaneous evaluations of flow curve and dynamic viscoelasticity as comparable rheological properties are similar to the conventional shear rheometer. Also, as shown by the histogram, the rheological evaluations of USR are statistically stable, allowing conclusion that USR is sustainable with long-duration measurements. This was also the case by the example in Chapter 2 that USR could perform evaluations for 3600 s, continuously.

Generally, the oscillatory tests using the standard rheometer evaluate $\phi$ relating to the storage modulus $G'$ and loss modulus $G''$ as $\tan\delta = G''/G'$. Further, the $G'$ and $G''$ are expressed as,

$$G'(\omega) = G_0 \frac{\omega^2\lambda^2}{1+\omega^2\lambda^2}, \tag{5.16}$$

$$G''(\omega) = G_0 \frac{\omega\lambda}{1+\omega^2\lambda^2}, \tag{5.17}$$

where the relaxation time is defined as $\lambda = \mu/E$. So, the obtained $\phi$ can be translated as $G'$ and $G''$ as the same indicator with standard rheometer tests. But usually in the conventional tests, the dynamic viscoelastic evaluations are done in the range of linear viscoelastic regime so that the both $G'$ and $G''$ keep constant with respect to shear strain $\gamma$. The applicable range of USR is much larger $\dot{\gamma}$ than that of the standard rheometers, so comparing the results of USR with the standard rheometer is not needed.

## 5.3.3 Mt dispersion

### 5.3.3.1 Rheology evaluated by a parallel-disk rotational rheometer

Rheological evaluations by the parallel-disk rotational rheometer were conducted for Mt dispersions in the same way as the procedures for validations in §5.3.2.2. The rheological behaviors of the Mt dispersions are time dependent and subject to large changes with the shear history as discussed in §5.3.1. In Fig. 5.9(a), shear-strain visualization to ensure what happened at the start of measurement shows clear differences from that in Fig. 5.6(c), where the Mt dispersions were left at rest for 100 min before the rotational shearing was applied. This difference arises as the Mt dispersions gave rise to shear localizations or wall-slip as shown in Fig. 5.9(a). Nechyporchuk *et al.* [5] visualized the shear strain of soft material with shear-thinning property and thixotropy during rheological measurement using cone-plate device. The test material in the previous work

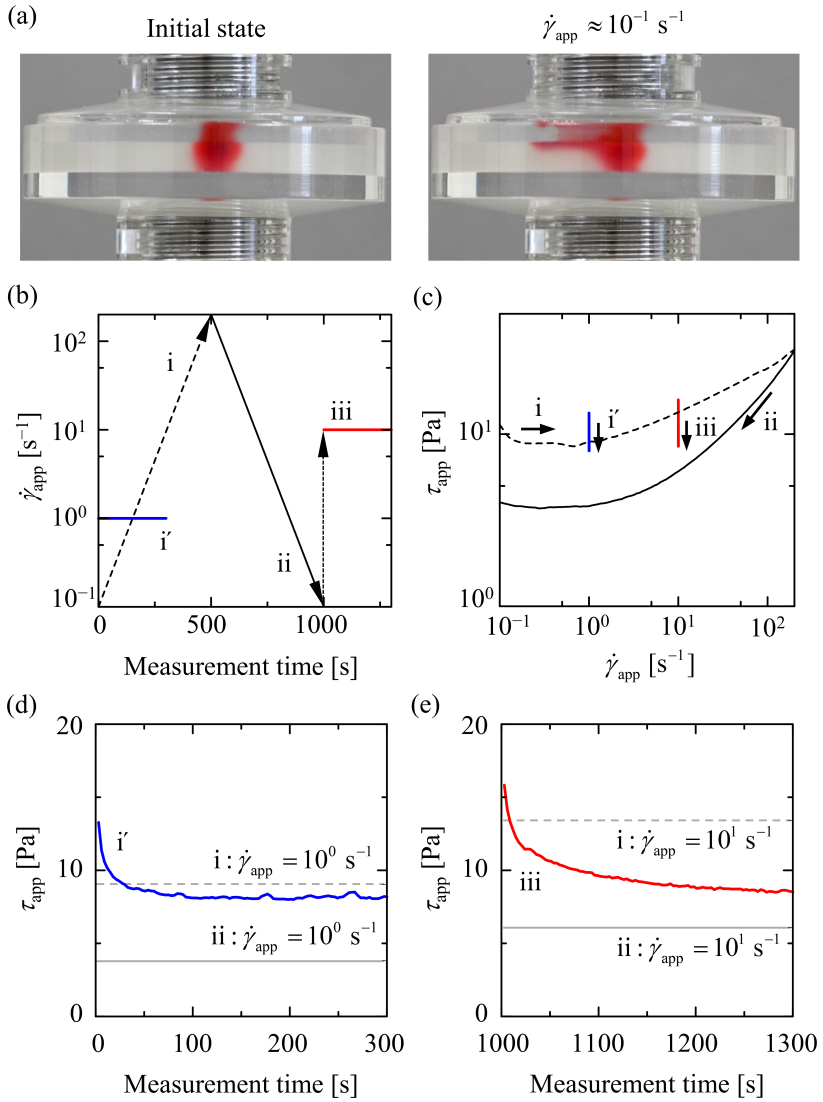


Figure 5.9: (a) Displacement of Mt dispersions (4.0 wt.% with 0.02 mol/L NaCl) under rotational shear at $\gamma_{app} = 10^{-1}$ s$^{-1}$ in (b-i), where the displacement was visualized with food dye after an initial stationary state at 100 min, (b) different pathways (i–iii and i') of the apparent shear rate $\gamma_{app}$ with elapsed measurement time, (c) flow curves (i–iii and i') obtained from the rotational rheometer, $\tau_{app}$, profiles with respect to the measurement time which are the same as (d) (b-i') and (e) (b-iii).

has similar rheological characteristics to Mt dispersion we used. From the result (Fig. 7 in [5]), shear stresses change and converge a certain equilibrium value; however, there exist nonlinear displacements in the shear strain.

Four rheological measurements were conducted along two different pathways (i-ii-iii and $i_0$) of shear-rate variations as shown in Fig. 5.9(b): (i) shear rates gradually increased in 5 s steps from $10^{-1}$ to $10^{2}$ s$^{-1}$; (ii) rotation speeds gradually decreased in 5 s steps from $10^{2}$ to $10^{-1}$ s$^{-1}$ immediately after measurement (i); (iii) rotation speed maintained constant at $10^{1}$ s$^{-1}$; (i') rotation speed maintained constant at $10^{1}$ s$^{-1}$ after leaving at rest for 100 min to be free from shear history effect. The shear rates in (i) and (ii) were applied with stepwise increment or decrement indicated in Fig. 5.6(a).

The progress of the measurements for each flow curve obtained along the different pathways (i)–(iii) and (i') are indicated by arrows in Fig. 5.9(c). Comparing the curves in (i) and(ii), they trace different histories of the flow curve, showing that the rheological properties of the Mt dispersions show hysteresis. Immediately after measurement in (ii), the Mt dispersion was measured at a constant shear rate $\dot{\gamma}_{app} = 10^{1}$ s$^{-1}$ (iii), and the resulting flow curve shows time elapse changes. The shear stresses $\tau_{app}$ in (iii) decrease gradually with time. However, it does not reach the $\tau_{app}$ value obtained in (ii) at the same value of $\dot{\gamma}_{app}$ but takes a value around $10^{1}$ Pa, a larger shear stress than that obtained in (ii). In (i'), assuming free from shear history effect at the initial condition, $\tau_{app}$ also has no coincidence with that in (ii) at the same $\dot{\gamma}_{app}$.

To clarify the time-dependent change of flow curve in (i') and (iii), time profiles of the $\tau_{app}$ along the pathways are

investigated. As shown in Fig. 5.9(d), $\tau_{app}$ in (i') quickly converges to the value somewhat smaller than that in (i) at the same $\dot{\gamma}_{app}$. As shown in Fig. 5.9(e), time variations of $\tau_{app}$ in (iii) seem to be saturated in the duration time converging to an equilibrium state. The former indicates shear-thinning with time, and the latter may reflect recovery effect of the particle networks in the Mt dispersions due to spending sufficiently long time under relatively weak shear along the pathway (ii).

From these measurements in the Mt dispersions, we speculate that the shear-rate profiles in the gap of the rheometer does not satisfy the linear shapes but in different shapes depending on elapsed time and shear history, which may be influenced by various conditions, including the gap $h$ between the disks, the loading shear stress, and others. As we mentioned in §5.1.1 (see Fig. 5.1), unexpected phenomena, such as in the shear history, the wall-slip, or shear localization and others, may occur simultaneously in combination. Especially in the case of fluids with time-dependency, the conventional rheometer is limited to measure specific-rheological responses corresponding to the measurement condition. Thus, especially in such thixotropic fluids, the flow curves obtained from the rotational rheometer do not always provide correct evaluations without influences from shear localization, wall-slip, and others, even if the shear stress seems to reach equilibrium states.

#### 5.3.3.2 Rheological evaluations using USR

The rheology of Mt dispersions may be subject to shear localization or shear history as investigated in §5.3.3.1. From our previous investigation of the time-dependence and shear history of Mt dispersions [Chapter 3], oscillation periods that are sufficiently long to achieve the equilibrium state are approximately equal to $tf_o = 1500$. In this section, the rheological evaluations of the Mt dispersions were conducted after an adequate time of oscillating of the cylindrical container to ensure attainment of a specific state of equilibrium condition between the time-dependent recovery and breakup the particle networks.

The azimuthal velocity distributions of the Mt dispersions were obtained as shown in Fig. 5.10(a). The distribution was transformed from the measured velocity fluctuations using UVP considering Eq. (5.1). Here, the parameters ($f_o$, $\Theta$) were properly chosen to realize the one-directional flow. The experimental conditions are detailed in Table 5.1. The momentum propagates from the wall to the center of the cylinder as instantaneous velocity fluctuations with a phase lag. Here, the phase lag in velocity fluctuations is decreasingly smaller close to $r/R \approx 0.7$, and for $r/R < 0.7$, no considerable phase difference in the radial direction is observed. Using DFT, the real and imaginary parts of the azimuthal velocity distributions were calculated [Fig. 5.10(b)]. The profiles also show very small variations in the phase difference. Figures 5.10(c) and 5.10(d) show the contours of $F(\mu, \delta)$ calculated by Eq. (5.11) at $r/R \approx 0.9$ and 0.65, respectively. These are very different in the $\mu - \delta$ coordinates showing minimum values. This difference indicates that the rheological characteristics of Mt dispersions change very much with the applied shear rate.

In the same way as the analytical procedure in §5.2.2, 2D histograms in $\dot{\gamma}_{eff}$ and $\mu$ [Fig. 5.11(a)], $\dot{\gamma}_{eff}$ and $\delta$ [Fig. 5.11(b)], and $\dot{\gamma}_{eff}$ and $\tau_{eff}$ [Fig. 5.11(c)] were counted from the 200 times of the measurements of USR. The (i) solid, (ii) dashed, and (iii) dotted curves indicate $\tau_{app}(\dot{\gamma}_{app})$ obtained from the parallel-disk rotational rheometer. The $\mu(\dot{\gamma}_{eff})$ result indicates a decreasing tendency as $\dot{\gamma}_{eff}$ increases [Fig. 5.11(a)], and it has a bending point at $10^0 < \dot{\gamma}_{eff} < 10^1$ s$^{-1}$. This histogram shows a very large difference from results obtained by the rheometer (i–iii).

One possible explanation for such a difference is that there are influences on the torque measurements reflecting shear banding or localization. This is supported by the fact that the visualization inside the gap could not be assumed as linear shear deformation. The visualization of food dye shown in Fig. 5.9(a) displays deformation at the edge of the disk. Since the shear rate is the biggest at the edge, it is speculated that fluid deformations inside the disks could be a stronger influence than at the edge. Moreover, as indicated in Fig. 5.1, the shear banding or localized influence may appear both in the axial direction of the rotational plates and in the radial direction. If this is the case, the influence from inadequacies in the assumption would lead to significant measurement errors considering integration of these differences arising from the assumptions made.

As indicated in Fig. 5.11(b), a three-phase region can be observed from the histogram of $\delta(\dot{\gamma}_{eff})$. At 5 s$^{-1}$ < $\delta(\dot{\gamma}_{eff})$, $\delta(\dot{\gamma}_{eff})$ reaches $\pi/2$ representing the rheological characteristics as trends of viscous behavior. At 0.5 s$^{-1}$ < $\delta(\dot{\gamma}_{eff})$ < 5 s$^{-1}$, the histogram of $\delta(\dot{\gamma}_{eff})$ is slightly smaller than that at 5 s$^{-1}$ < $\delta(\dot{\gamma}_{eff})$. At $\delta(\dot{\gamma}_{eff})$ < 0.5 s$^{-1}$, the histogram of $\delta(\dot{\gamma}_{eff})$ suggests very large changes. To confirm the relationship between the obtained result and flow behavior, the shear deformations of Mt dispersions are visualized by the azimuthal velocity profiles considering the geometric calculations [Fig. 5.11(d)]. The three-phase regions described in Fig. 5.11(b) correspond to Fig. 5.11(d). From these visualized images, no deformation is observed in the gel region, contrary to the large deformation observed in the sol regions. This suggests sudden rheological changes in radial direction of the cylinder. Overall, the CMC solution results using USR in §5.3.2.2 are in good agreement with the parallel-disk rotational rheometer, the rheological evaluations of Mt dispersions indicate large difference between USR and the parallel-disk rotational rheometer.

The $\tau_{eff}$ calculated from $\mu$ and $\delta$ is shown in Fig. 5.11(c). The minimum value of $\tau_{eff}$ is estimated on approximately 0.3 Pa at the shear rate $\dot{\gamma}_{eff} \approx 1$ s$^{-1}$. From the result of $\delta(\dot{\gamma}_{eff})$ and the visualizations as mentioned above, the minimum $\tau_{eff}$ represents

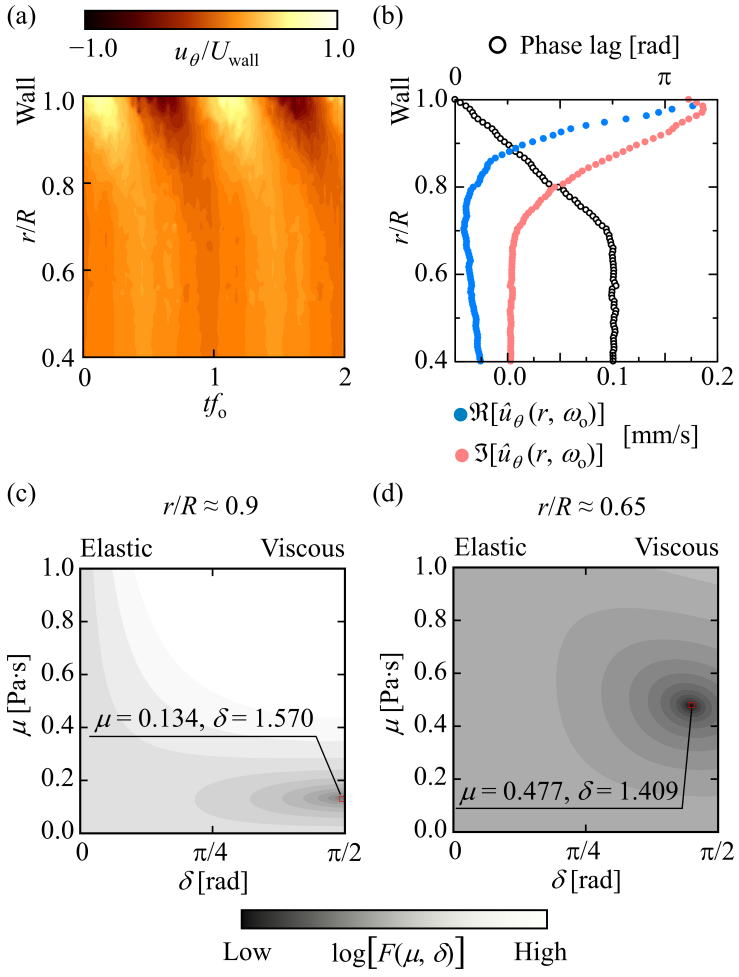


Figure 5.10: (a) Azimuthal velocity distributions for two oscillation periods, $tf_o = 2$, measured using UVP in 4.0 wt.% Mt dispersion with 0.02 mol/L NaCl after $tf_o > 1500$ from start of oscillations, with the wall angular velocity $U_{\mathrm{wall}} = 477.0$ mm/s, (b) magnitudes of real and imaginary components of $\hat{u}_\theta$ at the oscillation frequency $\omega = \omega_o (= 2\pi f_o)$ (closed circle) and phase lag calculated from the magnitudes of Fourier components (open circle), and $\mu$–$\delta$ distributions of the cost function $F(\mu, \delta; r)$ in (c) $r/R = 0.9$ and (d) 0.65.

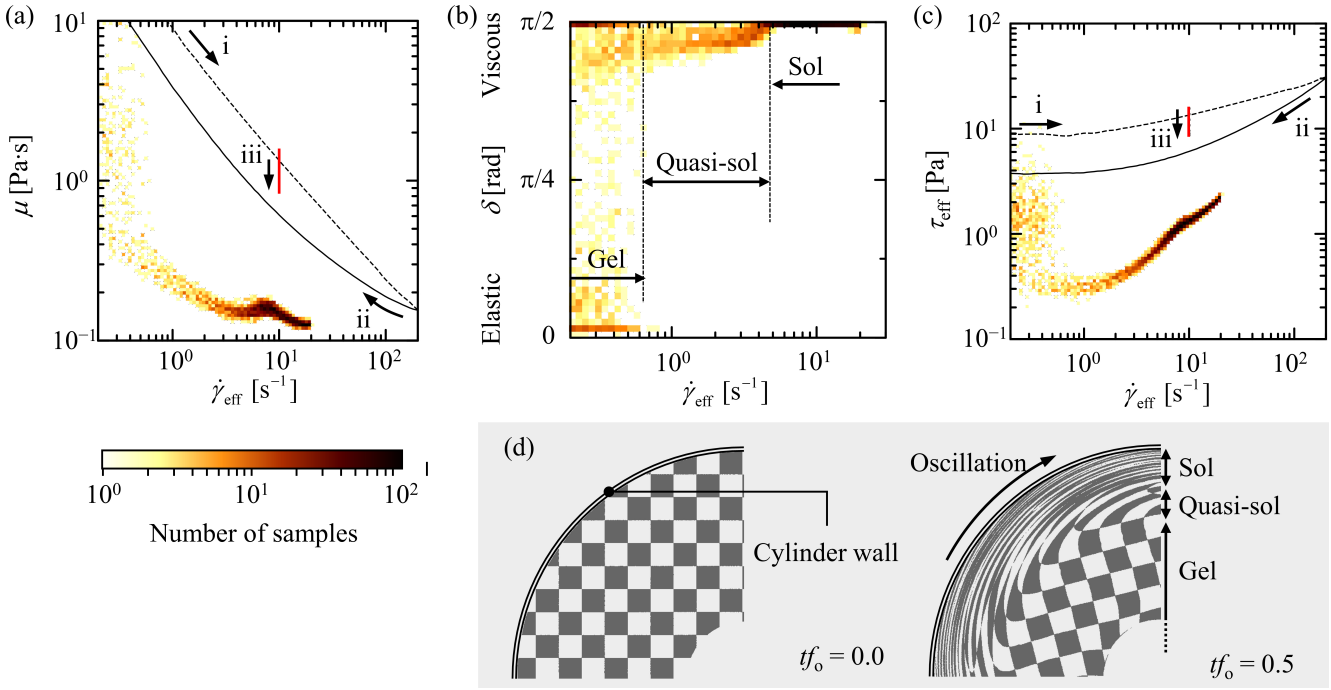


Figure 5.11: 2D histograms plotting 200 samples for the 2-s rheological measurements calculated by counting all of profiles (200 times); profiles of (a) $\mu$, (b) $\delta$, and (c) $\tau_{\text{eff}}$ with $\dot{\gamma}_{\text{eff}}$ in 4.0 wt.% Mt dispersion with 0.02 mol/L NaCl, where the broken (i), solid (ii), and dotted lines indicate measured results using the parallel-disk rotational rheometer shown in Fig. 5.9, (d) representations of deformations of Mt dispersion visualized by azimuthal velocity profiles at $tf_o = 0.5$; $f_o = 0.5$ Hz, $\Theta = 2\pi/3$ rad, and $U_{\text{wall}} = 477.0$ mm/s.

the yield stress of the Mt dispersion. Hence, this trend of the histogram was different from the results of the rheometer like in Fig. 5.11(a), and the differences in shear stress are $O(10$ Pa) at the maximum. As in the unsatisfactory condition for the rheometer mentioned above, flow curves (i–iii) are specific responses corresponding to the measurement conditions. Thus, the histogram of $\tau_{\text{eff}}$ shows flow curves of the Mt dispersions more accurately than the flow curves using the parallel-disk rotational rheometer.

#### 5.3.3.3 Rheological measurements of time-dependence in Mt dispersion

In §5.3.3.2, experiments for Mt dispersions were conducted by USR after reaching the equilibrium state between the time-dependent recovery and breaking up of the particle networks. As a further step in USR rheological evaluations here for time-dependent properties, evaluations of spatial profiles in individual oscillation cycles of period $O(1$ s) were performed for the transient rheology of Mt dispersions. This has importance to evaluate efficacy of USR, because time-dependent recovery and breaking up would be reflected on instantaneous velocity profiles that are analyzed to obtain instantaneous-rheological properties in USR.

By UVP, the instantaneous velocity fluctuations were measured for long-oscillation periods equal to 450 s to evaluate spatiotemporal profiles of rheological properties as shown in Figs. 5.12(a)–5.12(c). The velocity profiling was performed immediately after stirring the Mt dispersions to place the particle networks into intermediate states between the states of gelling and breaking up of the network structures. The rheological properties of the dispersions change with elapsed time as mentioned in §5.3.3.1, and there are time developments in the velocity fluctuations in the results in Figs. 5.12(a)–5.12(c), that show equilibrium states of the flow behaviors corresponding to the oscillations. This was also investigated in Chapter 2 and 3, and the rheological characteristics were qualitatively evaluated from the phase lag of the velocity fluctuations.

Following the procedures in §5.2.3, the rheological properties were evaluated as a function of time and shear strain rate, $\mu(\dot{\gamma}_{\text{eff}}, t)$, $\delta(\dot{\gamma}_{\text{eff}}, t)$, and $\tau_{\text{eff}}(\dot{\gamma}_{\text{eff}}, t)$ as depicted in Figs. 5.13(a)–5.13(c). Here, the determination of $\mu$, $\delta$, $\dot{\gamma}_{\text{eff}}$, and $\tau_{\text{eff}}$ was as outlined in §5.2.2. The color of the plots indicates spin-cycles, $tf_o$, and $tf_o = 0$ is the start of the velocity profiling immediately after the stirring of the Mt dispersions.

As shown in Fig. 5.13(a), immediately after starting the oscillations, $\mu(\dot{\gamma}_{\text{eff}})$ appears with a monotonic decrease, shown

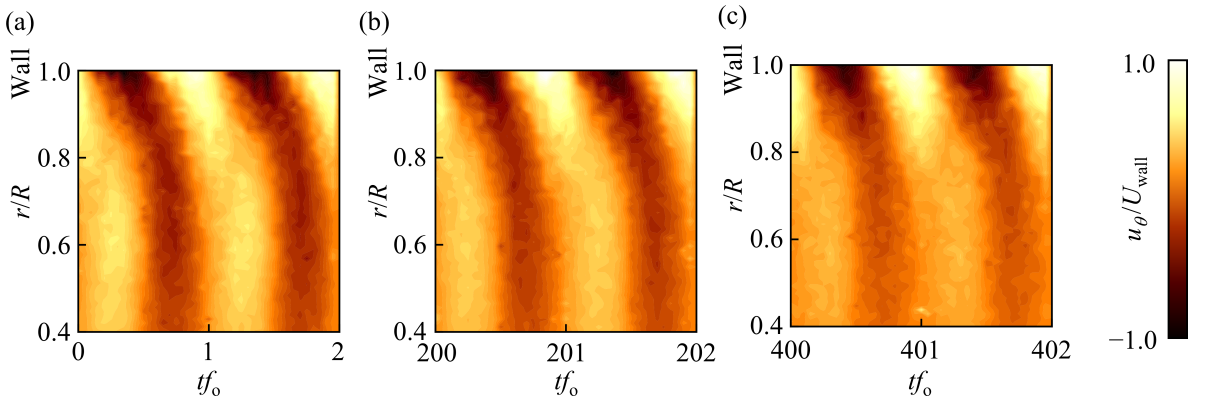


Figure 5.12: Azimuthal velocity distributions after different oscillation periods tfo measured using UVP in 4.0 wt.% Mt dispersion with 0.02 mol/L NaCl without recovery time left at rest; (a) immediately after starting oscillations, (b) after $tf_o = 200$, and (c) after $tf_o = 400$, where the wall angular velocity $U_{wall} = 357.8$ mm/s.

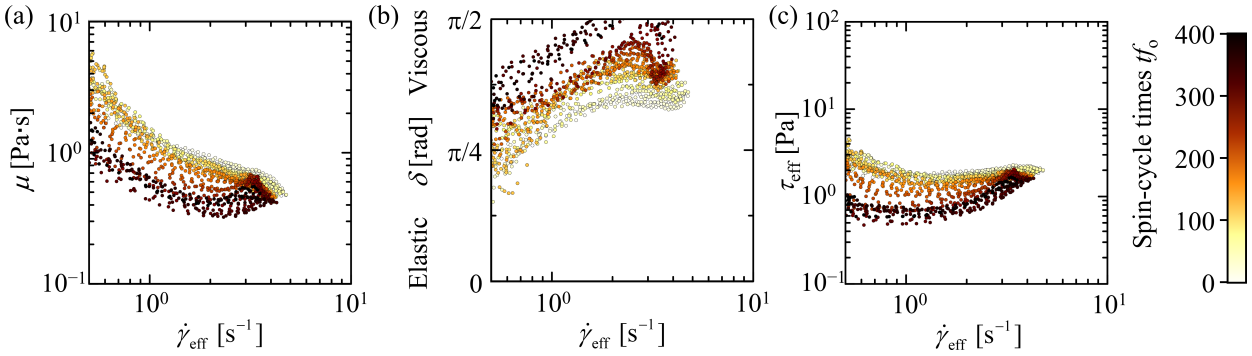


Figure 5.13: Linear viscoelasticity of Mt dispersions evaluated from short-time velocity profiles for 2-s, where (a) $\mu$, (b) $\delta$, and (c) $\tau_{eff}$ in $\dot{\gamma}_{eff}$ profiles; $f_o = 1.0$ Hz, $\Theta = \pi/4$ rad, and $U_{wall} = 357.8$ mm/s.

by the brighter plots. With $tf_o$, $\mu(\dot{\gamma}_{eff})$ gradually decreases approaching an equilibrium state in the whole of the $\dot{\gamma}_{eff}$ region. At $tf_o = 400$, there are two divided regions at $\mu(\dot{\gamma}_{eff})$ ($\dot{\gamma}_{eff} < 10^0$ s$^{-1}$), monotonically decreasing and constant regions. As in these results, the viscosity decreases with the oscillation duration also after initiating stirring of the fluids. From Fig. 5.13(b), immediately after the start of oscillations, $\delta(\dot{\gamma}_{eff})$ is smaller than $3\pi/8$ in the whole range of $\dot{\gamma}_{eff}$. Then, $\delta(\dot{\gamma}_{eff})$ increases and approaches $\pi/2$ with $tf_o$.

The rheological behavior of the Mt dispersion immediately after discontinuing the stirring shows the fluid to be more viscoelastic than that at the equilibrium state. As mentioned in Chapter 3, the viscoelastic characteristics result from microscopic structures maintained by the particle networks even after strong stirring. The reason why the viscoelastic characteristics gradually shift to viscous is that the particle networks break up and align by the unsteady oscillations. Considering linear viscoelasticity, the particle networks of the Mt dispersions play a role in the viscoelastic characteristics even if the gelled structures are made to yield by stirring as they are in an incomplete breakup state.

In Fig. 5.13(c), $\tau_{eff}(\dot{\gamma}_{eff})$ was calculated for each of the spin-cycle periods. Immediately after the start of the oscillations, $\tau_{eff}(\dot{\gamma}_{eff})$ is in a positive-low-gradient state at $10^0$ s$^{-1}$ < $\dot{\gamma}_{eff}$ , which means that it is subject to a strong viscous response. Then as with $\mu$ and $\delta$, $\tau_{eff}(\dot{\gamma}_{eff})$ gradually converge to an equilibrium state with $tf_o$.

From the results in Figs. 5.13(a)–5.13(c) representing the rheological properties at every $tf_o = 2$, the gradual changes in rheological characteristics of the dispersions due to breaking up or restoration of the particle networks were observed. The rheological characteristics with time-dependency may not be determined with the parallel-disk rotational rheometer because of the hysteresis of the dispersions during the measurements as mentioned in §5.3.3.1. This is of great importance, suggesting that the $\tau_{eff}(\dot{\gamma}_{eff})$ may represent novel flow curves as in the "time function". This experimental finding is significant in that USR has possibility to provide the flow curve for complex fluids with time-dependent rheological properties.

## 5.4 Efficacy of USR as a complementary technique

Through comparative experiments with the parallel-disk rotational rheometer, and from insights obtained in the previous work, the advantages and limitations in the range of application of USR are summarized in Table 5.2. The relations between the USR and typically available rheometers are evaluated by comparing the different advantages and limitation with exemplifications. There are two points of the significant complementary relations to note from the comparisons.

Table 5.2: Comparison of advantages and limitations for the conventional shear rheometer and USR.

| | **Conventional shear rheometer** | | **Ref.** |
|---|---|---|---|
| **Advantages** | · Small amount $O$(1 mL) of test material | §5.3.1 | ———— |
| | · Use in higher viscosities than $O(10\ \mathrm{Pa}\cdot\mathrm{s})$ | — | [34] |
| | · Adjustments for viscous layer thicknesses by the gap $h$ | — | [35] |
| **Limitations** | · Difficulties of application to non-linear behaviors | §5.3.3.1 | [36] |
| | · Approximation of apparent $\tau$ and $\dot{\gamma}$ values | §5.3.1 | ———— |
| | · Unsuitable for long-duration measurements | §5.3.3.1 | ———— |
| | **Ultrasonic spinning rheometry (USR)** | | **Ref.** |
| **Advantages** | · Evaluations including wall-slip, shear localization, etc | §5.3.3.2 | Chapter 3 |
| | · Local rheological evaluations; $O$(1 mm) | §5.2.2 | Chapter 4 |
| | · Sustainable long-duration measurements | §5.3.2.2 | Chapter 2 |
| **Limitations** | · Large amount $O$(1 L) of test material | §5.2.1 | ———— |
| | · Limitations of the given $\dot{\gamma}_{\mathrm{eff}}$ due to $\Delta t$, $\Delta r$, and $\Delta u_\xi$ | §5.4 | Chapter 2 |
| | · Optimization by oscillation parameters; $(\nu/2\omega_\mathrm{o})^{1/2}$ | | ———— |

Because of the measurement principles, evaluating momentum propagations, the applicable range on viscosity of USR is determined by the thickness of the viscous layer in the fluid flows. When the test fluids show a specific kinematic viscosity $\nu$, a radius $R$ of the cylinder that is larger than $(\nu/2\omega_\mathrm{o})^{1/2}$ is required. From practical issues on the ultrasonic measurement, the radius $R$ and oscillation frequency fo are limited in $O(10^2$ mm), and less than $O$(10 Hz) because of attenuation and divergence of ultrasonic wave and sampling rate of UVP measurements. In cases of higher viscosity than $O(10^2\ \mathrm{Pa}\cdot\mathrm{s})$, the radial gradient of the velocity would be too small to extract information for rheological evaluations. For such high viscous fluids, however, the influence of unknown velocity profiles, e.g., the shear localization or banding, would be negligible for the use of conventional rheometers. Overall, it may be concluded that there exists complementarity between conventional shear rheometers and USR.

For the reliability of rheological evaluations with non-Newtonian fluids, the rheological evaluations using typical rheometers cannot always be ensured to be accurate due to unexpected phenomena. Considering the results in this paper, the rheological properties of the Mt dispersion simply establishes a boundary of physical properties versus unsteady shear deformations. The reason why these problems occur lies in the appearances of spatial distributions of the rheological properties due to the shear-rate-dependence. In such cases, rheological evaluations with conventional rheometers would not be reliable. Here, USR can execute the rheological evaluations including accounting for any unexpected phenomena, so USR has clear advantages over conventional rheometers. From the results of CMC solutions, the rheological evaluations of USR agree well with those of conventional rheometers. This strongly supports the reliability of the linear viscoelastic analysis with USR for non-Newtonian fluids, even though the fine torque measurements in the conventional rheometers can provide more accurate evaluations than USR in cases that the assumptions are satisfied.

Finally, we should state here about limitations on USR arising from UVP measurements and the oscillating flow system for practical use of USR. The maximum range of the shear stress $\dot{\gamma}$ applied in USR is determined by the wall velocity of cylinder, $U_\mathrm{wall} = 2\pi f_\mathrm{o} R\Theta$, and rheological properties of the test fluids themselves. In addition to the limitations on $R$ and fo mentioned above, setting large amplitude of the oscillations, $\Theta$, may cause secondary flows in the cylinder. It may affect momentum propagations evaluated in USR, where the azimuthally directional flow is assumed to be dominant. Heightening of the cylinder can relax the influence of secondary flows, but not perfect. On the other hand, the minimum range of $\dot{\gamma}$ has no limitation in theory, because of distributions of $\dot{\gamma}$ from the maximum value at the wall to zero at the center of the cylinder. But in practical use, central region is not applicable, because of averaging effects due to considerably large measurement volume, and velocity resolution of UVP. Enlargement of $R$ and $U_\mathrm{wall}$, therefore, do not ensure widening the range of the shear stress. As the final point, the minimum size of the cylindrical vessel is also restricted; large curvature of the cylinder wall does not allow transmitting the ultrasonic wave into the test fluid. It is, therefore, not avoidable that considerably large amount of the test fluid is required in USR.

## 5.5 Conclusion

For Newtonian fluids, the linear viscoelastic analysis of USR was validated by statistics on multiple measurements, and the efficacy of USR for typical Newtonian fluids was proven. Even if the rheological evaluations are calculated from two-cycle-data (2-s), these offer high accuracy and precision avoiding noise amplifications.

As a further step with the USR, the efficacies for non-Newtonian fluids were clarified by experiments comparing a conventional rheometer with parallel-disk geometry. For the CMC solution, the rheological evaluations of USR agree well with those of the parallel-disk rotational rheometer. In addition, from visualization of the state of the solution with the parallel disks, we observed linear displacements during the onset of the rotation experiments. Therefore, USR proves the precision of the rheological evaluations if the conventional rheometer can measure the properties with precision. However, in the case of Mt dispersion, entirely different flow curves between USR and the rheometer were obtained. From the dye displacement of the dispersion [Fig. 5.9(a)], nonlinear displacements were observed at the onset of experiments, which was quite different from the visualization of the CMC solution [Fig. 5.6(c)].

One of the problems in the conventional rheometer is due to uncertainty in nonlinear shear deformations during the experiments. Instead, from the greater advantages on USR, the "local" rheological properties can be evaluated without any uncertainty of the deformations. Considering the advantages and limitations on conventional rheometers and USR, USR can be expected to offer complementary rheometry together with conventional rheometers on evaluations of non-Newtonian characteristics.

## References


[1] W. Wolthers, M. H. G. Duits, D. Van Den Ende, and J. Mellema, "Shear history dependence of the viscosity of aggregated colloidal dispersions," J. Rheol. 40, 799–811 (1996).

[2] M. Ito, Y. Yoshitake, and T. Takahashi, "Shear-induced structure change in shear-banding of a wormlike micellar solution in concentric cylinder flow," J. Rheol. 60, 1019–1029 (2016).

[3] C. J. Dimitriou, L. Casanellas, T. J. Ober, and G. H. Mckinley, "Rheo-PIV of a shear-banding wormlike micellar solution under large amplitude oscillatory shear," Rheol. Acta. 51, 395–411 (2012).

[4] G. Ovarlez, S. Rodts, X. Chateau, and P. Coussot, "Phenomenology and physical origin of shear localization and shear banding in complex fluids," Rheol. Acta 48, 831–844 (2009).

[5] O. Nechyporchuk, M. N. Belgacem, and F. Pignon, "Rheological properties of micro-/nanofibrillated cellulose suspensions: Wall-slip and shear banding phenomena," Carbohydr. Polym. 112, 432–439 (2014).

[6] T. Divoux, M. A. Fardin, S. Manneville, and S. Lerouge, "Shear banding of complex fluids," Annu. Rev. Fluid Mech. 48, 81–103 (2016).

[7] P. Fischer, E. K. Wheeler, and G. G. Fuller, "Shear-banding structure orientated in the vorticity direction observed for equimolar micellar solution," Rheol. Acta 41, 35–44 (2002).

[8] S. Manneville, "Recent experimental probes of shear banding," Rheol. Acta 47, 301–318 (2008).

[9] Y. L. Yeow, W. C. Ko, and P. P. Tang, "Solving the inverse problem of Couette viscometry by Tikhonov regulation," J. Rheol. 44, 1335–1351 (2000).

[10] C. Ancey, "Solving the Couette inverse problem using a waveletvaguelette decomposition," J. Rheol. 49, 441–460 (2005).

[11] *Ultrasonic Doppler Velocity Profiler for Fluid Flow*, Springer Science, edited by Y. Takeda (Springer, Tokyo, 2012).

[12] B. Derakhshandeh, D. Viassopoulos, and S. G. Hatzikiriako, "Thixotropy, yielding and ultrasonic Doppler velocimetry in pulp fibre suspensions," Rheol. Acta 51, 201–214 (2012).

[13] B. Ouriev, and E. Windhab, "Transient flow of highly concentrated suspensions investigated using the ultrasound velocity profiler–pressure difference method," Meas. Sci. Technol. 14, 1963–1972 (2003).

[14] J. Wiklund, and M. Stading, "Application of in-line ultrasound Doppler-based UVP–PD rheometry method to concentrated model and industrial suspensions," Flow Meas. Instrum. 19, 171–179 (2008).

[15] T. Gallot, C. Perge, V. Grenard, M. A. Fardin, N. Taberlet, and S. Manneville, "Ultrafast ultrasonic imaging coupled to rheometry: Principle and illustration," Rev. Sci. Instrum. 84, 045107 (2013).

[16] C. Perge, N. Taberlet, T. Gibaud, and S. Manneville, "Time dependence in large amplitude oscillatory shear: A rheo-ultrasonic study of fatigue dynamics in a colloidal gel," J. Rheol. 58, 1331–1357 (2014).

[17] A. Gurung, J. Haverkort, S. Drost, B. Norder, J. Westerweel, C. Poelma, "Ultrasound image velocimetry for rheological measurements," Meas. Sci. Technol. 27, 094008 (2016).

[18] C. Poelma, "Ultrasound imaging velocimetry: A review," Exp. Fluids 58, 3 (2017).

[19] F. Rodrigez-Gonzalez, J. Perez-Gonzalez, L. De Vargas, and B. M. Marin-Santibane, "Rheo-PIV analysis of the slip flow of a metallocene linear low density polyethylene melt," Rheol. Acta 49, 145–154 (2010).
[20] J. Perez-Gonzalez, J. J. Lopez-Duran, B. M. Marin-Santibanez, and F. Rodriguez-Gonzalez, "Rheo-PIV of a yield-stress fluid in a capillary with slip at the wall," Rheol. Acta 51, 937–946 (2012).
[21] S. Jarny, N. Roussel, S. Rodts, F. Bertrand, R. Le Roy, and P. Coussot, "Rheological behavior of cement pastes from MRI velocimetry," Cement Concrete Res. 35, 1873–1881 (2005).
[22] G. Ovarlez, F. Bertrand, and S. Rodts, "Local determination of the constitutive law of a dense suspension of noncolloidal particles through magnetic resonance imaging, " J. Rheol. 50, 259–292 (2006).
[23] L. M. Quinzani, R. C. Armstrong, and R. A. Brown, "Use of coupled birefringence and LDV studies of flow through a planar contraction to test constitutive equations for concentrated polymer solutions," J. Rheol. 39, 1201–1228 (1995).
[24] J. P. Rothstein, and H. M. Gareth, "Inhomogeneous transient uniaxial extensional rheometry," J. Rheol. 46, 1419–1443 (2002).
[25] T. Shiratori, Y. Tasaka, Y. Murai, and Y. Takeda, "Development of ultrasonic visualizer for capturing the characteristics of viscoelastic fluids," J. Vis. 16, 275–286 (2013).
[26] T. Shiratori, Y. Tasaka, Y. Oishi, and Y. Murai, "Ultrasonic velocity profiling rheometry based on a widened circular Couette flow," Meas. Sci. Thechnol. 26, 085302 (2015).
[27] Y. Tasaka, T. Kimura, and Y. Murai, "Estimating the effective viscosity of bubble suspensions in oscillatory shear flows by means of ultrasonic spinning rheometry," Exp. Fluids 56, 1867 (2015).
[28] T. Shiratori, Y. Tasaka, and Y. Murai, "Rapid rheological characterization of viscoelastic fluid based on spatiotemporal flow velocimetry," Exp. Therm. Fluids Sci. 71, 1–13 (2016).
[29] T. Yoshida, Y. Tasaka, H. J. Park, Y. Murai, H. Teramura, and S. Koseki, "Inner structure visualization of fresh fruits utilizing ultrasonic velocity profiler," J. Vis. 21, 253–265 (2018).
[30] A. Benchabane, and K. Bekkour, "Rheological properties of carboxymethyl cellulose (CMC) solutions," Colloid Polym. Sci. 286, 1173–1180 (2008).
[31] N. Cruz, and Y. Peng, "Rheology measurements for flotation slurries with high clay contents—A critical review," Miner. Eng. 98, 137–150 (2016).
[32] H. A. Barnes, "Thixotropy—A review," J. Non-Newtonian fluids Mech. 70, 1-33 (1997).
[33] S. Abend, and G. Lagaly, "Sol–gel transitions of sodium montmorillonite dispersions," Appl. Clay Sci. 16, 201–227 (2000).
[34] A. Namiki, and Y. Tanaka, "Oscillatory rheology measurements of particle-and bubble-bearing fluids: Solid-like behavior of a crystal-rich basaltic magma," Geophys. Res. Lett. 44, 8804–8813 (2017).
[35] G. Davies, and J. Stokes, "Thin film and high shear rheology of multiphase complex fluids," J. Nonnewton. Fluid Mech. 148, 73–87 (2008).
[36] A. Magnin, and J. Piau, "Shear rheometry of fluids with a yield stress," J. Nonnewton. Fluid Mech. 23, 91–106 (1987).

Chapter 6

# Effective viscoelasticity of non-Newtonian fluids modulated by large-spherical particles aligned under unsteady shear

## Contents


**6.1 Introduction** . . . . . **86**
**6.2 Method: Ultrasonic spinning rheometry (USR)** . . . . . **87**
6.2.1 Experimental setup and theoretical basis . . . . . 87
6.2.2 Experimental conditions . . . . . 89
**6.3 Experimental results of the linear viscoelastic analysis** . . . . . **90**
6.3.1 Rheological evaluations of test fluids without dispersed particles . . . . . 90
6.3.2 Rheological evaluation of silicone oil with dispersed particles . . . . . 91
6.3.3 Rheological evaluation of the PAM solution with dispersed particles . . . . . 93
6.3.4 Rheological evaluation of the CMC solution with dispersed particles . . . . . 94
**6.4 Discussion** . . . . . **96**
6.4.1 Verification of dominant factors of the alignment using a toy model . . . . . 96
6.4.2 Macro-rheological characteristics modulated by alignments . . . . . 98
**6.5 Conclusion** . . . . . **100**
**References** . . . . . **100**


## Preface

The aim in this chapter is to prove the capability of the kinematic rhometry to elucidate the unexplained phenomena which occurs when using a standard rheometer due to the limitation of methodology. As the target, effective viscoelasticity of non-Newtonian fluids as macro rheology is evaluated, and is modulated by the alignment of spherical particles that is closely related to the relaxation time of fluid media. This work was published in Yoshida *et al.*, Phys. Fluids (2019).

## Abstract


The effective viscoelasticity of non-Newtonian fluids with spherical particles has been examined by ultrasonic spinning rheometry [Yoshida *et al.*, J. Rheol. 63 (2019)]. Under unsteady shear flows, the dispersed particles make alignments in the sheared direction if the relaxation time of the fluid media is sufficiently long. The alignments modulate the effective rheological properties, and the effective viscosity does not reach the value estimated by Einstein's law; the effective elasticity increases significantly with increasing volume fraction in the bulk of the measurement volume. To establish further details of factors influencing the aligned particles under unsteady shear flows/deformations, numerical tests using a simple toy model assuming dispersed particles combined by spring forces considering yield stresses were conducted, and the model identified the importance of the relaxation process on the orientation of the particles. Finally, considering the experimental findings, local and macro rheological characteristics are strongly modulated by the particle alignment when the test fluid media have long relaxation times (or high Weissenberg numbers).

## 6.1 Introduction

In fluid mechanics, an understanding of the rheological properties of dispersive multi-phase fluids is of great importance to control and predict flow behaviors. To evaluate the bulk viscosity in control volumes of multi-phase fluids, the "effective viscosity" in dilute solid particle suspensions, $\mu^*$, can be theoretically derived as

$$\eta = \frac{\mu^*}{\mu} = 1 + \frac{5}{2}\phi, \tag{6.1}$$

where $\eta$, $\mu$, and $\phi$ denote the relative viscosity, the viscosity of the dispersing fluid media, and the volume fraction of particles dispersed in the media [1]. This formula is based on important conditions: (i) a steady simple shear flow, (ii) a low shear rate, i.e. satisfying Stokes's law, (iii) sufficiently low volume fractions ($\phi < 0.1$), (iv) perfectly spherical particles, and (v) neutrally buoyant particles. For more concentrated particle conditions, Eq. (6.1) is extended to an exponential form considering interactions between the dispersed particles [2]. Some formulae have been proposed to describe the viscosity of concentrated suspensions with parameters determined empirically or semi-empirically [3–5]. Subsequently, these attempts were theoretically substantiated by Frankel and Acrivos [6]. Several fundamental parameters of rheology for particle suspensions in Newtonian fluids have also recently been investigated (e.g. [7–9]).

Compared with the Newtonian fluids, the effective rheological properties in non-Newtonian fluids with dispersed particles are highly complex making it difficult to estimate the properties by theoretical considerations alone, as it is not possible to ensure that the important assumptions detailed above are fully considered. The orientation of particles dispersed in viscoelastic fluid flows in the sheared direction have been reported by experimental and numerical approaches [10–17]; Joseph *et al.* [10] found that there is a critical distance between the initial positions of each particle that enables the formation of particle strings in a viscoelastic fluid. Lyon *et al.* [11] reported experimental results on the evolution of particle microstructures with non-colloidal particles suspended in a viscoelastic medium, and investigated the formation of particle strings corresponding to a quantitative reduction in the simultaneously measured shear stress. Based on this, Scirocco *et al.* [12] investigated factors that lead to the development of string structures for several test fluids with different Weissenberg numbers $Wi$, and found that the critical $Wi$ for the onset of string formation ranges from 0.5 to 16.5, with $Wi$ defined as

$$Wi = \lambda\dot{\gamma}, \tag{6.2}$$

where $\lambda$ and $\dot{\gamma}$ represent the relaxation time of the test fluid and shear strain rate respectively. The $Wi$ describes the viscoelastic characteristics of test fluids, and the two limiting values, $Wi = 0$ and $Wi \to \infty$ reflect viscous and elastic characteristics.

These experimental approaches suggested that development of the particle orientations with time elapsed and the initial distance between particles play important roles. Also related to this, Won and Kim [13] established that shear thinning properties are responsible for the formation of string-like structures even when the driving force enabling the migration of the particles arises from the viscoelasticity in the relaxation of the fluid media. Numerical approaches [14–16] have indicated that the alignments are governed by rheological characteristics, such as the shear-thinning viscosity, relaxation time, shear amplitude, and other parameters even under limitations in the conditions of the steady state and instabilities arising from the initial position of particles.

As above, there has been several reports of triggers to generate the particle alignment in viscoelastic fluids, but no results have ever been reported of rheological evaluations of fluid properties with the particle alignments considered macroscopically. There have been a number of attempts to elucidate the rheological characteristics modified by the particle alignment: Pasquino *et al.* [17] investigated alignment factors with increasing shear rates. The controlling factor here was determined as a measure of the average length of particle strings determined by optical microscopy measurements. Van Loon *et al.* [18] evaluated the local force and torque balance of the rheological response experimentally, based on the aligned particles. In summary, depending on the rheological response of the particle alignment measured, they do not move beyond estimates based on optical observations in the steady shear state and do not involve measurements of mechanical responses because of the geometric limitations of standard torque rheometers. Rheological evaluations under unsteady shear are of great importance for how to deal with the rheology of particle orientation media.

Torque rheometers are not suitable to evaluate rheological properties that are modified by the aligned particles in non-Newtonian fluids because of two issues: (i) the rheometers can only measure the bulk rheology although the particles migrate locally; (ii) common problems, such as shear banding, shear localizations, slipping on the walls, are considerable, especially in multiphase conditions [19–21]. In Chapter 5, the condition of homogeneity of the fluid as one of several assumptions must be satisfied as a prerequisite for ensuring the reliability of rheometer measurements. In the case of dispersed particles in non-Newtonian fluid media, homogeneity may not be maintained due to the gradual migration or changes in the alignment of

the shear direction. Also, alignment phenomena may cause shear localization or jamming in gaps of standard rheometers.

To overcome the limitations of standard rheometers, utilizing spatiotemporal velocity distributions of the fluid motion reflecting all the rheological information of multiphase media is necessary. To respond to this, our group has developed a novel velocity-profiling rheometry, termed ultrasonic spinning rheometry (USR) as explained in Chapters 2–5. The basic concept of this rheometry is that velocity profiles are substituted into the equation of motion to estimate the rheological properties, and details of this will be summarized in §6.2. The efficacy of USR for various complex fluids has already been evaluated in Chapters 2–5. There the USR has been shown to be able to evaluate macro-rheological properties under conditions of the particle alignment in non-Newtonian fluids. The USR can also realize measurements of shear-rate distributions, the radial distribution of $Wi$ in a test fluid layer, and makes it possible to validate conditions to form the particle alignment simultaneously with the evaluation of the rheological properties. These two points are the objectives to be investigated with USR in this study.

In this paper, the conditions for particle alignment are validated through rheological evaluations by the USR on test fluids with three different rheological characteristics: Newtonian, viscoelastic, and pseudoplastic fluids. Next, the macro-rheological properties of particle dispersions of non-Newtonian fluid media with particle alignments were examined, and the effective viscoelasticity changing the bulk volume fraction of the dispersed particles are evaluated (§6.3). In §6.4, we examine numerical assessments of particle alignments under unsteady shear flows by employing a toy model representing spring forces with a known yield stress between dispersed particles. Finally, the rheological characteristics modulated by the aligned particles is discussed based on the experimental findings and with a schematic summary.

## 6.2 Method: Ultrasonic spinning rheometry (USR)

In this section, the experimental setup, theoretical basis, and experimental conditions of the USR are summarized. The process of the validation of the method was presented in the previous research (see Chapters 4 and 5, for details of the efficacy assessments for non-Newtonian fluids) and is omitted here.

### 6.2.1 Experimental setup and theoretical basis

Schematics of the cylindrical test container for the USR is shown in Fig. 6.1, its dimensions are diameter $2R$ = 145 mm and height 60 mm, with an ultrasonic transducer: Ultrasonic velocity profiler (UVP) Model Duo (Met-Flow S. A., Switzerland) was adopted to measure the instantaneous velocity distributions. To obtain the azimuthal velocity component, an ultrasonic transducer (resonance frequency 4 MHz and 5-mm active element diameter) is mounted at a displacement $\Delta y$ from the center coordinate of the container and 45 mm height from bottom of container. At the measurement position, thanks to the optimization of the system including a circular plate set inside the container (see Fig. 6.1), the flow can be assumed as quasi-one directional shear flow For the container oscillating with amplitude $\Theta$ and frequency $f_o$, and axisymmetric flow inside the cylinder can be assumed with a negligibly small radial velocity component, the azimuthal velocity $u_\theta$ is calculated from the geometric relation $u_\theta = u_\xi r/\Delta y$ (a circular disk fixed through a thin shaft is installed to prevent meridional circulation in the cylinder, see Fig. 6.1). Here, the radial position $r$ is calculated with the distance from the transducer $\xi$ by $r^2 = \Delta y^2 + [(R^2 - \Delta y^2)^{1/2} - \xi]^2$. Considering emissions of ultrasonic waves, the ultrasonic beams assume disk-like shapes at each measurement point, growing gradually larger as they propagate. Empirically, based on the results of previous studies, a $\Delta$ = 15 mm was used, and further details of the setup are detailed in Chapter 5.

If the fluid flows in the container are one directional and axisymmetric, the fluid motion obeys Cauchy's equation of motion given as

$$\rho \frac{\partial u_\theta}{\partial t} = \frac{\partial \tau}{\partial r} + \frac{2\tau}{r}, \tag{6.3}$$

where $\rho$ is the density of the test fluids, and $\tau$ represents the shear stress. To describe the relation between $u_\theta$ and $\tau$, Maxwell's model,

$$\tau + \frac{\mu}{E}\frac{\partial \tau}{\partial t} = \mu\left(\frac{\partial u_\theta}{\partial r} - \frac{u_\theta}{r}\right), \tag{6.4}$$

is selected as the simplest expression for the linear viscoelastic characteristics, where $\mu$ and $E$ denote the viscosity and elasticity of the fluid. The USR determines these rheological properties by satisfying Eq. (6.3) under the condition of Eq. (6.4) on the velocity data measured by the UVP. There are computational difficulties arising from noise augmentation in the differential calculations with the experimental data as provided in Eqs. 6.3 and 6.4, this was however successfully overcome to become able to evaluate the rheological properties by adopting an algorithm of viscoelastic analysis in a frequency domain

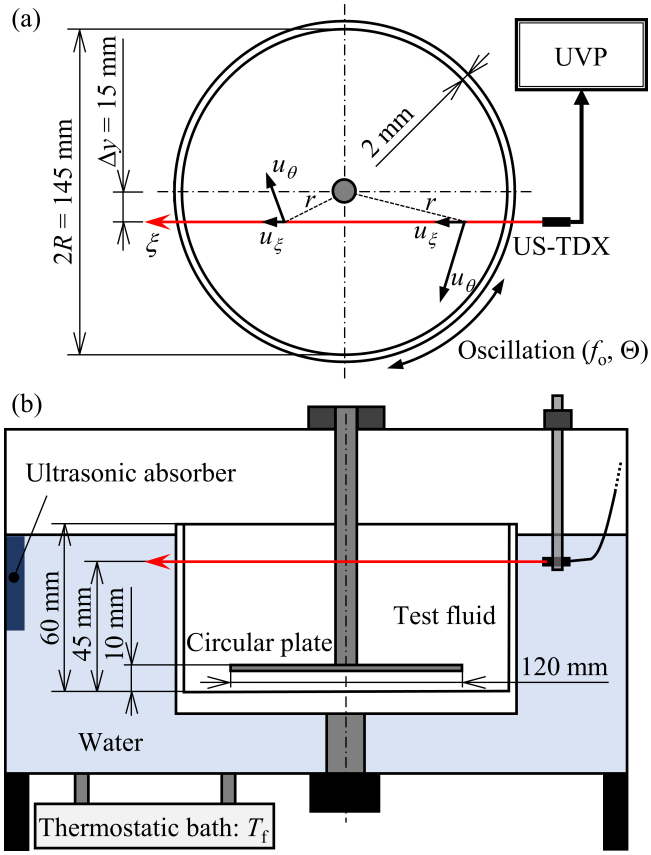


Figure 6.1: Schematic of the experimental setup for capturing oscillating shear flows coupled with an ultrasonic velocity profiler: (a) top view of the rotating cylinder and (b) side view.

[Chapters 4 and 5]. Using the Fourier transform with respect to $t$, Eqs. 6.3 and 6.4 can be modified as

$$i\omega\rho\hat{u}_\theta = \left(\frac{\partial}{\partial r} + \frac{2}{r}\right)\hat{\tau}, \tag{6.5}$$

$$\hat{\tau} + i\omega\frac{\mu}{E}\hat{\tau} = \mu\left(\frac{\partial\hat{u}_\theta}{\partial r} - \frac{\hat{u}_\theta}{r}\right), \tag{6.6}$$

where the Fourier-transformed velocity and shear stress are denoted as $\hat{u}_\theta(r,\omega) = \mathcal{F}[u_\theta(r,t)]$ and $\hat{\tau}(r,\omega) = \mathcal{F}[\tau(r,t)]$ with the angular frequency $\omega$. To determine the $\mu$ and $E$ satisfying the optimization problem, the cost function is given as

$$F(\mu, E; r) = \left| i\omega\rho\hat{u}_\theta - \left(\frac{\partial}{\partial r} + \frac{2}{r}\right)\hat{\tau}\right|^2_{\omega=\omega_o}, \tag{6.7}$$

where the spectrum was adjusted as having a single dominant frequency at the oscillation frequency $\omega = \omega_o (= 2\pi f_o)$.

### 6.2.2 Experimental conditions

Test fluids with three different rheological characteristics were selected: (i) silicone oil with 0.97 Pa · s in reported viscosity and 970 kg/m$^3$ in density at 25°C, (Shin-Etsu Chemical Co., Ltd., Japan), (ii) polyacrylamide (PAM) solution 0.5 wt.% (MT AquaPolymer, Inc.) with 1002 kg/m$^3$ in fluid density, (iii) carboxymethyl cellulose (CMC) solution 1.0 wt.% (Daicel Chemical Industries, Ltd., Japan) with 1007 kg/m$^3$ in fluid density. The silicone oil is well-known as a typical Newtonian fluid at lower shear rates than $O(10^2\ \mathrm{s}^{-1})$. The PAM solution has a strong viscoelasticity even at small concentrations due to the presence of long-length dispersive polymers. The CMC solution is known as a typical fluid having shear-thinning viscosity, which arises from polymer dispersion with weaker viscoelasticity than PAM.

To measure the flow velocity, small tracer particles were dispersed in the test fluids: CL-2507 (Sumitomo Seika Chemicals Co, Ltd., Japan) for the silicone oil, and HP20SS (Mitsubishi Chemical Co. Industry Ltd., Japan) for the CMC and PAM solutions. The mean diameter and density of the tracer particles are 100 $\mu$m and 1010 kg/m$^3$, and those of CL-2507 are 180 $\mu$m and 920 kg/m$^3$. The influence of the added tracer particles on the rheological properties is negligibly small for small concentrations (< 0.1%). Also, the optical visualization and echo amplitude showed that there was no aggregation of the dispersed tracer particles during the measurements of oscillations of the cylindrical container.

Table 6.1: Experimental parameters of different test fluids.

| # | Test fluid | $\phi$ [-] | $f_o$ [Hz] | $\Theta$ [rad] | $\Delta t$ [ms] | $\Delta\xi$ [mm] | $\Delta u_\xi$ [mm/s] | Section No. |
|---|---|---|---|---|---|---|---|---|
| (i) | Silicone oil | — | 1.0 | $\pi/4$ | 50 | 0.61 | 0.430 | §6.3.1 |
| (ii) | 0.97 Pa · s | 0.02 | 1.0 | $\pi/4$ | 50 | 0.61 | 0.430 | §6.3.2 |
| (iii) | | — | 0.5 | $\pi/2$ | 50 | 0.93 | 0.586 | §6.3.1 |
| (iv) | PAM solution | 0.02 | 0.5 | $\pi/2$ | 50 | 0.93 | 0.586 | §6.3.3 |
| (v) | 0.5 wt.% | 0.04 | 0.5 | $\pi/2$ | 50 | 0.93 | 0.586 | §6.3.3 |
| (vi) | | 0.06 | 0.5 | $\pi/2$ | 50 | 0.93 | 0.586 | §6.3.3 |
| (vii) | | — | 1.0 | $\pi/2$ | 25 | 0.93 | 1.301 | §6.3.1 |
| (viii) | CMC solution | 0.02 | 1.0 | $\pi/2$ | 25 | 0.93 | 1.301 | §6.3.4 |
| (ix) | 1.0 wt.% | 0.04 | 1.0 | $\pi/2$ | 25 | 0.93 | 1.301 | §6.3.4 |
| (x) | | 0.06 | 1.0 | $\pi/2$ | 25 | 0.93 | 1.301 | §6.3.4 |

To prepare multi-phase fluid media with set volume fractions ($\phi = 0 - 0.06$), relatively large spherical particles (HP20, Mitsubishi Chemical Co. Industry Ltd., Japan; CL-8007, Sumitomo Seika Chemicals Co., Ltd., Japan) were chosen as neutrally buoyant particles for the test fluids. In the experimental conditions of the previous research (e.g., [13, 17, 18]), the density of the dispersed particles was very different from the fluid density. The mean diameter and density of CL-8007 are 600 $\mu$m and 920 kg/m$^3$ [Fig. 6.2(a)], and of HP20 are 500 $\mu$m and 1010 kg/m$^3$ [Fig. 6.2(b)] , where the HP20 was used for CMC solution as well since the fluid density of CMC solution is almost equal to that of PAM solution.. The inertia moment of the test particles is very small compared to the torque due to viscous stress by the surrounding fluid, and the radial motion of the particles by rotation-induced lift forces can be disregarded. By calculating the volume of the particles from the weight of a particle, the test fluids with the dispersed spherical particles for specific volume fractions were prepared as listed in Table 6.1 together with further details of the experimental conditions and parameters.

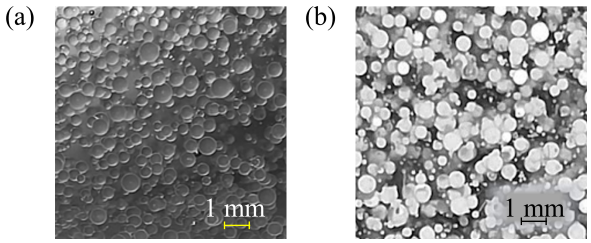


Figure 6.2: Photographs of dispersed particles; (a) CL-8007 in silicon oil [condition (ii) in Table 6.1], (b) HP20 in PAM solution [condition (iv) in Table 6.1].

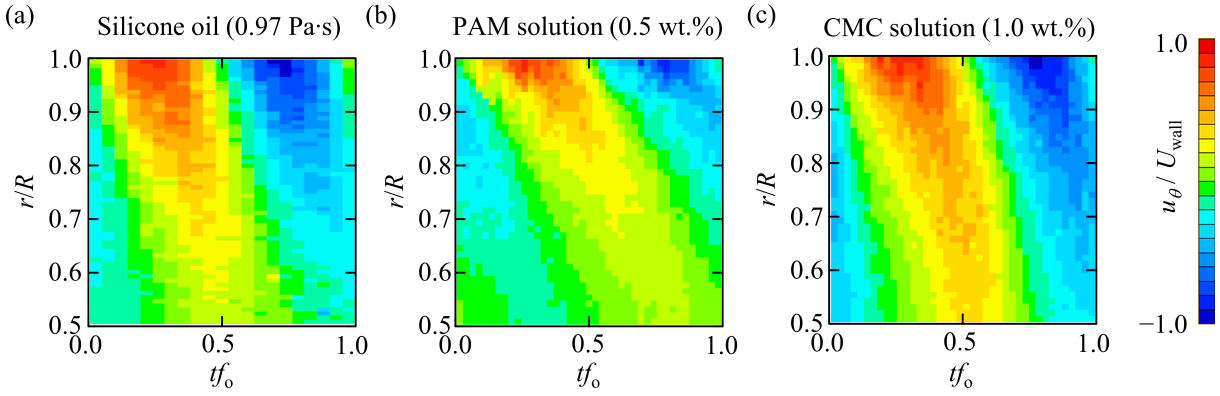


Figure 6.3: Radial-temporal velocity distribution of (a) silicon oil, (b) PAM solution, and (c) CMC solution.

## 6.3 Experimental results of the linear viscoelastic analysis

To capture base rheological characteristics of the three test fluids specified in the previous section, silicone oil, PAM solution, and CMC solution, a USR evaluation is conducted where the viscosity, elasticity, and relaxation times of the test fluids are evaluated. Here the details of the linear viscoelastic analysis using the USR are explained step by step in the process for ease of understanding the results obtained. The macro-rheological response in the case of multi-phase conditions is then examined by dispersing spherical particles with large diameters of $O(0.1\ \mathrm{mm})$ in the test fluids.

### 6.3.1 Rheological evaluations of test fluids without dispersed particles

The spatiotemporal velocity distributions were measured using the UVP as shown in Figs. 6.3(a)–(c). The vertical and horizontal axes show the radial positions normalized by the radius of the container, $R$, and the spin-cycle period $tf_o$. The contours represent the azimuthal velocity normalized by the maximum azimuthal velocity at the cylinder wall ($r = R$), $U_{\mathrm{wall}}(= 2\pi f_o R\Theta)$. Important experimental parameters in each experiment (silicone oil, PAM solution, and CMC solution) are detailed in Table 6.1.

The amplitude of the velocity fluctuations decreases with closeness to the center of the container since the momentum propagation is weakened by viscous damping. Comparing the velocity distributions in Fig. 6.3(a)–(c), there are differences in the phase lag of the fluctuations in the radial direction of the velocity profiles. These reflect the differences in momentum propagation rates arising from the different rheological properties of the test fluids as the momentum satisfies the equation of motion, Eq. (6.3). In Fig. 6.3(a), the phase-lag in the velocity fluctuations with respect to radial position is smaller than that of Fig. 6.3(b). Using Eq. (6.7) for the Fourier component obtained from the velocity profiles of the PAM solution at $r/R \approx 0.9$, the cost function $F$ is calculated as shown in Fig. 6.4, as an example, where phase difference in the linear viscoelasticity $\delta$ is used instead of $E$.

The $\delta$ is defined as $\tan\delta = G''/G' = E/\omega_o\mu$, where the phase values around $\pi/2$ indicate a fluid close to that of a purely viscous body and smaller values indicate larger elastic contributions to the stress in the fluids [Chapter 4]. The contours of Fig. 6.4 indicate the calculated values of the cost function for different $\mu$ and $\delta$, where the resolutions of these are approximately 0.001 Pa · s and 0.001 rad, respectively. The contour map shows a concave surface of $F$ and a single minimal point corresponding to the most probable values of $\mu$ and $\delta$ satisfying the equation of motion and the spatio-temporal velocity information. For a more efficient search for the minimal point, a randomly search method was adopted rather than calculating

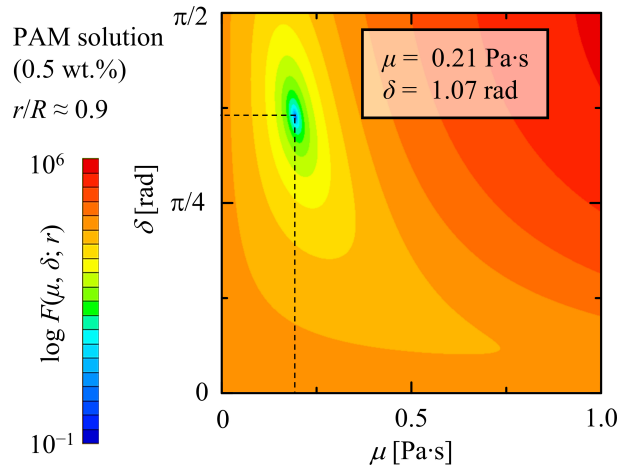


Figure 6.4: Cost function distribution obtained from the velocity profiles at $r/R \approx 0.9$ in the PAM solution [condition (iii) in Table 6.1].

the map of $F(\mu, \delta)$ as shown in Fig. 6.4.

For each radial position, the rheological evaluations summarized above are processed for velocity profiles of 1000 periods of oscillations (i.e. in the case of $f_o = 1.0$ Hz, the measurement duration in 1000 periods of oscillations corresponds to 1000 s). In determining the minimum of the cost function at different radial positions, Figs. 6.5(a) and (b) show average and standard deviations of the viscosity $\mu$ and phase difference $\delta$.

The results for silicone oil show a constant viscosity independent of the radial position as is characteristic of a typical Newtonian viscosity [Fig. 6.5(a)]. The results with the PAM solution show the viscosity decreasing to the radial position around $r/R = 0.75$, representing a shear-thinning viscosity. The viscosity in the CMC solution decreases gradually through the all radial positions suggesting a typical pseudo plastic fluid. In the phase difference $\delta$, the silicone oil takes values around $\pi/2$ like a purely viscous fluid [Fig. 6.5(b)]. With the PAM solution, $\delta$ maintains values in a narrow range, $\pi/4 < \delta < 3\pi/8$, like that of a viscoelastic fluid. The CMC shows $\delta = \pi/2$ near the cylinder wall but it detaches from $\pi/2$ at $r/R = 0.8$. This means that the rheological property is suggested as an elastic behavior at a shear rate lower than a certain critical value, here around $8 - 10$ s$^{-1}$.

Next, to evaluate the viscoelastic effects, the relaxation time $\lambda$ of the test fluids is calculated [Fig. 6.5(c)]; the physical meaning of $\lambda$ is the time at which the shear deformation reaches an equilibrium state after fully relaxed, represented by a ratio of the viscosity $\mu$ and the elastic modulus $E$,

$$\lambda = \frac{\mu}{E} = \frac{1}{\omega_o \tan \delta}. \tag{6.8}$$

Generally, $\lambda$ of pure Newtonian fluids is considered to be an extremely small value. Radial profiles of corresponding $Wi$ numbers calculated by Eq. (6.2) are shown in Fig. 6.5(d). According to [12], for experimental conditions of a steady shear, different from the present conditions, the $Wi$ required for the onset of particle alignments is empirically determined as the range from 0.5 to 16.5. It is speculated that the $Wi$ is from $O(0.1)$ to $O(10)$ here. From the calculated $Wi$, in the silicone oil, there is no formation of any particle alignment in the range examined ($0.5 < r/R < 0.9$) because of the extremely small value of $Wi$ than the range of $Wi$ required as indicated above. For the PAM and CMC solutions, there is the possibility to form alignments in the range of $0.5 < r/R < 0.9$ and $0.75 < r/R < 0.9$, respectively, according to this criterion.

### 6.3.2 Rheological evaluation of silicone oil with dispersed particles

After 100 periods of oscillation, the dispersed particles in the silicone oil do not show any migration as expected and detailed in the previous section as shown in Fig. 6.6(a); the photograph was taken from the top of cylinder under room lighting, and the number of particles on the picture seems to be larger than the actual one; The particles are homogeneously dispersed in the fluid medium. For the particle suspension of silicone oil at each radial position, the relative viscosity $\eta$, ratio of the viscosity with particles modified from the viscosity without particles [Table 6.1 (i) and (ii)] was calculated.

To include a sufficiently large number of particles in the control volume used to evaluate the effective viscosity, the rheological evaluations were conducted at every radial position in $r/R = 0.5 - 1.0$, making the volume around 1000 times larger than the size of the dispersed particle. As shown in Fig. 6.6(b), the relative viscosity remains constant at all radial

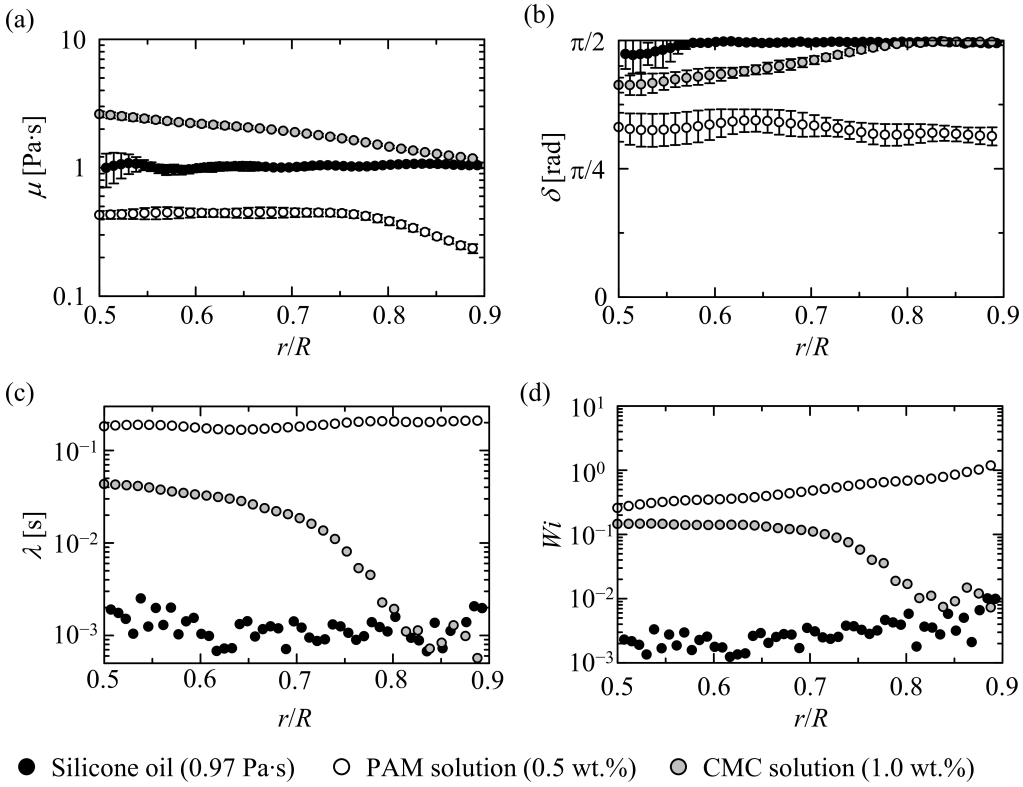


Figure 6.5: Radial profiles of (a) viscosity $\mu$, (b) phase difference $\delta$, (c) relaxation time $\lambda$, and (d) Weissenberg number $Wi$ calculated by Eq. (6.2) in the test fluids.

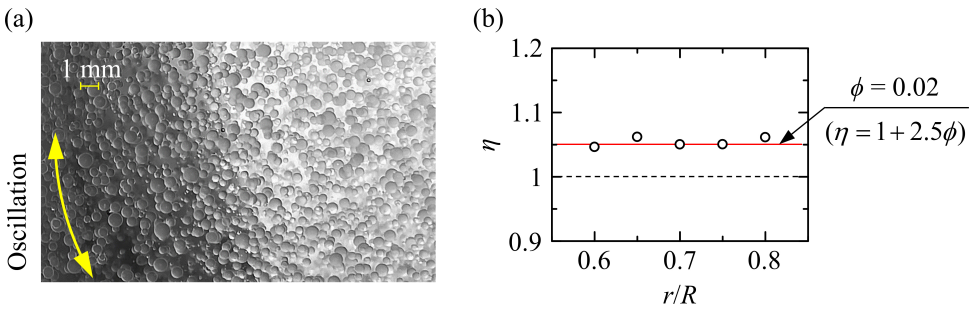


Figure 6.6: (a) Photograph taken from the top of the cylinder under room lighting in silicon oil during oscillations [condition (i) in Table 6.1], (b) radial profile of the relative viscosity $\eta$, where the solid line indicates the relative viscosity estimated by Eq. (6.1).

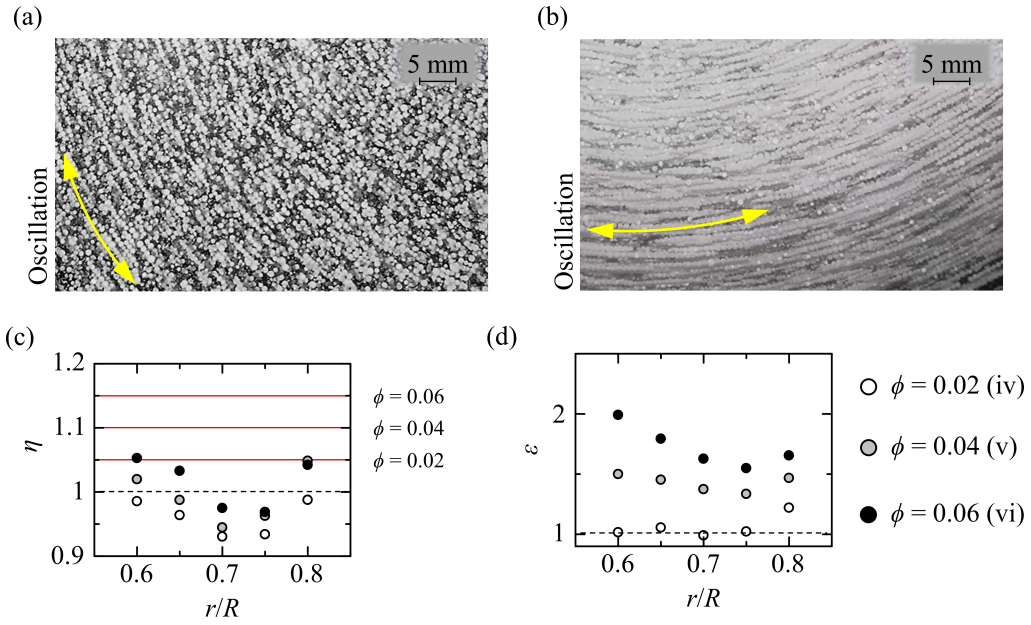


Figure 6.7: Photograph taken from the top of the cylinder under room lighting in the PAM solution during oscillations; (a) condition (iv) in Table 6.1, (b) condition (vi) in Table 6.1, (c) radial profile from the top at relative viscosities $\eta$, where from the top of the solid line indicates from the top at the relative viscosity estimated by Eq. (6.1), (d) radial profiles of relative elasticities $\varepsilon$.

positions in the range examined, $0.6 < r/R < 0.8$. This constant value corresponds well to the calculated value by substituting $\phi = 0.02$ into Eq. (6.1) [solid line in Fig. 6.6(b)]. Eq. (6.1) is the simplest notation of effective viscosity to evaluate the impact of the particle suspensions. It is valid when suspension is dilute as it is derived by taking the leading order of the Maclaurin expansion of the exponential type function of effective viscosity with respect to the volume fraction (e.g. [2]). The leading term cannot express the influence of direct-contact interactions among particles. In the experiments on the three test fluids, modifications of the local shear rates by increasing the amount of the spherical particles were within 5%, and do not affect evaluations of the effective rheological properties as radial profiles.

### 6.3.3 Rheological evaluation of the PAM solution with dispersed particles

Seen in the top view of the cylinder at the volume fraction, $\phi = 0.02$ [condition (i) in Table 6.1], after 100 periods of oscillation, the particles were aligned in the azimuthal direction as shown in Fig. 6.7(a). Here, the "alignment" expresses that the dispersed particles form a corded structure in the azimuthal direction. Increasing the volume fraction of dispersed particles, the aligned particles appeared more corded when comparing this aspect as in Figs. 6.7(a) and (b). The photographs were taken from the top of cylinder under room lighting. During the oscillations, the test fluid oscillates maintaining the alignments. From the experimental observations, particles dispersed in the PAM solution were aligned in the shear direction. As explained in §6.1, this suggests that a factor acts as a restorative force between the particles and that it is arising from viscoelastic effects.

To investigate the effective viscoelasticity of the PAM solution with dispersed particles in different volume fractions, three volume fractions were chosen as listed in Table 6.1. From each rheological evaluation, the relative viscosity and elasticity $\varepsilon(= E^*/E)$ can be evaluated as shown in Fig. 6.7(c) and (d). The vertical and horizontal axes indicate the radial position and the relative values. In the Fig. 6.7(c), the solid lines show the estimated relative viscosity in each volume fraction by Eq. (6.1); This estimate compares the viscosity modulated by aligned particles with that of the ideal-homogeneous fluid medium.

From the result in Fig. 6.7(c), the relative viscosities do not reach the estimated relative viscosity. There are a number possible reasons for this difference from the estimated values: (i) a smaller momentum transfer of aligned particles than with the particles in the homogeneously dispersed media, (ii) a relatively higher shear rate around the aligned particles, and (iii) a dominance of elastic characteristic brought about by the particle alignment.

In the case of reason (i), the difference would arise as the aligned particles could oscillate as an ensemble maintaining the string structures. It may be postulated that an effective momentum transfer in this case would be lower than that at a homogeneously dispersed medium. For reason (ii), there is some data from previous studies examined by numerical

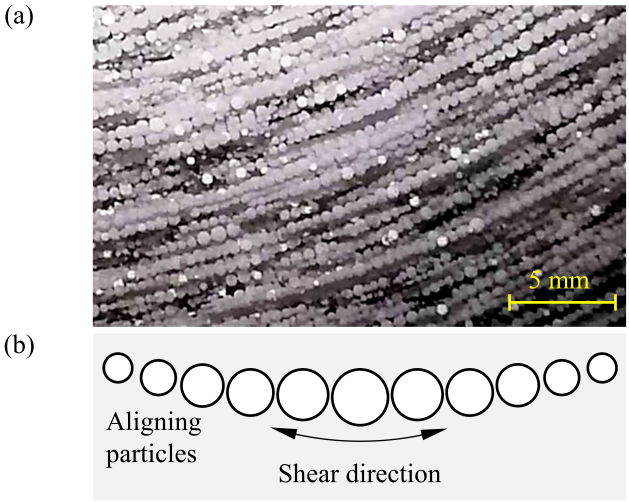


Figure 6.8: (a) Enlarged and contrast modified photograph of Fig. 6.7(b) and 6.7(b) schematic of particle alignment feature observed from the experiment [condition (vi) in Table 6.1

simulations [14–16], and here a lower viscosity region around the particle chain was quantified, with high polymer extensions confirmed in the region between chained particles. This suggested reason is supported by the experimental result that the viscosity decreases drastically from the viscosity of the PAM solution without the particles as noted in §6.3.1. These results of numerical simulations strongly support the anomalous shear-thinning behavior in the PAM solution with the dispersed particles. For reason (iii), energy conservation considerations of the fluid flow (or deformation) must be considered together with the dynamic viscoelasticity. If this is the reason, then according to previous investigations [11], using a simple parallel plate with a stress transducer, the apparent shear stress in polymer solutions with spherical particles in the diameter range here $O(10^0\ \mu\text{m})$ would gradually decrease with increasing applied strain.

In the case of $\phi = 0.02$ [condition (iv) in Table 6.1], the relative elasticity is close to $\varepsilon = 1$ at all radial positions. Increasing the volume fraction of the included particles in the fluid medium increases the effective elasticities significantly [Fig. 6.7(d)]. As mentioned above, the length of the aligned particles makes the appearance increasingly corded with increasing volume fractions of added particles. This would support the speculation that there is a close relationship between the particle alignment and the effective elasticity. This effective elasticity would appear as the most likely reason to describe the multi-phase condition in non-Newtonian fluid media, because it is difficult to evaluate the dynamic viscoelasticity with particle alignments using standard torque rheometers due to the limitations as elaborated in §6.1. From the observation of PAM experiment [condition (vi) in Table 6.1], the particles were aligned as shown in Fig. 6.8(a), which was enlarged from Fig. 6.7(b). Clearly seen, the particle diameter at the middle of aligning particles is larger, and the diameter is gradually smaller as it gets closer to the end of aligning particles [Fig. 6.8(b)]. From the feature of particle alignment, the restorative force may be weaker as the particle diameter gets smaller, because particle alignment is structured with optimizing arrangements by the unsteady deformations.

### 6.3.4 Rheological evaluation of the CMC solution with dispersed particles

For the CMC solution, looking from the top of the cylinder at the volume fraction, $\phi = 0.02$ [condition (viii) in Table 6.1], after 100 periods of oscillations, the particles were aligned in the azimuthal direction as shown in Fig. 6.9(a). The photograph was taken from the top of cylinder by vertically sheet lighting with 2 mm thickness. Taken by flash lightning differently from the photograph in Fig. 6.9(a), Fig. 6.9(b) is a macro-photograph to clarify features of the aligned particles at $r/R = 0.65$. Although the alignment is not clearer when comparing it to that of the PAM solution, the dispersed particles were aligned in the shear direction except in the area close to the cylinder wall. Comparing with the radial profiles of this relaxation time in the CMC solution as indicated in Fig. 6.5(c), it decreases as it gets closer to the cylinder wall, i.e. the viscoelasticity in the CMC solution is modulated with respect to the shear amplitude, suggesting that the particle alignment may become more distinguishable as the relaxation time gets longer.

To investigate the effective viscoelasticity of the CMC solution with dispersed particles in different volume fractions, three volume fractions were chosen as listed in Table 6.1. From each of the rheological evaluations, the relative viscosity

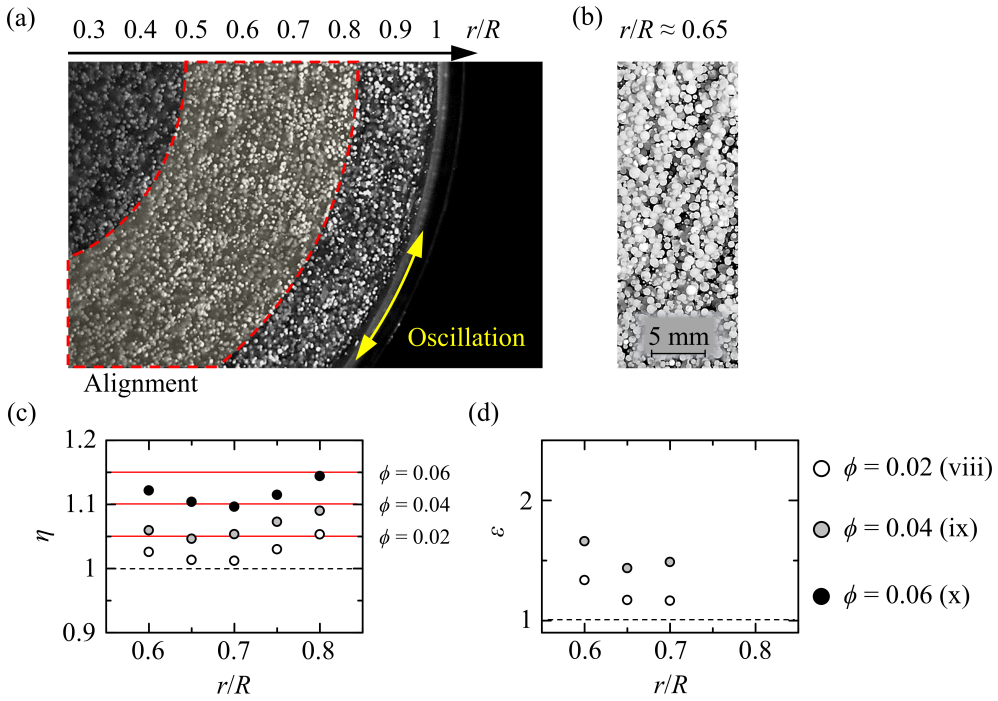


Figure 6.9: (a) Photograph taken from the top of the cylinder in CMC solution during oscillations [condition (viii) in Table 6.1, (b) macro-photograph at $r/R \approx 0.65$, (c) radial profile of relative viscosity $\eta$, where the solid line indicates the relative viscosity estimated by Eq. (6.1), (d) radial profiles of relative elasticities $\varepsilon$.

and elasticity can be evaluated as shown in Fig. 6.9(c) and (d). The vertical and horizontal axes show the radial position and the respective relative values. In Fig. 6.9(c), the solid lines show the relative viscosity in each volume fraction estimated by Eq. (6.1).

From the results in Fig. 6.9(c), the relative viscosity remains considerably smaller than the estimated relative viscosity except in the area close to the wall ($r/R \approx 0.8$), but the gap is much smaller than that of the PAM solution at the same volume fraction. Further, the relative viscosity of the CMC solution at $r/R \approx 0.8$ agrees well with the estimate. From this it may be deduced that the particle dispersions remain homogeneous as Einstein's law of viscosity assumes and as mentioned in §6.1. It may also be that the change in viscosity versus the estimated value arises from the degrees of particle alignments.

The important consideration here regarding effective viscosity is that applicability of Eq. (6.1) may not be limited in a Newtonian fluid, rather, the importance to ensure the applicability is also placed on relaxation time of the fluid media. This is consistent with the experimental result for three different fluids (§6.3.2–6.3.4). Even if the test fluid shows non-Newtonian characteristics, depending on the shear rate, the particles can be homogeneously dispersed in the fluid media, e.g. experiment of CMC solution. In the case of the relaxation time almost equals to $O(10^{-3}$ s), the effective viscosity can be described by Eq. (6.1).

In the cases of $\phi = 0.02$ and 0.04 [condition (viii) and (ix) in Table 6.1], the relative elasticities increase gradually but elasticity could not be determined at $r/R > 0.7$, because the phase difference, $\delta$ here is equal to $\pi/2$ in the radial position. In the case of $\phi = 0.06$ [condition (x) in Table 6.1], the elasticity was not evaluated as the phase difference reaches $\delta \approx \pi/2$ over the whole of the radial position. Overall then, modulation of the elasticity in CMC solution is less than that of the PAM solution. The behavior in this modulation can be explained by assuming that the degree of viscoelasticity arises as a result of the particle alignments. A possible interpretation of the factor of particle alignments should be here; single-phase fluids showing low viscoelasticity may have less influence on the alignments because the particles will be aligned during the relaxation process. From the alignment features in Fig. 6.7(a) and (b), interparticle distances of the alignments in the PAM solution appear contiguous while those in the CMC solution are intermittent, as shown in Fig. 6.9(a) and (b). It may be deduced that the inter-particle distances reflect the degree of viscoelasticity which could explain and provide a reason why the phase difference for $\phi = 0.06$ [condition (x) in Table 6.1] suggested $\delta \approx \pi/2$ over the whole of the radial positions. This point will be discussed further in next section.

## 6.4 Discussion

From the experimental findings in §6.3, the alignment of particles under unsteady shear flows is closely related to the relaxation time of the fluid media. Further, the effective properties with respect to the volume fraction of included dispersed particles will be modulated by the particle alignments. Two subjects are discussed in this following sections; one is considering a physical model to represent the alignment of the dispersed particles observed in the experiments explained in §6.3 above; the second is the effects of the particle alignment on the macro-rheological properties.

### 6.4.1 Verification of dominant factors of the alignment using a toy model

The relaxation time of fluid media is of great importance to understand the factors affecting aligned (and alignment of) particles as determined from the experiments. We will consider a simple toy model representing a minimally essential mechanism for the particle alignment, namely that particle behavior can be explained as a result of their being held together by a spring model with a yield stress, and that the base flow is simulated by Newtonian fluids. The purpose of this numerical simulation using the toy model is to express the mechanical characteristics necessary to orient dispersed particles as the polymer relaxation takes place in the dissolving water.

The basic conditions we include are as follows: (i) considering the phenomena in a 2-dimentional plane; (ii) random distribution for the initial position of the dispersed particles; (iii) volume fraction of the dispersed particles $\phi$ determined as the ratio of the total volume of the dispersed particles to the disk-like volume within a radius $R$ and height corresponding to the particle diameter; (iv) one-way interaction from the flowing fluid on the particles (no influence of the particles on the fluid flow); (v) one directional, axisymmetric flow given as an exact solution of the Navier-Stokes equation; and (vi) inelastic collisions between particles.

The algorithm of the numerical calculation is explained here step by step: **(1)** displacement of the particles due to the fluid flow as passive actors in the time elapsed, $\Delta t$, is calculated [$P_{1'}$ and $P_{2'}$ in Fig. 6.10(a)], as $(x_{1'}, y_{1'}) = (x_1 + u_1 \Delta t \cos\varphi, y_1 + u_1 \Delta t \sin\varphi)$, where the velocity distribution of the fluid flow $u_1(x, y)$ is given from exact solutions (see Chapter 4) and $\varphi = \tan^{-1}(y_1/x_1)$. **(2)** Choosing a target and a surrounding particle [$P_1$ and $P_2$ in Fig. 6.10(a)], then **(3)** variations in the distance between the particles via the displacement, $\Delta l$, is calculated by $\Delta l = l_{1'\to 2'} - l_{1\to 2}$. **(4)** If the variation in $\Delta l$ is positive, a restorative force $F_{1'\to 2'}$ between the particles is calculated from

$$\begin{aligned} F_{1'\to 2'} &= \sqrt{F_x^2 + F_y^2}, \theta_{1'\to 2'} = \tan^{-1}\frac{y_{2'} - y_{1'}}{x_{2'} - x_{1'}}, \\ F_x &= k\Delta l W_{1'\to 2'} \cos\theta_{1'\to 2'}, F_y = k\Delta l W_{1'\to 2'} \sin\theta_{1'\to 2'}, \end{aligned} \tag{6.9}$$

where $k$ denotes the spring constant and $W_{1'\to 2'}$ represents the Gaussian distribution given by

$$W_{1'\to 2'} = \frac{1}{2\pi\sigma^2} \exp\left[-\frac{(x_{2'} - x_{1'})^2}{2\sigma^2}\right] \exp\left[-\frac{(y_{2'} - y_{1'})^2}{2\sigma^2}\right] \tag{6.10}$$

representing the Gaussian weight of multiple springs on the force as shown in Fig. 6.10(b). **(5)** If the force $F_{1'\to 2'}$ is smaller than the threshold value $k_Y$ describing the yielding behavior of the polymer, it is included in the integrated restorative force as $F_X = \Sigma F_x$ and $F_Y = \Sigma F_y$. **(6)** Alternatively, when the variation $\Delta l$ is negative, the contribution of the corresponding spring on the restorative force is disregarded. **(7)** The steps from (2) to (6) are repeated for all particles considered, then the displacements of the particles are modified by considering the restoration force as

$$x_{1''} = x_1 + \frac{F_X \Delta t}{V_1} + u_\theta \Delta t \cos\varphi, y_{1''} = y_1 + \frac{F_Y \Delta t}{V_1} + u_\theta \Delta t \sin\varphi, \tag{6.11}$$

from the integrated force $F_X$ and $F_Y$ [$P_{1''}$ and $P_{2''}$ in Fig. 6.10(a)]. This series of calculations is repeated for a set number of repetitions (iterations).

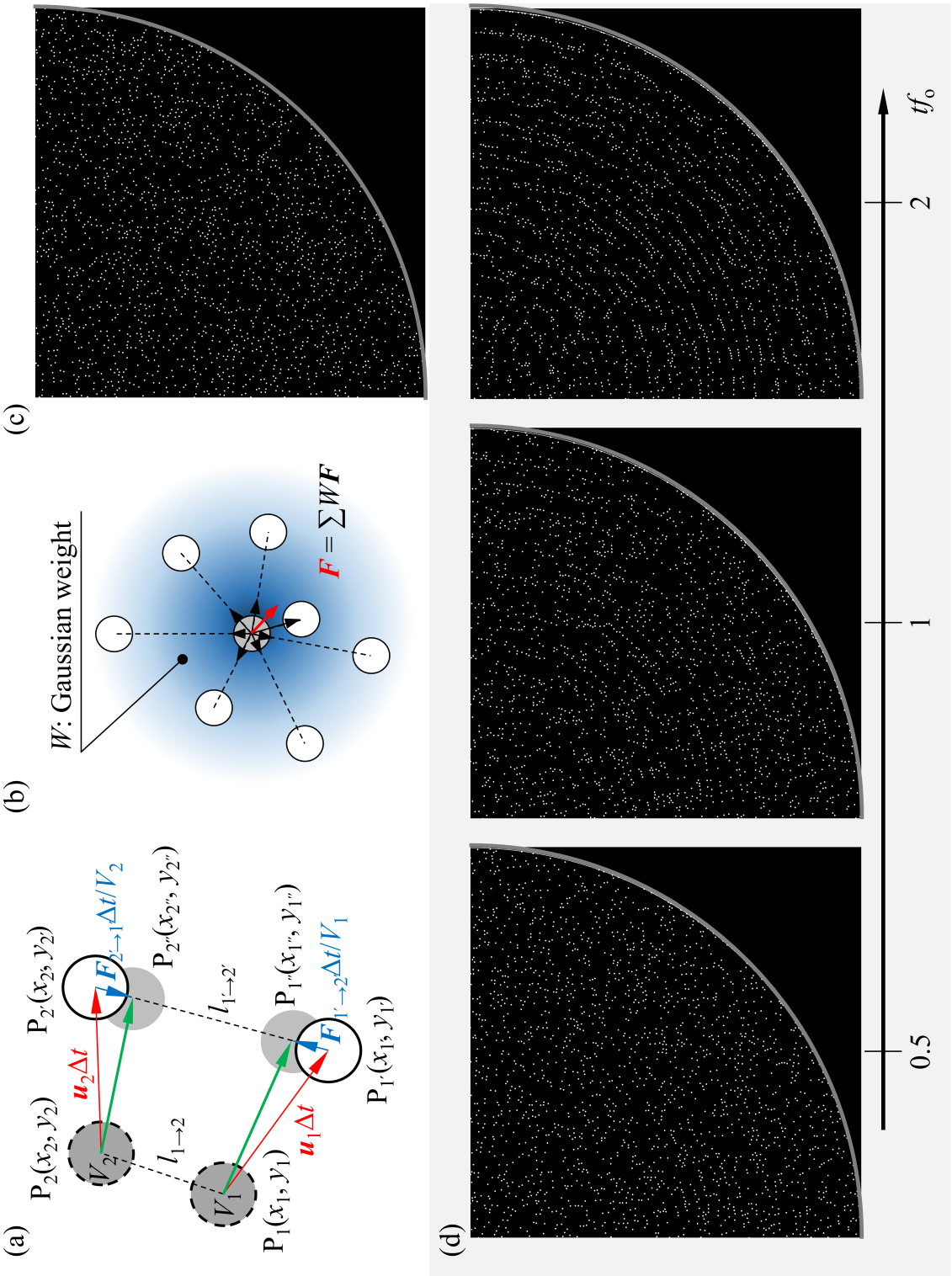


Figure 6.10: (a) Schematic of the numerical conditions of particle displacements, (b) schematic of Gussian weights around target particles for the calculations, (c) initial displacement arranging randomly, and (d) calculated results of particle displacement for $tf_o$ = 0.5, 1, 2.

An example of the initial positions of the particles with $\phi = 0.1$, particle radius $r_p = 0.25$ mm, and $R = 72.5$ mm, is shown in Fig. 6.10(c). The numerical data of the fluid flow here are given as: kinematic viscosity $\nu = 500$ mm$^2$/s, oscillation frequency $f_o = 0.5$ Hz, oscillation amplitude $\Theta = \pi/2$ rad, and time resolution $\Delta t = 50$ ns. Additionally, standard deviation in Gaussian distribution and the volume of dispersed particles were given as $\sigma = 5.0 \times 10^{-4}$ m and $V_1 = 5.2 \times 10^{-7}$ m$^3$. Now, the condition of the spring constant as $k_p = 2$ N/m are examined with the yield stress of the spring, $k_Y = 1.0 \times 10^{-5}$ N.

Particle distributions are modulated as shown in Fig. 6.10(d); in the case of $tf_o = 0$ [Fig. 6.10(c)], the particles maintain the initial homogeneous distribution. This distribution arises because the dispersed particles follow the motions of a Newtonian fluid maintaining homogeneity in this case of an absence of elastic forces between the particles. With the oscillating period, $tf_o = 0.5$, the particles aggregate somewhat, and the aggregation trends become prominent with $tf_o$. After $tf_o = 2$, the particles are clearly aligned as the terminal state. Comparing the results for $tf_o = 0.5$ and 2 [Fig. 6.10(d)], it can be seen that the development of the particle alignments depends on the applied shear deformations between the dispersed particles. Also, for $k_p = 2$, the particles are unaligned in the region close to the center due to insufficient fluid deformation applied to the particles here. This clearly shows that fluid deformation plays an important role for particles to reach the aligned state, and this would explain why there are no aligned particles at the inner region of the cylindrical container in the case of the CMC solution [see Fig. 6.9(a)]. In the simulation discussed in this section, the fluid viscosity is assumed constant, but in an actual case the elasticity between particles would be modulated with respect to the displacement of the particles, that is, the relaxation time (ratio of viscosity and elasticity) may be assumed to change locally. In conclusion, the particle alignment is arising from the relaxation characteristics which play a large role in the case of the strong spring assumption.

In our experimental conditions examined, the hydrodynamic interaction is overshadowed by the viscoelastic function, i.e. the effective viscosity is mostly governed by relaxation process. This can be said so because kinematic viscosity is so high (500 mm$^2$/s) that particles fall in Stokes flow regime in case of Newtonian fluid. In Stokes regime, particles do not show relative displacement due to the kinematic reversibility in oscillating shear, and thus contribution of the hydrodynamic interaction is negligible.

We may now conclude that particle alignments can be simulated by using the present toy model, and the spring force and yield stress can be assumed as the essential governing factors affecting the alignments in this simulation. Our understanding is that there is no clear threshold of bulk volume fraction to sway the phenomenon as long as the flow is less influenced by the solid collision among particles. Although the shear thinning viscosity is responsible for the formation of string-like structures according to Won and Kim [13], the relaxation time [e.g. in this investigation where it is higher than $O(10^{-2}$ s)] arising from the viscoelastic characteristic is also a necessary factor in the formation of the particle alignment by uniformly dispersed particles.

### 6.4.2 Macro-rheological characteristics modulated by alignments

As suggested by the results of the effective viscoelasticity in §6.3, the modulated macro-rheology and behavior of the dispersed particles are discussed in this section as summarized in Fig. 6.11. For silicone oil, the dispersed particles do not align due to shear deformation, and the effective viscosity increases as per the theoretical estimate based on Eq. (6.1). For the PAM solution, the fluids deform unsteadily maintaining the particle alignment in the sheared direction. Here the measured relative viscosity does not reach the relative viscosity estimated by the theory, while at the same time the relative elasticity increases with increasing volume fractions of dispersed particles in the bulk solution. For the CMC solution, the particle alignments were less regular than those in the PAM solution, while however alignments were observed in the region where the relaxation time of the CMC solution increases as suggested in §6.3.1. Additionally, in the region where the particle alignments were observed, the effective viscoelasticity was modulated by forces acting on the individual particles.

Combining and integrating these experimental results and situations, the local-rheological factors to align the dispersed particles and the macro-rheological effect from the aligned particles can be discussed. A number of attempts to simulate the phenomena of particle alignments by modelling with numerical schemes have been proposed, however, based on the above it would be reasonable to assume that there are also spring forces acting on the aligned particles.

Considering spring functions, relaxation processes arise as a result of the relaxation time of the fluid medium and the magnitude of the oscillations, and the process involved is the most important in achieving alignment of the dispersed particles. This hypothesis for local-rheology, that spring forces function to align the particle can be explained based on the macro-rheological properties in the results of §6.3.2–6.3.4. It may therefore be postulated that if the interparticle mechanism appears among all aligned particles, the particle alignments affect the effective elasticity as a macro-rheological phenomenon, expressed differently, the overall particle alignment functions as a macro-spring. In the experiments in the viscoelastic fluid (PAM), the effective elasticity was twice that of the single-phase fluid. It is noteworthy here that the alignments affected by the macro-spring lead to a modulation of the effective viscosity as it remains at lower values due to the shear localization at

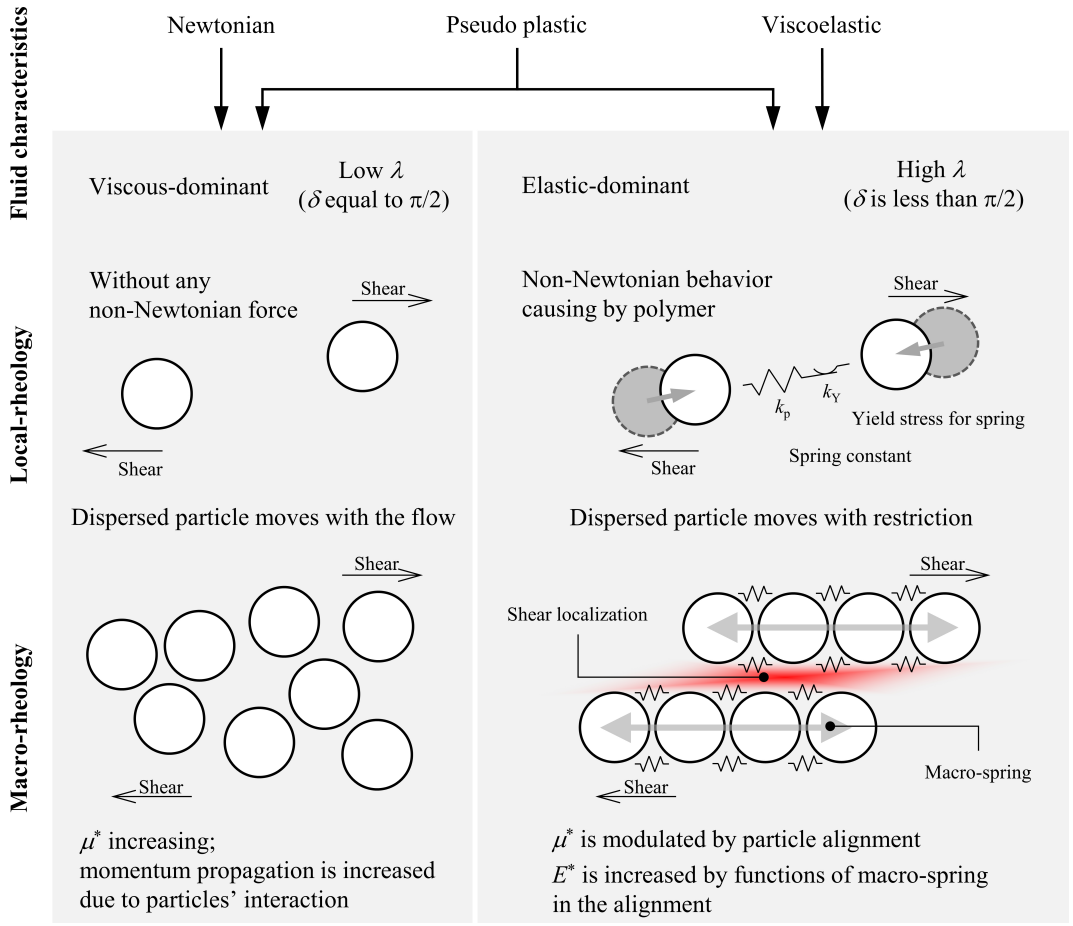


Figure 6.11: Schematic details of dispersed particle modulation from the top of the local- and macro-rheology of the test fluids.

inter-alignments as suggested by and depicted in Fig. 6.11. The modulation of effective viscosity established here provides definitive evidence for the background to the shear stress decreasing with time elapsed as found in previous reports [13, 17, 18]. The discussion above suggests a reason for the disappearance of elasticity in the CMC solution at the densest condition of particles, $\phi = 0.06$, shown in Fig. 6.9(d): Since there are lower viscous effects of the CMC solution without particles, the particle alignment in the solution is weaker than in the PAM solutions [see Fig. 6.7(a) and Fig. 6.9(a)]. This allows a relatively uniform distribution of the particles in the CMC solution to be established, especially for dense particle conditions, and the effective viscosity increases as the conditions approach those of the theory. This makes the solution increasingly viscous and the effects of the macro-spring due to the particle alignment may be buried (overwhelmed) and become impossible to visualize in the case of the increased effective viscosity. The most important result of the findings and discussion here is that the rheological properties modulated by the particle alignments can be evaluated. We emphasize that this result has so far been considered as unexamined rheological properties.

## 6.5 Conclusion

Aligned particles in non-Newtonian fluid media and corresponding modification of the effective viscoelasticity were investigated by means of ultrasonic spinning rheometry (USR) are introduced. From experimental observations of three test fluids with different rheological characteristics (Newtonian, viscoelastic, and pseudo plastic fluid), the particles orient in the sheared direction in the case of the fluid media having characteristics of long relaxation times. Because the particle alignments occur at the radial positions satisfying the condition of the relaxation time (the $Wi$ number) suggested in previous studies [12], it is speculated that elastic forces act between the particles and that these are essential for the alignment of particles. Numerical simulations adopted by considering a simple toy-like model, in which particles connect via springs and considering that the yield stresses are dispersed in a Newtonian fluid, supported the results of the simulations. Effective rheological properties modulated by aligned particles in non-Newtonian fluid media were then evaluated by USR; non-uniformity of the particles due to the alignment provides less of an increase the effective viscosity than with uniform distributions; the particle alignment strengthens the elastic force of the test media as macro-springs and the corresponding effective elasticity reaches a maximum of twice that of the single-phase condition.

## References

[1] A. Einstein, “Eine neue Bestimung der Molekuldimensionen,” Ann. Phys. 19, 289–306 (1906).
[2] M. Mooney, “The viscosity of a concentrated suspension of spherical particles, ” J. Colloid Sci. 6, 162–170. (1951).
[3] R. Simha, “A treatment of the viscosity of concentrated suspensions,” J. Appl. phys. 23, 1020–1024 (1952).
[4] I. R. Rutgers, “Relative viscosity and concentration,” Rheol. Acta 2, 305–348 (1962).
[5] D. G. Thomas, “Transport characteristics of suspension: VIII. A note on the viscosity of Newtonian suspensions of uniform spherical particles,” J. Colloid Sci. 20, 267–277 (1965).
[6] N. A. Frankel, and A. Acrivos, “On the viscosity of a concentrated suspension of solid spheres,” Chem. Eng. Sci. 22, 847–853 (1967).
[7] H.-O. Park, J. M. Bricker, M. J. Roy, and J. E. Bulter, “Rheology of oscillating suspensions on noncolloidal spheres at small and large accumulated strain,” Phys. Fluids 23, 013302 (2011).
[8] K. Yeo, and M. R. Maxey, “Dynamics and rheology of concentrated, finite-Reynolds-number suspensions in a homogeneous shear flow,” Phys. Fluids, 25, 053303 (2013).
[9] H. Haddadi, and J. F. Morris, “Microstructure and rheology of finite inertia neutrally buoyant suspensions,” J. Fluid Mech. 749, 431–459 (2014).
[10] D. D. Joseph, Y. J. Liu, M. Poletto, and J. Feng, “Aggregation and dispersion of spheres falling in viscoelastic liquids,” J. Non-Newton. Fluid Mech. 54, 45–86 (1994).
[11] M. K. Lyon, D. W. Mead, R. E. Elliott, and L. G. Leal, “Structure formation in moderately concentrated viscoelastic suspensions in simple shear flow,” J. Rheol. 45, 881–890 (2001).
[12] R. Scirocco, J. Vermant, and J. Mewis, “Effect of the viscoelasticity of the suspending fluid on structure formation in suspensions,” J. Non-Newton. Fluid Mech. 117, 183-192 (2004).
[13] D. Won, and C. Kim, “Alignment and aggregation of spherical particles in viscoelastic fluid under shear flow,” J. Non-Newton. Fluid Mech. 117, 141–146 (2004).
[14] W. R. Hwang, and M. A. Hulsen, “Structure formation of non- colloidal particles in viscoelastic fluids subjected to simple shear flow,” Macromolecular Materials and Engineering 296, 321–330 (2011).

[15] Y. J. Choi, and M. A. Hulsen, "Alignment of particles in a confined shear flow of a viscoelastic fluid," J. Non-Newton. Fluid Mech. 175, 89–103 (2012).
[16] N. O. Jaensson, M. A. Hulsen, and P. D. Anderson, "Direct numerical simulation of particle alignment in viscoelastic fluids," J. Non-Newton. Fluid Mech. 235, 125–142 (2016).
[17] R. Pasquino, D. Panariello, and N. Grizzuti, "Migration and alignment of spherical particles in sheared viscoelastic suspensions. A quantitative determination of the flow-induced self-assembly kinetics," J. Colloid Interf. Sci. 394, 49–54 (2013).
[18] S. Van Loon, J. Fransaer, C. Clasen, and J. Vermant, "String formation in sheared suspensions in rheologically complex media: The essential role of shear thinning," J. Rheol. 58, 237–254 (2014).
[19] P. Fischer, E. K. Wheeler, and G. G. Fuller, "Shear-banding structure orientated in the vorticity direction observed for equimolar micellar solution," Rheol. Acta 41, 35-44 (2002).
[20] O. Nechyporchuk, M. N. Belgacem, and F. Pignon, "Rheological properties of micro-/nanofibrillated cellulose suspensions: Wall-slip and shear banding phenomena," Carbohydr. Polym. 112, 432–439 (2014).
[21] T. Divoux, M. A. Fardin, S. Manneville, and S. Lerouge, "Shear banding of complex fluids," Annu. Rev. Fluid Mech. 48, 81–103 (2016).
[22] Y. Tasaka, T. Kimura, and Y. Murai, "Estimating the effective viscosity of bubble suspensions in oscillatory shear flows by means of ultrasonic spinning rheometry," Exp. Fluids 56, 1867 (2015).
[23] T. Shiratori, Y. Tasaka, and Y. Murai, "Rapid rheological characterization of viscoelastic fluid based on spatiotemporal flow velocimetry," Exp. Therm. Fluids Sci. 71, 1–13 (2016).

Chapter 7

# USR test on the rheology of gelled food for making better tasting desserts

## Contents


**7.1 Introduction . . . 104**
**7.2 Materials and methodology . . . 105**
7.2.1 Recipe for test materials . . . 105
7.2.2 Steady rotational and oscillatory shear tests with the standard rheometer . . . 105
7.2.3 Ultrasonic spinning rheometry (USR) . . . 106
**7.3 Rheological evaluations by the standard rheometer . . . 107**
7.3.1 Results of the steady rotational tests . . . 107
7.3.2 Results of oscillatory tests . . . 109
7.3.3 Summary: the sources of physical inaccuracies in a standard rheometer . . . 111
**7.4 USR tests of the rheology of gelled food . . . 111**
7.4.1 Rheological evaluation on phase lag in velocity distributions . . . 111
7.4.2 Results of the linear viscoelastic analysis . . . 113
7.4.3 Discussion: the rheology of a better-prepared dessert . . . 116
**7.5 Conclusion . . . 116**
**References . . . 117**


## Preface

The aim in this chapter is to prove the capability of the kinematic rhometry to elucidate the unexplained phenomena which occurs when using a standard rheometer due to the limitation of methodology; this aim is similar to that in Chapter 6. The rheological properties of gelled foods that may relate to flows in the swallowing process of complex food materials is clarified. This work was published in Yoshida *et al*., Phys. Fluids (2019).

## Abstract


Rheological properties of gelled foods that may relate to the physics of the fluids in the swallowing process of complex food components are determined by ultrasonic spinning rheometry (USR). Through rheological evaluations of thixotropic gelled food, the inaccuracies in standard rheometer data to capture the true-rheological property is discussed first with steady rotational and oscillatory tests; the inaccuracies arise from commonly existing problems that cannot be directly observed in standard rheometers (wall-slip, shear banding, shear localization, elastic instability, and more). The results evaluated by standard rheometers would be related to the measurements being specific response depending on the geometry of the measurement device. The USR test discussed here shows the potential to overcome these problems in the rheological evaluation of gelled foods and reflects the advantages offered by USR, such as spatial, local, and oscillation cycle measurements; the results with the transient flow curve that has not previously been discussed can be usefully interpreted, and the stability of the food materials in the unsteady shear displayed is of great importance in understanding which rheology indicates the better texture.

## 7.1 Introduction

Rheology of foods related to the chewing and swallowing processes has been extensively investigated as a safety issue, and recently also to improve the quality of life of consumers; for example, usual oatmeal is good for people who have weak chewing and swallowing abilities especially among older people and infants but due to very soft texture for chewing is not enjoyable in the eating when good taste and good texture are valued. Differently, Jellied foods have problems with aspiration even with the better impression arising from the eating. Both questionnaires and rheological tests have been used in rheological research, but questionnaire research is affected by personal preferences and rheological tests are not always suitable despite attempts to provide quantitative evaluations; this is because of both the complexity of the chewing and swallowing processes and the rheological properties of foods. Rheological evaluations, therefore, require an understanding of complex properties together with development of a rheometry that captures both the complex properties and individual and preferential processes of swallowing involved.

Developments in research have tried to evaluate complex-rheological properties, such as shear thinning, yield stress, viscoelasticity, effective viscosity with multi-phase dispersion, and other qualities, by creating novel rheometers with different geometries. The precision expressed in the results with recent rheometers (different from measurement accuracy) is ensured with sensitive torque sensors and with the improvements in geometry of rotational part, but little attention has been paid to the "physics of fluids". This is a reason why there are "common problems of the rheometers" arising from, for example, the Couette inverse problem [1], and no fully acceptable solution for these problems are known, though extensive trials to overcome specific problems have been made [2–4].

It is thought that non-Newtonian characteristics could be one source of the common problems (not directly observable), which include shear history effects [5], shear banding [6, 7], shear localization [8], wall-slip [9, 10], elastic instability [11–14], and other phenomena. When rheological evaluations are attempted without considering these influences, the obtained results will reflect the specific response as it is dealt with in the measurement device, not exposing or clarifying the true-rheological properties. These problems occur due to the fluid characteristics, and efforts to solve the problems have to be approached from the perspective of fluid mechanics.

To improve the quality of rheometry, utilizing spatiotemporal velocity distributions of the fluid motion is required because the velocity information reflects all the rheological information of a complex fluid. Approaches to achieve this from fluid mechanics have mainly focused on standard rheometers coupled with inner visualization techniques (e.g. [12–14]), and have made it possible to directly identify the common problems (usually invisible). Then the influence exerted by those problems have been investigated by integrating standard rheometer readings with ultrasonic imaging. Gallot *et al*. [12] proposed a technique that explains the unstable shear-banding flow of non-Newtonian fluids, on this basis, Fardin *et al*. [13] found that that the potential impact of inner flow patterns could be observed for both complex as well as Newtonian fluids in the large amplitude oscillatory shear (LAOS).

Research into velocity-profiling rheometry [15–17] has dealt with time-averaged velocity profiles limited to steady flow states; as one of the examples of velocity-profiling rheometry, Derakhshandeh *et al*. [15] performed measurements of transient behaviors of thixotropic fluids using a Couette rheometer with a wide gap and ultrasonic velocity profiling (UVP) [18]. This was able to detect yielding regions of the fluid from quasi-steady velocity profiles, also when the torque measurements may be influenced by wall-slip something that could lead to errors in evaluations of the rheological characteristics. This leaves problems, as one of the non-Newtonian characteristics involves both shear-rate-dependence in the rheological properties and time-dependence (structural recovery, relaxation, and other aspects), and techniques and measurements must be able to detail time-dependent properties for evaluations of transient rheological properties.

We have developed a novel velocity-profiling rheometry that supplements the rheological evaluations beyond the capabilities of standard rheometers, and have termed it ultrasonic spinning rheometry (USR) [19] and Chapters 2–5. Based on the ultrasonic measurement of instantaneous velocity profiles, the technique has advantages, such as offering ease of handling and the option of employing it with opaque fluids and it has been applied to the measurement of foods in general [20]. The basic concept of this rheometry is that velocity profiles are substituted into the equation of motion to estimate the rheological properties, and the potential value of USR with various complex fluids has been established in Chapters 2–5.

In this paper, the rheological properties of gelled foods that may relate to flows in the swallowing process of complex food materials are investigated by means of USR. We examine both test materials prepared with a recipe suggested by a food company developed to enable better eating and also intentionally modified recipes. A comparison of results of rheological evaluations of the both materials could lead to the establishment of a methodology necessary to understand what is involved in optimum swallowing sensations. Here, as a test material, a milk dessert gelled by the chemical attraction between low-methoxyl (LM) pectin (mainly used as a thickener for foods, such as fruit jam, paste-like sweets, and similar) and including calcium ions was chosen, and three test fluids prepared with different recipes were examined by comparative experiments

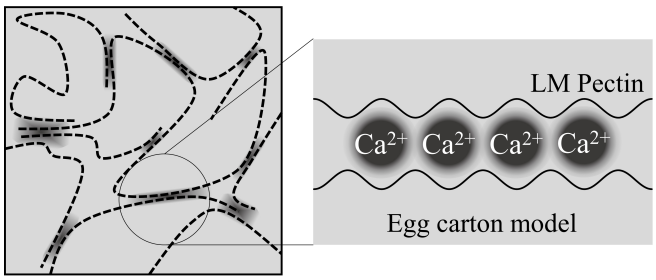


Figure 7.1: Schematic outlines of LM-pectin cluster and the egg-carton model.

involving the standard rheometer and the USR. In §7.3, the inaccuracies in the capture of the true-rheological property with standard rheometers is discussed by examining the rheological evaluations of steady rotational and oscillatory tests. After that, a rheology for better texture of complex food materials are discussed by considering the findings obtained by USR (§7.4).

## 7.2 Materials and methodology

### 7.2.1 Recipe for test materials

The test material, "Fruiche" is a popular dessert in Japan and is available as a basic source material from House Foods Group, Inc., Japan. The Fruiche source includes much fruit pulp, $O(1-10$ mm) in mean diameter, irregularly shaped and deforming easily under shear stress. Mixed with whole milk, the completed Fruiche dessert changes drastically into a gel due to the aggregating reaction between low-methoxyl (LM) pectin [21] (see the detailed chemical features in [22]) dispersed in the Fruiche source and calcium ions dissolved in the milk as depicted in Fig. 7.1. Here, the whole milk is provided by Yotsuba Milk Products Co., Ltd, Japan; the nutrient composition is protein 34 g/L, lipid 40.5 g/L, carbohydrate 48.5 g/L, Na 0.39 g/L, and Ca 1.14 g/L. The chained molecules of the LM pectin structures the network linked by the calcium ions, and the structure is commonly called an "Egg carton model". From the perspective of rheology, the complete Fruiche displays highly complex-rheological properties (shear-thinning viscosity, viscoelasticity, yield stress, thixotropy, and modifications of the effective viscosity by multi-phase dispersion). These would give rise to the common problems with the standard rheometer mentioned in §7.1.

The basic source of Fruiche is designed by the company for good texture in chewing and the following swallowing, and to do that, the best weight ratio of the milk to the source is set as 1 : 1. Here, to evaluate how differences from the recipe affect the rheology, we intentionally prepared the Fruiche in different ratios (milk : source = 2 : 1 and 1 : 2) from the recipe. Putting the mixed materials on a 30-degree-inclined glass plate for 10 minutes, different behaviors were observed as shown in Fig. 7.2. In Fig. 7.2(a) (milk : source = 2 : 1), the mix has fluidity and adheres on the surface of the plate. In Fig. 7.2(b) (1 : 1), the material is firmly adhering to the glass surface, and its shape deformed only a little toward the lower part of the slope within 10 minutes. In Fig. 7.2(c) (1 : 2), the material was slipped on the surface with keeping its shape as the same with the feature in Fig. 7.2(b). These observations represent the simplest rheological test, and reflect important rheological characteristics of the test materials qualitatively, such as adhesion, deformability, fluidity, and others qualities, and these features can be used to verify the evaluated properties.

### 7.2.2 Steady rotational and oscillatory shear tests with the standard rheometer

A rheometer with a geometry of Taylor-Couette (Anton Paar MCR-502, parallel-plate geometry PP25) was used in the rheological tests of the completed Fruiche prepared by the different recipes (§7.2.1). As is obvious from Fig. 7.2, all the three different test materials show large difference in the rheological characteristics. Although a variety of geometries depending on the characteristics of the test materials should be chosen, the same parallel plate was used for all the test materials to evaluate the test materials under the same condition. Otherwise, the geometric difference will affect the rheological evaluations. The test materials are maintained at a constant temperature ($T_0 = 15°$C).

For the steady rotational and oscillatory tests, the following conditions and considerations are maintained to ensure accuracy: (a) one-directional flow (strain), (b) the shear rate is a linear function in the axial direction, (c) the walls are subject

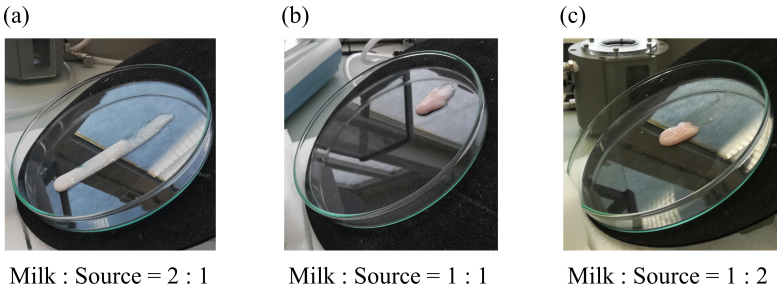


Figure 7.2: Photographs of qualitative rheology for test materials prepared by different recipes and placed on 30 degrees inclined glass plates. (a) Milk : Source = 2 : 1 mix, (b) Milk : Source = 1 : 1 mix, and (c) Milk : Source = 1 : 2 mix.

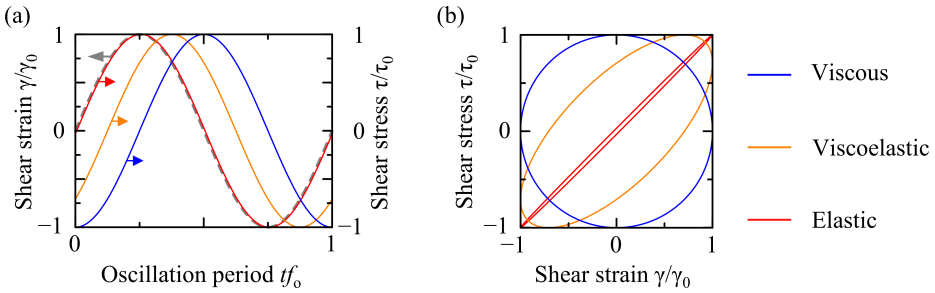


Figure 7.3: (a) Ideal fluid response representing shear stress against the applied shear strain, (b) ideal features of Lissajous curve in the case of shear strain versus shear stress.

to nonslip conditions (d) the fluid is homogeneous, (e) inertial effects from fluid motion are disregarded, and (f) there are no secondary flows. A thin layer $O(0.1-1$ mm) of the test material is required to satisfy the assumptions, however, this thickness is inadequate to prevent the appearance of non-Newtonian behaviors ([9, 10] and Chapter 5), the shear rate $\dot{\gamma}$ and shear stress $\tau$ are regarded as an apparent shear rate $\dot{\gamma}_{\text{app}}$ and an apparent shear stress $\tau_{\text{app}}$.

In ideal condition of oscillatory tests, the fluid response should be determined depending on its rheological characteristics (e.g. viscous, viscoelastic, and elastic) as shown in Fig. 7.3(a), and Lissajous curves can be derived by considering shear strain/shear rate and shear stress as horizontal and vertical axes [Fig. 7.3(b)]. Clearly seen, the rheological characteristics can be distinguished by the feature of the Lissajous curves. Lissajous curves consisting of shear strain and shear stress draw circles for viscous, ellipse for viscoelastic, and diagonal lines for elastic materials. In the non-linear viscoelastic regime, the fluid response may not show clear sinusoidal characteristics due to occurrences of unexpected phenomena. To understand the invisible phenomena of the fluid motion with the non-linearity in the gap of the rheometer, large amplitude oscillatory shear (LAOS) measurements [23, 24] are performed for the rheological evaluations of complex fluids. The basic concept behind the LAOS measurement is that the shear stress in the response to sinusoidal shear deformations are evaluated with the approximations mentioned above. Non-sinusoidal responses depending on the rheological characteristics with complexities (e.g. viscoelasticity, yield stress, multi-phase dispersions, and more) will be obtained using the LAOS. So, it is possible to qualitatively understand the non-linear rheological response caused by the complex fluid characteristics. The purpose of LAOS measurement in this paper was to clarify the rheological complexities in the test material, and it also will help to reveal the vagueness in the rheological evaluations of standard rheometer.

### 7.2.3 Ultrasonic spinning rheometry (USR)

The experimental apparatus is an open cylindrical container made of acrylic resin; the container has 2-mm-thick side walls, 145-mm inner diameter, and is 60-mm high. The container was mounted at the center of a water bath to control the temperature, $T_0$, of the test fluids and to avoid any influence from co-reflected ultrasonic waves. Oscillations of the cylinder were controlled by a stepping motor to a set oscillation angle $\Theta$ and frequency $f_o$, where the motor was attached at the bottom of the container. The oscillating motion was controlled as a sinusoidal angular velocity, $U_{\text{wall}} \sin 2\pi f_o t$, where $U_{\text{wall}} = 2\pi f_o R\Theta$ (see Chapter 5 for details). The UVP-Model Duo (Met-Flow S.A., Switzerland) was used to measure instantaneous velocity distributions. To obtain the azimuthal velocity component, an ultrasonic transducer (resonance frequency 4 MHz and 5-mm active element diameter) was mounted with a gap offset $\Delta y$ from the center coordinates of the cylindrical container. With

axisymmetric flow and the radial velocity component negligible, the azimuthal velocity $u_\theta$ is calculated from the geometric relation $u_\theta = u_\xi r/\Delta y$. Empirically, $\Delta y = 15$ mm was selected, and further details of the setup for the transducer were detailed in [19].

Important theoretical considerations for the linear viscoelastic analysis in USR are as follows: assuming that the fluid flows are one-directional and axisymmetric, Cauchy's equation of motion is given as $\rho\partial u_\theta/\partial t = \partial\tau/\partial r + 2\tau/r$, where $\rho$ is the density of the test fluids and $\tau$ is the shear stress. To describe the relation of $u_\theta$ and $\tau$, Maxwell model: $\tau + (\mu/E)\partial\tau/\partial t = \mu(\partial u_\theta/\partial r - u_\theta/r)$, is selected as the simplest expression to represent the linear viscoelastic characteristics, where $\mu$ and $E$ indicate the viscosity and elasticity of the fluid. From the Fourier transform with respect to $t$, Cauchy's equation and Maxwell model can be modified as

$$i\omega\rho\hat{u}_\theta = \left(\frac{\partial}{\partial r} + \frac{2}{r}\right)\hat{\tau}, \tag{7.1}$$

$$\hat{\tau} + i\omega\frac{\mu}{E}\hat{\tau} = \mu\left(\frac{\partial\hat{u}_\theta}{\partial r} - \frac{\hat{u}_\theta}{r}\right), \tag{7.2}$$

where the Fourier-transformed velocity and shear stress are denoted as $\hat{u}_\theta(r,\omega) = \mathcal{F}[u_\theta(r,t)]$, $\hat{\tau}(r,\omega) = \mathcal{F}[\tau(r,t)]$, with the angular frequency $\omega$. Considering the cost function,

$$F(\mu,E;r) = \left[i\omega\rho\hat{u}_\theta - \left(\frac{\partial}{\partial r} + \frac{2}{r}\right)\hat{\tau}\right]^2_{\omega=\omega_o} \quad \text{s.t. } \hat{\tau} + i\omega\frac{\mu}{E}\hat{\tau} = \mu\left(\frac{\partial\hat{u}_\theta}{\partial r} - \frac{\hat{u}_\theta}{r}\right), \tag{7.3}$$

the $\mu$ and $E$ can be determined by satisfying the optimization problem, determining the $\mu$ and $E$ to minimize the cost function $F$. From Eqs. (7.2) and (7.3), the shear stress and shear rate, the flow curve, can be obtained from the Fourier components obtained from the velocity (see Chapters 4 and 5 for detailed calculations).

In Chapter 2, the radial profile of the phase lags calculated from the velocity distributions,

$$\phi(r) = \tan^{-1}\left\{\frac{\Im[\hat{u}_\theta(r,\omega_o)]}{\Re[\hat{u}_\theta(r,\omega_o)]}\right\} - \phi_{\text{wall}}, \tag{7.4}$$

can be used to distinguish the rheological characteristics of test fluids: Constant phase lag regimes correspond to rigid rotation and such regimes may be regarded to occur with fluids having elastic properties or very high viscosity values. Regimes with a changing phase lag indicate fluidization areas and thereby can be regarded as fluids with viscous or viscoelastic properties. For example, radial profiles showing discontinuous variations indicate the existence of boundaries between different regimes of a rheological property.

Simultaneous consideration both of the linear viscoelastic analysis and phase lag in the USR offers the possibility to elucidate the rheological properties with the transient behaviors. Such transient-rheological properties cannot be measured by standard rheometers because of the limitations of methodology, and a number of valuable findings by the USR will be discussed next.

## 7.3 Rheological evaluations by the standard rheometer

In this section, rheological evaluations of the test materials prepared with different recipes are examined by the standard rheometer with the parallel plate geometry described in §7.2.2. The steady rotational and oscillatory tests using the standard rheometer measured the rheological properties of the test materials (§7.3.1 and 7.3.2), then, inaccuracies with the standard rheometer in measuring the true-rheological properties, arising from the common problems that may occur between the plates are discussed in §7.3.3.

### 7.3.1 Results of the steady rotational tests

The original source of Fruiche includes numerous strawberry pulp particles as mentioned in §7.2.1 [see Fig. 7.4(a)]. The sizes of this pulp component vary up to approximately 30 mm. The completed Fruiche with the dispersed ingredients is critically influencing the rheological evaluations using the standard rheometer [Fig. 7.4(b)] as exemplified by jamming of the gap between the parallel plates. Because the rheological evaluations in the standard rheometer should be done without very large ingredients in the test fluids, the pulp components were removed for all of the experiments in §7.3.

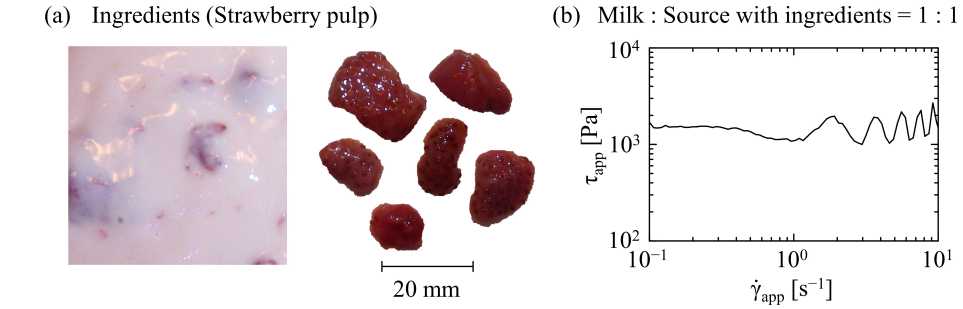


Figure 7.4: (a) Photographs of ingredients dispersed in the original source and (b) apparent shear stress versus apparent shear rate obtained by the standard rheometer with the ingredients dispersed in test material Milk : Source = 1 : 1 mix.

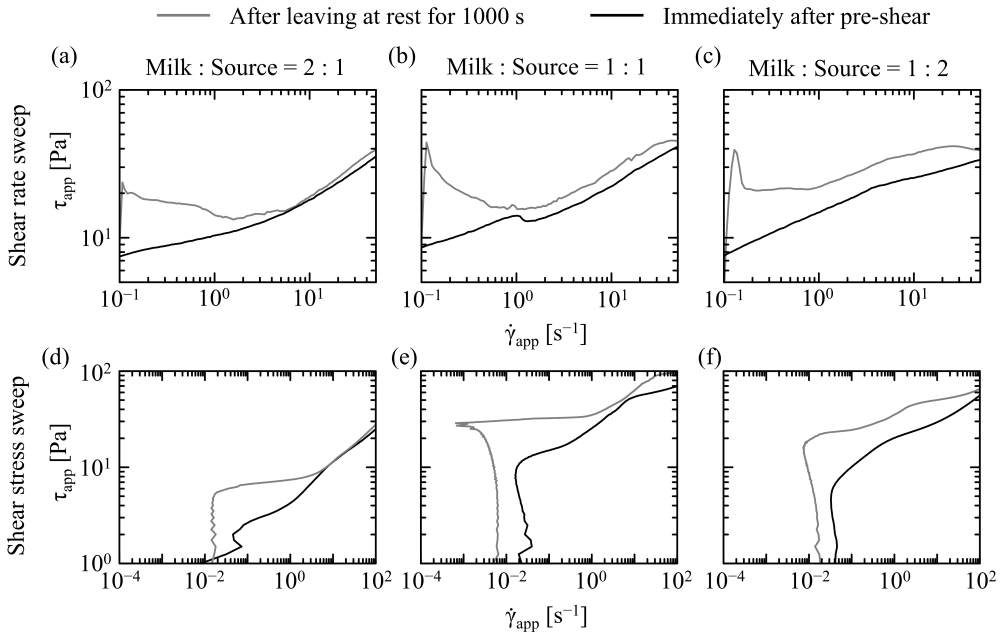


Figure 7.5: Rheological evaluations by the steady rotational tests with the standard rheometer for test materials prepared by different recipes: (a)–(c) shear strain controlled measurements and (d)–(f) shear stress controlled measurements; gray and black curves represent flow curved obtained after being left at rest for 1000 s and immediately after the pre-shearing.

The steady rotational tests were conducted by both shear rate and shear stress sweeps. In the shear rate sweep, the angular speed representing the shear strain rate were logarithmically ramped up from $10^{-1}$ s$^{-1}$ to $5.0\times10^{1}$ s$^{-1}$ [Fig. 7.5(a)–(c)]. In the shear stress sweep, the angular speed representing the shear stress was ramped up linearly from 0 to 100 Pa [Fig. 7.5(d)–(f)]. The vertical and horizontal axes indicate the apparent shear strain rate and shear stress defined in §7.2.2. The gray and black solid curves represent the results obtained with or without settling for 1000 s, after pre-shearing, respectively.

In the shear rate sweep results in Fig. 7.5(a)–(c), the apparent shear stresses, $\tau_{app}$, at low shear rates showed large differences in the condition of time left at rest: the 2 : 1 mix [Fig. 7.5(a)] in $\dot{\gamma}_{app} < 4$ s$^{-1}$, the $\tau_{app}$ immediately after the pre-shearing is much lower than that after being left at rest, while the $\tau_{app}$ agrees between the conditions in the 4 s$^{-1}$ < $\dot{\gamma}_{app}$; the 1 : 1 mix [Fig. 7.5(b)], at $\dot{\gamma}_{app} < 1$ s$^{-1}$, the $\tau_{app}$ immediately after the pre-shearing is much lower than that after being left at rest similar to 2 : 1 mix, however, the $\tau_{app}$ immediately after the pre-shearing around $\dot{\gamma}_{app} = 1$ s$^{-1}$ showed an abrupt but slight drop. Then the curves obtained in the different conditions behave with similar manner at the 1 s$^{-1}$ < $\dot{\gamma}_{app}$ value. For the 1 : 2 mix [Fig. 7.5(c)] and for all of the $\dot{\gamma}_{app}$ range, there are clearly different manners between the conditions in the leaving time; after leaving at rest, the $\tau_{app}$ shows a plateau at 0.2 s$^{-1}$ < $\dot{\gamma}_{app}$ < 1 s$^{-1}$. These results show significant differences that have to be understood for the different rheological characteristic, for example, at the 1 : 2 mix [Fig. 7.5(c)], as a typical flow curve [9] the measured plateau $\tau_{app}$ indicates the occurrence of wall-slip (or shear banding) that would be caused by a weakly thixotropic behavior.

In the measurements with a shear stress sweep conducted to evaluate the critical yield stresses at 2 : 1 mix [Fig. 7.5(d)],

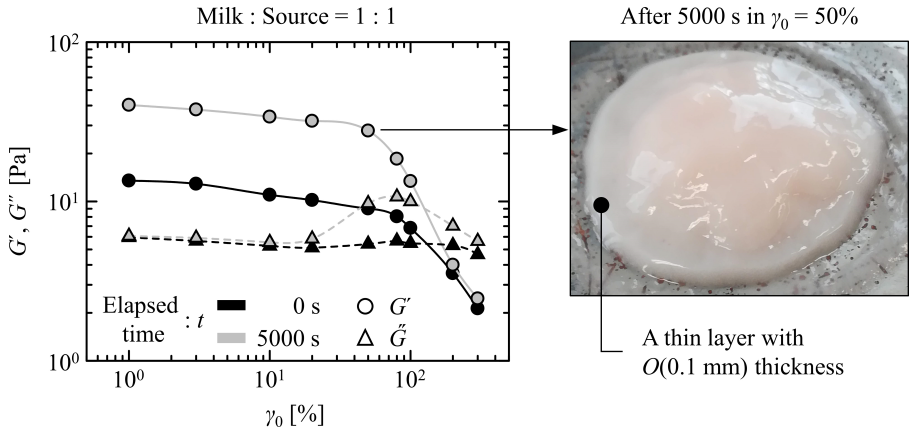


Figure 7.6: (a) Storage and loss modulus ($G'$, $G''$) versus the maximum shear strain amplitude, where the black and gray symbols representing the elapsed time, circle and triangle symbol representing storage and loss modulus ($G'$, $G''$), and (b) the photography of the condition of Fruiche when removing the shaft of the standard rheometer immediately after the long duration measurements at $\gamma_0$ = 50%.

the $\tau_{app}$ after being left at rest for 1000 s is larger than that immediately after the pre-shearing. This feature is also observed at 1 : 2 mix [Fig. 7.5(f)], while the $\tau_{app}$ at 1 : 1 mix [Fig. 7.5(e)] after being left at rest shows more drastic changes than the others, suggesting that the rheological response at 1 : 1 mix [Fig. 7.5(e)] has a stronger slippage on the wall than the others. This would be caused by the adhesion differences of the tested mixture detailed in Fig. 7.2. It is important to bear in mind that in sweeping the shear stress, these trends represent the wall-slip and are generally considered as showing a "yielding behavior" [25]; this strongly affects accuracy on the rheological evaluation as mentioned in §7.1. So usually, these critical responses are regarded as the "apparent yield stress" to estimate the specific rheological response when depending on standard rheometer readings.

All together the rheological characteristics obtained from Fig. 7.5(a)–(f), representing the rheological properties of the Fruiche, show large difference depending on the length of time it was left undisturbed, indicating a structure that recovers with time, i.e. thixotropy. Generally, rheological properties of thixotropic fluids would be evaluated as the equilibrium state, or as an equilibrium flow curve [26]. However, especially in such thixotropic fluids, the flow curves obtained from rotating rheometers do not always provide correct evaluations without influence of shear localization, wall-slip, and other factors, even when the shear stress apparently assumes equilibrium states (Chapter 5). This clearly suggests that alternative tests have to be used to evaluate these test materials to capture the true-rheological properties. The results evaluated by steady rotational tests provided some hints to understand the rheological features. For instance, it is speculated that the strength of the gelled structure would be in the order of the mixtures, 1 : 1, 1 : 2, and 2 : 1 here.

### 7.3.2 Results of oscillatory tests

From the measurements of steady rotational tests (§7.3.1), it is found that the rheological characteristics of the completed Fruiche are time dependent, they display thixotropy. To evaluate the equilibrium state in oscillatory tests, long duration measurements at different shear strain amplitudes (1 – 300%) with the same frequency (1.0 Hz) for the 1 : 1 mix were conducted (Fig. 7.6). The $G'$ and $G''$ amplitudes here were measured twice immediately after pre-shearing and at 5000 s elapsed after the start of oscillation. Immediately after the pre-shearing [solid line in Fig. 7.6(a)], the $G'$ amplitudes decrease monotonically as the shear amplitude increases, while $G''$ amplitudes remain constant. After 5000 s, the two amplitudes are very different to those immediately after the pre-shearing; the $G''$ amplitude displays a local maximum at around $\gamma_0$ = 100%.

It is hard to guarantee exact linearity of the test material deformation in the oscillatory test shown in Fig. 7.6(a), because there may be shear banding effects in the gap of the rheometer; the photo in Fig. 7.6(b) shows the condition of Fruiche when removing the shaft of the standard rheometer immediately after the long duration measurements at $\gamma_0$ = 50%. As clearly seen in Fig. 7.6(b), a thin layer with $O$(0.1 mm) thickness was formed, and the diameter was almost same with the parallel plate. Here, material sticks to the bottom plate forming a thin layer, whereas the material at the top can be deformed because of shearing by the upper plate. This would be clear evidence that the Fruiche was influenced by shear banding resulting in thixotropic characteristics here with the time scale longer than $O(10^3$ s). In such case, the obtained $G'$ and $G''$ should be considered as "apparent" value.

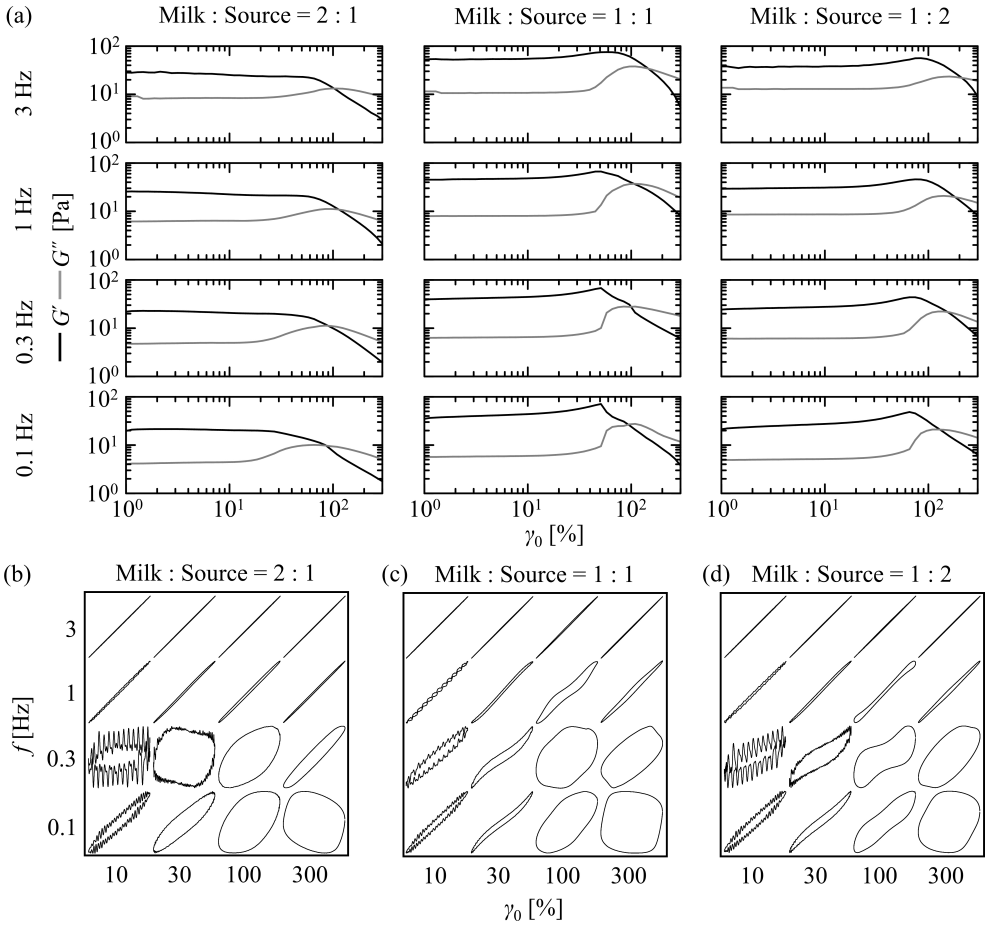


Figure 7.7: (a) Storage and loss modulus ($G'$, $G''$) of the shear amplitude sweep for different oscillating frequency and test conditions for different materials and (b) the Lissajous curves (shear strain versus shear stress normalized by the maximum value) for different shear amplitudes and oscillating frequencies that were obtained from the measurements plotted in (a).

To estimate the relaxation characteristic of the test materials, with different frequencies (0.1, 0.3, 1, and 3 Hz), oscillatory tests in a shear amplitude sweep from $\gamma = 1\%$ to 300% were conducted after pre-shearing and leaving at rest for 5000 s. The storage and loss moduli ($G'$ and $G''$) obtained are shown in Fig. 7.7(a). For the 2 : 1 mix, the $G'$ and $G''$ gradually change with respect to the strain amplitude, while more abrupt variations are obtained in the other mixtures (1 : 1 and 1 : 2). For the 1 : 1 mix, an abrupt variation is observed at around $\gamma_0 = 50\%$ in all conditions at 0.1 – 3 Hz. For the 2 : 1 mix, the abrupt variation appears at very similar $\gamma_0$ as for the 1 : 1 mix, there with a lower frequency than 0.3 Hz. Although the amplitude sweep measurements would be influenced by shear history effects like the oscillations, the abrupt variation would suggest that phenomena invisible here possibly arising from wall-slip or some other effect, suggesting that there may be significant differences in the relaxation behaviors of the test materials at $O(0.1 - 1$ s).

To understand details of the rheological response during oscillations, LAOS measurements were conducted simultaneously with the $G'$ and $G''$ evaluations in Fig. 7.7(a). Figure 7.7(b) shows the changes in Lissajous curves (shear strain versus shear stress) with respect to the oscillation frequency $f_o$ (0.1, 0.3, 1, and 3 Hz) and the maximum shear strain amplitude $\gamma_0$ (10, 30, 100, and 300%). As in §7.2.2, the Lissajous curves have been used to distinguish the rheological properties from the curve shape as three kinds of features representing viscous, viscoelastic, and elastic.

At the high frequency (3 Hz) in Fig. 7.7(b), the Lissajous curves in each test material suggest an elastic response irrespective of the shear amplitude, and at $f_o = 1$ Hz and $\gamma = 100\%$ the shapes of Lissajous curves represent more viscoelastic characteristics compared to the others of shear amplitude $\gamma_0$. At $f_o = 0.3$ Hz all of the curves for all test materials are less regular with kinks than at higher frequencies; these results can be explained by the qualitative deformation features described in Fig. 7.2 for the behavior on the inclined glass plates.

For the 2 : 1 mix, the Lissajous curve at $f_o = 0.3$ Hz and $\gamma = 30\%$ has a nearly circular shape representing a viscous reaction coexisting with irregular features [Fig. 7.7(b)]. Here, Fig. 7.2 shows easily deformable characteristics of the material.

For the 1 : 1 mix, the Lissajous curve at $f_o = 0.3$ Hz and $\gamma = 30\%$ shows a close to to elastic response with some kinks [Fig. 7.7(c)], similar to the more viscoelastic 1 : 2 mix [Fig. 7.7(d)]. The factors causing this difference can be understood by the qualitative differences shown in Fig. 7.2. The 1 : 2 mix (the right hand column in Fig. 7.7) may more easily be exposed to wall-slip than the 1 : 1 mix, and the Lissajous curves at the 1 : 2 mix suggest results influenced by wall-slip. This suggestion is supported by the results in the steady rotation tests under the shear stress sweep (§7.3.1); the critical yielding behavior the 1 : 1 mix was larger than that of the 1 : 2 mix as shown in Fig. 7.5(e) and (f). It may be concluded that the gelled appearance in Fig. 7.2 is accompanied by wall-slip.

The wavy features observed on the curves at frequencies lower than $f_o = 1$ Hz at low shear strain amplitudes, and the wavy features of the 2 : 1 and 1 : 2 mixtures are larger than those of the 1 : 1 mix. These features are observed at lower shear strain amplitudes than those resulting in abrupt changes in the Lissajous curves, for example at the 2 : 1 mix at $f_o = 0.3$ Hz from 10% to 30% of $\gamma_0$. According to Fardin *et al.* [14], unstable shear banding would be arisen from elastic instabilities, when shear stress in flow curves exhibits plateau with respect to the shear rate under unsteady shear conditions. The geometry used in this study is different from Taylor-Couette system used in the previous study, and it is of importance to be aware that elastic instability would be triggered by a transient state in the rheological characteristics of complex materials.

### 7.3.3 Summary: the sources of physical inaccuracies in a standard rheometer

The standard rheometer has great advantages in the measurement of viscous or elastic materials without abrupt phase transitions, such as yielding behavior. As shown by the experimental findings in §7.3.1 and 7.3.2, the torque sensitivity in measuring the rheological response will augment inaccuracies arising from bias errors in the understanding of the rheology of test materials in the standard rheometer; the influence from the presence of a depleted layer arising from abrupt phase transitions is very significant here; the data output is a "specific-mechanical response" influenced by the geometry of rheometer. Many reports have attempted to explain such shear banding problems as mentioned in §7.1, most focusing on measuring the shear rate profiles in the gap of the rheometer. However, the problems arising from standard rheometer cannot be solved by looking at only the influence of elastic instability even under steady state variations, as there are 3-dimensional unsteady flows as reported elsewhere [11]. Further, it may not be possible to correct the data obtained from oscillatory tests because the unsteady changes depend on the rheological characteristics of complex fluids. In oscillatory tests, inaccuracies will be significantly magnified as the basic principle of oscillatory tests do not consider "fluid inertia". Experimental proof of such inaccuracies will be discussed in §7.4 by comparing the rheological evaluations of standard rheometers with those by USR.

## 7.4 USR tests of the rheology of gelled food

In this section, inaccuracies in the rheological properties evaluated by standard rheometers (§7.3) will be explained using USR. The USR has the great advantage that it is capable of evaluating materials with dispersed ingredients contained in the original source. Further, based on the equation of motion and rheological model detailed in §7.2.3, rheological evaluations can be realized in unsteady shear conditions by frequency domain analysis (detailed explanations of the algorithm can be found in Chapters 4 and 5).

### 7.4.1 Rheological evaluation on phase lag in velocity distributions

Spatiotemporal velocity distributions measured for the 1 : 1 mix using UVP are shown in Fig. 7.8. The vertical and horizontal axes indicate the radial positions normalized by the radius of the container, $R$, and the spin-cycle period $tf_o$. The contours represent the azimuthal velocity normalized by its maximum value at the cylinder wall ($r/R = 1$), $U_{\text{wall}}$ ($= 2\pi f_o R\Theta$). The distributions here were obtained at different elapsed oscillation times with $f_o = 1.0$ Hz in the oscillation frequency and $\Theta = 60$ deg in amplitude. The resolutions of the UVP are 25 ms in time, 0.7–0.8 mm in space, and 1.35–1.4 mm/s in velocity. To eliminate the shear history effects, UVP measurements were conducted leaving the test materials at rest longer than 15 min after stirring the fluid medium.

Immediately after the start of oscillation ($tf_o = 0-1$), the test material oscillates in the azimuthal direction almost in phase from the wall to the center of the cylinder as in a rigid body. As the gel structures of the test material are gradually broken and become fluidized due to the shear stress from the oscillating wall, the oscillations of the test material assume small phase lags in the radial direction, for example at $tf_o = 60$ (center column), and this is significant after $tf_o = 1800$. This phase lag development can be used to distinguish the rheological characteristics of test fluids [Chapter 2].

From Eq. (7.4), and after calculating the Fourier components from the velocity distribution, radial profiles of the phase lag for the test materials can be quantified as shown in Fig. 7.9(a)–(c). The vertical axis represents the radial position normalized

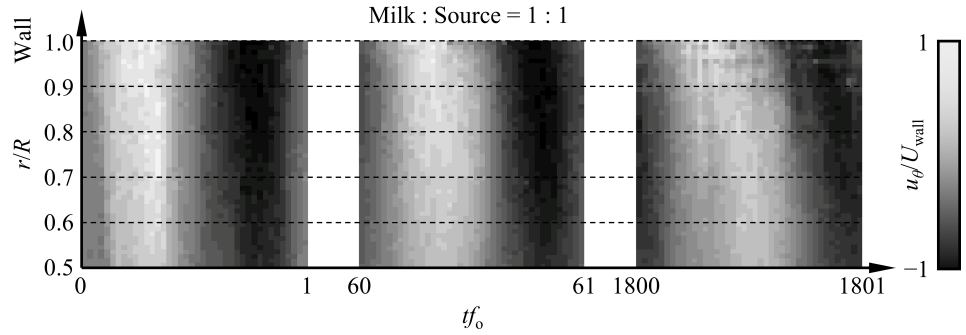


Figure 7.8: Time variations in the azimuthal velocity distributions of a test material (the Milk : Source = 1 : 1 mix) at different elapsed oscillating times, with the oscillation frequency, amplitude, temperature, and the maximum angular velocity, $f_o$ = 1.0 Hz, $\Theta$ = 60 degree, $T_0$ = 15°C, and $U_{wall}$ = 477 mm/s respectively.

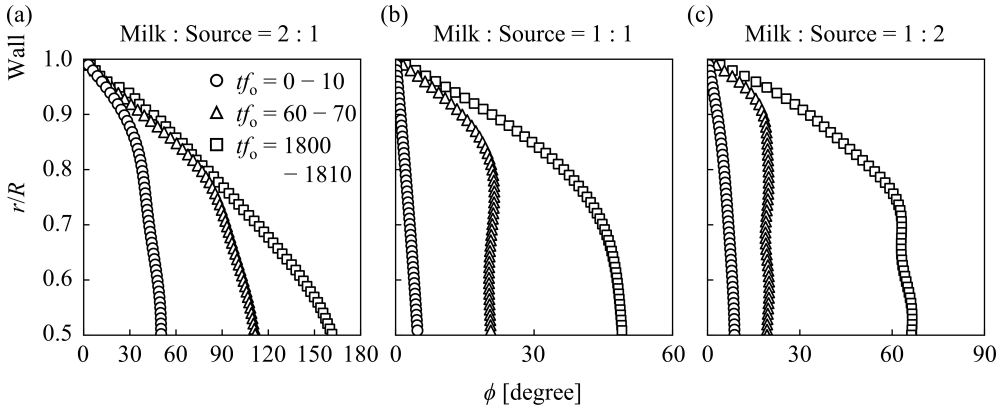


Figure 7.9: Radial profiles of the phase lag of the local velocity fluctuations from the cylinder wall for 10 s times averaging at different elapsed times: (a) Milk : Source = 2 : 1 mix, (b) Milk : Source = 1 : 1 mix, and (c) Milk : Source = 1 : 2 mix, with the oscillation frequency, amplitude, temperature, and the maximum angular velocity, $f_o$ = 1.0 Hz, $\Theta$ = 60 degree, $T_0$ = 15°C, and $U_{wall}$ = 477 mm/s respectively.

by the cylindrical wall, $R$, where the horizontal axis shows the phase lag. Here, the range of phase lags are different for the three materials in Fig. 7.9(a)–(c) to show the differences in the phase lags. The profile shape does not change so much at least after $tf_o$ = 1800, and the profiles are assumed to reach the terminal state at $tf_o$ = 1800. The figures show some similarities in the changes accompanying the development of the phase lag with the oscillation period $tf_o$. These suggest shear thinning of the test material with the shear deformations taking place during oscillations. For the 2 : 1 mix in Fig. 7.9(a), the development is more rapid than for the other mixtures in Figs. 7.9(b) and (c). The terminal phase lag profile ($tf_o$ = 1800−1810) for the 1 : 2 mix [Fig. 7.9(c)] shows a knee around $r/R$ = 0.7 − 0.75, while the profile for the 1 : 1 mix [Fig. 7.9(b)] has smoother variation around the radial position. It suggests that the 1 : 1 mix has a viscoelastic layer functioning as a buffer for the momentum propagation between the liquid and gelled regions. There are also large difference in the terminal phase lag profile between the 1 : 1 and 1 : 2 mixtures, that is, the gradient of the terminal phase lag for the 1 : 2 mix [Fig. 7.9(c)] near the wall ($0.8 < r/R < 1.0$) shows as much larger than that at the 1 : 1 mix [Fig. 7.9(b)]. This can be interpreted as showing a lower viscosity of the 1 : 2 mix [Fig. 7.9(c)] than that of the 1 : 1 mix [Fig. 7.9(b)].

The rheological characteristics of the different test materials can be summarized from experimental results above as follows: the rheological characteristic of the 2 : 1 mix is the one that is most like a liquid and where it is easiest for the gelled structure to break down; in the 1 : 1 mix, the rheological characteristics show a strong viscoelastic response at the interface between the liquid and gelled regions; in the 1 : 2 mix, the rheological characteristic has a more abrupt change at the interface between the regions than is the case for the 1 : 1 mix. These results may then be interpreted to be in close agreement with both the qualitative features of each mixture (Fig. 7.2), as well as that they display the differences suggested by the standard rheometer measurements (§7.3), and overall the rheological characteristics may be described by the terminal shape of the phase-lag, the spatial gradient of the phase-lag.

From the gradient of the phase differences calculated by numerical differential of the phase lag in the radial direction,

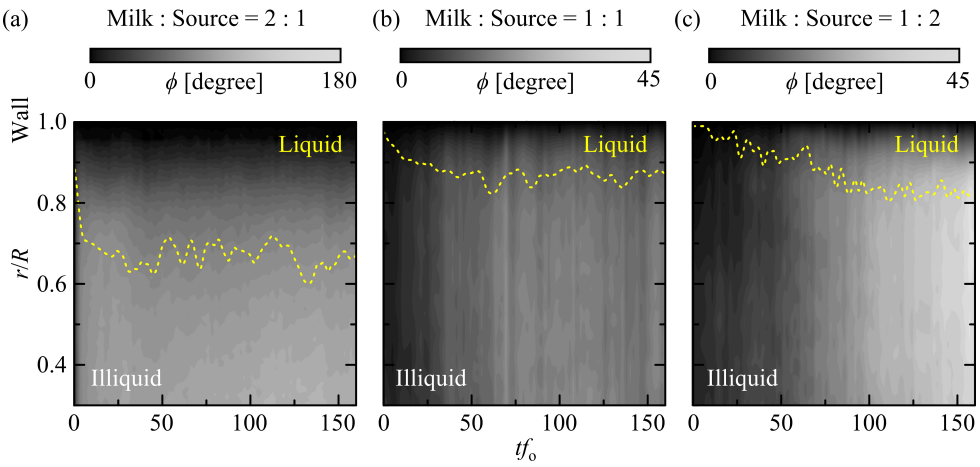


Figure 7.10: Radial-time distribution of phase lags in the local velocity fluctuations from a cylinder wall for (a) Milk : Source = 2 : 1 mix, (b) Milk : Source = 1 : 1 mix, and (c) Milk : Source = 1 : 2 mix, where the dotted curves represent the border between liquid and gelled regions estimated from the gradient of the phase lag, with the oscillation frequency, amplitude, temperature, and the maximum angular velocity, $f_o$ = 1.0 Hz, $\Theta$ = 60 degree, $T_0$ = 15°C, and $U_{wall}$ = 477 mm/s respectively.

the fluid motions in the oscillations suggests a division into liquid and gelled regions. The borderline of the division is now defined as the appearance of "yielding" as determined in this study. The threshold value of the gradient here is set at 10 rad/m corresponding to around $10^4$ mm$^2$/s [Chapter 2]. Figure 7.10 shows the phase lag with respect to the oscillation period $tf_o$. Here, the phase lag profiles in Fig. 7.9 were averaged by 10 periods of oscillations, while those in Fig. 7.10 are not averaged but are as measured profiles calculated from the velocity distributions for 1 s intervals.

For the 2 : 1 mix as shown in Fig. 7.10(a), the phase lag and the yielding border described with a dotted curve varies more rapidly, immediately after the oscillation starts than in the case for the other mixtures shown in Figs. 7.10(b) and (c). Here the gray scale in Fig. 7.10(a) showing the phase lag is different from the others [Figs. 7.10(b) and (c)] because of the drastic changes in the rheological characteristics. In the 1 : 1 [Fig. 7.10(b)] and 1 : 2 [Fig. 7.10(c)] mixtures, the variations in the positions where yielding starts show similar changes and vary more gradually, even immediately after the oscillation starts. The phase lags with the 1 : 2 mix [Fig. 7.10(c)], however, display larger values than that for the 1 : 1 mix [Fig. 7.10(b)].

### 7.4.2 Results of the linear viscoelastic analysis

In the linear viscoelastic analysis by USR, the values of the rheological properties, such as viscosity, elasticity, shear strain rate, shear strain, and shear stress are obtained from the measured spatiotemporal velocity distributions (e.g. Fig. 7.8) [Chapter 5]. Further, by utilizing the gradient of phase-lag as described in §7.4.1, the physical borderline between liquid and gelled states can be simultaneously estimated for every oscillation cycle. To quantify the rheology of the test materials, the rheological evaluations were performed by calculating flow curves from the viscosity and elasticity obtained via the linear viscoelastic analysis.

Figure 7.11 shows the flow curves obtained from averaged Fourier components for each of the test materials, with the vertical and horizontal axes representing the shear rate and shear stress respectively. The gradation of the plots indicates the corresponding radial position in the cylindrical container normalized by $R$. Each symbol in the plots shows the period of the oscillation cycle, $tf_o$, circles: 0–4, triangles: 4–8, squares: 16–20, diamonds: 32–36, pentagons: 64–68, and crosses: 1800–1900. Figures 7.11(a)–(c) show the flow curves in each period for each of the mixtures, and Figure 7.11(d) plots the terminal flow curves ($tf_o$ = 1800 − 1900) obtained from each material together. Such "transient flow curve" is typical in the liner viscoelastic analysis by USR and is not obtained by standard rheometers. Here the ranges of $r/R$ used for the flow curves are from $r/R$ = 0.95 to the radial position corresponding to the physically determined borderline between liquid and gel $r/R > 0.6$.

For the 2 : 1 mix [Fig. 7.11(a)], the flow curves have almost monotonically increasing trends with respect to the shear rate, but the shear stress shows larger values locally at the lowest shear rates in the periods from $tf_o$ = 0 − 4 to $tf_o$ = 64 − 68. The tendencies of these changes are quite similar to the typical flow curves observed in shear banding fluids [7], where most of the results were evaluated by steady rotational tests with standard rheometers in combination with a technique to visualize the inside of the gap between the plates. In the terminal flow curve for the 2 : 1 mix, the gradients of the flow curve are almost constant in the double logarithmic expression in the present range of shear rates. Comparing the initial and terminal

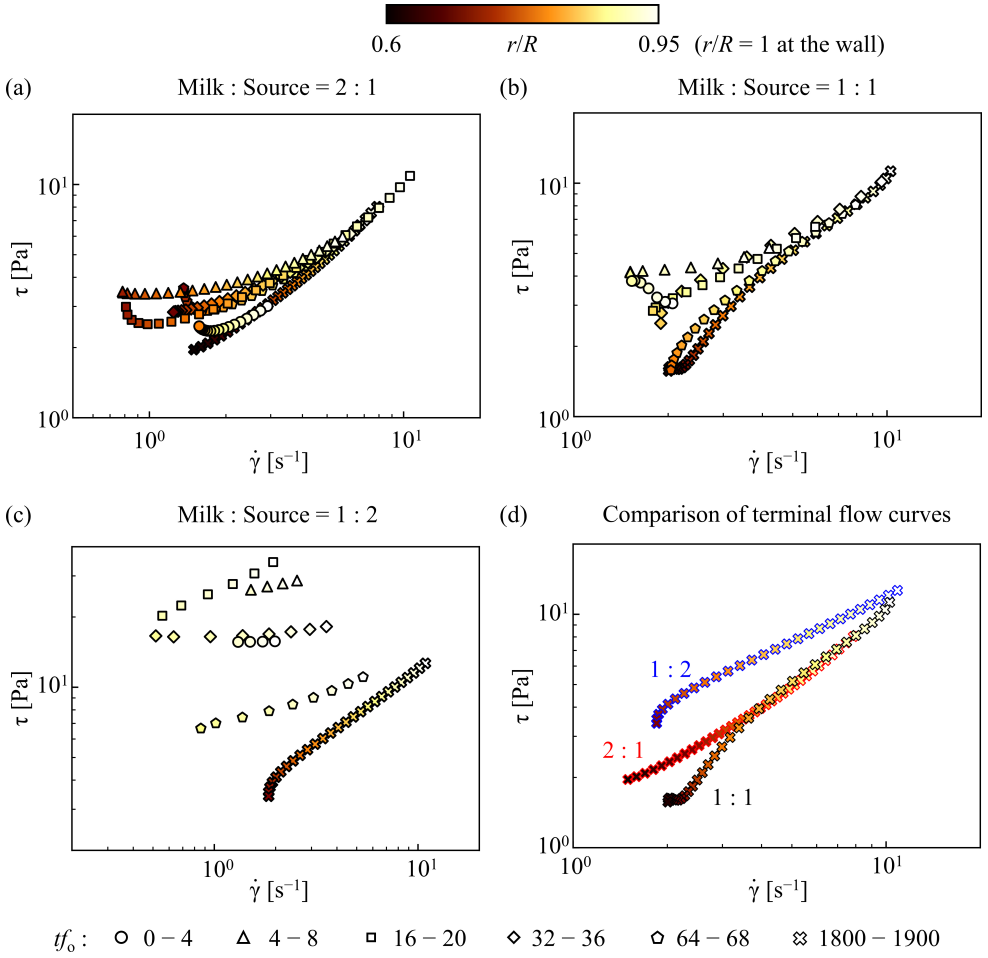


Figure 7.11: Flow curves ($\dot{\gamma}$ versus $\tau$) at different oscillating cycles; (a) Milk : Source = 2 : 1 mix, (b) Milk : Source = 1 : 1 mix, and (c) Milk : Source = 1 : 2 mix, and (d) terminal flow curves at $tf_o = 1800 - 1900$ in each test material, with the oscillation frequency, amplitude, temperature, and the maximum angular velocity, $f_o = 1.0$ Hz, $\Theta = 60$ degree, $T_0 = 15°C$, and $U_{wall} = 477$ mm/s respectively.

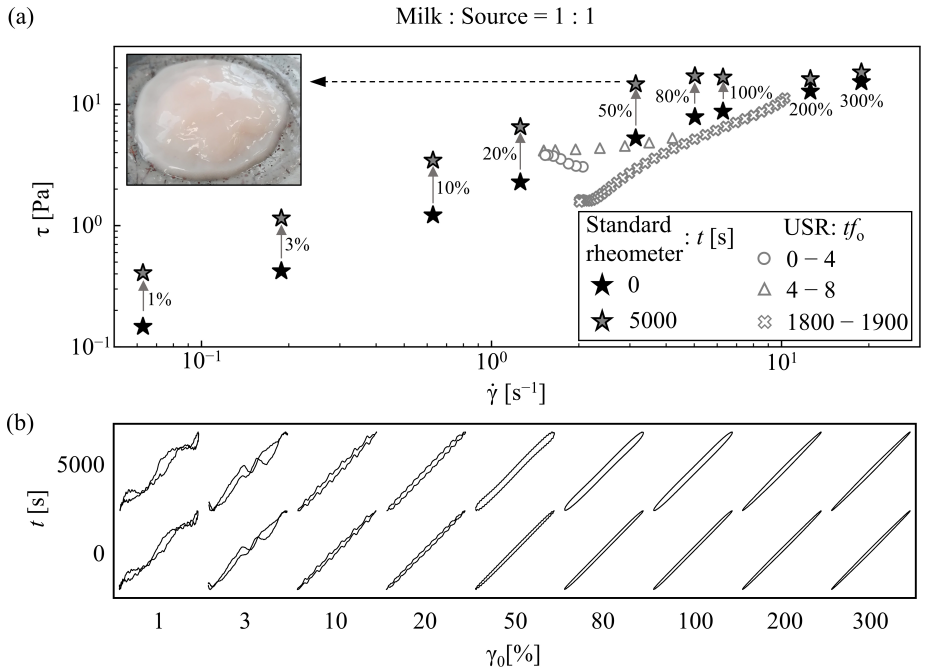


Figure 7.12: (a) Flow curves of the test material (Milk : Source = 1 : 1 mix) in LAOS plotted with USR results and (b) the Lissajous curves (shear stress versus shear strain) plotted with oscillating time versus maximum shear strain $\gamma_0$.

flow curves, it is noteworthy that the flow curves overlap over a wide range of shear rates. For the 1 : 1 mix [Fig. 7.11(b)], the initial flow curve ($tf_o = 0 - 4$) has a negative gradient at smaller shear stresses, and after some periods of oscillations ($tf_o \sim 4 - 16$), the flow curve appears similar to that of the 2 : 1 mix. At the terminal state ($tf_o = 1800 - 1900$), however, the flow curve bends around $\dot{\gamma} = 4$ $s^{-1}$, this may be physically understood to show that the viscous resistance of the test material changes greatly at a specific critical shear rate. For the 1 : 2 mix [Fig. 7.11(c)], the shear stresses in the flow curves from $tf_o = 0 - 4$ to $tf_o = 64 - 68$ are much larger than those of the other materials, and after reaching the terminal state ($tf_o = 1800 - 1900$), the flow curve becomes linear except around the lowest shear rates.

In comparison of terminal flow curves [Fig. 7.11(d)], the gradient of the flow curve of the 1 : 2 mix is the smallest of the three mixtures, and the gradient of the 1 : 1 mix in 4 $s^{-1} < \dot{\gamma} < 10$ $s^{-1}$ is in good agreement with that of the 2 : 1 mix. Further, at shear rates lower than 4 $s^{-1}$, the flow curve of the 1 : 1 mix shows the steepest gradient. Relating these differences in the flow curve to the qualitative observations for each mixture (Fig. 7.2) suggest rheological explanations of behaviors for each of the mixtures: for the 2 : 1 mix, the mixture behaves as a liquid due to the lower yield stresses, however, the mixture sticks to the glass surface after placing the glass plate at flat surface; for the 1 : 1 mix, the main feature is a large viscous resistance in the range of low shear rates, which contributes to sticking to the inclined glass plate (Fig. 7.2). For the 1 : 2 mix, the agglutinating property is much smaller than in the other mixtures because of the decrease in viscous resistance after yielding.

Figure 7.12(a) shows both flow curves for the 1 : 1 mix in the rheological evaluations of USR and with the standard rheometer, where the flow curves (stars) were calculated from experiment in Fig. 7.6. The vertical and horizontal axes represent the shear rate and shear stress respectively, but the values for the standard rheometer are apparent values as mentioned in §7.3. The shear stresses at $t = 5000$ s by the standard rheometer are much larger than those by USR, but at $t = 0$ s the standard rheometer values show good agreement with the 5 $s^{-1} < \dot{\gamma}$ values by USR at the terminal state. Figure 7.12(b) shows the Lissajous curves, obtained by LAOS at the experiments in Fig. 7.12(a), and help to elucidate the factors causing the differences in the flow curves. The amplitude of the apparent shear stresses increases with time because of the restoration of the structures present in the mixtures, i.e. thixotropy, however, an increased influence of the viscous characteristics can be observed from the shape of the Lissajous curves at $\gamma_0 = 50$, 80, and 100%. If the test materials display thixotropy, the rheological properties would shift from somewhat viscous to elastic, but the results of the Lissajous curves show an opposite change. It may be suggested that the rheological evaluations of the standard rheometer are influenced by shear banding causing the occurrence of a depleted layer at the oscillating wall. The apparent shear rate would increase if there is a thin layer causing the shear banding, and the presence of this can be assumed from the changes in the rheological properties displayed in the flow curves obtained by USR.

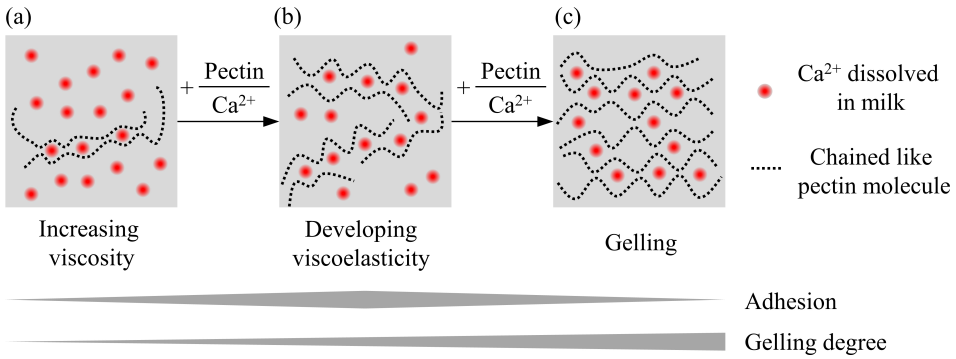


Figure 7.13: Schematic visualization of the gelling features for different ratios of included pectin and calcium ions; (a) Pectin/$Ca^{2+}$ ratio is low, e.g. whole milk : Fruiche source = 2 : 1, (b) Pectin/$Ca^{2+}$ ratio is moderate, e.g. whole milk : Fruiche source = 1 : 1, and (c) Pectin/$Ca^{2+}$ ratio is high, e.g. whole milk : Fruiche source = 1 : 2.

The depleted layer as the result of shear banding can be seen on the photograph [Fig. 7.12(a)] taken after removing the shaft of the standard rheometer following the long duration measurements at $\gamma_0 = 50\%$. As also described in §7.3.2, material was attached to the bottom plate in the form of a solid structure of a thin layer of $O(0.1$ mm) thickness, with the material at the top was softer and could be deformed because of shearing by the upper plate. The speculations of a shear banding effect in the gap is strongly supported by this observation.

### 7.4.3 Discussion: the rheology of a better-prepared dessert

From the rheological evaluations by USR based on fluid mechanics, the relations of the shear strain rate and shear stress around the critical shear rate for yielding were quantified. These findings are significant as it is difficult to evaluate the true-rheological properties mentioned in §7.3 with the standard rheometer. The schematic illustrations in Fig. 7.13 summarize the findings: The figure represents the gelling behavior schematically with the ratio of included $Ca^{2+}$ and pectin. When the ratio is low [Fig. 7.13(a)], for the whole milk : Fruiche source = 2 : 1 there is a low concentration of structured pectin, and it does not contribute to gelling but it increases the viscosity. With moderate ratios [Fig. 7.13(b)] for whole milk : Fruiche source = 1 : 1, the flow curve indicates a secondary critical shear rate that should be distinguished from the critical shear rate for yielding. It is thought that the pectin inclusion caused the formation of structures of chained networks that lead to the viscoelastic behaviors at lower shear rates than the critical shear rate for yielding. The result of this would be that the material shows strong viscoelasticity arising from the electrical attraction between the included calcium ions and dispersed pectin. Finally, for higher pectin ratios [Fig. 7.13(c)], for whole milk : Fruiche source = 1 : 2, the yield stress estimated by USR shows larger values, and the viscosity is lower than the mixture with intermediate ratios; this may be interpreted to suggest that the gelled structures were fully developed and that further the material has only a small influence on the viscosity increase arising from the electrical attraction after yielding.

If the recipe suggested by the food company is assumed to provide the best eating quality (or texture), evaluations of these are given as the rheological property of moderate viscoelasticity and yield stress as described above. Further, the stability of gelled structures with moderate yield stress is also required to be evaluated, and the stability might be supported by the thixotropic behavior as the structures need to be maintained after stirring.

## 7.5 Conclusion

Rheological evaluations on three test mixtures, prepared by adding whole milk to Fruiche (a commercially available desert) source in different ratios, were conducted by both a standard rheometer and by USR for a better understanding of qualities and physical features evaluated as better quality for eating. By the standard rheometer with parallel plate geometry, the evaluations showed inaccuracies in measuring accurate rheological properties caused by commonly existing problems in the rheometers (wall-slip, shear banding, shear localization, elastic instability, and more); for steady rotational tests, there are the problems around the critical shear causing yielding or slipping of the test material on walls, and the rheological evaluations showed significant differences between the shear rate and stress sweep data. In oscillatory tests, there were drastic changes in the storage and loss moduli in shear amplitude sweeps, especially at low oscillation frequencies, and the Lissajous curves suggested unexplained problems by LAOS measurements.

To better understand the inaccuracies in measuring the true-rheological properties by the standard rheometer, the rheology representing the textures of complex food materials was suggested using USR based on the equation of motion and spatiotemporal velocity information. In conclusion, the flow curves for all the test materials evaluated by USR showed more reliable rheological characteristics than the data obtained by the standard rheometer. The word "reliable" here means guaranteed precisions with physical meaningfulness. Some unclarities in the rheological evaluations using standard rheometer were found from the experimental results (§7.3). Not surprisingly, such complex test fluid showing rheological changes drastically against shear deformations must affect the rheological tests. Based on the equation of motion, the USR can evaluate rheological properties from the measured velocity profiles, and in this paper, presented true-rheological properties from the perspective of physics of fluids compared to standard rheometers.

The significant findings were represented as follows; transient flow curves were acquired by linear viscoelastic analysis in USR at each period of oscillations and that could not be obtained using the standard rheometer; comparing the rheological evaluations by USR and LAOS measurements, the efficacy of USR was ensured by the obtained Lissajous curves; the qualitative-rheological characteristics of the test materials prepared by different recipes support the validity regarding the evaluated flow curves.

## References


[1] G. Heirman, L. Vandewalle, D. Van Gemert, and O. Wallevik, "Integration approach of the Couette inverse problem of powder type self-compacting concrete in a wide-gap concentric cylinder rheometer," J. Non-Newtonian Fluid Mech. 150, 93–103 (2008).

[2] Y. L. Yeow, W. C. Ko, and P. P. Tang, "Solving the inverse problem of Couette viscometry by Tikhonov regulation," J. Rheol. 44, 1335–1351 (2000).

[3] C. Ancey, "Solving the Couette inverse problem using a waveletvaguelette decomposition," J. Rheol. 49, 441–460 (2005).

[4] L. P. Paduano, T. Schweizer, C. Carotenuto, J. Vermant, and M. Minale, "Rough geometries with viscoelastic Boger fluids: Predicting the apparent wall slip with a porous medium approach," J. Rheol. 63, 569–582 (2019).

[5] W. Wolthers, M. H. G. Duits, D. Van Den Ende, and J. Mellema, "Shear history dependence of the viscosity of aggregated colloidal dispersions," J. Rheol. 40, 799–811 (1996).

[6] P. Fischer, E. K. Wheeler, and G. G. Fuller, "Shear-banding structure orientated in the vorticity direction observed for equimolar micellar solution," Rheol. Acta 41, 35–44 (2002).

[7] T. Divoux, M. A. Fardin, S. Manneville, and S. Lerouge, "Shear banding of complex fluids," Annu. Rev. Fluid Mech. 48, 81–103 (2016).

[8] R. Artoni, and P. Richard, "Torsional shear flow of granular materials: shear localization and minimum energy principle," Computational Particle Mechanics 5, 3–12 (2018).

[9] O. Nechyporchuk, M. N. Belgacem, and F. Pignon, "Rheological properties of micro-/nanofibrillated cellulose suspensions: Wall-slip and shear banding phenomena," Carbohydr. Polym. 112, 432–439 (2014).

[10] K. Yang, and W. Yu, "Dynamic wall slip behavior of yield stress fluids under large amplitude oscillatory shear," J. Rheol. 61, 627–641 (2017).

[11] G. H. McKinley, J. A. Byars, R. A. Brown, and R. C. Armstrong, "Observations on the elastic instability in cone-and-plate and parallel-plate flows of a polyisobutylene Boger fluid," J. Non-Newton. Fluid Mech. 40, 201–229 (1991).

[12] T. Gallot, C. Perge, V. Grenard, M. A. Fardin, N. Taberlet, and S. Manneville, "Ultrafast ultrasonic imaging coupled to rheometry: Principle and illustration," Rev. Sci. Instrum. 84, 045107 (2013).

[13] M. A. Fardin, C. Perge, L. Casanellas, T. Hollis, N. Taberlet, J. Ortín, S. Lerouge, and S. Manneville, "Flow instabilities in large amplitude oscillatory shear: a cautionary tale," Rheol. Acta 53, 885–898 (2014).

[14] M. A. Fardin, L. Casanellas, B. Saint-Michel, S. Manneville, and S. Lerouge, "Shear-banding in wormlike micelles: Beware of elastic instabilities," J. Rheol. 60, 917–926 (2016).

[15] B. Derakhshandeh, D. Viassopoulos, and S. G. Hatzikiriako, "Thixotropy, yielding and ultrasonic Doppler velocimetry in pulp fibre suspensions," Rheol. Acta 51, 201–214 (2012).

[16] B. Ouriev, and E. Windhab, "Transient flow of highly concentrated suspensions investigated using the ultrasound velocity profiler–pressure difference method," Meas. Sci. Technol. 14, 1963–1972 (2003).

[17] T. Shiratori, Y. Tasaka, Y. Oishi, and Y. Murai, "Ultrasonic velocity profiling rheometry based on a widened circular Couette flow," Meas. Sci. Thechnol. 26, 085302 (2015).

[18] *Ultrasonic Doppler Velocity Profiler for Fluid Flow*, Springer Science, edited by Y. Takeda (Springer, Tokyo, 2012).

[19] Y. Tasaka, T. Kimura, and Y. Murai, "Estimating the effective viscosity of bubble suspensions in oscillatory shear flows by means of ultrasonic spinning rheometry," Exp. Fluids 56, 1867 (2015).
[20] T. Yoshida, Y. Tasaka, H. J. Park, Y. Murai, H. Teramura, and S. Koseki, "Inner structure visualization of fresh fruits utilizing ultrasonic velocity profiler," J. Vis. 21, 253–265 (2018).
[21] J. T. Fu, and M. A. Rao, "Rheology and structure development during gelation of low-methoxyl pectin gels: The effect of sucrose," Food Hydrocolloid 15, 93–100 (2001).
[22] M. A. V. Axelos, and J. F. Thibault, "The chemistry of low-methoxyl pectin gelation," The chemistry and technology of pectin 6, 109–108 (1991).
[23] A. J. Giacomin, and J. M. Dealy, "Large-amplitude oscillatory shear," In Techniques in rheological measurement (pp. 99–121). Springer, Dordrecht (1993).
[24] C. Perge, N. Taberlet, T. Gibaud, and S. Manneville, "Time dependence in large amplitude oscillatory shear: A rheo-ultrasonic study of fatigue dynamics in a colloidal gel," J. Rheol. 58, 1331–1357 (2014).
[25] B. Derakhshandeh, S. G. Hatzikiriakos, and C. P. Bennington, "The apparent yield stress of pulp fiber suspensions," J. Rheol. 54, 1137–1154 (2010).
[26] H. A. Barnes, "Thixotropy—A review," J. Non-Newtonian fluids Mech. 70, 1–33 (1997).

Chapter 8

# Thixotropic effects on a standard rheometer test, elucidated by large amplitude oscillatory shear & USR

## Contents


**8.1 Introduction . . . 120**
**8.2 Materials and method . . . 121**
8.2.1 Thixotropy in montmorillonite (Mt) dispersion . . . 121
8.2.2 Ultrasonic spinning rheometry (USR) . . . 122
8.2.3 Standard shear rheometer . . . 123
**8.3 Rheological evaluations of Mt dispersions w/o and with NaCl . . . 124**
8.3.1 Dynamic viscoelasticity examined by rotational rheometer . . . 124
8.3.2 Comparison of rotational rheometer data of LAOS and USR . . . 126
**8.4 Discussion . . . 128**
8.4.1 Summary of findings from LAOS/USR measurements . . . 128
8.4.2 Fourier analysis of the waves considered to result from elastic instabilities . . . 128
8.4.3 Consideration of artifacts due to thixotropy in standard rheometers . . . 130
**8.5 Conclusion . . . 131**
**References . . . 131**


## Preface

The aim in this chapter is to elucidate the measurement difficulties of a standard rheometer that is caused by a transient phenomena in the thixotropic features, by means of both LAOS and USR. The potential of the kinematic rheometry to assume the role of filling "a hole" in the standard rheometer measurements as a complementary methodology is supported by this work.

## Abstract


Rheological evaluations of thixotropic fluids were examined by both the oscillatory test using a standard rheometer with Taylor–Couette geometry and ultrasonic spinning rheometry (USR); the USR is a novel velocity-profiling rheometry with details presented in [Yoshida *et al.*, J. Rheol. 63 (2019)]. In the conclusions, measurement difficulties with the standard rheometer due to thixotropy causing a transient state were elucidated by considering the findings in both large amplitude oscillatory shear (LAOS) and USR. The flow curves obtained from the standard rheometer did not show physically meaningful results with any assurance of accuracy due to unexpected issues including shear localization, shear banding, slip on the walls, and elastic instabilities, even when an equilibrium state is reached by conducting long duration measurements. The significant findings are summarized as follows: (i) when the torque response measured by the standard rheometer represents clearly sinusoidal waves, the flow curve by the USR coincides with that by the standard rheometer; (ii) when the shapes of the Lissajous curve in LAOS represent occurrences of the unexpected problems, the shear stress obtained by the standard rheometer was around ten times higher than that by the USR; (iii) the onset of elastic instability in the Lissajous curves could be observed near the critical shear rate evaluated by the USR.

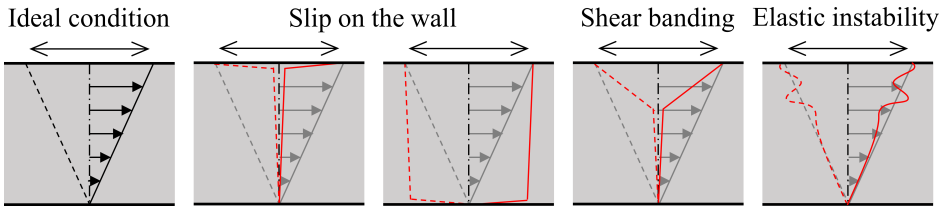


Figure 8.1: Shear deformation types in the measurement gap between the moving wall for ideal and non-ideal conditions.

## 8.1 Introduction

To fully understand the rheology of "complex" fluids, measurements of the axial torque via solid walls with specific gaps, rheometers with various geometries such as parallel plates, cone-plates, and Taylor–Couette (TC), are used. As described in Fig. 8.1, there are however common problems among these, related to shear history effects [1], slip on the walls [2, 3], shear banding [2, 4–7], elastic instability [8–10], and more. Rheometers can measure a simple shear resistance as an axial torque represented by the viscous resistance (the elastic response) in the fluid media. A narrow gap $O$(0.1–1 mm) is required to satisfy conditions of constant shear rates or strains in the gap (i.e. linear velocity profiles or linear deformations); however, most actual flows and deformations in complex fluids show non-linearities in the gap arising from the common problems mentioned above. The measured results merely represent apparent viscosities because of unexpected actual shear-rate profiles arising during the measurements.

To solve these problems, there is the semi-analytical approach which involves solving an inverse problem, i.e. the "Couette inverse problem", to estimate original velocity profiles in wider gap TC rheometry. There are a number of approaches for rheological evaluations of non-Newtonian fluids [11, 12] most of which are limited to treatments of the problem for specific test fluids, influenced by the elastic instability that is a difficult issue to overcome. As another approach there are efforts involving surface modifications to the plates in the rheometers [3, 13]. These however offer solutions to only the slip on the walls, leaving out the influences from shear banding, shear localization, elastic instability, and others, unavoidable because such phenomena will present transient (unsteady) behaviors arising from non-Newtonian effects.

Utilizing spatiotemporal velocity distributions of fluid motion, complete flow field measurements would provide the most appropriate solutions because the velocity information reflects all rheological information in the solutions. As examples of velocity-profiling rheometries based on ultrasonic velocity profiling (UVP) [14], approaches coupled with velocimetries have been proposed; Derakhshandeh *et al.* [15] performed measurements of transient behaviors of thixotropic fluids using a Couette rheometer with a wide gap and UVP. This can detect yielding regions in the fluid with quasi-steady velocity profiles, while the torque measurements may be influenced by the wall-slip leading to errors in the evaluation of the rheological properties. Ouriev and Windhab [16] proposed a combined technique of UVP measurements and pressure difference measurements, termed UVP-PD in-line rheometry. These reports have dealt with time-averaged velocity profiles limited to steady flow states, while techniques are required to detail time-dependent properties considering the applicability to more complex fluids and solutions (Thixotropic fluid).

In Chapters 2–7, Ultrasonic spinning rheometry (USR) has been developed as a novel velocity-profiling rheometry; the important improvements over conventional velocity-profiling rheometries in the results here lie in the ability to examine unsteady shear flows and to substitute experimental data into the equation of motion to solve the rheological flow problem. In Chapters 2 and 3, the phase-lag analysis of USR was established by performing a series of rheological measurements, including the effective Newtonian viscosity of clay dispersions with thixotropy, liquid food gelling behaviors with tiny ingredients, and curry paste containing larger ingredients. Because the phase-lag analysis still limits the evaluation of rheological parameters, a linear viscoelastic analysis in a frequency domain was presented in Chapter 4, and it was suggested that the equation of motion with the rheological model can be satisfied by substituting Fourier components of velocity fluctuations. In the theory of linear viscoelastic analysis of USR, making it possible for multiple rheological properties to be determined with the velocity profile measurements alone.

The efficacy of this methodology for non-Newtonian fluids was strongly supported by previous work in Chapter 5, where comparative assessments of the rheological evaluations of a standard rotational rheometer and USR were performed. In the efficacy assessments, significant differences were found in rheological evaluations of clay dispersions displaying thixotropy between a standard rheometer with a parallel plate geometry and USR, with experiments using a standard rheometer examined under steady state conditions. Most recently, the USR has described the rheology in complex fluids, the effective viscoelasticity modulated by particle alignment [Chapter 6] and the rheology of gelled food useful in making better tasting desserts [Chapter 7]. Overall, the USR may be expected to be able to elucidate outstanding problems in complex fluid dynamics.

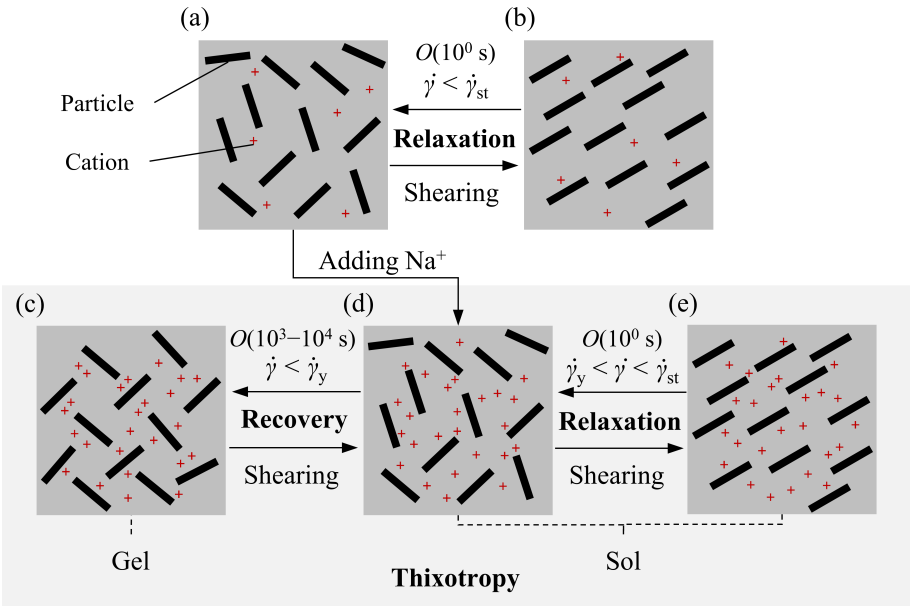


Figure 8.2: Transition diagrams of particle structuring in the Mt dispersion: swelling in deionized water, (a) after leaving at rest, (b) shearing; and swelling in an ionic solvent, (c) left at rest for long durations, (d) transient state, and (e) shearing.

Rheological evaluations by USR have been validated in Chapter 5 by steady rotational tests with a standard parallel plate geometry rheometer, however one remaining issue is whether oscillatory tests with TC geometry that are considered to be more precise as determined in experiments comparing with the USR and considering consistency between various experimental geometries still needs to be verified. The research objective here is to clarify ambiguities in the methodologic difficulties in standard rheometers, and the rheological evaluations of thixotropic fluids were examined by large amplitude oscillatory shear (LAOS) using TC geometry (§8.3). Further, a comparison in the evaluations of LAOS and USR is examined to ensure the efficacy of USR in understanding the measurements of the thixotropic fluids. The approach to using LAOS measurements to understand the unexpected differences in the rheologic data when studying thixotropic fluids was outlined by Perge *et al*. [17]. Finally, from the findings of the comparison of the rheological evaluations of LAOS and USR, methodologic difficulties to evaluate thixotropic fluids using standard rheometers is discussed (§8.4).

## 8.2 Materials and method

### 8.2.1 Thixotropy in montmorillonite (Mt) dispersion

As the test fluid, a montmorillonite (Mt) dispersion was chosen (Kunipia-F; Kunimine Industries Co., Ltd., Japan). In the case of dilute concentration $O$(1 wt.%), the particles are dispersed homogeneously without sedimentation in deionized water; here cations in the medium are supplied by the ionization of the swelled particles [Fig. 8.2(a)]. Oriented in the sheared direction, the rheological properties of the dispersion show a shear-thinning viscosity. The particle orientations would be relaxed due to the Brownian motion for shear rates, $\dot{\gamma} < \dot{\gamma}_{st}$ [Fig. 8.2(b)], where $\dot{\gamma}_{st}$ is a threshold of shear strain rates for the onset of the particle orientation relaxation.

The dispersion of Mt particles swelled in ionic solvents shows thixotropy due to networks of the particles structured by particle interactions in non-sheared situations [18]. At higher pH than the isoelectric point and with dilute concentrations of cations, the dispersed particles form structures termed “House-of-cards” [19] showing fluctuations with time due to the structuring by the particle interactions [Fig. 8.2(c)]. These are structurally stable, because the surface of the dispersed particles is electrically charged by the particles swelling in water. As shown in Fig. 8.2(d), these global particle networks are easily broken into smaller clusters with Mt concentrations of less than $O$(10 wt.%). In simple shear cases, the macroscopic rheological properties involve shear-thinning due to the alignment of the particles in parallel to the shear direction [Fig. 8.2(e)]. The aligned particles relax with time similar to the condition in Fig. 8.2(b), but the relaxation is influenced by the concentration of cations. Generally, the series of rheological characteristics outlined in Figs. 8.2(c)–8.2(e) is categorized as thixotropy [18], and the thixotropic behavior plays a critical role in shear localization or shear banding.

Important factors to determine the rheological features in Mt dispersions may be summarized by the: volume fraction of

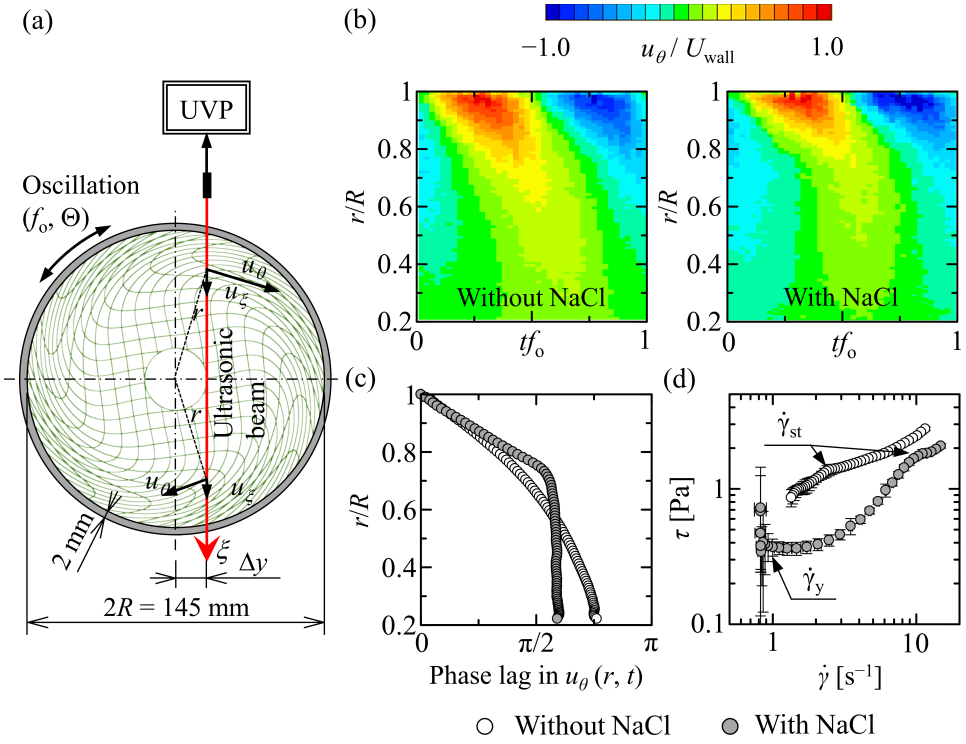


Figure 8.3: (a) Schematic of the experimental apparatus for measuring velocity distributions of oscillating shear flows using UVP, (b) spatiotemporal velocity distribution without NaCl and with 0.02 mol/L NaCl, (c) phase-lag profiles calculated from the $u_\theta(r,t)$ in (b), and (d) flow curves evaluated by linear viscoelastic analysis by USR [Chapter 5], where the $\dot{\gamma}_y$ and $\dot{\gamma}_{st}$ denote the critical shear rate at the onset of yielding and shear thinning [Chapter 3], $T_f$ = 25°C, $f_o$ = 0.5 Hz, Θ = 2π/3 rad; $U_{wall}$ = 477.0 mm/s.

the dispersed particles, cation concentration, pH value of the fluid medium, fluid temperature, relaxation time, recovery time, shear amplitude, and more. In this paper the focus is on modifications of the rheology in the shear amplitude, to simplify the problem setting.

### 8.2.2 Ultrasonic spinning rheometry (USR)

One of the main characteristics of the experimental apparatus is an open cylindrical container made of acrylic resin [Fig. 8.3(a)]. The container has 2-mm-thick side walls, 145-mm inner diameter, and is 60-mm high. To control the temperature of the test fluids at $T_f$ = 25°C, and to avoid any influence from ultrasonic waves co-reflected at the wall, the container was mounted at the center of a water bath. Oscillations of the cylinder was controlled by a stepping motor to an oscillation angle Θ and frequency $f_o$, with the motor attached at the bottom of the container. The oscillation was controlled by the sinusoidal angular velocity, $U_{wall}\sin(2\pi f_o t)$, where $U_{wall} = 2\pi f_o R\Theta$ (see [18] for further details). The UVP-Model Duo (Met-Flow S.A., Switzerland) was used to measure instantaneous velocity distributions. To obtain the azimuthal velocity component, an ultrasonic transducer (resonance frequency 4 MHz and 5-mm active element diameter) was mounted with a gap of $\Delta y$ from the center coordinates of the cylindrical container. Assuming that the axisymmetric flow and the radial velocity components are negligible, the azimuthal velocity $u_\theta$ is calculated from a geometric relation given as $u_\theta = u_\xi r/\Delta y$. Empirically, $\Delta y$ = 15 mm was selected, and further details of the setup for the transducer are detailed in Chapters 2–5.

The spatiotemporal velocity distributions of different test fluids were measured using UVP as shown in Fig. 8.3(b); Mt dispersions without NaCl and with 0.02 mol/L NaCl were used as test fluids. The vertical and horizontal axes indicate the radial positions normalized by the radius of the container, $R$, and the spin-cycle period $tf_o$. The contours represent the azimuthal velocity normalized by $U_{wall}$ = 477.0 mm/s, the maximum azimuthal velocity at the cylinder wall ($r/R$ = 1). The azimuthal velocity fluctuations decrease towards the center of the container since the momentum propagation is diffused by viscous damping. To quantify these phase lags in the velocity fluctuation, a discrete Fourier transform (DFT) was applied. The oscillation in this system kept the frequency and angle at a constant value ($f_o$ = 0.5 Hz, Θ = 2π/3 rad), so the response of the fluid motion appears at this dominant frequency. Radial profiles of the phase lag, $\varphi(r) = \tan^{-1}(\Im[\hat{u}_\theta(r,\omega_o)]/\Re[\hat{u}_\theta(r,\omega_o)])$ –

$\varphi_{wall}$, calculated from the velocity distributions shown in Fig. 8.3(b) are detailed in Fig. 8.3(c) (see Chapters 2 and 3 for more details). The vertical and horizontal axes show the radial position normalized by the radius of the cylindrical container and the phase lag that is propagated from the wall. There is a significant difference between the phase lags for the dispersions without NaCl and with 0.02 mol/L NaCl. Further the phase lag with the NaCl has a sharp knee at $r/R = 0.7$. The relation between the shear stress and shear rate, the flow curve, can be obtained as shown in Fig. 8.3(d), utilizing the Fourier components obtained from the velocity (see Chapter 5 for details of the derivation of the rheological properties).

In Chapter 3, flow curves in the Mt dispersion have critical shear rates that would be caused by modifications of the particle networks; $\dot{\gamma}_y$ and $\dot{\gamma}_{st}$ express the critical shear rates at the yield stress and the critical shear rate at the onset of shear thinning. As seen in Fig. 8.3(d), the trends with the flow curves are similar to those in Chapters 3 and 5, and the critical points defined in those are used in this work.

### 8.2.3 Standard shear rheometer

A rheometer with a geometry of TC (Anton Paar MCR-502, Couette geometry CC27; radius of inner cylinder, $R_i = 27$ mm; gap between inner and outer cylinder $R_o - R_i = 1.13$ mm with a length $L = 40$ mm) was used to compare the results with the rheometer to the USR measurements for the Mt dispersions (§8.2.2). The test fluids were maintained at a constant temperature ($T_f = 25°C$). In the oscillatory test, the phase lag $\delta$ can be calculated from the phase angle difference between the maximum value of the torque amplitude and deflection angle at the inner cylinder. As suggested in Fig. 8.4(a), the $\delta$ can represent the degree of fluid viscoelasticity: $\delta = 0$ rad, $0 < \delta < \pi/2$ rad, and $\delta = \pi/2$ rad indicating elastic, viscoelastic, and viscous characteristics, respectively. The shapes of Lissajous curves plotted by the shear strain/shear rate and shear stress as the horizontal and vertical axes help in distinguishing the rheological characteristics [Fig. 8.4(b)]. Lissajous curves expressing shear strain and shear stress plot as circles for viscous, ellipses for viscoelastic, and diagonal lines for elastic behaviors [20] and Chapter 7. If the torque response from the test fluid versus the shear deformation can be assumed as an ideal sinusoidal function, the storage and loss moduli, $G'$ and $G''$, are given by

$$G' = \frac{\tau_0}{\gamma_0}\cos\delta, \quad G'' = \frac{\tau_0}{\gamma_0}\sin\delta, \tag{8.1}$$

where $\tau_0$ and $\gamma_0$ are the maximum value of the shear stress and shear amplitude. Further, the $\delta$ can be measured in two ways: (1) by calculating the difference between the maxima of the shear stress and shear strain or (2) fast Fourier transform. Expressions to determine $\tau_0$ and $\gamma_0$ are,

$$\tau_0 = \frac{M_i}{2\pi R_i^2 L}, \quad \gamma_0 = \frac{R_o + R_i}{R_o - R_i}\frac{\theta}{2}, \tag{8.2}$$

where $M_i$ and $\theta$ denote the maximum torque measured at the inner cylinder and angular displacement, respectively. To derive Eq. (8.2) from the geometric relation, assumptions satisfying linearity with respect to the radial position for the shear stress $\tau$ and shear strain $\gamma$ are required. If the torque response does not follow a sinusoidal curve due to shear banding, wall slip, and other confounding factors, artifacts showing apparent values obtained from the rheometer will be included.

The applicable range, therefore, should be limited to that within the obtained sinusoidal waves showing a linear response in the oscillatory tests, this is termed the linear viscoelastic range (LVE range). However, users of a rheometer must generally evaluate the ranges solely based on the output profiles of $G'$ and $G''$ in amplitude sweep measurements. The oscillatory tests in the LVE range are regarded as small amplitude oscillatory shear (SAOS) measurements, and larger shear amplitudes (non-linear viscoelastic range) are defined as large amplitude oscillatory shear (LAOS) [3, 6, 8, 17, 20]. By LAOS, non-sinusoidal responses can be qualitatively interpreted as the non-linear rheological response, depending on the rheological characteristics with complexities (viscoelasticity, yield stress, multi-phase dispersions, and more). The purpose of utilizing LAOS measurements here is to establish and understand the rheological complexities in the test solution, and it will also help to show and highlight ambiguities in the rheological evaluations of the standard rheometer.

In this study, the output stress was obtained under a strain-controlled condition, and the output strain was calculated from the rotation angle of the TC shaft. To assess the rheological properties in the time development of the Mt dispersion, the LAOS measurements were conducted under sinusoidal shear strain $\gamma = \gamma_0 \sin(2\pi f_o t)$, where the maximum shear strain and oscillation frequency are given as $\gamma_0 = 1 - 500\%$ and $f_o = 0.5$ Hz after pre-shearing (400 $s^{-1}$) for 120 s [Fig. 8.4(c)]. By conducting sufficient pre-shearing to break the particle networks in the Mt dispersion, the influence of slip on the walls and inhomogeneities in the rheological properties could be eliminated at the start of the oscillatory tests. Following this, the tests were continued for 5000 s under unchanged experimental conditions to evaluate the rheological modulation with elapsed time, the thixotropic effect.

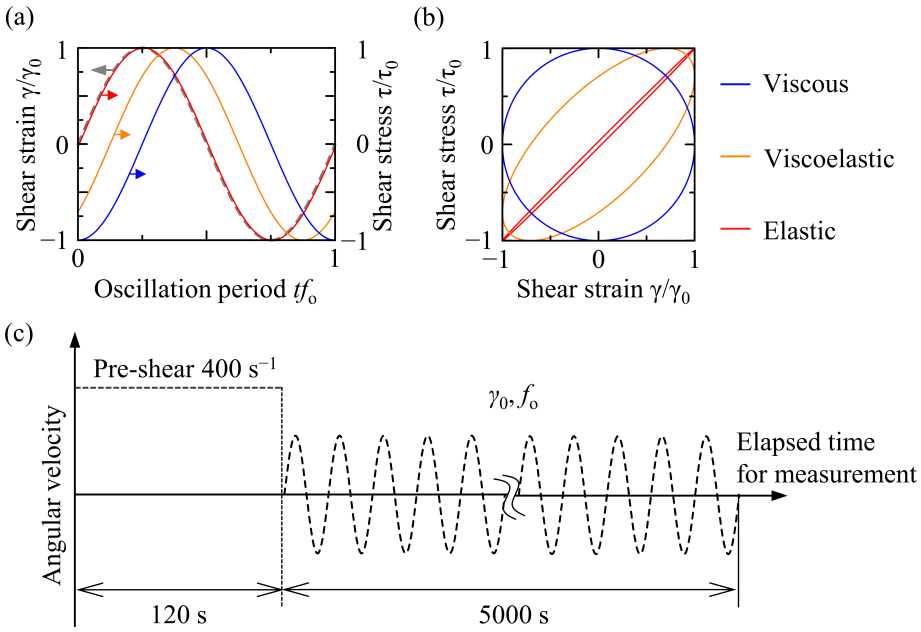


Figure 8.4: (a) Ideal fluid responses plotting the shear stress versus the applied shear strain, (b) ideal features of Lissajous curves in shear strain versus shear stress, and (c) pathway of the angular velocity for oscillatory tests using the rheometer with the TC geometry.

## 8.3 Rheological evaluations of Mt dispersions w/o and with NaCl

### 8.3.1 Dynamic viscoelasticity examined by rotational rheometer

The profiles of $G'$ and $G''$ for a Mt dispersion both w/o and with NaCl were measured at various shear amplitude $\gamma_0$ for 5000 s with the oscillation frequency fo set to $0.5Hz$. In Fig. 8.5, the vertical and horizontal axes depict the shear amplitude $\gamma_0$ and elapsed time $t$, and the logarithmic contour from 0.1 Pa to 300 Pa shows the magnitudes of $G'$ and $G''$. The contours show clear differences between Figs. 8.5(a) and 8.5(c), and also between Figs. 8.5(b) and 8.5(d); the contours remain unchanged with time without NaCl [Figs. 8.5(a) and 8.5(b)], while there are intense modulations in the contours when NaCl has been added, especially at $2 < \gamma_0 < 20\%$ [Figs. 8.5(c) and 8.5(d)]. The start of occurrence of the modulations is suggested by the red dotted curves in Figs. 8.5(c) and 8.5(d), suggesting that the duration for the occurrences of the modulation to arise becomes shorter with increasing $\gamma_0$. This suggests the possibility that unexpected phenomena like wall-slip may happen in the unstable balance between the shear amplitude and recovery of the particle networks in the Mt dispersions.

To better understand the shear strain and time contours [Fig. 8.5], Fig. 8.6 shows the profiles of $G'$ and $G''$ extracted from the contours at $\gamma_0$ at $t$ = 100, 1000, and 5000 s. In comparison of Figs. 8.6(a)–8.6(c), these profiles are very similar at $\gamma_0 > 5\%$ but show slight difference at $\gamma_0 < 5\%$ due to the structure relaxation as described in Fig. 8.2. The measurements for the Mt dispersion with 0.02 mol/L NaCl here were conducted with smaller steps in the shear strain $\gamma_0$ than that without NaCl, as it was speculated that the condition of Mt dispersion without NaCl could be more unstable. Figs. 8.6(d)–8.6(f) show the profiles of $G'$ and $G''$ versus the shear amplitude $\gamma_0$, extracted from the contours in Figs. 8.5(c) and 8.5(d) at $t$ = 100, 1000, and 5000 s. In Fig. 8.6(d), the cross-point of $G'$ and $G''$ is around $\gamma_0 = 30\%$, and the profiles bend at $10 < \gamma_0 < 20\%$, with the peak gradually shifting to lower shear amplitudes as shown in Fig. 8.6(e). Finally, in Fig. 8.6(f), the profiles overlap in a wide shear amplitude range, $3 < \gamma_0 < 30\%$.

The profiles show a plateau region at shear amplitudes below 2%, and the measurement range at $\gamma_0 > 2\%$ may be regarded as the LVE range shown in Fig. 8.6(d). However, the plateau region representing the LVE range shifts to the non-LVE range in Fig. 8.6(f). This may be seen to show that the LVE range is modified after longer elapsed times than $O(10^3$ s), where the modifications are caused by the thixotropic behaviors of the Mt dispersion. In general, the cross-point of $G'$ and $G''$ is regarded as the position where yielding of test solutions occurs in oscillatory tests. The profiles in Fig. 8.6(f) in the range of $3 < \gamma_0 < 30\%$ overlap suggesting that measuring terminal conditions with sufficiently long elapsed times as is presently thought to be the best way to evaluate the rheological properties of thixotropic fluids need to be rethought [18] and Chapter 3.

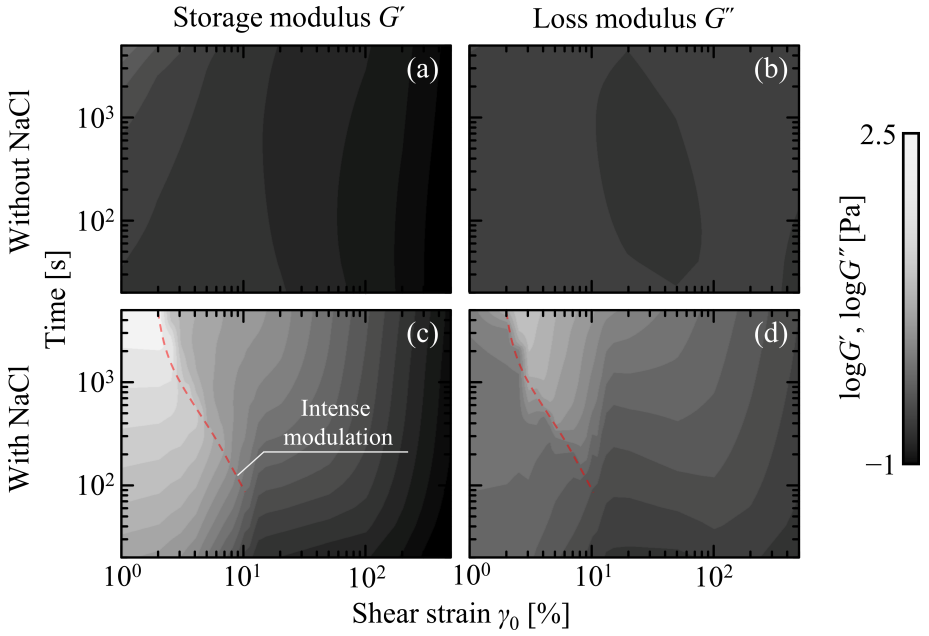


Figure 8.5: Shear strain and time contours of (a) storage modulus $G'$ and (b) loss modulus $G''$ in the Mt dispersion without added NaCl; (c) storage modulus $G'$ and (d) loss modulus $G''$ in the Mt dispersion with 0.02 mol/L NaCl added.

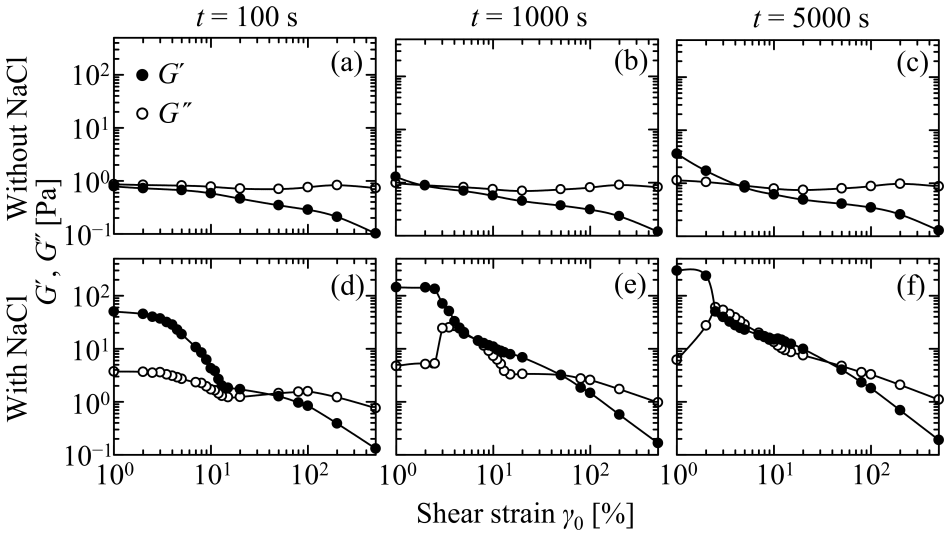


Figure 8.6: The profiles of $G'$ and $G''$ versus shear strain extracted at (a) 100 s, (b) 1000 s, and (c) 5000 s from the contours in Figs. 8.5(a) and 8.5(b); and from the contours in Figs. 8.5(c) and 8.5(d) at (d) 100 s, (e) 1000 s, and (f) 5000 s.

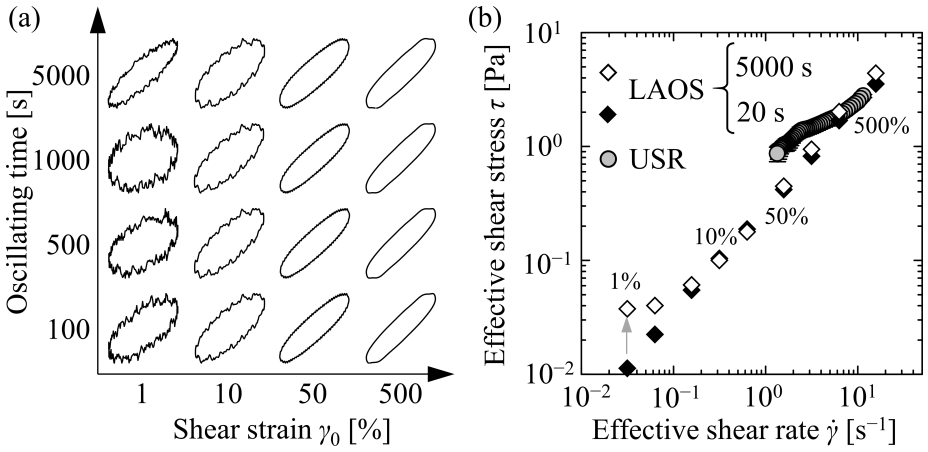


Figure 8.7: (a) Variations in Lissajous curves of the Mt dispersion without added NaCl from the parameters, oscillating time and maximum shear strain $\gamma_0$, where the Lissajous curves express the $\tau/\tau_0$ versus $\gamma/\gamma_0$, (b) flow curves of the Mt dispersion without added NaCl in LAOS compared to that in USR.

### 8.3.2 Comparison of rotational rheometer data of LAOS and USR

An iso-material plot of Lissajous curves plotting shear stress versus shear strain is shown in Fig. 8.7(a), where the vertical and horizontal axes show the maximum amplitude of shear strain and oscillation time after the start of measurements. The shape of the curves displays no significant changes along both the time and shear amplitude axes though noise increases as the shear amplitudes decrease. The shape of Lissajous curves, an ellipse without kinks at a period, indicates ideal viscoelastic characteristics. At $\gamma_0 = 500\%$, the curve displays small kinks at the maximum shear stress because of inertial effects arising from the momentum of the test fluid.

From Eq. (8.2), flow curves, which express the effective shear stress versus the shear rate, were calculated as plotted in Fig. 8.7(b). By comparing with the flow curve obtained with USR (§8.2.2), a good agreement of the two is observed around $\dot{\gamma} = 10^1\ s^{-1}$. The shear stress in USR becomes slightly higher than that with LAOS as the shear rate decreases below $\dot{\gamma} \approx 5\ s^{-1}$. The reason for this would be differences in the restraint condition of the experimental geometry, as the measurement of LAOS is conducted by TC geometry with a narrow gap and the measurement of USR is conducted with a simple open container. Test fluids with the TC geometry may be more stable than those involved with USR, and this would generate the difference in the rheometry of the development of the Mt particle alignments, the difference in shear stresses is however still less than an order of magnitude.

Figure 8.8(a) shows iso-material plots of Lissajous curves plotting the shear stress versus the shear strain and these enable a detailed evaluation of $G'$ and $G''$ . Here, these expressions suggest the non-linearity in the response of a test solution. The Lissajous curves of the Mt dispersion without NaCl does not show any very large changes in the shape with time and shear amplitude [see Fig. 8.7(a)], the curves with the NaCl added display various shapes with respect to time and shear amplitude as classified in Fig. 8.8(a); the Kinked outlines I and II appear in the kinked curve at the second and fourth quadrants and the first and third quadrants of the Lissajous curve; the Wavy outlined shape represents low-frequency waves (5–20 Hz) on the curves, which can be clearly distinguished from the mechanical noise shown in the curve at $\gamma_0 = 1\%$ [Fig. 8.7(a)].

In Fig. 8.8(a), immediately after the pre-shear as explained in Fig. 8.4(c), the Lissajous curves resemble an ellipse, however, at $\gamma_0 = 5$–$12\%$, the shapes could not be discerned due to multiple waves in Fig. 8.8(a). With time the shapes gradually modify into the various types at all the shear amplitudes, $\gamma_0$ (1–500%). For example, at $\gamma_0 = 5\%$, the curve is a sharp elongated shape with waves at $t = 20$–$100$ s, and it changes greatly to a kinked sharp shape at $t = 500$–$1000$ s. This feature may be interpreted as showing wall slip or shear localization due to recovery of particle networks in the Mt dispersion with elapsing time. For $\gamma_0 > 3.5\%$, the enclosed area of the curves increases remarkably with time from the initial elongated shape at around 500 s. This suggests an increasing energy loss due to the presence of a thin low viscosity layer. Remarkably, the wavy features remain after the occurrence of the kinks, for example the case of $\gamma_0 = 5\%$ and $t = 1000$ s.

Considering that the boundary defined in Eq. (8.2) fluctuates with time, the effective shear stress and shear rate of the LAOS measurements, the flow curve, can be calculated as shown in Fig. 8.8(b), where the diamond and circular symbols denote the flow curves obtained from LAOS and USR, respectively. The vertical and horizontal axes are the effective shear strain rate and shear stress. As mentioned in §8.2.2, the flow curve obtained by USR indicates two critical shear rates, $\dot{\gamma}_y$ and $\dot{\gamma}_{st}$. When both flow curves of USR and LAOS are superimposed as shown in Fig. 8.8(b), the flow curve in USR is approx-

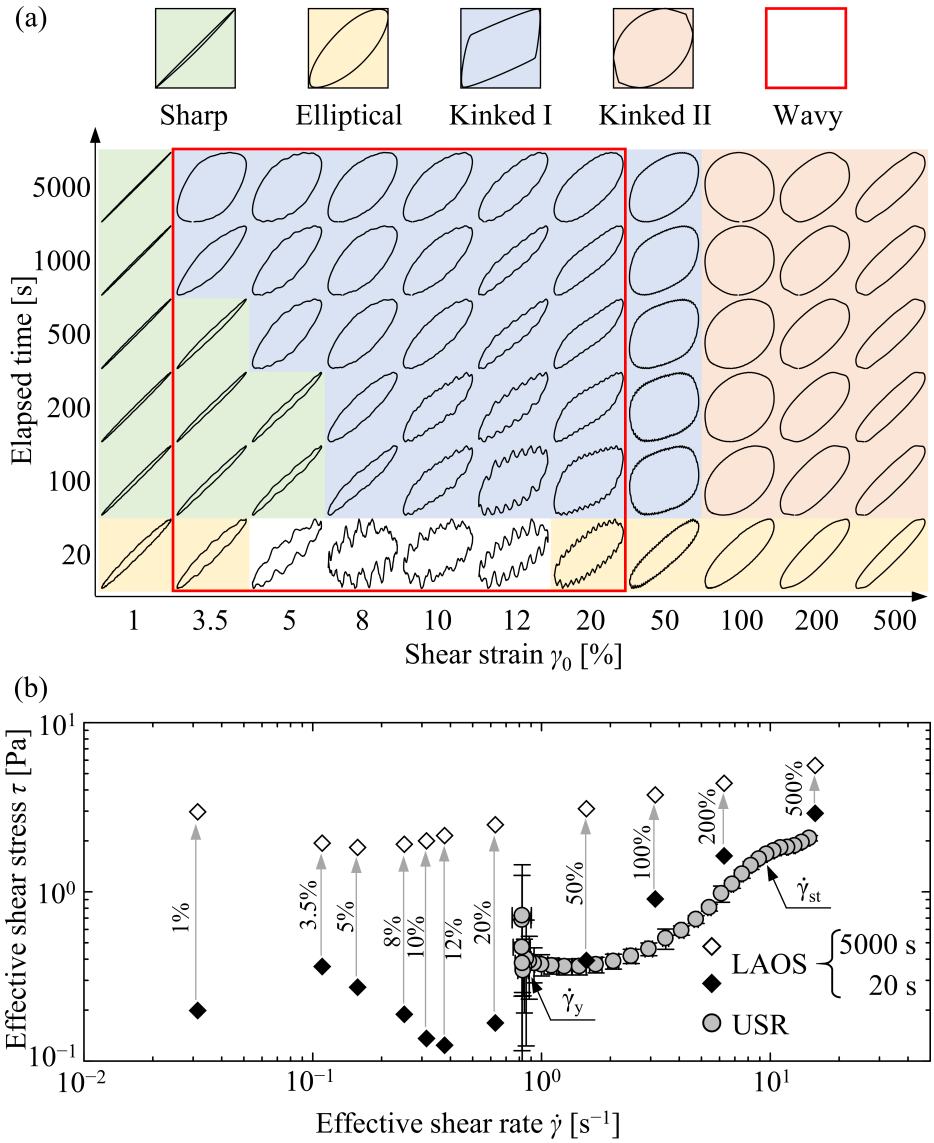


Figure 8.8: (a) Variations in Lissajous curves between $\tau/\tau_0$ and $\gamma/\gamma_0$ of the Mt dispersion with 0.02 mol/L NaCl added plotted against the parameters, oscillating time and maximum shear strain $\gamma_0$. The top schematic diagrams represent the classification of the characteristic shapes, (b) flow curves of the Mt dispersion with 0.02 mol/L NaCl added by LAOS plotted against those by USR.

imately overlapped immediately after the pre-shearing (elapsed time; 20 s) except at $\dot{\gamma} < 1$ s$^{-1}$ in the LAOS measurements. After 5000 s for the LAOS values shown in Fig. 8.8(b), the effective shear stresses in the $\gamma_0$ = 1–500% conditions increase with time. Here there are significant differences between results from the LAOS and USR measurements, with the shear stress obtained from LAOS 10 times that obtained with USR, the flow curves largely agree for the Mt dispersion without NaCl [see Fig. 8.7(b)].

The wavy features in the Lissajous curves occur at lower shear amplitudes than the critical shear rate $\dot{\gamma}_y$ estimated by USR; the elastic instability here arises from the unstable shear banding when shear stress in flow curves exhibits a plateau with respect to the shear rate according to Fardin *et al*. [8]. It is possible that the shear rate calculated by LAOS is qualitatively different from the shear rate obtained with USR, and this agreement between the appearance of wavy shapes in the Lissajous curves and critical events with USR ($\dot{\gamma}_y$ and $\dot{\gamma}_{st}$) will be discussed further in §8.4.1, where the features of the wavy response in the Lissajous curves are investigated with Fourier spectra.

## 8.4 Discussion

### 8.4.1 Summary of findings from LAOS/USR measurements

Unique features were identified by comparing the results obtained with LAOS and USR in §8.3, and this will be discussed below: First, the flow curve in LAOS agrees closely with that in USR in the Mt dispersion without added NaCl. The Lissajous curves are elliptical, and the shapes are maintained with increasing shear amplitude and elapsed time. There are no common unexpected phenomena in the standard rheometer results, such as shear banding, wall slip and others, and the fluid motion in this case may be assumed to satisfy the hypothesis that requires the linearity of flow/deformation in the narrow gap of the rheometer. Second, the flow curve obtained by the LAOS measurements immediately after the pre-shear stage agrees with that obtained by USR at $\dot{\gamma} > 1$ s$^{-1}$ for the Mt dispersion with added NaCl. At $\dot{\gamma} > 1$ s$^{-1}$ ($\gamma_0$ = 50, 100, 200, and 500%) and $t$ = 20 s, the Lissajous curves do not have the kinked shapes, suggesting that the fluid motion would satisfy the hypothesis at this time. Third, the flow curve obtained with LAOS after 5000 s plots considerably above that by USR with the Mt dispersion with added NaCl. The Lissajous curves at $\gamma_0$ = 3.5% indicate kinked characteristics, suggesting influence from thixotropic factors. Fourth, the wavy state seen in the Lissajous curves became stable at around the critical shear rate $\dot{\gamma}_y$ evaluated by USR. These phenomena including the onset of wavy states around the critical shear rate evaluated by USR were also investigated in Chapter 7, though the experimental geometry and test fluid there are different from those in this study. This coincidence may be postulated as a causal connection with elastic instability arising from the thixotropic factors, and below the conditions where wavy states were identified were further investigated with Fourier trans-formation for the Lissajous curves.

### 8.4.2 Fourier analysis of the waves considered to result from elastic instabilities

To better understand the difference between mechanical noise and waves from the elastic instability, the power spectrum in the raw data of the Lissajous curves were calculated; the solid curves in Figs. 8.9(a) and 8.9(b) show the raw data of the shear stress versus the phase angle obtained from the Mt dispersion without NaCl, $\gamma_0$ = 1%, and $t$ = 5000 s, and from the Mt dispersion with added NaCl, $\gamma_0$ = 12%, and $t$ = 5000 s. Plotted against smoothed variations in the normalized shear strain amplitude shown as the dashed curve in each figure, both variations in shear stress display quite large fluctuations.

As shown in Fig. 8.9(c), the spectra for the dispersion without NaCl has a dominant frequency component corresponding to the input frequency of 0.5 Hz, whereas the spectra for the dispersion with NaCl has strong components in the frequency range of $f$ = 5–15 Hz. Figure 8.9(d) shows residual waves calculated by inverse Fourier transform after high-pass filtering (larger than 5 Hz). Compared with the changes in the residual waves and the shear strain amplitude, the amplitude of the waves in the Mt dispersion with NaCl increases as the shear amplitude increases, and that in the Mt dispersion without NaCl does not change the trends of the wave.

Further, residual waves have modulations influenced by the maximum shear strain amplitude $\gamma_0$ (Fig. 8.10); the frequency of the waves increase with increasing maximum shear strain amplitude, and the waves decrease during the shear strain around at $\gamma/\gamma_0 = 0$. This makes is possible to speculate that there would be a phenomenon like that occurring as waves in a chord tightens, something that may be rephrased as that the frequency arising from the instability could depend on the elastic modulus of the Mt dispersion.

The phenomena reported by [8–10] and Chapter 7 bear a strong resemblance to the existence of such an elastic instability; technically, these reports focus on instabilities in steady shear conditions, the influence from such instabilities under unsteady oscillation would be more significant than that those working under steady rotation conditions. This may be rephrased as

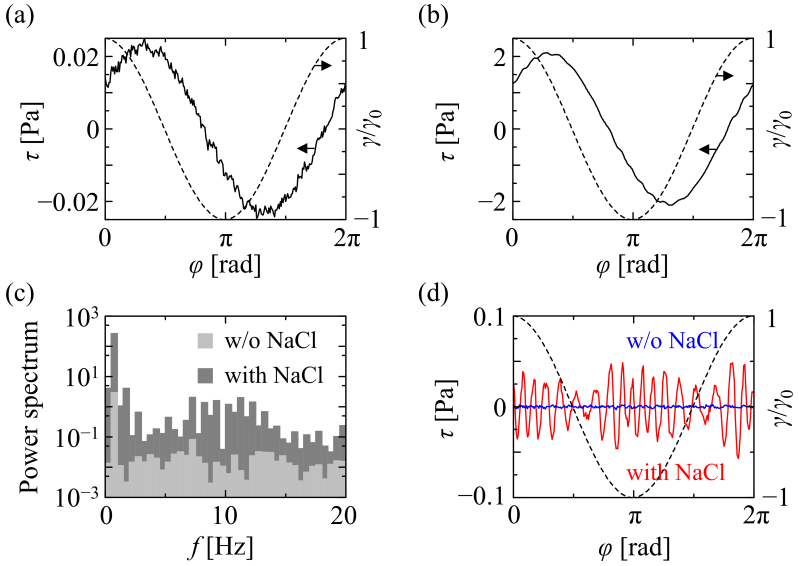


Figure 8.9: Shear stress profiles (a) without adding NaCl, $\gamma_0$ = 1%, and $t$ = 5000 s [Fig. 8.7(a)]; and (b) with 0.02 mol/L NaCl added, $\gamma_0$ = 12%, and $t$ = 5000 s [Fig. 8.8(a)]; (c) power spectrum calculated from the shear stress profiles in (a) and (b); and (d) residual shear stress profiles calculated by high pass filtering (> 5 Hz) for the shear stress profiles in the Lissajous curves in Fig. 8.7(a) and Fig. 8.8(a).

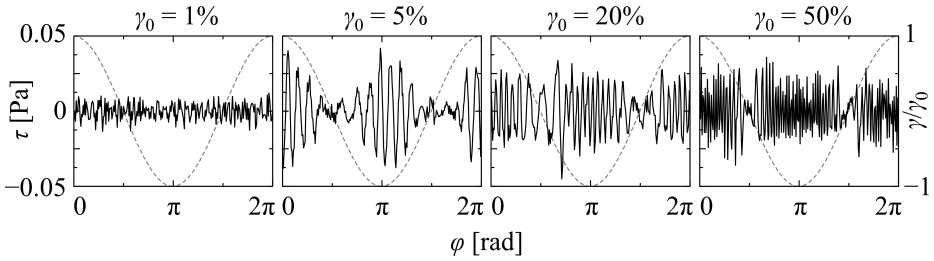


Figure 8.10: Residual shear stress profiles calculated by high pass filtering (> 5 Hz) for the shear stress profiles in the Lissajous curves of $\gamma_0$ = 1, 5, 20, and 50% in Fig. 8.8(a).

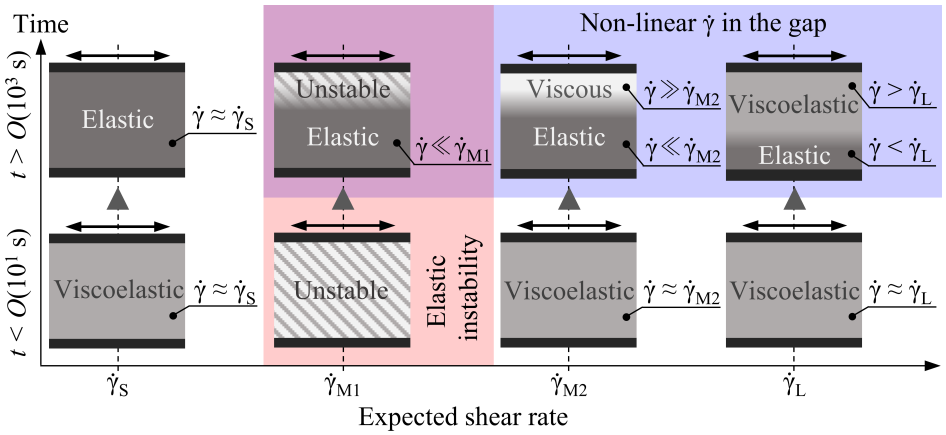


Figure 8.11: A detailed map explaining the methodologic difficulties in the rheometer by considering the experimental findings, where the vertical and horizontal axes indicate the elapsed time of the oscillatory tests and the characteristic shear amplitude.

an important point to notice where: The $G'$ and $G''$ can be measured/evaluated even if the elastic instability occurs during oscillatory tests for fluids with elastic characteristics, this implication may be stated because these values are calculated from only the phase shift $\delta$ as explained in §8.2.3.

### 8.4.3 Consideration of artifacts due to thixotropy in standard rheometers

Based on the findings in the experimental results (§8.3), a map to explain important aspects of measurement difficulties in rheometer for thixotropic fluids are detailed in Fig. 8.11, where characteristic shear rates assuming rheological features in the gap of TC are represented by $\dot{\gamma}_S$, $\dot{\gamma}_{M1}$, $\dot{\gamma}_{M2}$, and $\dot{\gamma}_L$.

At the $\dot{\gamma}_S$ in Fig. 8.11, $\gamma_0 = 1\%$ in Fig. 8.8(a), the rheological property would shift from viscoelastic to elastic when considering the time modulation of the Lissajous curves. The shear amplitude of $\dot{\gamma}_S$ is here much lower than the critical shear rate $\dot{\gamma}_y$ depicted in Fig. 8.2(c). Further, the actual shear rate is very similar to the expected shear rate $\dot{\gamma}_S$ because the Lissajous curves show an ideal shape in the linear response.

At $\dot{\gamma}_{M1}$ in Fig. 8.11, $\gamma_0 = 10\%$ in Fig. 8.8(a), it is possible to determine the wave arising from the elastic instability, and it remains after 5000 s while the Lissajous curves gradually shift to kinked shapes. This suggests that the thin-unstable layer maintains a delicate state between the Figs. 8.2(c) and 8.2(d) states because the shear amplitude is at the transient state. Here, at the terminal condition, most of the momentum energy from the oscillation will dissipate in the unstable layer, and the actual shear rate may be regarded as $\dot{\gamma} \ll \dot{\gamma}_{M1}$.

At $\dot{\gamma}_{M2}$ in Fig. 8.11, $\gamma_0 = 100\%$ in Fig. 8.8(a), the Lissajous curves take on circular forms, suggesting that the rheological characteristic here is viscous, however, some kink features remain in the curves. Because higher shear rates than the critical shear rate $\dot{\gamma}_y$ obtained by USR was applied due to the occurrence of shear banding, this eventually causes the formation of a thin layer with low viscosity as described in Fig. 8.11. Because of the depleting of the momentum in the thin layer, shear banding would continuously be maintained at some equilibrium. So, the actual shear rate may be much larger than the expected shear rate, $\dot{\gamma} \gg \dot{\gamma}_{M2}$ and $\dot{\gamma} > \dot{\gamma}_{st}$, and the other layer will be slightly stretched with $\dot{\gamma} \ll \dot{\gamma}_{M2}$ due to a large rate of dissipation of momentum energy at the low viscosity layer.

At $\dot{\gamma}_L$ in Fig. 8.11, $\gamma_0 = 500\%$ in Fig. 8.8(a), the Lissajous curves are elliptical with kinks, and the closed area of the curves at $t = 5000$ s is larger than that immediately after the pre-shear. This may be explained as the inhomogeneity of rheological property arising from the re-covery of particle networks of the Mt dispersion at the bottom of the gap depicted in Fig. 8.11. The kinked shape in the Lissajous curves can be explained by considering a relaxation of the Mt dispersion as depicted in Fig. 8.2(d) and 8.2(e).

From the considerations in this section, the critical factors causing artifacts in the standard rheometer would be as follows; (1) the geometric restraint condition that requires a narrow gap; (2) spatial inhomogeneity of the shear history of the dispersion. There are numerous examples of rheological evaluations of thixotropic fluids, with most of these analyses focusing on the "equilibrium state" or "equilibrium flow curve" as the most suitable way to evaluate these thixotropic fluids. From the experimental findings, the equilibrium states do not always show a true-rheological property, where the word, true, is meant to suggest accuracy in the physics involved in the evaluations.

We wish to stress the need for a novel rheometry instead of the present standard rheometer, required to ensure an accurate determination of the thixotropic properties that show transient behaviors modulating with the time and shear histories; the potential of USR to measure such transient behaviors was already presented in Chapters 5 and 7.

Without such rheometric determinations, the obtained results will be limited to "specific responses depending on the geometry of the experimental apparatus"; this point can be seen to be supported by previous study [17] and Chapter 7.

## 8.5 Conclusion

The rheological evaluations of thixotropic fluids by LAOS using TC geometry were compared with those obtained by USR to clarify factors in the ambiguity regarding the methodologic difficulties in standard rheometers. For non-thixotropic fluids (Mt dispersion without added NaCl), the flow curves obtained from the standard rheometer are in good agreement with those obtained in USR, because there are no kinks on the Lissajous curves, suggesting a close to ideal linear viscoelastic response. For thixotropic fluid (Mt dispersion with added NaCl), the flow curves obtained with the standard rheometer agree with those obtained in USR immediately after pre-shearing, and the Lissajous curves are elliptical without kinks. In the $3.5 < \gamma_0 < 20\%$ range, there are unstable waves caused by elastic instabilities that appear here; this elastic instability was observed at lower shear amplitudes than the critical shear rate measured by USR, $\dot{\gamma}_y$. With time, the differences in shear stress between the standard rheometer and USR gradually increased as shown in Fig. 8.8(b), and the maximum difference is 10 times larger than the shear stress in USR. At very long times of operation (longer than 5000 s), kinked shapes are observed in all Lissajous curves in the measured range, $3.5 < \gamma_0 < 500\%$. This result shows that the flow curves for thixotropic fluids obtained with the standard rheometer do not always reflect the true-rheological properties even if the rheological response reaches an equilibrium state; this consideration may be seen to be supported by investigation in Chapter 7, where a similar issue has also been discussed using the standard rheometer with parallel plate geometry.

Although the idea of oscillatory tests is feasible to understand the rheology relating to the relaxation time of non-Newtonian fluid, the standard rheometers present these unavoidable difficulties because thixotropic fluids cause the elastic instabilities and transient behaviors. The potential of USR to assume the role of filling "a hole" in the standard rheometer measurements as a complementary methodology is supported by this study, and we hope the USR will provide an avenue to further rheometry developments.

## References

[1] W. Wolthers, M. H. G. Duits, D. Van Den Ende, and J. Mellema, "Shear history dependence of the viscosity of aggregated colloidal dispersions," J. Rheol. 40, 799–811 (1996).

[2] O. Nechyporchuk, M. N. Belgacem, and F. Pignon, "Rheological properties of micro-/nanofibrillated cellulose suspensions: Wall-slip and shear banding phenomena," Carbohydr. Polym. 112, 432–439 (2014).

[3] K. Yang, and W. Yu, "Dynamic wall slip behavior of yield stress fluids under large amplitude oscillatory shear," J. Rheol. 61, 627–641 (2017).

[4] P. Fischer, E. K. Wheeler, and G. G. Fuller, "Shear-banding structure orientated in the vorticity direction observed for equimolar micellar solution," Rheol. Acta 41, 35–44 (2002).

[5] C. J. Dimitriou, L. Casanellas, T. J. Ober, and G. H. Mckinley, "Rheo-PIV of a shear-banding wormlike micellar solution under large amplitude oscillatory shear," Rheol. Acta. 51, 395–411 (2012).

[6] G. Ovarlez, S. Rodts, X. Chateau, and P. Coussot, "Phenomenology and physical origin of shear localization and shear banding in complex fluids," Rheol. Acta 48, 831–844 (2009).

[7] T. Divoux, M. A. Fardin, S. Manneville, and S. Lerouge, "Shear banding of complex fluids," Annu. Rev. Fluid Mech. 48, 81–103 (2016).

[8] M. A. Fardin, C. Perge, L. Casanellas, T. Hollis, N. Taberlet, J. Ortín, S. Lerouge, and S. Manneville, "Flow instabilities in large amplitude oscillatory shear: a cautionary tale," Rheol. Acta 53, 885–898 (2014).

[9] M. A. Fardin, L. Casanellas, B. Saint-Michel, S. Manneville, and S. Lerouge, "Shear-banding in wormlike micelles: Beware of elastic instabilities," J. Rheol. 60, 917–926 (2016).

[10] G. H. McKinley, J. A. Byars, R. A. Brown, and R. C. Armstrong, "Observations on the elastic instability in cone-and-plate and parallel-plate flows of a polyisobutylene Boger fluid," J. Non-Newton. Fluid Mech. 40, 201–229 (1991).

[11] Y. L. Yeow, W. C. Ko, and P. P. Tang, "Solving the inverse problem of Couette viscometry by Tikhonov regulation," J. Rheol. 44, 1335–1351 (2000).

[12] C. Ancey, "Solving the Couette inverse problem using a waveletvaguelette decomposition," J. Rheol. 49, 441-460 (2005).
[13] L. P. Paduano, T. Schweizer, C. Carotenuto, J. Vermant, and M. Minale, "Rough geometries with viscoelastic Boger fluids: Predicting the apparent wall slip with a porous medium approach," J. Rheol. 63, 569–582 (2019).
[14] *Ultrasonic Doppler Velocity Profiler for Fluid Flow*, Springer Science, edited by Y. Takeda (Springer, Tokyo, 2012).
[15] B. Derakhshandeh, D. Viassopoulos, and S. G. Hatzikiriako, "Thixotropy, yielding and ultrasonic Doppler velocimetry in pulp fibre suspensions," Rheol. Acta 51, 201–214 (2012).
[16] B. Ouriev, and E. Windhab, "Transient flow of highly concentrated suspensions investigated using the ultrasound velocity profiler–pressure difference method," Meas. Sci. Technol. 14, 1963–1972 (2003).
[17] C. Perge, N. Taberlet, T. Gibaud, and S. Manneville, "Time dependence in large amplitude oscillatory shear: A rheo-ultrasonic study of fatigue dynamics in a colloidal gel," J. Rheol. 58, 1331–1357 (2014).
[18] H. A. Barnes, "Thixotropy—A review," J. Non-Newtonian fluids Mech. 70, 1–33 (1997).
[19] S. Abend, G. Lagaly, "Sol–gel transitions of sodium montmorillonite dispersions," Appl. Clay Sci. 16, 201–227 (2000).
[20] A. J. Giacomin, and J. M. Dealy, "Large-amplitude oscillatory shear," In Techniques in rheological measurement (pp. 99–121). Springer, Dordrecht (1993).

CHAPTER 9

# Development of ultrasonic in-line rheometry (UIR): Evaluation of viscosity and pressure gradient from velocity profiles of exact solution

## Contents


**9.1 Introduction . . . 134**
**9.2 Theoretical basis of ultrasonic in-line rheometry (UIR) . . . 135**
**9.3 Algorithm validations of UIR by inverse evaluations from the exact solution . . . 136**
9.3.1 Velocity profiles of exact solution with artificial noise . . . 136
9.3.2 UIR validations as a viscometry . . . 140
**9.4 Conclusion . . . 146**
**References . . . 147**


## Preface

The aim in this chapter is to establish a novel in-line rheometry by measuring the velocity profiles of pulsatile flows. Through the work, applicability of kinematic rheometry is widen for a practical use in industry.

## Abstract


To establish a novel rheometry to realize in-line measurement of rheological evaluations, termed ultrasonic in-line rheometry (UIR), the fundamental algorithm was presented and ensured the accuracy and precision in the evaluations of viscosity and pressure gradient. The rheometry is based on solving an optimization problem; the rheological properties are determined by minimizing the cost function regarding the equation of motion and constitutive equation. For ensuring the accuracy and precision of the evaluations, the velocity profiles given from solving exact solution of pulsatile flows are substituted into the cost function. At the first step, Newton's law of viscosity was chosen as the simplest constitutive equation to describe the rheological property. Calculating the statistical values regarding the rheological evaluation by the UIR algorithm, the important parameters to assure the capability of UIR are discussed.

## 9.1 Introduction

In the industry of food and chemical engineering, most fluid products are processed and transported using a pipeline system as the highly efficient and productive way. To operate the whole system of huge pipelines, there is a strong demand of measurement technique to evaluate the quality of products; the difficulty to realize the demand here is to establish "in-line measurement technique". The establishment of in-line measurement technique gives a benefit for realizing a feed-back controlling the system by monitoring the property changes in real time. Though the measurement techniques of temperature and flow rate attain have established with adequate accuracy, in-line technique for rheological evaluations is now still developing. Commercially-supplied in-line rheometers are devices inserting the measurement torque sensor with Couette-type geometry in a pipe, e.g. [1]. This technique is essentially the same with a standard Couette rheometer basically that performs rheological evaluations as an off-line measurement. Standard off-line rheometers measure a simple shear resistance as an axial torque represented by the viscous resistance (or the elastic response) in the fluid media. A narrow gap $O(0.1–1$ mm) is required to satisfy conditions of constant shear rates or strains in the gap (i.e. linear velocity profiles or linear deformations).

Most actual flows and deformations in complex fluids, however, show non-linear profiles in the gap arising from common issues, which are exampled as shear history effect [2], wall-slip [3, 4], shear banding [5–8], elastic instability [9–11], and more. The measured results merely represent apparent viscosities because of unexpected actual shear-rate profiles arising during the measurements [Chapters 5 and 7]. The standard rheometers, therefore, still is required to be innovated to solve the considerable issues, so we must be with cautions and should raise a concern about the applicability in the practical uses of the diverted rheometer. There are a number of approaches for rheological evaluations of non-Newtonian fluids [12–14], most of which are limited to treatments of the problem for specific test fluids, influenced by the elastic instability that is a difficult issue to overcome. Due to such unavoidable problems, in the present industry, a standard off-line rheometer is generally chosen for evaluating the rheological behavior in order to estimate the important parameters for controlling the pipeline operation.

To overcome such limitations on the developments, various kinds of velocity-profiling rheometry [15–17] has been developed in recent years. Complete flow field measurements would provide the most appropriate solutions considering spatiotemporal velocity distributions of fluid motion, because the velocity information reflects all rheological information in the solutions. Several approaches coupled with velocimetries have been proposed as examples of velocity-profiling rheometries based on particle imaging velocimetry (PIV) [18] and ultrasonic velocity profiling (UVP) [19]; Perez-Gonzalez *et al*. [15] developed a Rheo-PIV technique that evaluates the rheological properties for non-Newtonian fluid measuring steady flow velocity in capillary tube. Derakhshandeh *et al*. [16] performed measurements of transient behaviors of thixotropic fluids using a Couette rheometer with a wide gap and UVP. This can detect yielding regions in the fluid with quasi-steady velocity profiles, while the torque measurements may be influenced by the wall-slip leading to errors in the evaluation of the rheological properties. Ouriev and Windhab [17] proposed a combined technique of UVP measurements and pressure difference measurements, termed UVP-PD in-line rheometry.

These reports have similar principles; measuring time-averaged velocity profiles (i.e. limited to steady flow states), functional approximation with the velocity profiles that is described by rheological model equation. If the test fluids indicate viscoelastic features, the simplest constitutive equation to describe the fluid behavior is a "Maxwell model" that indicates the rheological characteristics with a spring (elastic behavior) and a dash pod (viscous behavior). In this case, we have to take account of the relaxation time of the test fluids. As a limitation of rheometries mentioned above, the evaluations of rheological properties relating to the relaxation time are impossible because of the requirement of steady flow state. Further, to solve the equation of motion, the measurement of pressure gradient (or shear stress) is required. So, the pipeline has to be pitted to directly install pressure sensors, meaning the test fluids are contacted with the sensors. Such contact-measurement directly to the test fluids is not suitable from perspective of quality preservation, such as liquid food. This is the reason why engineers in the industry are not willing to use the conventional rheometry.

To establish in-line rheometry that can satisfy demands of the engineers, the measurement process has to be completed with non-contact and non-invasive. Ultrasonic spinning rheometry (USR) has been developed as a novel velocity-profiling rheometry in Chapters 2–8; the important improvements over conventional velocity-profiling rheometries in the results here lie in the ability to examine unsteady shear flows and the requirement is substituting only velocity data into the equation of motion for solving the unexamined issues in non-Newtonian fluid flows. To determine the rheological properties, optimization problems for the equation of motion considering cost function to satisfy the given constitutive equation are solved. In this study, a novel in-line rheometry based on ultrasonic velocity profiling termed ultrasonic in-line rheometry (UIR), which is conceived from the principle of USR, is presented and validated. In §9.2, the theoretical basis of UIR to evaluate the rheological property for Newtonian fluids is explained. In §9.3, the viscosity and pressure gradient of pulsatile fluctuation are examined by analyzing the velocity profiles given from exact solution of pulsatile flows. By evaluating the obtained results

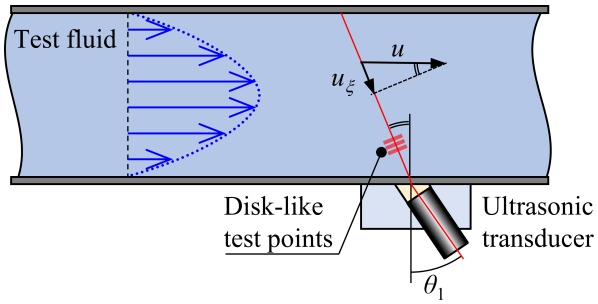


Figure 9.1: Schematic configuration of velocity profiling of test fluid flows in a pipe.

statistically, as well as the validations of UIR algorithm, important parameters to assure high accuracy and precision of UIR are fully examined.

## 9.2 Theoretical basis of ultrasonic in-line rheometry (UIR)

The one-directional and unsteady shear flows in a pipe are described by the equation of motion,

$$\rho\frac{\partial u(r,t)}{\partial t} = \alpha(t) + \frac{\partial \tau(r,t)}{\partial r} + \frac{\tau(r,t)}{r}, \tag{9.1}$$

where $u(r,t)$, $\alpha(t)$, and $\tau(r,t)$ denote velocity as the function of time and space, pressure difference, and shear stress. The shear stress can be represented by considering constitutive equations of rheological model, e.g. Newton's law of viscosity, Maxwell model, Kelvin-Voigt model, Herschel-Bulkley model, and more. In general, those models are chosen according to rheological characteristics of test fluid to fit the flow curve obtained using standard rotational rheometer. In this study, such constitutive equations will use to satisfy the equation of motion, so the brief purpose of this rheometry is similar to that of conventional rheometer, but the actual meaning is different here. To simplify Eq. 9.1, the terms in the equation of motion are rewritten as

$$f(r,\ t) = \frac{\partial \tau}{\partial r} + \frac{\tau}{r}, \quad g(r,\ t) = \frac{\partial u}{\partial t}. \tag{9.2}$$

To avoid from the influence of noise augmentations because of differential calculation, by Fourier transforming the momentum equation with respect to $t$, the equation can rewrite as

$$-i\omega\rho\hat{g}(r,\ \omega) = \hat{\alpha}(\omega) + \hat{f}(r,\ \omega), \tag{9.3}$$

where the mark "$\hat{}$" denotes Fourier transformed term in the function. So, the equation of motion becomes function of $r$ and $\omega$.

As shown in Fig. 9.1, measuring the pipe flow by UVP, the spatio-temporal velocity profiles can be obtained as discretized velocity data with respect to $r$ in the measured points of $N$. Naturally, the data regarding time is also discretized, but the temporal variation in the pulsatile fluctuation can be measured enough. So, in this study, the temporal variation is assumed as a continuous function.

When the appropriate model representing rheological characteristics of test fluid is selected, the measured velocity profiles, $u_\mathrm{m}(r_N,\ t)$ satisfy the equation of motion ideally. Also, when the temporal variation of $u_\mathrm{m}(r_N,\ t)$ has dominant frequency ($f_\mathrm{p} = 2\pi\omega_\mathrm{p}$), the velocity profiles calculated from the Fourier components in the frequency will satisfy the equation of motion. So, Eq. 9.3 can be modified as

$$-i\omega_p\rho\hat{g}_\mathrm{m}(r_N,\ \omega_p) = \hat{\alpha}(\omega_p) + \hat{f}_\mathrm{m}(r_N,\ \omega_p), \tag{9.4}$$

where the suffix m denotes the measured result.

Practically, Eq. 9.4 is not always satisfied as identity formula due to measurement error and the velocity profiling not fulfilling the assumption. So, to estimate the optimal values of rheological parameters, cost function $F$,

$$F[\hat{\alpha}(\omega_p), A, B, C, \cdots]_{\omega=\omega_p} = \sum_{n=0}^{N}\left\{\left[\hat{\alpha}(\omega_p) + \hat{f}_\mathrm{m}(r_N,\ \omega_p)\right]^2 + \rho^2\omega_p^2\hat{g}_\mathrm{m}^2(r_N,\ \omega_p)\right\}, \tag{9.5}$$

is defined, where neighboring measurement points are required to satisfy the equation according to the variable parameters in the rheological model. The parameters are determined as minimizing the cost function $F$, i.e. the most feasible parameters satisfying the equation of motion. The point here is the Fourier component of pressure difference is also considered as a variable parameter, that is, there are no requirements for measurement of the pressure difference in this algorithm. To validate this algorithm, the cost function $F$ are modified considering Newton's law of viscosity $\tau = \mu\dot{\gamma}$ as

$$F[\hat{\alpha}, \mu]_{\omega=\omega_p} = \int_0^R 2\pi r \left| i\omega_p \rho \hat{u}_{\mathrm{m}}(r, \omega_p) + \hat{\alpha} + \mu \frac{1}{r}\frac{\partial}{\partial r}\left[ r \frac{\partial \hat{u}_{\mathrm{m}}(r, \omega_p)}{\partial r} \right] \right|^2 dr, \tag{9.6}$$

where

$$\hat{\alpha} = \alpha_a + i\alpha_b. \tag{9.7}$$

## 9.3 Algorithm validations of UIR by inverse evaluations from the exact solution

### 9.3.1 Velocity profiles of exact solution with artificial noise

In the case of steady state in pipe flow, the velocity profiles are calculated by

$$u_0(r, t) = \frac{\Delta P_0}{4\rho\nu}\left(R^2 - r^2\right) = U_0\left(1 - \frac{r^2}{R^2}\right), \tag{9.8}$$

where $\Delta P_0$, $\rho$, $\nu$, $U_0$ denote pressure difference per unit length, density, kinematic viscosity of test fluid, and maximum velocity of Poiseuille flow at the center of pipe.

The spatio-temporal velocity distribution of pulsatile flow can be described by the governing equations,

$$\frac{\partial u_1}{\partial t} = -\frac{1}{\rho}\frac{\partial p}{\partial z} + \nu\left(\frac{\partial^2 u_1}{\partial r^2} + \frac{1}{r}\frac{\partial u_1}{\partial r}\right), \tag{9.9}$$

where $\partial p/\partial z = \Delta P_1 \exp(i\omega_p t)$ (angular frequency, $\omega_p = 2\pi f_p$). Assuming a unidirectional flow in the direction of axis of pipe, the exact solution of the pulsatile flow is calculated as

$$u_1(r, t) = U_1 \left\{ 1 - \frac{2}{i^{3/2} R\left(\omega_p/\nu\right)^{1/2}} \frac{J_1\left[i^{3/2} R\left(\omega_p/\nu\right)^{1/2}\right]}{J_0\left[i^{3/2} R\left(\omega_p/\nu\right)^{1/2}\right]} \right\}^{-1} \left\{ 1 - \frac{J_0\left[i^{3/2} r\left(\omega_p/\nu\right)^{1/2}\right]}{J_0\left[i^{3/2} R\left(\omega_p/\nu\right)^{1/2}\right]} \right\} e^{i\omega_p t} \tag{9.10}$$

according to [20], where $U_1$, $J_0$, and $J_1$ denote pulsatile amplitude of cross-sectional average flow velocity, and Bessel functions. Because they are enable to be considered as relation of linear combination, exact solution of the pulsatile flow can be calculated as

$$u(r, t) = u_0(r, t) + u_1(r, t) \tag{9.11}$$

from Eq. (9.8) and (9.10). The velocity profiles of pulsatile flow in a pipe can be calculated from Eq. (9.11); as shown in Fig. 9.3, the phase lag of the velocity profiles are shifted from the wall of pipe ($r/R = -1.0, 1.0$) with respect to the pulsatile frequency $f_p$ and kinematic viscosity $\nu$.

To give more reality on the calculated velocity profiles for the measured velocity profiles, the artificial random noises assuming experimental conditions are created by a noise-model function using Box-Muller method [21] to create uniform random values with (0, 1], which are generated by Mersenne Twister [22]. The creation process of artificial noise in the velocity profiles was already established (see Appendix B); The artificial noise that is defined as $\varepsilon$(average, standard deviation) with Gaussian distribution is added to velocity profiles of exact solution as,

$$u'(r, t) = u(r, t) + \varepsilon\left[0, \zeta \times u(r, t)\right]. \tag{9.12}$$

From this equation, the characteristics that the noise intensity increases with increasing velocity amplitude can be represented.

Figures 9.4(a)–(d) are the velocity profiles calculated from exact solution by the artificial noise added with $\zeta$ = 0, 0.5, 0.1, 0.15, along the calculating parameters summarized as follows; $U_0$ = 0.1 m/s, $U_1$ = 0.05 m/s, $f_p$ = 0.2 Hz, $\nu$ = 50 mm$^2$/s, $\rho$ = 1000 kg/m$^3$, $\Delta t$ = 50 ms, $\Delta r$ = 0.74 mm. From the velocity distribution, the noise intensity in the velocity calculated from the exact solution increases. By Fourier transforming the velocity distribution in time direction, the

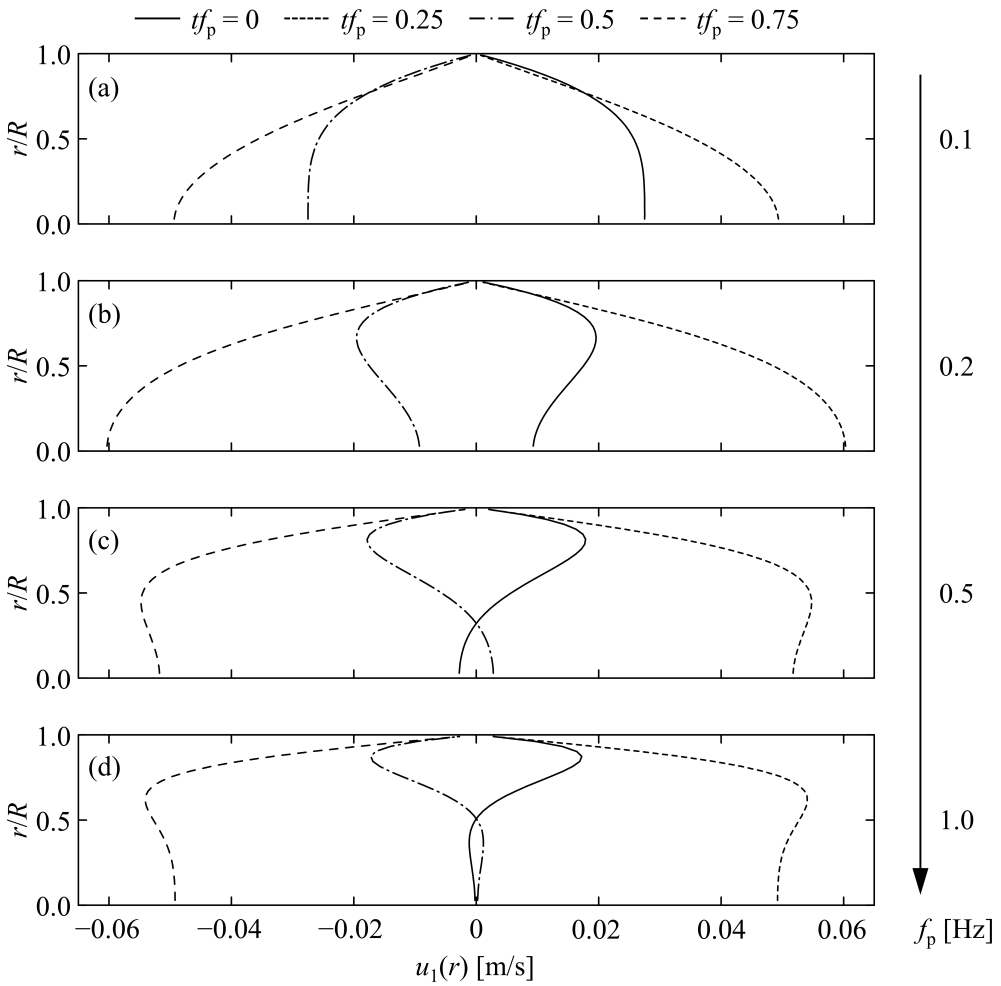


Figure 9.2: Instantaneous velocity-profiles, $u_1(r)$, solving exact solution (Eq. 9.10); palsatile frequency, (a) $f_p$ = 0.1 Hz, (b) $f_p$ = 0.2 Hz, (c) $f_p$ = 0.5 Hz, (d) $f_p$ = 1.0 Hz, where kinematic viscosity $\nu$ = 50 mm$^2$/s, pulsatile amplitude $U_1$ = 0.05 m/s.

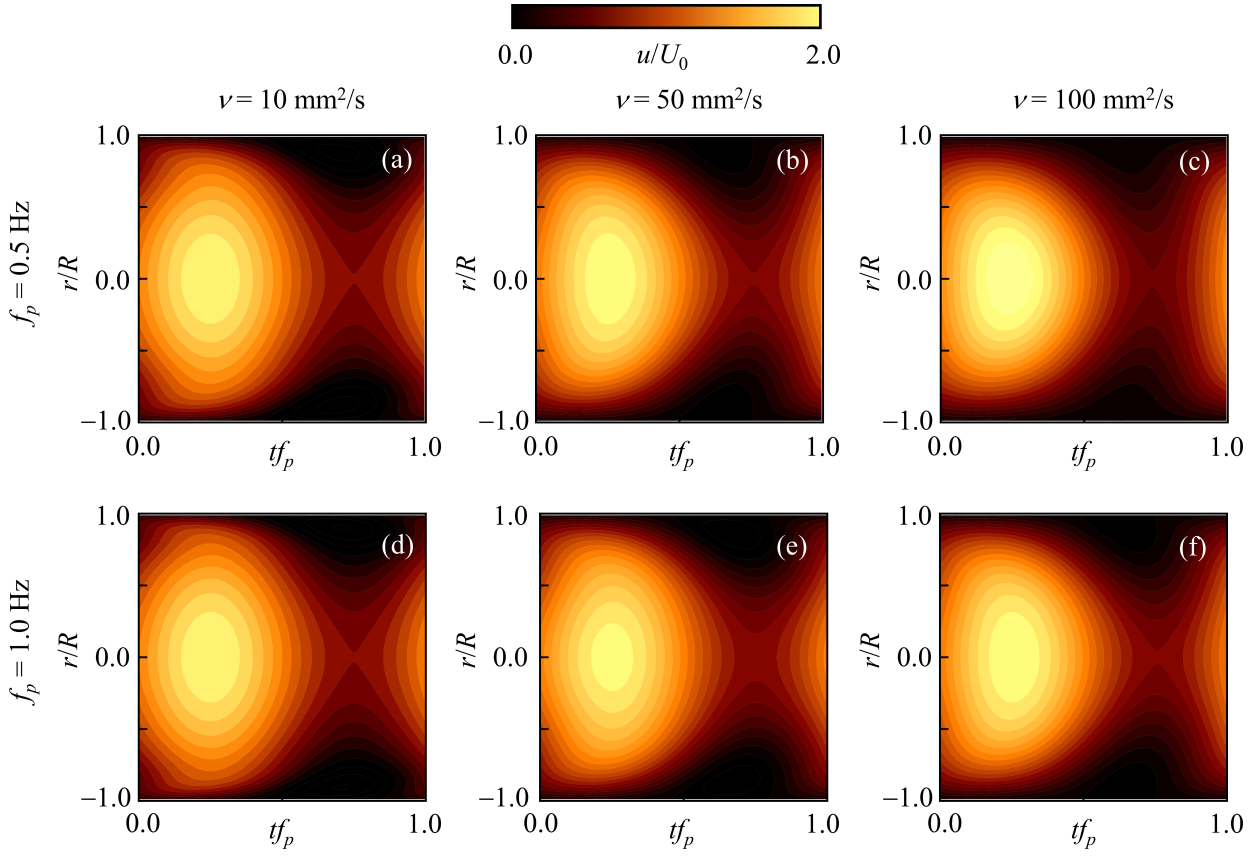


Figure 9.3: Spatiotemporal velocity distribution calculated from Eq. 9.11 with different kinematic viscosity $\nu$ and frequency of flow pulsating, (a)–(f).

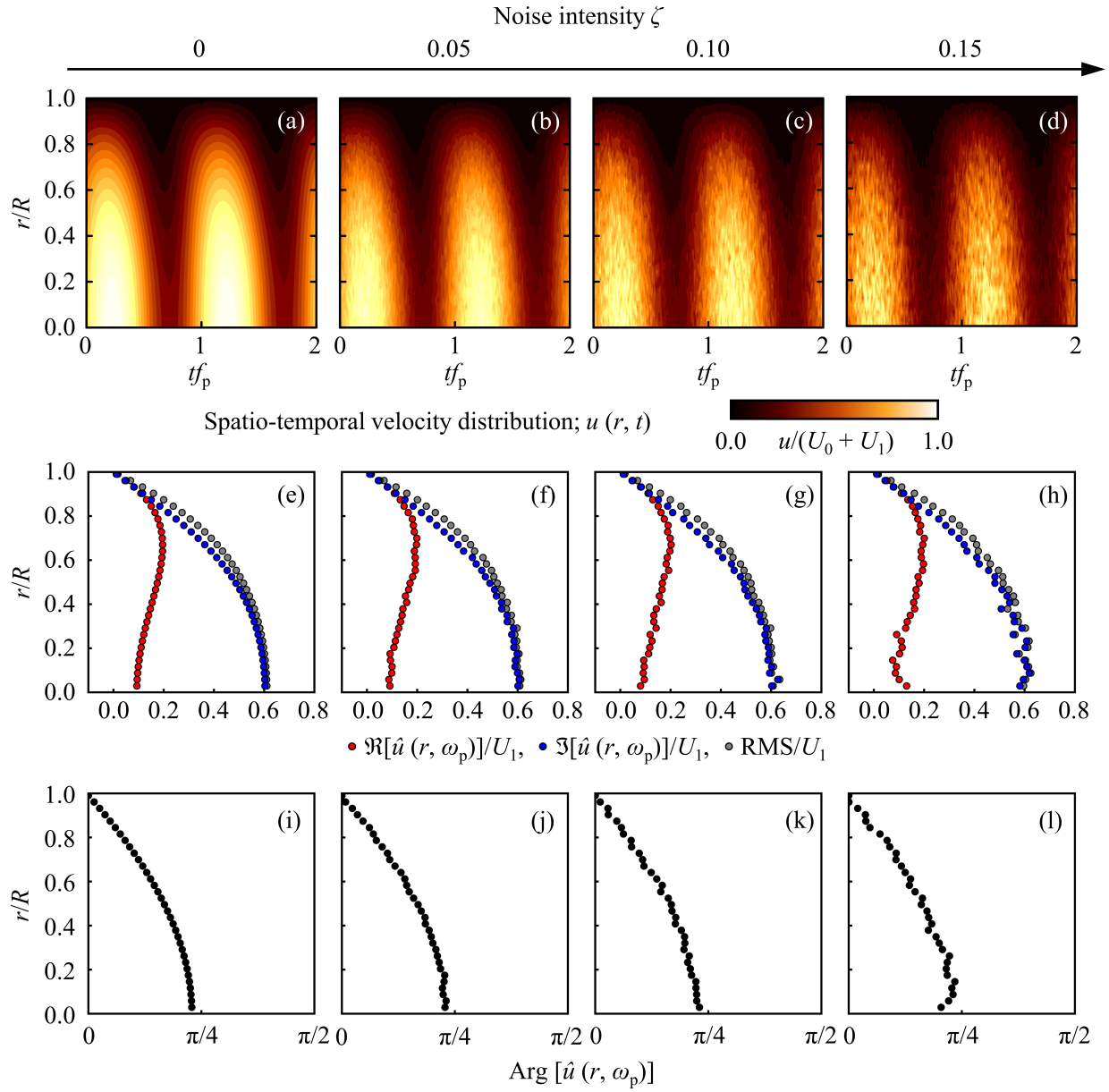


Figure 9.4: (a)–(d) Spatiotemporal velocity distribution, (e)–(h) Fourier components of real and imaginary parts and that of RMS profiles, (i)–(l) phase-lag profiles calculated from the Fourier components of velocity, with changing noise intensity $\zeta$.

real and imaginary components of the velocity profiles can be calculated, where the real, imaginary, and root-mean-square of each component are shown in Fig. 9.5(e)–(h). And, figures 9.5(i)–(l) show phase-lag profiles calculated from the real and imaginary components. As the same with the velocity distribution, although the obtained profiles of Fourier components indicate the noise intensity, the profiles with noise show almost similar trend with the original profile.

Next, the modulations of viscous layer thickness with respect to pulsatile frequency in the calculation parameter are examined. The viscous layer thickness $\delta_v$ of pulsatile flows in a pipe here can be estimated as

$$\delta_v \sim \sqrt{\frac{2\nu}{\omega_p}}. \tag{9.13}$$

The velocity distributions with changing the pulsatile frequency are shown in Fig. 9.5(a)–(d). Here, the temporal resolutions are constant, so the sampling number of velocity distribution decreases with increasing the pulsatile frequency. From the calculated velocity distribution, subtle modulations can be observed as shown in Fig. 9.5(a)–(d). By Fourier transforming as the same with Fig. 9.4, the real and imaginary components have the difference in each frequency condition as shown in Fig. 9.5(e)–(h). The differences are also observed in the phase-lag profiles calculated from both Fourier components as indicated in Fig. 9.5(i)–(l). Here, the phase-lag profiles can be divided into two regions (i) that have large-gradient of phase-lag at close to the pipe wall and (ii) that keep constant phase-lag value near the center of pipe. Also, the latter trend increases with increasing the pulsatile frequency. This spatial information of phase-lag profiles indicate the momentum propagation modulated by viscous resistance at the inner pipe wall. So, the region where the spatial gradient of phase-lag is large represents viscous modulations of velocity information in pulsatile flows, but the region where the phase-lag profile is flat does not include the feasible information for viscosity in the velocity profiles. Thus, for assurances of UIR using information of velocity profiles in pulsatile flow, the viscous layer thickness must be taken account to satisfy the thickness for measurement points.

### 9.3.2 UIR validations as a viscometry

As mentioned in §9.2, the cost function can be calculated by substituting the information obtained from the Fourier components of velocity profiles into Eq. 9.6. However, as measured velocity profiles include noise, the influence from noise is augmented by differential calculations. In the time direction, this problem can be moderated by band-pass filtering process based on Fourier transform. In addition to this, by $n^{th}$ polynomial fitting, it is necessary to moderate the influence from noise augmentations by spatial differential term. In this study, we selected least squared method to achieve the polynomial fitting calculation, although there exist several types to approximate the function. Proper order number of polynomial fitting is required since the shapes of curve of real and imaginary components vary with respect to rheological properties, pulsatile frequency, and more. Higher-ordered polynomial fitting can describe even sharp curves, however, we need to take account of over ordered fitting that would not be appropriate way to approximate the function, because it would result in the functional fitting including noise components adversely.

To determine the minimal point of cost function $F$, unknown variables are viscosity coefficient $\mu$, real and imaginary component of pressure gradient coefficient, $\alpha_a$ and $\alpha_b$, respectively. Technically, the imaginary (or real) component of pressure gradient can be assumed as negligible by adjusting the phase of velocity profiles in processing the Fourier transform. In this study, the unknown variables are set all three to aim the practical uses in the experiment as the capability of measurement or control devices may be unexpected.

Figure 9.6 shows three-dimensional plots $F(\mu, \alpha_a, \alpha_b)$, where color of plots means the magnitude of cost function value. By random-search method, the minimal point of cost function is determined on three-dimensional space. In principle, at least, neighboring three measurement points are required to satisfy the equation of motion, so the viscosity and pressure gradient measurements are carried out every measurement points including the nearest points in this section.

To evaluate the estimated value of viscosity and pressure gradient statistically, the results are expressed as boxplot with each radial range (i)–(iv); (i) $0.1 \leq r/R < 0.3$, (ii) $0.3 \leq r/R < 0.5$, (iii) $0.5 \leq r/R < 0.7$, (iv) $0.7 \leq r/R < 0.9$. In the boxplot expression, the mode value is shown as red line, 50% of elements is included in the box-shaped figure, and 99.3% of elements is included in the range of bar line. To ensure the statistical stability, the analytical process measuring the viscosity and pressure gradients from the velocity profiles are examined 1000 times. The both results were standardized by the true values, $\mu_{\text{true}}$ and $\alpha_{\text{true}}$ which are parameters to calculate the velocity profiles of exact solution. So, the values of $\mu/\mu_{\text{true}}$ and $\alpha/\alpha_{\text{true}}$ distribute close to unity are assumed as highly correct results.

Figure 9.7(a) shows the statics of the estimated value with respect to the noise intensity $\zeta$. When the velocity distribution without noise ($\zeta = 0$), both viscosity and pressure gradients are highly accurate and precise in whole radial ranges (i)–(iv).

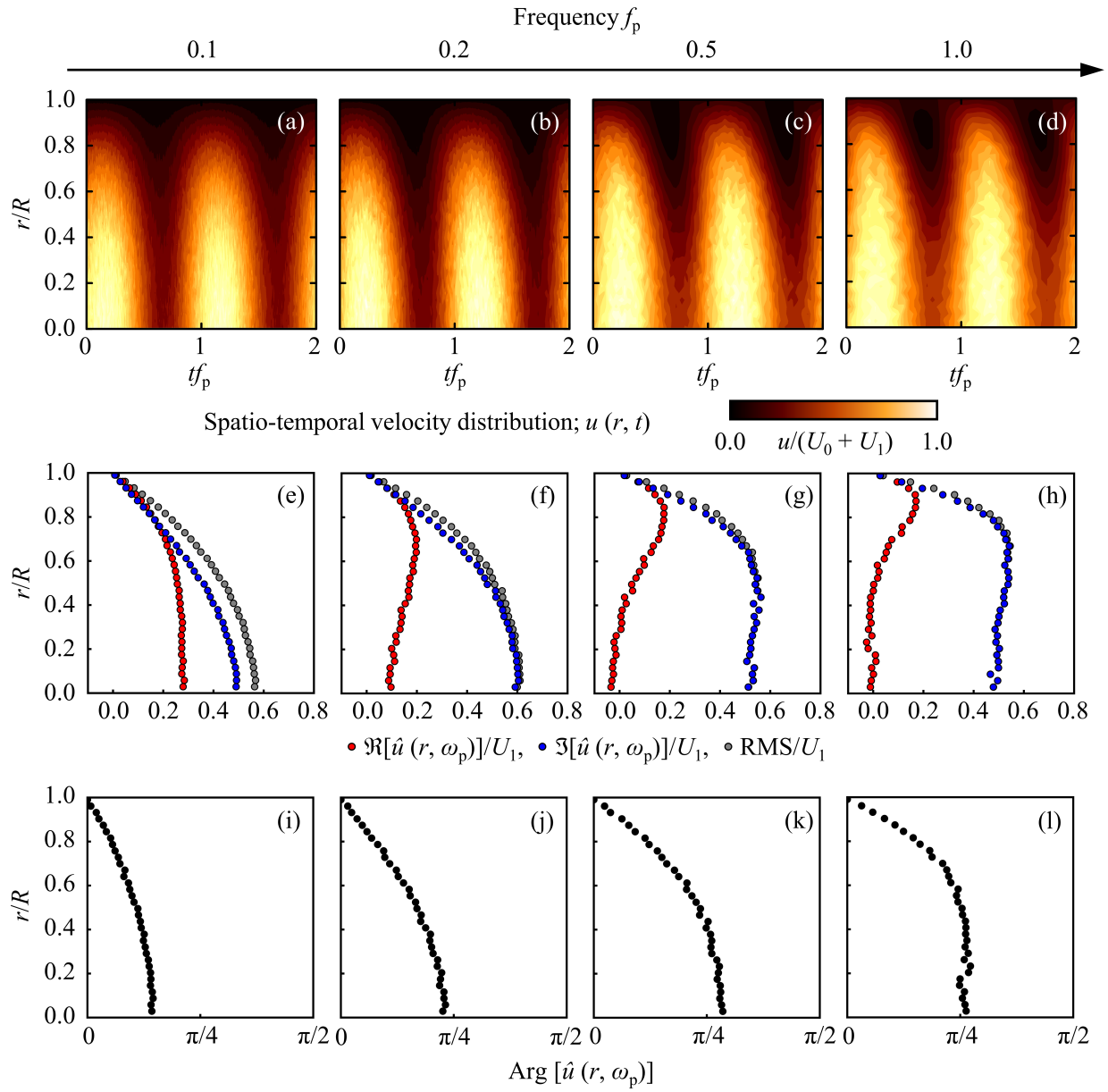


Figure 9.5: (a)–(d) Spatiotemporal velocity distribution, (e)–(h) Fourier components of real and imaginary parts and that of RMS profiles, (i)–(l) phase-lag profiles calculated from the Fourier components of velocity, with changing pulsatile frequency $f_p$.

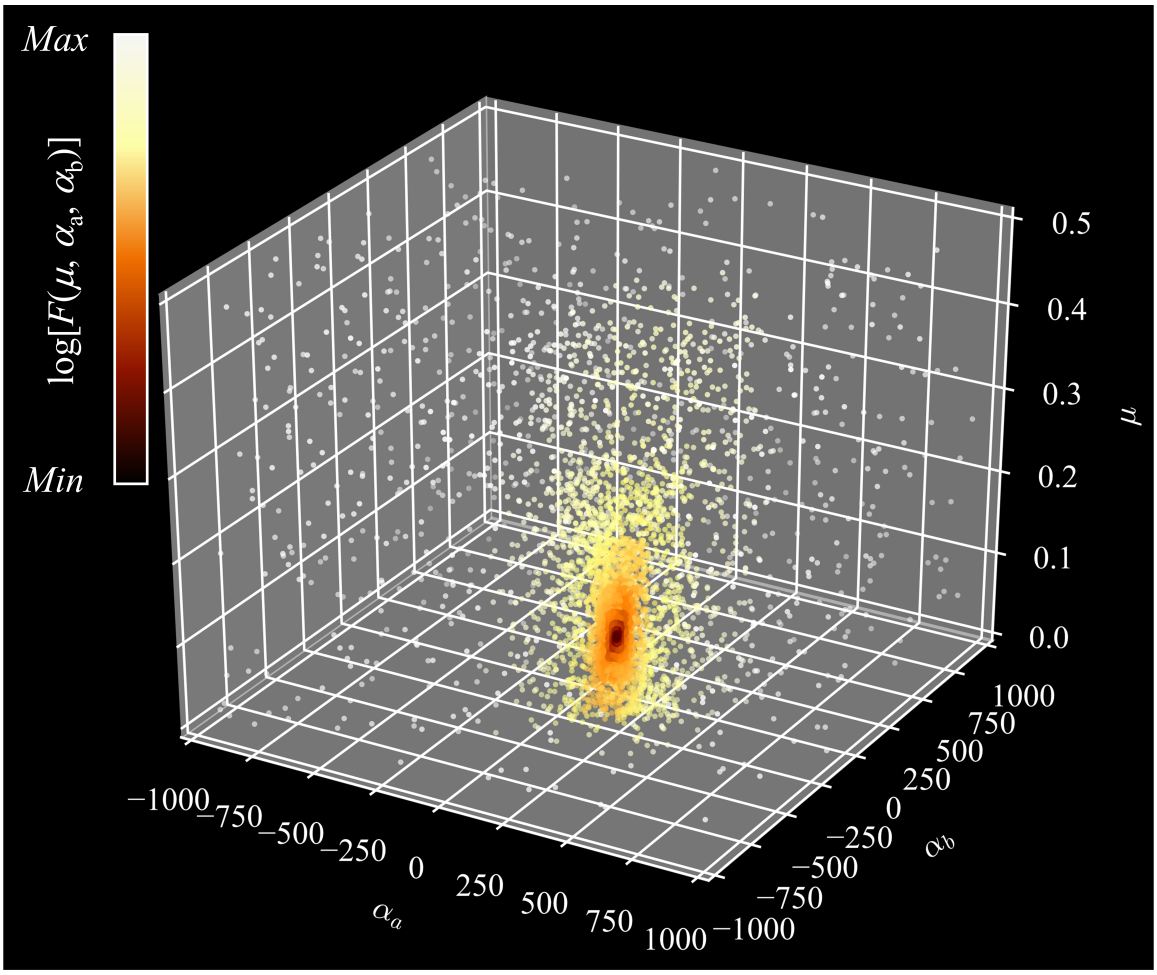


Figure 9.6: Three-dimensional plots of cost function $F(\mu, \alpha_a, \alpha_b; r)$.

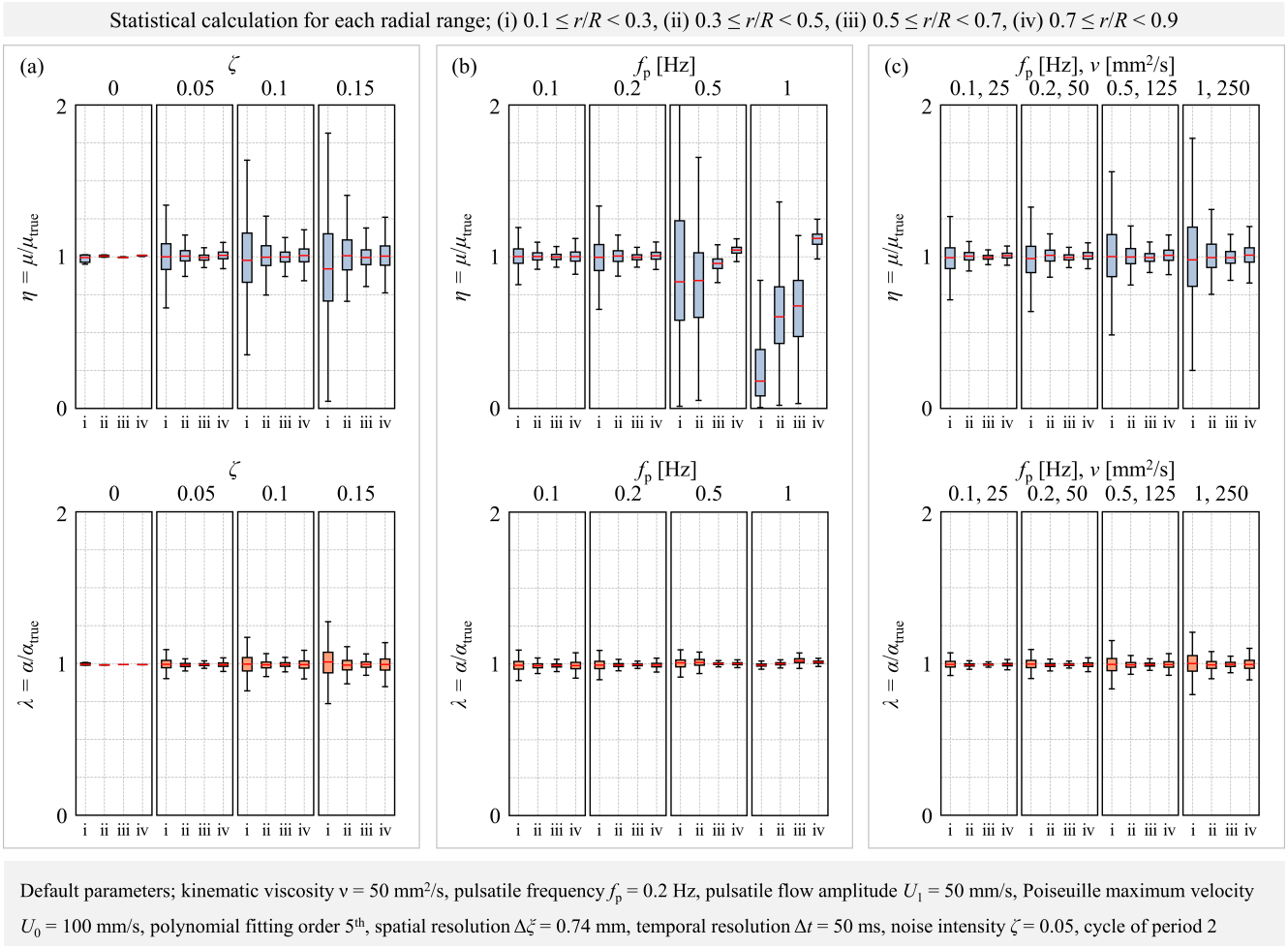


Figure 9.7: Statistics of estimated value of viscosity and pressure gradient with respect to (a) noise intensity $\zeta$, (b) pulsatile frequency $f_p$, (c) pulsatile frequency $f_p$ and kinematic viscosity $\nu$, where the other calculation parameters are listed at the bottom of figure.

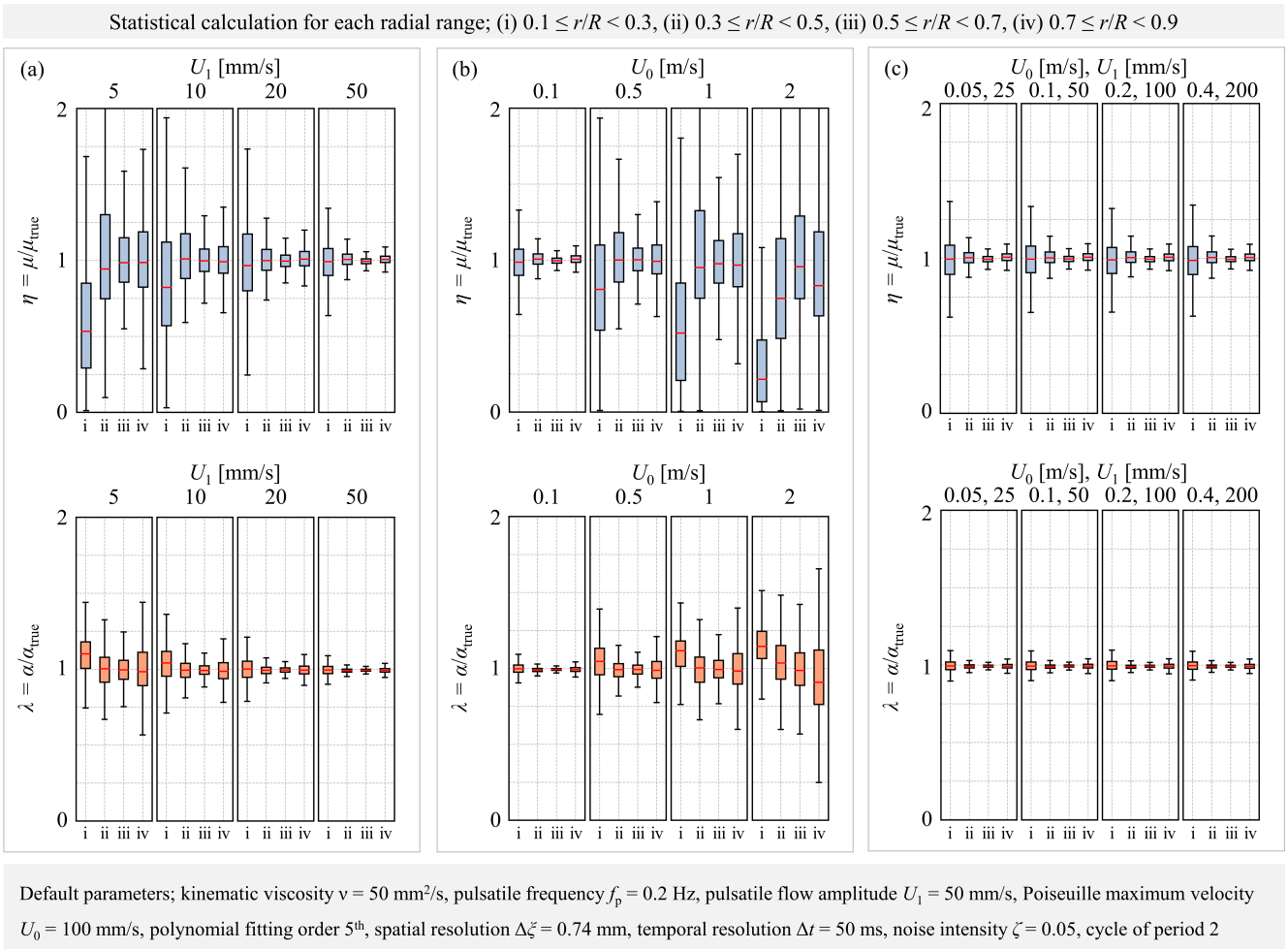


Figure 9.8: Statistics of estimated value of viscosity and pressure gradient evaluations with respect to (a) amplitude of pulsatile flow $U_1$, (b) main flow amplitude $U_0$, (c) main flow and pulsatile flow amplitude keeping constant ($U_1/U_0 = 0.5$), where the other calculation parameters are listed the bottom of figure.

And, the precision of these results decreases with increasing the noise intensity as observed from Fig. 9.7(a). Especially in the case of $\zeta = 0.15$, the statistics of viscosity show lower accuracy and precision at inner radial region (iv), because the influence of the noise intensity at inner radial region, where the magnitude of velocity fluctuation is high, may be larger than that at close to the wall. Further, considering Eq. 9.6, the term including the viscosity coefficient is a product of radial differential, on the other hand, the term of pressure gradient consists in its own. Thus, the term including viscosity coefficient is easier to be influenced from the noise intensity compared to the term of pressure gradient.

Figure 9.7(b) shows the statistics of the estimated value with respect to the pulsatile frequency $f_p$. The parameters of the results in Fig. 9.7(b) are the same with the velocity profiles in Fig. 9.5. As mentioned above, the viscous layer thickness $\delta_v$ including viscous modulations becomes thin with increasing the pulsatile frequency, so it may be difficult to get significant information regarding viscosity at out side of the viscous layer. Here, the viscous layer thicknesses in pulsatile frequency ($f_p = 0.1,\ 0.2,\ 0.5,\ 1.0$ Hz) are $\delta_v/R = 0.497,\ 0.351,\ 0.222,\ 0.157$, respectively. As shown in Fig. 9.7(b), the consideration is confirmed as the accuracy and precision of viscosity measurements decrease except the region (i) in the case of $f_p > 0.5$ Hz. However, there are no influence on the accuracy and precision of pressure gradient evaluations. In the case of outer range of viscous layer, the pressure gradient estimations work well.

To ensure the importance of the viscous layer satisfaction, the statistical results as shown in Fig. 9.7(c) were adjusted so that the viscous layer thickness keeps constant ($\delta_v/R = 0.351$); the pulsatile frequency $f_p$ in Fig. 9.7(c) is the same with that in Fig. 9.7(b), but the kinematic viscosity $\nu$ also varies with respect to $f_p$. From the results of Fig. 9.7(c), the accuracy and precision of viscosity estimations are clearly higher than the same frequency in Fig. 9.7(b).

Next, the statistical investigation regarding ratio between the velocity of main flow $U_0$ and amplitude of pulsatile compo-

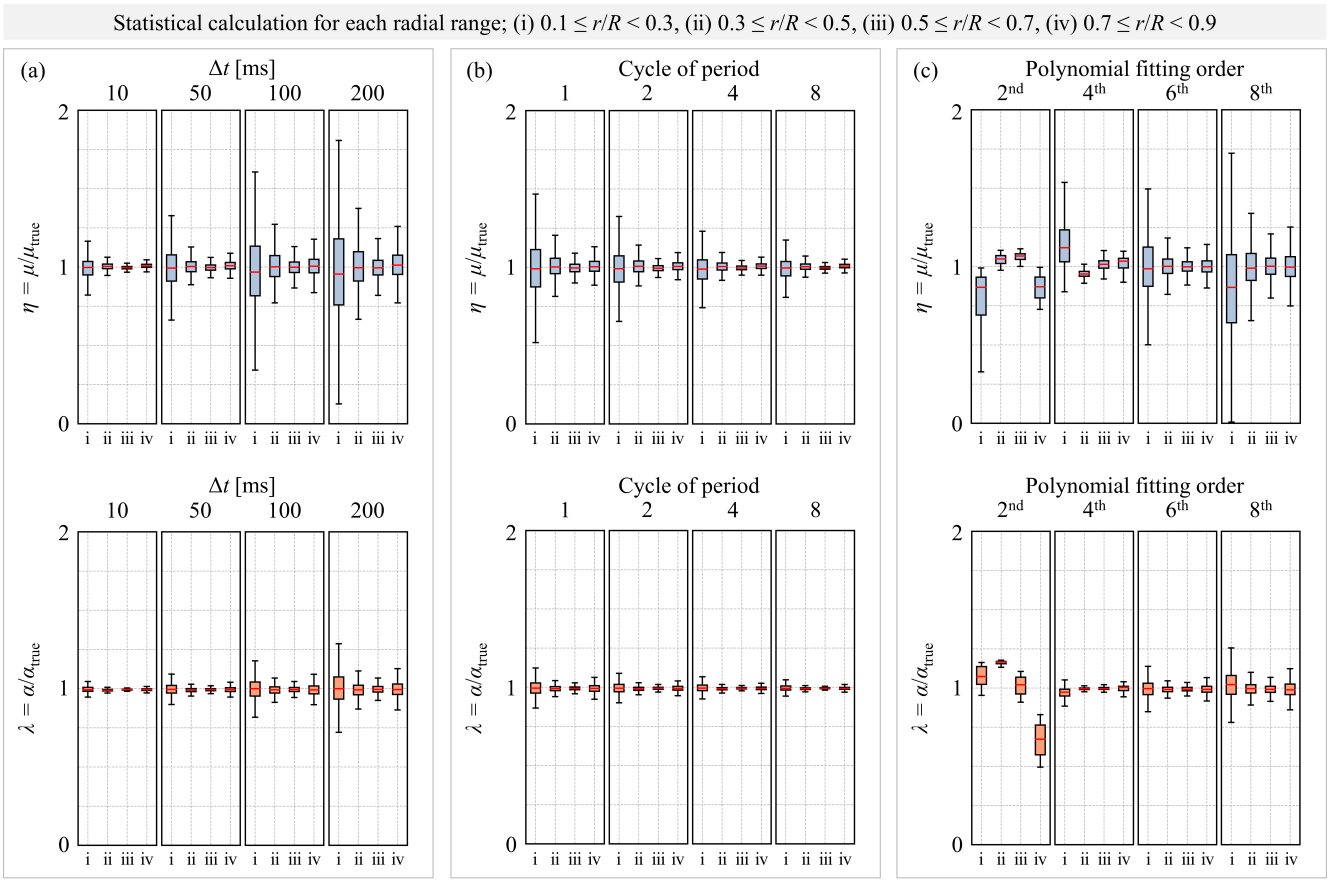


Figure 9.9: Statistics of estimated value of viscosity and pressure gradient evaluations with respect to (a) temporal resolution $\Delta t$, (b) cycle of period in the pulsatile flow fluctuation, (c) the order of polynomial approximation of real and imaginary profiles, where the other calculation parameters are listed the bottom of figure.

nent $U_1$ is examined. Figure 9.8(a) shows the statistics of the estimated values with respect to the pulsatile flow amplitude $U_1$, where $U_0$ keeps constant and $U_1/U_0 = 0.05,\ 0.1,\ 0.2,\ 0.5$. At the case of $U_1 = 5$ mm/s, $U_1/U_0 = 0.05$, the accuracy and precision of both viscosity and pressure gradient estimations become lower. The accuracy and precision become higher with increasing the amplitude $U_1$, and the error bar showing 99.3% is within the range $0.9 < \eta < 1.1$ when $U_1/U_0 > 0.2$. So, it is speculated that the required ratio $U_1/U_0$ is more than $O(0.1)$ approximately, because the relative noise ratio is higher when $U_1/U_0$ is small, vice versa. Conversely, in Fig. 9.8(b), the speculation above is confirmed as the main flow velocity $U_0$ changes with keeping the amplitude of pulsatile flow $U_1$ constant. The main flow velocity $U_0$ is set as $0.1,\ 0.5,\ 1,\ 2$ m/s, that is, the ratios are $U_1/U_0 = 0.5,\ 0.1,\ 0.05,\ 0.025$ respectively. In comparison of the results in Figs. 9.8(a) and 9.8(b), the obtained statistical results have great accordance when the ratios $U_1/U_0$ are the same. The importance of $U_1/U_0$ is ensured as shown in Fig. 9.8(c) indicating the statistical result in keeping constant in $U_1/U_0 = 0.5$.

To ensure the capability of UIR, higher accuracy and precision are required enough to evaluate the viscosity within $O(1-10\%)$ error, as perspective of practical uses. As mentioned above, the accuracy of UIR is ensured by setting appropriate parameters; pulsatile frequency making sufficiently large viscous layer thickness and the ratio between the amplitudes of $U_0$ and $U_1$. In the following, improvement of the precision is focused; in the principle of UIR, the influence from the noise augmentations is moderated by calculating the Fourier components against the measured velocity fluctuations. The important parameters to enhance the function moderating the influence of noise are temporal resolution $\Delta t$ for velocity profiling, cycle of period in the periodic pulsatile flows to calculate the Fourier components, and adequacy of polynomial fitting for the real and imaginary components of velocity distribution.

Figure 9.9(a) shows statistics of the estimated value with respect to temporal resolution $\Delta t$. The precision increases with

becoming temporal resolution smaller,and vice versa, and the accuracy is not so influenced from changes of the temporal resolution. So, simply say, the high precision surely results if the measurement repetitions are sufficiently high against a cycle of the period of pulsatile flows. However, as a trade-off problem of actual velocity profiling, the noise intensity included in the velocity distribution becomes significantly large, when the temporal resolution gets smaller.

Figure 9.9(b) shows statistical results with respect to the cycle of period in the periodic pulsatile flows to calculate the Fourier components. The precisions of viscosity and pressure gradient become higher as the cycle of period increases, because the frequency resolution becomes high with increasing the number of data for Fourier transforming. This results in avoiding influences of the noise from the real and imaginary part of Fourier spectra at the dominant frequency component, calculated from the velocity distribution.

Figure 9.9(c) shows statistical results with respect to the order number of polynomial approximation for the obtained Fourier components. In the case of $2^{nd}$ and $3^{rd}$ order of polynomial approximation, the accuracy is not ensured because the fitting order cannot approximate the original profiles of Fourier components. In the case of the $6^{th}$ order, as the same with the case of the $5^{th}$ order, the high accuracy is observed at whole radial range (i)–(iv). However, in the case of the $8^{th}$ order, the accuracy and precision become lower especially at the region (i) that is close to the center of pipe. This is regarded as over-approximation; if the order of polynomial approximation is too high, the approximated function would include the features modulated by noise. Thus, the order of polynomial approximation should be appropriate to describe the obtained Fourier components.

## 9.4 Conclusion

To aim the establishment of in-line rheometry applying to pipelines in actual industrial situations, the algorithm to evaluate the rheological properties without pressure gradient measurement was proposed. The establishment of UIR is expected to provide high applicability for quality assessments of fluid products in the present industry. As the research objective in this chapter, the viscosity and pressure gradient evaluations were examined by analyzing the velocity profiles given from an exact solution for Newtonian fluid. The presented rheometry here is based on the methodology, which determines appropriate value of rheological properties by minimizing the value of cost function. The cost function can be calculated by substituting the velocity information into the equation of motion satisfying the given constitutive equation. To realize fundamental approach of rheometry establishment, Newton's law of viscosity was used as a constitutive equation.

The examined parameters for deriving the velocity profiles of exact solution in a Newtonian fluid are the artificial noise intensity to assume the measurement noise in practical situations, frequency generating pulsatile flows, viscosity of test fluid, amplitude of pulsatile flows, maximum velocity of main flow, temporal resolution for velocity profiling, cycle of period for velocity profiles calculating Fourier components, order of polynomial approximation. By changing these parameters, the essential knowledges to assure the accuracy and precision of the rheometry are summarized below. (i) Upper limit of noise intensity included into velocity profiling is around $\zeta \sim O(0.1)$; (ii) optimal pulsatile frequency is required so that the viscous layer thickness becomes larger than pipe radius; (iii) the accuracy and precision become higher with increasing the measurement points in time direction; (iv) optimal order of polynomial approximation is required to describe the obtained Fourier components as a radial function.

As noteworthy results examining the accuracy and precision for the rheometry, the evaluations of pressure gradient assure higher accuracy and precision compared to evaluations of viscosity coefficient. Further, although the viscosity evaluations are influenced significantly, the pressure gradient evaluations ensures high accuracy and precision even in the case that the viscous layer thickness is less than the pipe radius. To explain these findings regarding robustness difference between viscosity and pressure gradient evaluations, the term of pressure gradient in Eq. 9.6 to calculate the cost function is denoted alone, on the other hand, the term of viscosity is denoted as the product of differential of the velocity.

As future prospects to realize the UIR as a measurement tool, the issues to be solved are putted in order of priority below: (1) Velocity measurement near the pipe wall — Optimization design of jigs for fixing the transducer; (2) applications to non-Newtonian fluids — Expansion of spatial evaluation for understanding shear rate dependence; (3) developments of complex fluid evaluation — More complex constitutive equations to express complex rheology; (4) clarifying the upper limitation of velocity measurement of the pipeline in the actual industry; (5) applicability confirmation of harsh condition such as under multiple pusatile frequency or developing flow state; (6) practicable experiments for aiming to apply to the pipeline in the chemical or food industry; (7) understanding unexamined issues for viscoelastic instability arising from the natural resonance frequency in the pulsatile flow.

## References


[1] T. O. Broadhead, W. I. Patterson, and J. M. Dealy, "Closed loop viscosity control of reactive extrusion with an in- line rheometer," Polymer Engineering & Science, 36(23), 2840–2851 (1996).

[2] W. Wolthers, M. H. G. Duits, D. Van Den Ende, and J. Mellema, "Shear history dependence of the viscosity of aggregated colloidal dispersions," J. Rheol. 40, 799–811 (1996).

[3] O. Nechyporchuk, M. N. Belgacem, and F. Pignon, "Rheological properties of micro-/nanofibrillated cellulose suspensions: Wall-slip and shear banding phenomena," Carbohydr. Polym. 112, 432–439 (2014).

[4] K. Yang, and W. Yu, "Dynamic wall slip behavior of yield stress fluids under large amplitude oscillatory shear," J. Rheol. 61, 627–641 (2017).

[5] P. Fischer, E. K. Wheeler, and G. G. Fuller, "Shear-banding structure orientated in the vorticity direction observed for equimolar micellar solution," Rheol. Acta 41, 35–44 (2002).

[6] C. J. Dimitriou, L. Casanellas, T. J. Ober, and G. H. Mckinley, "Rheo-PIV of a shear-banding wormlike micellar solution under large amplitude oscillatory shear," Rheol. Acta. 51, 395–411 (2012).

[7] G. Ovarlez, S. Rodts, X. Chateau, and P. Coussot, "Phenomenology and physical origin of shear localization and shear banding in complex fluids," Rheol. Acta 48, 831–844 (2009).

[8] T. Divoux, M. A. Fardin, S. Manneville, and S. Lerouge, "Shear banding of complex fluids," Annu. Rev. Fluid Mech. 48, 81–103 (2016).

[9] G. H. McKinley, J. A. Byars, R. A. Brown, and R. C. Armstrong, "Observations on the elastic instability in cone-and-plate and parallel-plate flows of a polyisobutylene Boger fluid," J. Non-Newton. Fluid Mech. 40, 201–229 (1991).

[10] M. A. Fardin, C. Perge, L. Casanellas, T. Hollis, N. Taberlet, J. Ortín, S. Lerouge, and S. Manneville, "Flow instabilities in large amplitude oscillatory shear: a cautionary tale," Rheol. Acta 53, 885–898 (2014).

[11] M. A. Fardin, L. Casanellas, B. Saint-Michel, S. Manneville, and S. Lerouge, "Shear-banding in wormlike micelles: Beware of elastic instabilities," J. Rheol. 60, 917–926 (2016).

[12] Y. L. Yeow, W. C. Ko, and P. P. Tang, "Solving the inverse problem of Couette viscometry by Tikhonov regulation," J. Rheol. 44, 1335–1351 (2000).

[13] C. Ancey, "Solving the Couette inverse problem using a waveletvaguelette decomposition," J. Rheol. 49, 441-460 (2005).

[14] L. P. Paduano, T. Schweizer, C. Carotenuto, J. Vermant, and M. Minale, "Rough geometries with viscoelastic Boger fluids: Predicting the apparent wall slip with a porous medium approach," J. Rheol. 63, 569–582 (2019).

[15] J. Perez-Gonzalez, J. J. Lopez-Duran, B. M. Marin-Santibanez, and F. Rodriguez-Gonzalez, "Rheo-PIV of a yield-stress fluid in a capillary with slip at the wall," Rheol. Acta 51, 937–946 (2012).

[16] B. Derakhshandeh, D. Viassopoulos, and S. G. Hatzikiriako, "Thixotropy, yielding and ultrasonic Doppler velocimetry in pulp fibre suspensions," Rheol. Acta 51, 201–214 (2012).

[17] B. Ouriev, and E. Windhab, "Transient flow of highly concentrated suspensions investigated using the ultrasound velocity profiler–pressure difference method," Meas. Sci. Technol. 14, 1963–1972 (2003).

[18] J. G. Santiago, S.T. Wereley, C. D. Meinhart, D. J. Beebe, and R. J. Adrian, "A particle image velocimetry system for microfluidics," Exp. Fluids, 25(4), 316–319 (1998).

[19] *Ultrasonic Doppler Velocity Profiler for Fluid Flow*, Springer Science, edited by Y. Takeda (Springer, Tokyo, 2012).

[20] S. Uchida, "The pulsating viscous flow superposed on the steady laminar motion of incompressible fluid in a circular pipe," Zeitschrift für angewandte Mathematik und Physik ZAMP, 7(5), 403–422 (1956).

[21] G. E. Box, "A note on the generation of random normal deviates," Ann. Math. Stat., 29, 610–611 (1958).

[22] M. Matsumoto, and T. Nishimura, "Mersenne twister: a 623-dimensionally equidistributed uniform pseudo-random number generator," ACM Transactions on Modeling and Computer Simulation (TOMACS), 8(1), 3–30 (1998).

Chapter 10

# Concluding remarks

A novel rheometry, termed kinematic rheometry, is established through Chapters 2–9, for sophistication of rheological method contributing the wide fields of academic researches and industrial development. In Chapter 2, effective Newtonian viscosity analysis was performed with demonstrations of the methodology. The kinematic rheometry was applied to various kinds of fluids with different rheological characteristics. The complex fluid rheology can be equally evaluated without changing the geometry and analytical method while the standard shear rheometer requires the both depending on the rheological characteristics of the test fluid. The kinematic rheometry revealed the existence of characteristic viscoelasticity in montmorillonite clay dispersion, especially its thixotropic behavior (Chapter 3). As further development of the kinematic rheometry, an idea of linear viscoelastic analysis was introduced to allow viscoelastic analysis for understanding complex rheology in Chapter 4. The benefit of this idea is that the elastic characteristics that have been understood as the inclusive effect to the effective viscosity can be evaluated separately. Further, this kinematic rheometry based on the linear viscoelastic analysis was validated by comparative experiment with a rotational shear rheometer with parallel plate geometry in Chapter 5; the results proved efficacy of the present methodology and its applicability as the complementary role of the standard rheometers. To ensure the potential for elucidating the unexamined issues on complex rheology, which have never been unexplained by standard rheometers, the studies in Chapters 6–8 were examined using the presented kinematic rheometry as follows; (1) The effective viscoelasticity of non-Newtonian fluids as macro rheology modulated by the alignment of spherical particles that is closely related to the relaxation time of fluid media (Chapter 6). (2) Clarifying the rheological properties of gelled foods that may relate to flows in the swallowing process of complex food materials by utilizing both the standard rheometer and kinematic rheometry (Chapter 7). (3) Elucidating the thixotropic effects on standard rheometer tests by considering the rheological evaluations using both large amplitude oscillatory shear (LAOS) measurement in the standard rheometer and the kinematic rheometry (Chapter 8). To raise the applicability of kinematic rheometry, a novel in-line algorithm, which is based on the theory of ultrasonic spinning rheometry, was presented to be used in the industry as a clamping on system; evaluations of the rheology from the velocity profiles in a pipe flow were validated by inverse-calculations from the velocity profiles obtained by an exact solution in Chapter 9.

To conclude this dissertation through Chapters 2–9, the presented kinematic rheometry has a great potential to contribute to understanding and controlling the complex fluid rheology with higher accuracy than the conventional rheometers, thanks to introducing the perspective of fluid mechanics. Figure 10.1 shows a schematic diagram to summarize a procedure of rheological evaluation using kinematic rheometry. The applicability of kinematic rheometry can be ensured by evaluating phase-lag of velocity profiles; (i) the apparent viscosity estimated from viscous layer thickness ($\delta_\nu = \sqrt{\nu/\omega}$) is larger than $O(0.01\ \mathrm{Pa \cdot s})$, (ii) the apparent viscosity estimated from gradient of the phase lag is smaller than $O(10\ \mathrm{Pa \cdot s})$. In the other case of both (i) and (ii), the commercially-supplied rheometers are more suitable than the presented kinematic rheometry. If the conditions (i) and (ii) are satisfied, by calculating the minimal value of cost function in each constitutive equation, the appropriate equation should be determined for realizing better rheological evaluation. As future prospects, determining the constitutive equation would give profits to realize appropriate numerical simulation of test fluid flow behavior. In this dissertation, Newton's law of viscosity or Maxwell's model was chosen as the constitutive equation for describing fluid characteristics. Here, the kinematic rheometry (ultrasonic spinning rheometry) was proposed as laboratory-scale use with a simple open container (e.g. Chapters 2–8). Especially in Chapters 2–5, various methods to evaluate the rheological properties, such as $\dot{\gamma}$, $\tau$, $\mu$ etc, were established as shown in the flow diagram in Fig. 10.1. Installing cylinder geometry into storage tank of test fluid, this methodology can be diverted to an industry-scale use. Also, as mentioned in Chapter 9, the kinematic rheometry can be applied to unsteady pipeline flow to evaluate the rheological properties.

To promote spreading the efficacy of the kinematic rheometer to the scientists and engineers, some novelties using the presented kinematic rheometry were found out on the physics of fluids. As the expected social impacts of this work, the idea of the presented rheometry will provide an avenue to further rheometry developments to be able to fill "a hole" in the standard rheometer, such as coupling usages with standard torque rheometer tests. For realizing the expectation with easily handling to general users, the analytical and measurement process should be improved and optimized to evaluate the complex fluid behaviors. From the future prospects of technical issues on this work, the enhancements of the capability of velocity profiling technique would give a breakthrough on the full-understanding from microscopic to macroscopic rheological issues.

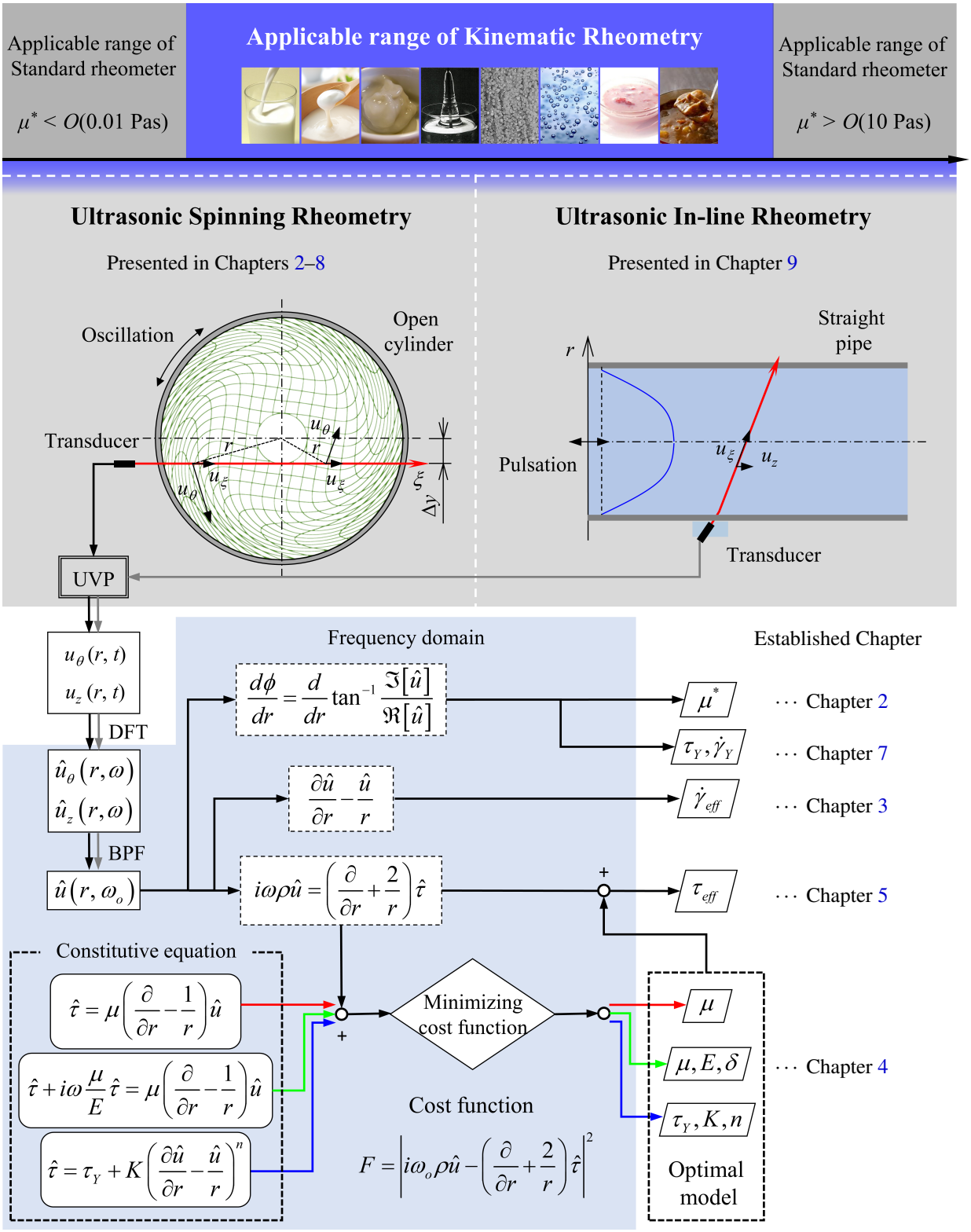


Figure 10.1: Schematic diagram of universal criteria of rheological evaluation for test fluids.

The breakthrough may give us significant benefits for understanding the rheological issues between the macro, meso, and micro-rheology. As unexamined issues in this study, the understanding rheological evaluations with respect to frequency characteristics (Deborah number) is still not completed; it would help to quantify the complex features relating to the relaxation time of test fluids (or dispersed materials), such as the deformable bubble dynamics, viscoelasticity causing polymer functions, and more.

Appendix A

# Inner structure visualization of fresh fruits utilizing ultrasonic velocity profiler

## Contents


**A.1 Introduction** . . . . . **154**
**A.2 Ultrasonic Doppler–echo visualization** . . . . . **155**
A.2.1 System configuration . . . . . 155
A.2.2 Procedure of ultrasonic Doppler–echo visualization . . . . . 155
A.2.3 Echo intensity field expected from numerical simulation . . . . . 159
**A.3 Practical application to fresh fruits** . . . . . **162**
**A.4 Conclusion** . . . . . **166**
**References** . . . . . **166**


## Abstract


We proposed a novel ultrasonic Doppler–echo visualization method that is expected to realize nondestructive visualization using an ultrasonic velocity profiler. The visualization uses information of both the Doppler velocity and echo intensity that have usually been used by the ultrasonic velocity profiler to obtain instantaneous velocity profiles. The feasibility of the method is confirmed by measurements of a rubber ball, apple, and tomato having different acoustic impedances, pulp hardnesses, shapes, and inner structures. Mathematical relations and image processing parameters were discussed to obtain images of the inner structures of test objects using the ultrasonic velocity profiler. Trial measurements of test objects elucidated that the Doppler velocity and echo intensity detect different features of the test objects. Using the Doppler velocity and echo intensity, the outlines and inner structures of the objects can be visualized.

## A.1 Introduction

The ultrasonic velocity profiler (UVP), which uses ultrasonic echography and Doppler velocimetry to capture instantaneous velocity profiles in fluid media [1], is a powerful tool for fundamental fluid mechanics studies (e.g., [2–4]) and fluid engineering investigations (e.g., [5, 6]). Recent applications of the UVP with advanced postprocessing makes it possible to evaluate the rheological properties of test fluid media [7–9] and to detect interfaces in multiphase media [10–12]. An original idea that will motivate further development of the UVP is applying the UVP to evaluate the inner structures and rheological properties of fresh fruit.

Owing to the increasing worldwide consumer demand for high-quality fresh fruit, rapid evaluations of the maturity and quality of fresh fruits require a breakthrough in the development of a nondestructive, reliable, and noninvasive methodology. Sensing the inner structures of fruits together with evaluating the pulp hardness is important to this purpose. In the field of food engineering, sensing techniques have been developed using ultrasonic waves, magnetic resonance imaging (MRI) [13–15], computed tomography (CT) [16, 17], optical coherence tomography (OCT) [18–20], and a laser Doppler vibrometer (LDV) [21]. The capabilities of these techniques are summarized in Table A.1. MRI measurement systems require a huge facility to obtain a visualized image, and they may, therefore, not be suited to practical use. For the same reason, CT using X-rays should be disregarded as an option. OCT can realize higher spatial resolution $O(10\mu\mathrm{m})$ adopting near-infrared radiation; however, the maximum transmitting distance of the radiation is limited to $O(1\mathrm{mm})$ in the application to botanical tissues. The LDV can estimate the hardness of pulps obtained by minute vibrations, and is a point measurement system. Thus, only the local point of the target can be estimated. Mizrach [23–25] reported an evaluation method for determining fruit tissue properties using a high-power and low-frequency ultrasound system. The system, however, determines the properties usually from a single measurement point and increasing the number of measurement points requires additional pairs of an ultrasonic emitter and receiver. Generally, fruit pulps have heterogeneous tissues, such as parenchyma cells, fiber cells, and stone cells, which have different properties owing to differences in fiber orientation and moisture content. In these cells of fruit and vegetables, which have an inhomogeneous microstructure, the depression of ultrasonic propagations is higher than that in homogeneous media. Thus, a one-directional or one-point ultrasonic measurement may have obvious disadvantages. The development of the multidirectional sensing of fruit properties in a simple and convenient way is desirable.

Table A.1: Comparison of the capabilities of different methods to obtain the inner information of test materials.

| Method | Dimension | Convenience | Multi-direction | Cost | References |
|---|---|---|---|---|---|
| Rotational system using 1D-UVP | 2D | ✓ | ✓ | Low | – |
| Conventional ultrasonic system | 0D(Point) | ✓ | | Low | [23–25] |
| Array echography | 2D | ✓ | | High | [22] |
| LDV | 1D | ✓ | | Low | [21] |
| MRI | 2D | | ✓ | High | [13–15] |
| OCT | 2D | ✓ | | Low | [18–20] |
| CT using X-ray | 2D | | ✓ | High | [16, 17] |

To realize the multidirectional sensing of inner structures of fresh fruit using the UVP, a rotating cylinder system is used on the basis of our understanding of ultrasonic spinning rheometry [9, 26], where the test fruit is rotated by a cylindrical vessel and passes through a single ultrasonic propagation line. This realizes multiple sensing lines for the test fruit without using multiple sensors or rotating a sensor. To recognize inner structures, the Doppler velocity is used in addition to basic echo intensity information. The Doppler velocity is obtained as the velocity of ultrasonic reflection particles dispersed in fluid media, and it reflects local acoustic characteristics. Murai *et al.* [27] found that there are pseudo-low Doppler velocity regions near the interfaces of bubbles flowing in fluid media because of the interference of ultrasonic waves around the interface. Additionally, they used this phenomenon to detect interfaces [27].

In the present paper, we investigate the feasibility of applying the UVP to the visualization of inner structures of fresh fruit, especially $O(\mathrm{mm})$ in size comparable to the wavelength of the ultrasonic wave used in the present measurement, which is termed ultrasonic Doppler–echo visualization. Points of investigation are (1) the incidence of the ultrasonic wave with a relative high frequency used in UVP measurements and (2) how the Doppler velocity and echo intensity information work to visualize the inner structures. When a test fruit is set in the cylinder, it rotates at constant speed. The incidence angle to a test fruit gradually changes with cylinder rotation. The ultrasonic wave is affected by the surface roughness, surface shape, and acoustic characteristics of materials, and the reconstruction of images of inner structures by ultrasonic Doppler–echo visualization is thus not so simple. With consideration of this aspect, the feasibilities of standard ultrasonic echography and ultrasonic Doppler information on different inner structures, outer shapes, and surface conditions are evaluated. After explaining the system of ultrasonic Doppler visualization, results of a preliminary visualization experiment on a rubber ball are presented. Numerically predicted visualization patterns reflecting fundamental behaviors of ultrasonic waves are then

explained to consider how to interpret visualization images. Finally, trial visualization measurements of fresh fruit, such as an apple and a tomato, are performed.

## A.2 Ultrasonic Doppler–echo visualization

### A.2.1 System configuration

Experiments were conducted in the open-top rotating cylinder made of acrylic resin shown in Fig. A.1. The cylinder had an inner diameter of 145 mm ($2R$), height of 60 mm, and lateral-wall thickness of 2 mm. The cylinder was filled with a gelling suspension, test objects were put into the suspension to ensure incidence of the ultrasonic wave into objects, and the objects were placed at their initial positions. The gelling suspension was made of montmorillonite powder (4.0 wt.%) and NaCl solution (1.0 mol/L), and contained resin particles having a diameter of 100 $\mu$m to obtain echo information from the suspension. Gelling behaviors of the suspension could maintain the object position against centrifugal forces acting on the object, and the incidence of ultrasonic waves into the object was improved by the acoustic characteristics of the suspension being close to those of water, which occupies a large part of the test fruit. The cylinder was mounted at the center of a 1000 mm $\times$ 1000 mm water bath to maintain a uniform temperature at 25°C and to allow ultrasonic waves to propagate from outside the cylinder. Rotations of the cylinder were controlled by a stepping motor set with a given rotation speed $\Omega$ ($= 2\pi\omega/60$). After all fluid in the cylinder reached a steady state of rigid rotation, repetitive ultrasonic emitting and receiving were performed using a Duo UVP monitor (Met-Flow S.A., Switzerland), and ultrasonic echo signals from test objects were processed using the same equipment to extract Doppler velocity information (termed the "Doppler velocity" hereafter). The UVP originally provided a spatiotemporal velocity distribution $u_\xi(\xi, t)$ and corresponding echo intensity. In cases of measurements on rigid rotation flows with a certain displacement of the set measurement line n from the center line of cylindrical vessels as in the present experiment, the measured velocity profiles become constant as

$$u_\xi(\xi, t) = \Omega\Delta y, \tag{A.1}$$

where $\Delta y$ indicates the horizontal displacement of the measurement line.

To obtain the multi-directional Doppler velocity at inner structures of test objects, an ultrasonic transducer with a resonance frequency of 4 MHz and effective element diameter of 5 mm was mounted in the chamber. The corresponding measurement line was set 40 mm from the cylinder bottom with $\Delta y$ = 15 mm. Test objects were located inside the vessel at the off-center position, shown in Fig. A.1, and the single measurement line sensed inner structures of the objects multiple times at different positions during cylinder rotations. The sampling rate and spatial resolution determining the number of scanning lines were set at 66 ms and 0.74 mm during the measurement. Important parameters of the ultrasonic measurement are summarized in Table 2.

Table A.2: Parameters of the UVP measurement.

| | | | | | |
|---|---|---|---|---|---|
| Time resolution | 66 | ms | TDX diameter | 5 | mm |
| Velocity resolution | 0.391 | mm/s | Length of US beam | 0.74 | mm |
| Spatial resolution | 0.74 | mm | Pulse repetition | 32 | – |

### A.2.2 Procedure of ultrasonic Doppler–echo visualization

The procedure of ultrasonic Doppler-echo visualization is explained in detail through a preliminary visualization experiment using a rubber ball as the test object because of the following advantages. (1) The ball is hollow and thus has a clear inner structure. (2) The acoustic impedance of natural rubber materials is almost equal to that of water, and the transmission rate of the ultrasonic wave at the ball surface is relatively high. Furthermore, (3) rubber materials generally have a high absorbency of acoustic waves, including ultrasonic waves, and there is therefore less effect of multiple reflections of the ultrasonic wave. The rubber ball is 72 mm in diameter and is hollow with a regularly dented surface, and has a thickness of about 10 mm as shown in Fig. A.2(a). Figure A.2(b)–(e) shows the cross-sectional test objects, which will be explained in §A.3. Here, the rubber ball was set at an arbitral position in the cylinder filled with the montmorillonite suspension. The ball was rotated with the cylinder at 15 rpm. The recording of ultrasonic echo information started after the flow inside reached a steady rotation.

Figure A.3a shows the Doppler velocity distribution extracted from the echo information. The axes indicate time normalized by the rotation period of the cylinder and distance from the transducer, and the area between the two broken lines

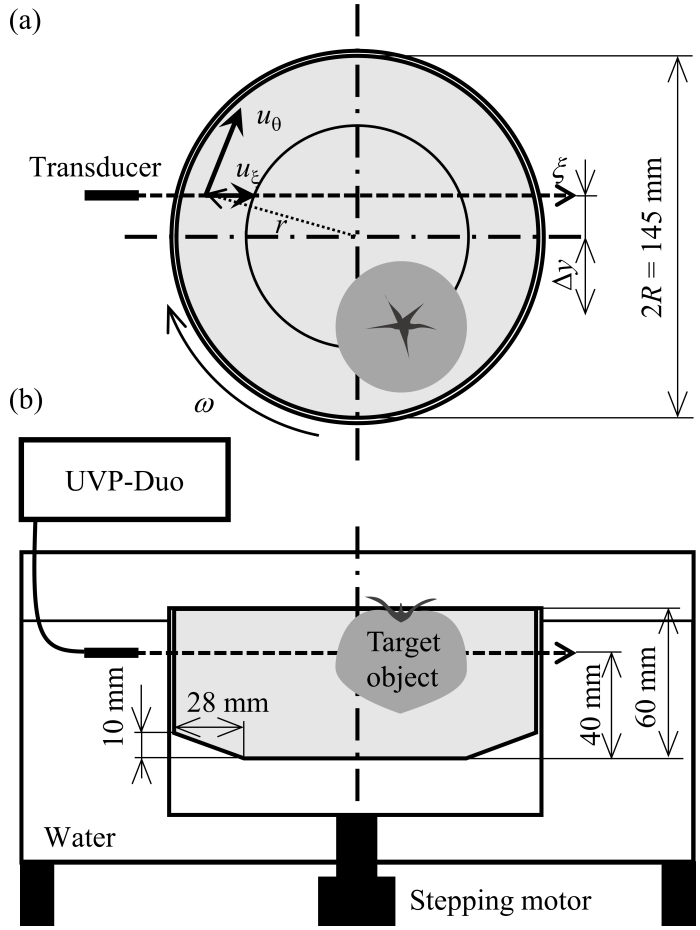


Figure A.1: Schematic diagram of the experimental setup for multi-directional ultrasonic visualization using the UVP; (a) top view of the cylinder and (b) side view with outer water bath.

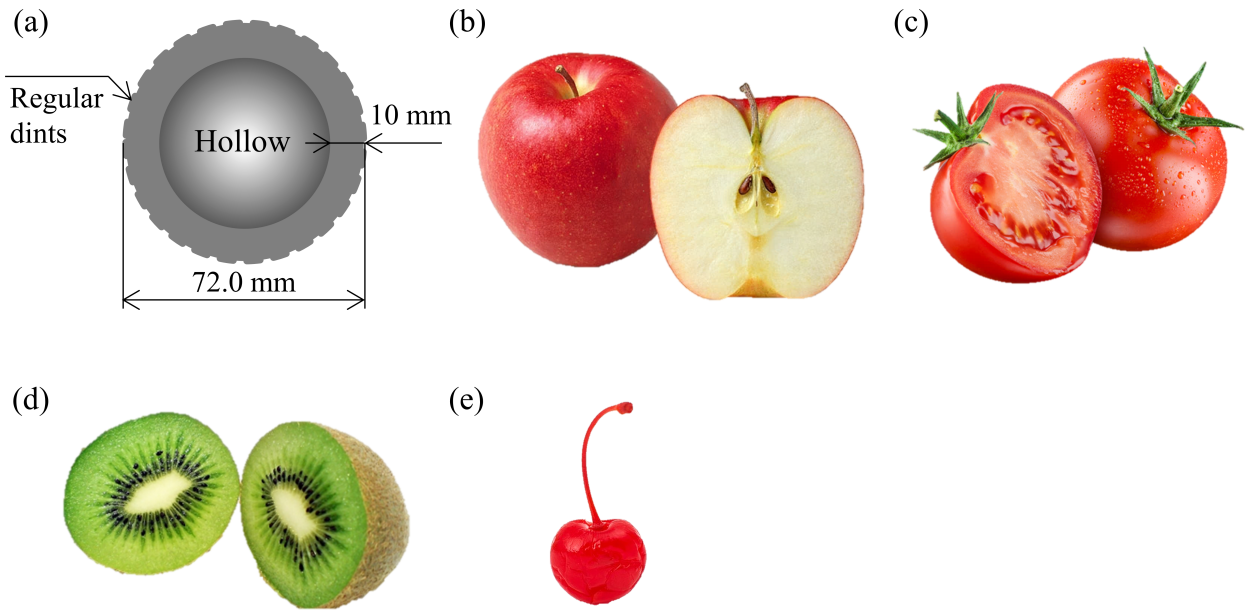


Figure A.2: Image and photographs of test materials; (a) rubber ball, (b) apple, (c) tomato, (d) kiwi, (e) syruped cherry.

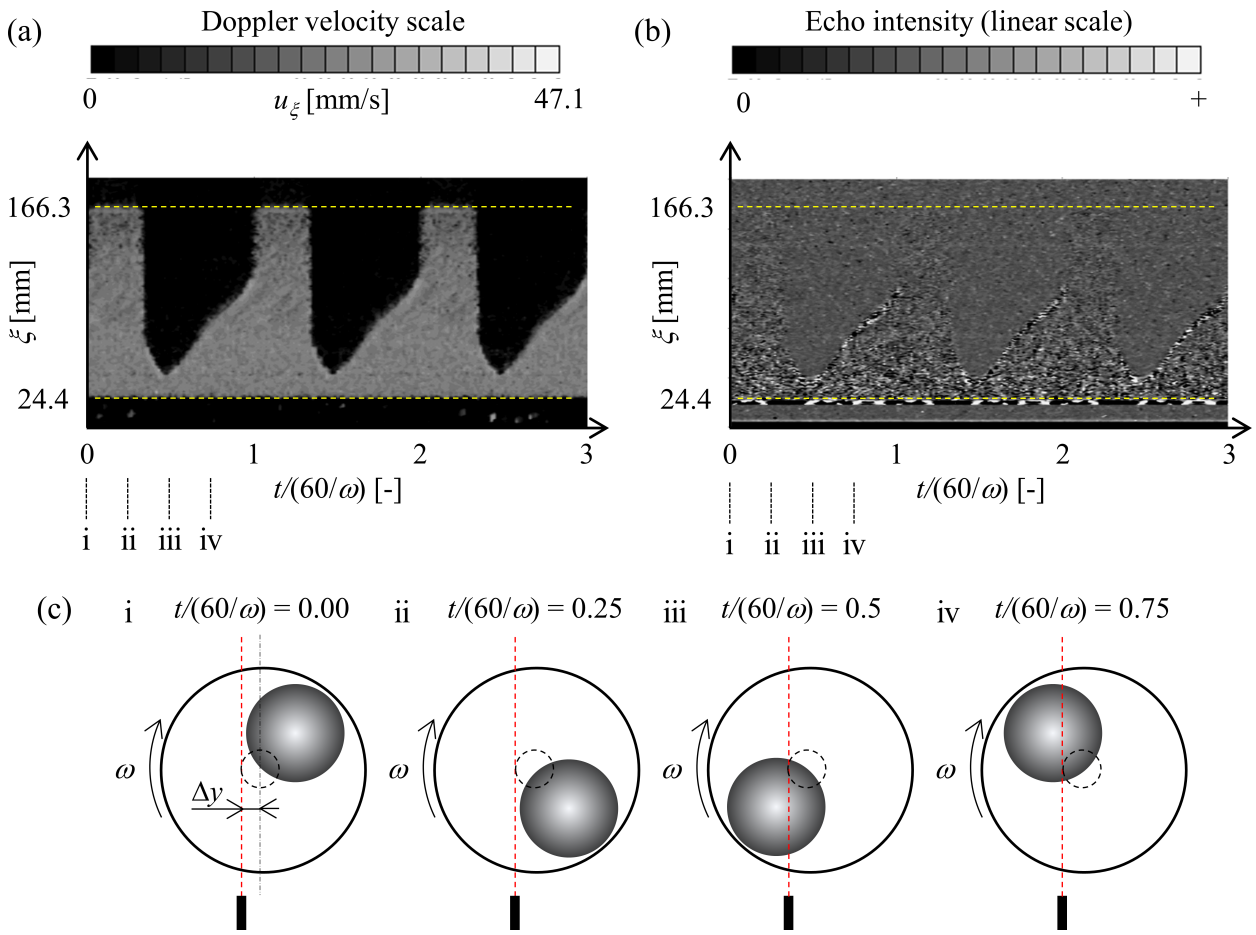


Figure A.3: (a) Spatiotemporal Doppler velocity distribution, (b) spatiotemporal echo intensity distribution, and (c) schematic drawing of the instantaneous position of the ball, where i–iv are relative to the measurement line represented by red dashed lines.

corresponds to the interior of the cylinder. If the cylinder is filled with the suspension, the distribution has a uniform value as given by Eq. (A.1) owing to rigid-body rotation inside. The distribution has a clear contrast of gray and black parts, which vary periodically in synchronicity with the cylinder rotation. The black and gray parts, respectively, indicate an area of a very weak echo signal and an area moving with the same rotation speed as the suspension. This is because the ultrasonic waves may be almost completely absorbed and scattered at the interface between the inside rubber and hollow part, which is filled with air. The Doppler velocity distributions were, therefore, measured as almost zero. Such variation is also seen for the echo intensity distribution shown in Fig. A.3(b), but it is not as clear as that for the Doppler velocity distribution. The complex distribution of the intensity means that the scattering condition of the ultrasonic wave for the echo is not constant in the cylinder because of the random dispersion of resin particles in the suspension. The variation is translated as Fig. A.3(c), illustrating the relative position of the ball to the measurement line. When the ball is off the measurement line [Fig. A.3(c)i–ii], the Doppler velocity distribution takes the constant value calculated by Eq. (A.1), and there are no high echo intensities. When the ball is located on the measurement line as in Fig. A.3(c) iii–iv, the Doppler velocity and echo intensity distributions sense the existence of the ball. The echo intensity is higher on the ball surface away from the measurement line, because of the relative angle of the surface to the measurement line.

As explained above, the Doppler velocity and ultrasonic echo information have different characteristics in the visualization of objects. Therefore, a novel method of creating visualized images using both types of information was established at the same time. Although the measurement line is fixed against the cylindrical vessel, test objects rotate with the cylinder at constant speed and pass through the measurement line periodically. The visualization is developed by providing line information with a certain displacement $\phi$ depending on the rotation speed, $\omega$, and sampling period of the UVP, $\Delta\tau$, as shown in Fig. A.4(a). Single rotation provides a coarse drawing, however, continuing rotation fills the visualized domain of $N \times N$ pixels set on the cylinder without the central region corresponding to a circle with off-axis displacement $\Delta y$ as the radius. The

time required to complete the visualization depends on $\omega$, $\Delta\tau$, and the spatial resolution of the UVP, $\Delta\xi$. The theory used to evaluate the time is explained below.

With arrangement of the scanning line shown in Fig. A.4(a), the domain size $N$ should be smaller than $2R/\Delta\xi$. In the present case, $\Delta\xi = 0.74$ mm and $2R = 145$ mm, and $N$ is thus set at 196 pixels. The time variation of the displacement angle $\varphi(t)$ on the scanning line is derived as

$$\varphi(t) = 2\pi\frac{\omega}{60}\sum_{k=0}^{t} k\Delta\tau, \tag{A.2}$$

The visualized position in the domain, $x_i$ (width) and $y_i$ (height) from the left-upper corner of the image, is derived as

$$x_i = \left\lfloor \frac{r_i N}{2}\cos\left[\varphi(t) + \sin^{-1}\left(\frac{\Delta y}{r_i R}\right)\right] + \frac{N}{2}\right\rfloor \tag{A.3}$$

$$y_i = \left\lfloor \frac{r_i N}{2}\sin\left[\varphi(t) + \sin^{-1}\left(\frac{\Delta y}{r_i R}\right)\right] + \frac{N}{2}\right\rfloor \tag{A.4}$$

where $r_i$ is the radial position. As shown in Fig. A.1, $r_i$ is determined from the measurement position of the UVP (i.e., the distance from the ultrasonic transducer $\xi_i$) as

$$r_i = \sqrt{\Delta y^2 + \left(\sqrt{R^2 - \Delta y^2} - \xi_i + \xi_0\right)^2}, \tag{A.5}$$

where $\xi_0$ indicates the distance from the inner cylinder wall to the transducer. To fill the $N \times N$ pixel domain, the relationship among the number of profiles, the temporal resolution $\Delta\tau$, and the rotation speed is of great importance. A high temporal resolution does not mean that the domain is sufficiently filled. Additionally, increasing the number of profiles does not fill the domain. Instead, avoiding an overlap of the scanning line is important to efficient visualization or, at least, it should be avoided conditions such that the rotation period of the cylinder corresponds to an integer multiple of the sampling period. Figure A.4(b) shows the filling rate of the $N \times N$-pixel domain with respect to the number of rotation cycles at different time resolutions $\Delta\tau$. In trials with different values of $\Delta\tau$, visualizations with $\Delta\tau = 25,\ 30,\ 32$ ms cannot completely fill the domain, while visualizations with $\Delta\tau = 13,\ 66$ ms can do that in 3 and 25 cycles of rotation, respectively. In the failed cases above, the rotation period, 4 s at $\omega = 15$ rpm, corresponds to integral multiples of $\Delta\tau = 25,\ 32$ ms, and the scanning lines thus overlap after a single rotation. Furthermore, the case of $\Delta\tau = 30$ ms has the lowest common multiple with the rotation period as 12 s (three rotations), and overlapping thus occurs after three rotations. These results indicate a condition that the least common multiple between the sampling and rotation periods has to be less than the time required to create a sufficient number of scanning lines.

In addition to the above, higher temporal resolutions achieve a shorter elapsed time for measurements if the measurement quality of the single line visualization is kept high enough. If the coordinates of the point derived from Eqs. (A.3) and (A.4) overlap, their averaged Doppler velocities are given. In drawing the visualized image, the Doppler information is represented as 256 brightness tones of grayscale as

$$V = \frac{u_\xi(\xi, t)}{u_{\max}} \times 255 \tag{A.6}$$

where $u_{\max} = 2\Omega\Delta y$ is twice the rotation speed. Meanwhile, the ultrasonic echo intensity $\sigma$ is displayed as a colored scale value through a coloring process using statistical values ($\sigma_{\text{ave}}$: average, $\sigma std$: standard deviation) as thresholds; the statistical values are defined as

$$\sigma_{\text{ave}} = \frac{1}{M_t M_\xi}\sum_{i=1}^{M_t}\sum_{j=1}^{M_\xi}\sigma_{i,j} \tag{A.7}$$

and

$$\sigma_{\text{std}} = \sqrt{\frac{1}{M_t M_\xi}\sum_{i=1}^{M_t}\sum_{j=1}^{M_\xi}\left(\sigma_{i,j} - \sigma_{\text{ave}}\right)^2}, \tag{A.8}$$

where $M_t$ and $M_\xi$ indicate the total numbers of scanning lines and measurement points on a single line. An example of coloring along a single scanning line is shown in Fig. A.5(a): Here the points satisfying the condition $\sigma > \sigma_{\text{ave}} + \sigma_{\text{std}}$ or $\sigma < \sigma_{\text{ave}} - \sigma_{\text{std}}$ are drawn in red as strong echo points, and other points are drawn using a gray linear scale according to the red-gray scale legend. The echo intensity distribution shown in Fig. A.5(b) is the coloring of Fig. A.3(b), where strong echo

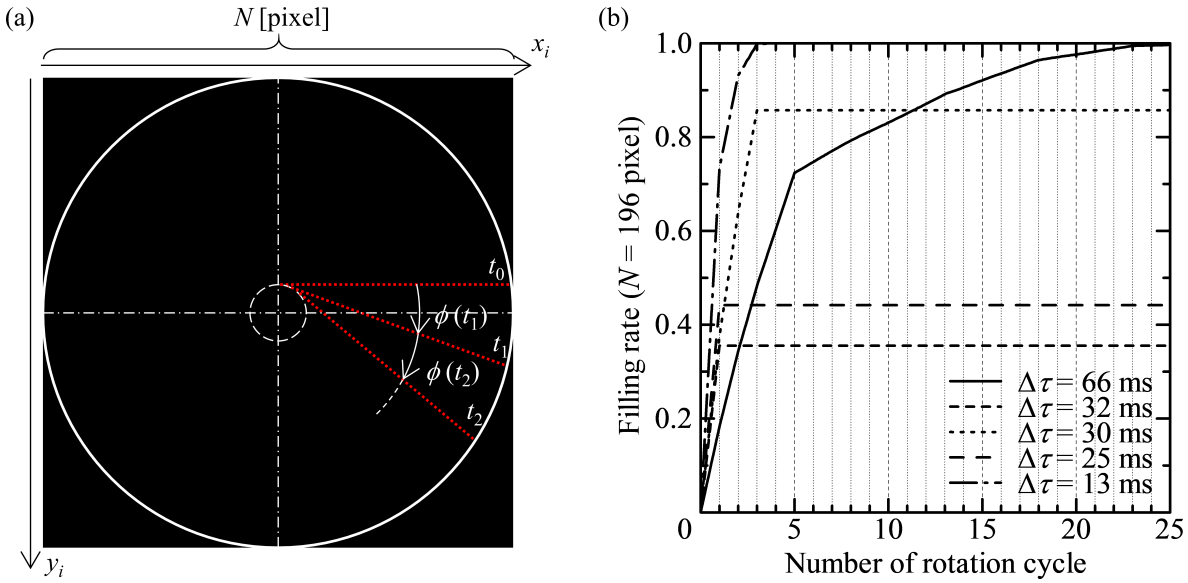


Figure A.4: (a) Schematic drawing of the visualization process using the geometric relationship, (b) filling rate of the image drawing versus number of profiles at each temporal resolution; $N$ = 196 pixels, $\omega$ = 15 rpm, $\Delta\xi$ = 0.74 mm

signals affected by reflection at interfaces are displayed clearly.

Figure A.6 shows the results of the visualization process as described above. Figure A.6(a) presents the result obtained from the Doppler velocity distribution, Fig. A.6(b) that from the echo intensity distribution, and Fig. A.6(c) that from superposition of the Doppler velocity and echo intensity distributions. As shown in these figures, the spatiotemporal information could be converted into a two-dimensional image by the drawing process mentioned above. Considering the actual diameter and thickness of the rubber ball in Fig. A.6(c) (i.e., 71.0 and 9.6 mm, respectively), the black circular region in Fig. A.6(a) may correspond to the hollow part of the rubber ball. Additionally, the strong echo intensity distribution in Fig. A.6(b) may also indicate the diameter of the rubber ball. The rubber ball is hollow, and the acoustic impedance of air is different from that of rubber. From the echo information in Fig. A.6(b), however, the strong echo is only detected at the outer surface of the rubber ball owing to the attenuation characteristics of ultrasound inside the ball. Even though ultrasonic waves were reflected at places inside the rubber ball, they were not detected owing to the low sound pressure of the reflected waves. In contrast, Doppler velocity information in Fig. A.6(a) shows similar values even inside the ball except for the inner hollow. This is because the Doppler shift frequency is calculated from variations in sound pressure of the echo and is not greatly affected by the degree of the echo intensity itself, where sources of the ultrasonic echo from inside the ball are impurities and bubbles in the rubber. Furthermore, it is expected that a silent layer forms near interfaces having a large drop in acoustic impedance, where incident and reflected waves interfere and create an area of very low acoustic pressure [27]. Furthermore, no Doppler velocity is obtained in the layer. Detections of the effect of the reflected wave at the surface of the hollow part in Fig. A.6(c) around the interior of the hollow are evidence of the formation of the layer.

In summary, the preliminary visualization experiment conducted for a rubber ball elucidated the condition required to fill the visualization domain and advantages of using two types of information — of the Doppler velocity and echo intensity — that allow visualization according to different characteristics.

### A.2.3 Echo intensity field expected from numerical simulation

Acoustic characteristics of attenuations, reflections, and refractions at interfaces in the present scanning system are discussed here to clarify images obtained from the ultrasonic Doppler-echo visualization. Numerical simulations of sound pressures $P_s$ for ultrasonic waves propagating in media are performed for different situations of the incidence of ultrasonic waves under different acoustic conditions. Considered situations that modify incident ultrasonic waves are summarized in Fig. A.7, for (a) attenuation, (b) modifications of the ultrasonic path length, and (c) total and (d) partial reflections at an interface.

As shown in Fig. A.7(a), the attenuations of sound pressure depend on the media and are expressed as

$$P_s = P_0 \exp(-\alpha\xi), \tag{A.9}$$

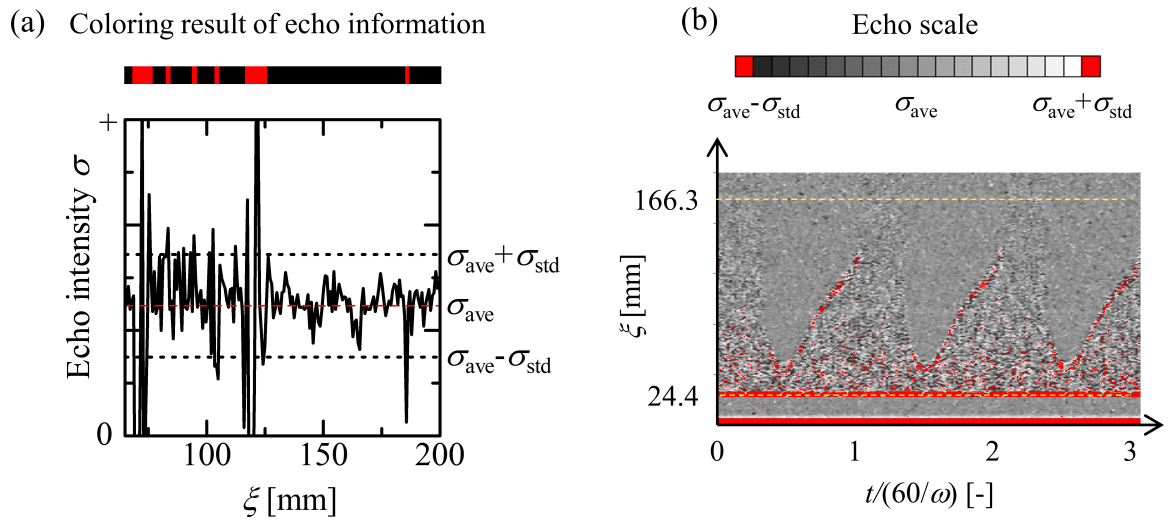


Figure A.5: (a) Instantaneous echo intensity at the measurement line and thresholds for coloring and (b) binarized echo intensity distribution, where the original echo intensity distribution (Fig. A.33b) is superimposed for comparison

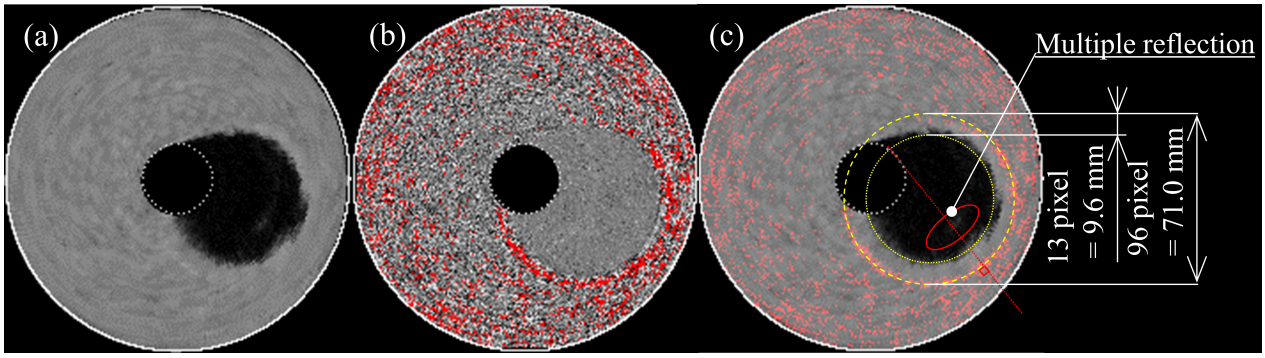


Figure A.6: Visualization results of the rubber ball; (a) Doppler velocity, (b) echo intensity, where intensity higher than the set threshold is indicated by red pixels, and (c) composite view of the Doppler velocity and the binarized echo intensity, where the red dashed line indicates the vertical incidence of ultrasonic pulses to the rubber ball surface.

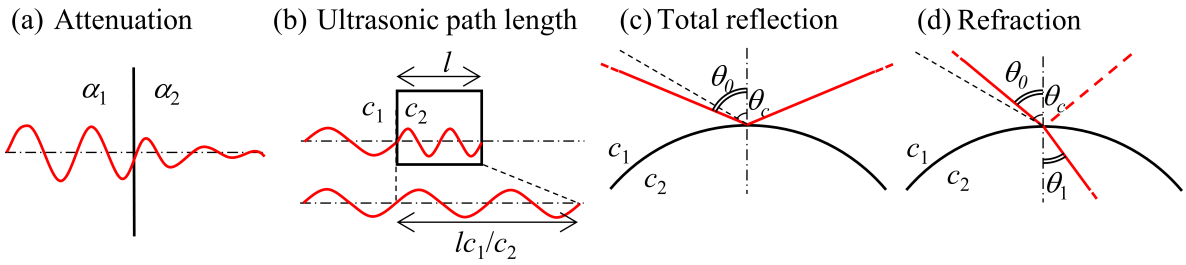


Figure A.7: Schematic overviews of considered acoustic effects in cases of the speed of sound $c_1 > c_2$ for (a) attenuation, where $\alpha_1$ and $\alpha_2$ indicate attenuation coefficients in each medium, (b) ultrasonic path length in media, (c) total reflection, and (d) partial reflection at an interface.

Table A.3: Parameters used in numerical simulations.

| Condition | $\alpha_2$ [1/mm] | $c_2$ [m/s] | $Z_2$ [$10^6$ kg/m$^2$s] |
|---|---|---|---|
| i | 0.001 | 1500 | 1.50 |
| ii | 0.005 | 1500 | 1.50 |
| iii | 0.001 | 1100 | 1.10 |

where $P_0$ and $\alpha$, respectively, indicate the initial sound pressure and attenuation coefficient, and the transmission distance $\xi$ is the distance of the round trip from reflectors to the transducer. The speed of sound is defined as $c = (K/\rho)^{1/2}$, where $\rho$ and $K$ are the density and elastic modulus of media, and this parameter thus indicates material hardness. In general cases with an acoustic wave incident on solid media, the mode transforms from longitudinal waves to, for example, transversal and Rayleigh waves. The speed of sound depends on the media, and the ultrasonic path length can thus be modified by the difference [Fig. A.7(b)]. The reflection and refraction of the incident acoustic waves at interfaces are also determined by the speed of sound in the media [Fig. A.7(c)]. Total reflections occur in the case that $c_1 > c_2$ and $\theta_0 > \theta_c$, where $\theta_0$ is the angle of incidence and the critical angle $\theta_c$ is derived from Snell's law as $\theta_c = \sin^{-1}(c_2/c_1)$. When the angle of incidence is smaller than the critical angle [Fig. A.7(d)], the waves can propagate to the inner medium with refraction angle $\theta_1 = \sin^{-1}(c_2/c_1 \sin\theta_0)$. The incident wave is partially reflected with the reflection ratio $\gamma$ defined as

$$\gamma = \left( \frac{Z_2 \cos\theta_0 - Z_1 \cos\theta_1}{Z_1 \cos\theta_1 + Z_2 \cos\theta_0} \right)^2, \tag{A.10}$$

where $Z_1$ and $Z_2$ indicate the acoustic impedance in each medium defined as $Z = \rho c$.

According to the fundamental knowledge of acoustics described above, numerical simulations of echo intensity fields were performed as investigations regarding the sound pressure under the three conditions summarized in Table A.3. Acoustic conditions for the present system configuration are summarized in Fig. A.8, where acoustic properties of the medium around the test object are assumed to be the same as those for water; i.e., the speed of sound $c_1$, density $\rho_1$, acoustic impedance $Z_1$, and attenuation coefficient $\alpha_1$ are given as 1500 m/s, 1000 kg/m$^3$, $1.5\times10^6$ kgs/m$^2$, and 0.002 mm$^{-1}$, respectively. The radial position of the test object $R_c$, radius of the test object $r_c$, and density $\rho_2$ of the test object are fixed at 25 mm, 45 mm, and 1000 kg/m$^3$, respectively.

Figure A.9(a) shows color contours of the radial-azimuthal sound pressure distribution obtained from numerical simulation under condition i. The vertical and horizontal axes indicate the rotation angle and distance from the transducer. Solid and broken lines indicate the material interface and rotation angles of $\phi = 80,\ 160,\ 240,\ 320°$. The attenuation is set larger in the inner material than in the outer materials, and the decrease in sound pressure in the inner region is thus greater than that in the outer region as shown in Fig. A.9(a). Figure A.9(b) shows the results of polar rearrangement using the algorithm explained in §A.2.2. A comparison of results for conditions i and ii shows that differences in attenuation strongly affect the propagation of the sound pressure, and decreases in the sound pressure depend on the incidence angle. In addition, results for conditions i and iii show results for different speeds of sound. Condition i gives a complete circle of the color contour. Meanwhile, condition iii gives a partial circle having a clear border. These wanes of the circle are affected by total reflection at the interface of the material. The position of the interface is indicated with an asterisk in Fig. A.9(b)-iii. Occurrences of the clear border are from the ratio of the reflection described by Eq. (A.10). These changes in the sound pressure field are essential in consideration of propagations of the ultrasonic wave, and suggest thresholds that determine whether returned ultrasonic waves are sufficiently strong to be detected.

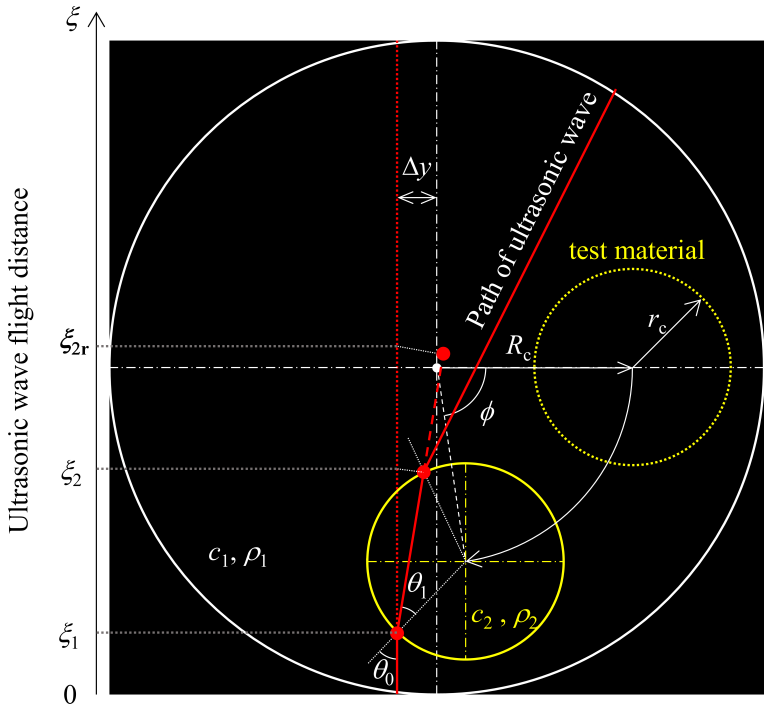


Figure A.8: Configurations of the numerical simulation ($c_1$, $c_2$: speed of sound, $R_c$: radial position of center of the test object, $r_c$: radius of the test object, $\theta_0$: angle of incidence of the ultrasonic wave into the test object, $\theta_1$: refraction angle of the ultrasonic wave, $\xi_1$, $\xi_2$: actual flight distance of the ultrasonic wave from a transducer, $\xi_{2r}$: apparent flight distance as the ultrasonic path length)

Table A.4: Qualitative characteristics of test objects.

| Objects | Roughness | Hardness | Inner structure | Cross-sectional shape |
|---|---|---|---|---|
| Rubber ball | Regular dents | Elastic | Hollow | Circle |
| Apple | Smooth | Hard | Semi-homogeneous | Ill-shaped circle |
| Tomato | Smooth | Semi-soft | Complex | Ellipse |
| Kiwi | Fuzzy | Semi-hard | Fibriform | Small circle |
| Syruped cherry | Smooth | Soft | Seed | Tiny circle |

## A.3 Practical application to fresh fruits

To investigate the applicability of the present visualization method to fresh fruit, test fruit with different acoustic characteristics was chosen for the visualization of inner structures. The qualitative characteristics of the test objects (including a rubber ball), such as the surface roughness, hardness, and cross-sectional shape, are summarized in Table A.4. Fresh apples have a smooth surface, have pulp that is generally harder than that of other fruits, and have a slightly distorted circular shape. Fresh tomatoes have a smooth skin surface, relatively soft inner pulp, and complex inner tissues, which can be observed for the cut tomatoes shown in Fig. A.2. We can evaluate the feasibility of the present method using these different characteristics of test fruit. In this section, we demonstrate the ultrasonic Doppler–echo visualization for the test fruit and discuss the practical applications of the visualization for fresh fruit.

Figure A.10 shows results of the visualization for a fresh apple held in the montmorillonite suspension, Fig. A.10(a) the spatiotemporal Doppler velocity distribution, and Fig. A.10(b) the ultrasonic echo intensity. These were obtained at elapsed rotation times for rotation speed $\omega = 15$ rpm, temporal resolution $\Delta t = 66$ ms, and spatial resolution $\Delta\xi = 0.74$ mm by the UVP measurement. The vertical and horizontal axes indicate the radial position normalized by the radius of the cylindrical container, $R$, and the rotation time. The grayscale contours represent the Doppler velocity normalized by $u_{\max} = 2\Omega\Delta y$. The spatiotemporal distribution of the echo intensity in Fig. A.10(b) is drawn using a linear grayscale and red for points at which the intensity is higher than the threshold. The strong echo points have a periodic variation. According to the preliminary results for the rubber ball summarized in the last section, the variation corresponds to the outer surface of the apple. Clear boundaries observed here are reasonable considering the large difference in acoustic impedance due to pulp

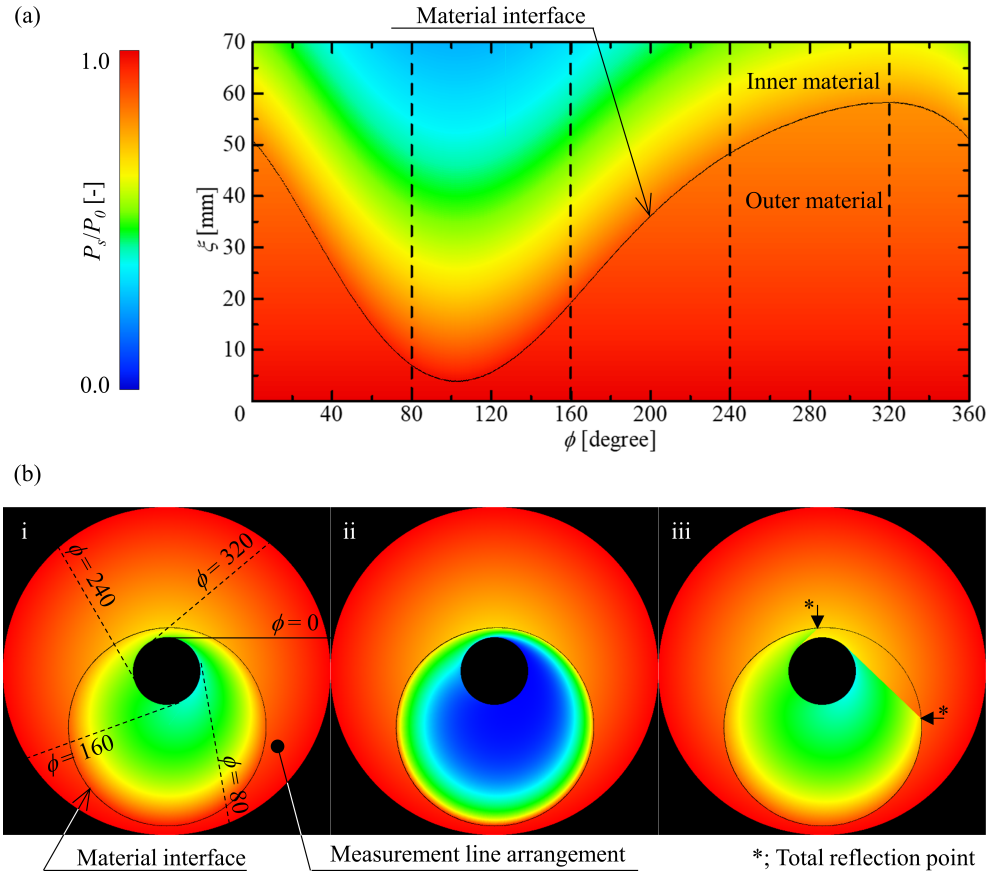


Figure A.9: (a) Color contours of the spatioangular sound pressure distribution under condition i and (b) results of numerical simulation for the sound pressure field under conditions i–iii specified in Table A.3

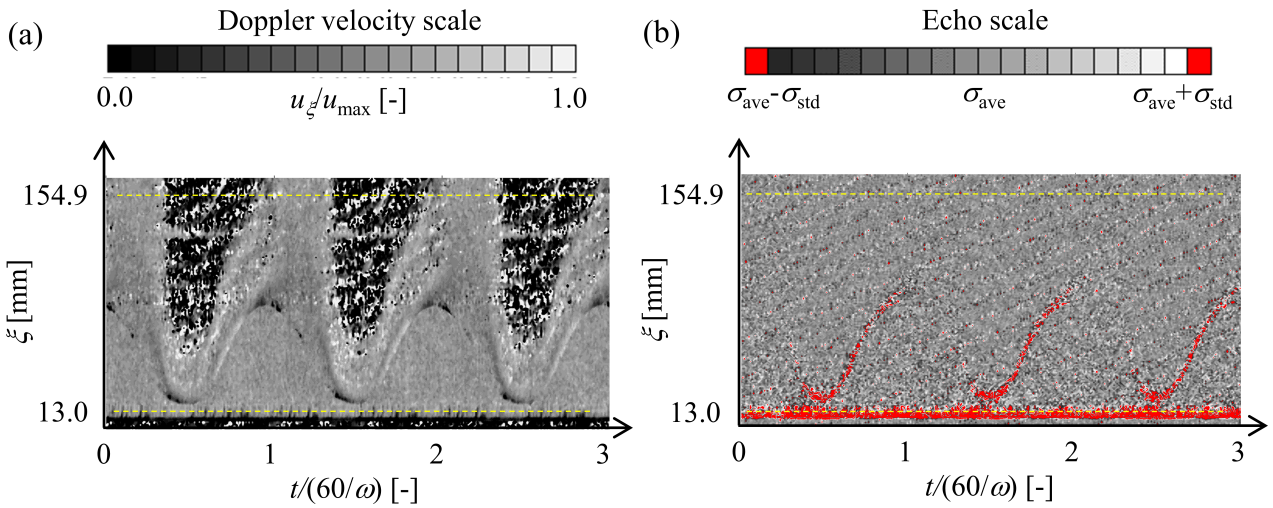


Figure A.10: (a) Spatiotemporal Doppler velocity distribution of a test apple and (b) corresponding spatiotemporal echo intensity distribution

hardness and higher density for the pulp than for water. The Doppler velocity distribution in Fig. A.10(a) indicates the corresponding outline of the apple surface as an area of low velocity. There are also complex variations on the middle-far side of the scanning line. Doppler velocity distributions take a constant value in cases of steady rigid-body rotations Eq. (A.1). Variations in the value indicate acoustic effects on the scanning line as summarized in Fig. A.7.

Visualization images are constructed from spatiotemporal distributions of the Doppler velocity and echo intensity shown in Fig. A.10 by adopting the procedure described in §A.2.2, and the results are summarized in Fig. A.11. These figures reveal that the shape of the apple may be visualized with both the Doppler velocity and echo distributions obtained from differences in acoustic characteristics between the apple and suspension. The arc shape of the strong echo distributions in Fig. A.11(b) is from total reflection at the interface of the apple and a similar pattern is observed in the results of numerical simulation shown in case iii of Fig. A.9. According to the literature [29], the speed of sound in apple pulp is lower than that in suspension (1480 m/s) and so this consideration is reasonable. The low-velocity region in the Doppler velocity distribution shown in Fig. A.11(a) almost agrees with the distribution of the high echo intensity in Fig. A.11(b), and partially compensates for the lack of high echo intensity along a deformed circular shape that may correspond to the outline of the apple. The basis of this compensation using the Doppler velocity is that silent layers having low Doppler velocities are due to the interference of incident and reflected ultrasonic waves, and the silent layers are not so strongly affected by echo intensity. Furthermore, formations of the layer depend on the incident angle and the layers are not always observed in regions of high echo intensity. Therefore, the shape of the apple is displayed by complementary visualization using both the Doppler velocity and echo intensity. The inner region of the outline of the apple on the visualization plane seems to have an almost uniform Doppler velocity and low echo intensity without dispersed dots of high echo intensity due to multiple reflections. This suggests that the interior of the apple has an almost uniform acoustic property. Attenuation of the incident ultrasonic waves inside the apple is strong and no echo was detected, and the effects of multiple reflections thus appear as spiky noise.

A fresh tomato as the second test object has characteristics of a pulp softer than other fruit pulps and a peel thinner than other fruit peels. In comparison with apples as the first test object, tomatoes are expected to be penetrated far more by ultrasonic waves. Figure A.11(d)–(f) presents the visualization results of the Doppler velocity distributions and echo intensities of a fresh tomato. The tendency of the Doppler velocity and echo intensity distributions corresponding to the outline of the tomato is similar to that of the apple shown in Fig. A.11(a)–(c), and the approximate external shape of the tomato can be recognized from the Doppler velocity and echo information. Compared with Fig. A.11(c), where apples have homogeneous and fibrous tissue, Fig. A.11(f) shows a complex pattern inside the visualized outline and the largest pattern seems to be a second circular layer of low Doppler velocity. There is a possibility that the circular layer is caused by multiple reflections between the cylinder wall and tomato peel. In fact, there are parts of high intensity in the inner region and multiple circular patterns with lower intensity generated by multiple reflections. However, at the least, the thicker layer of low Doppler velocity forming the circular pattern cannot be explained only by multiple reflections. We, therefore, conclude that the visualization pattern in Fig. A.11(f) represents the inner structure of the tomato. However, in the case of measurement of kiwi [Fig. A.11(g)–(i)], it is difficult to assure the applicability of the visualization, as the skin of kiwi fruits is so fuzzy. Such skin feature may make it difficult to propagate the ultrasonic wave inside the fruit pulp. The measurement limitation is possible to

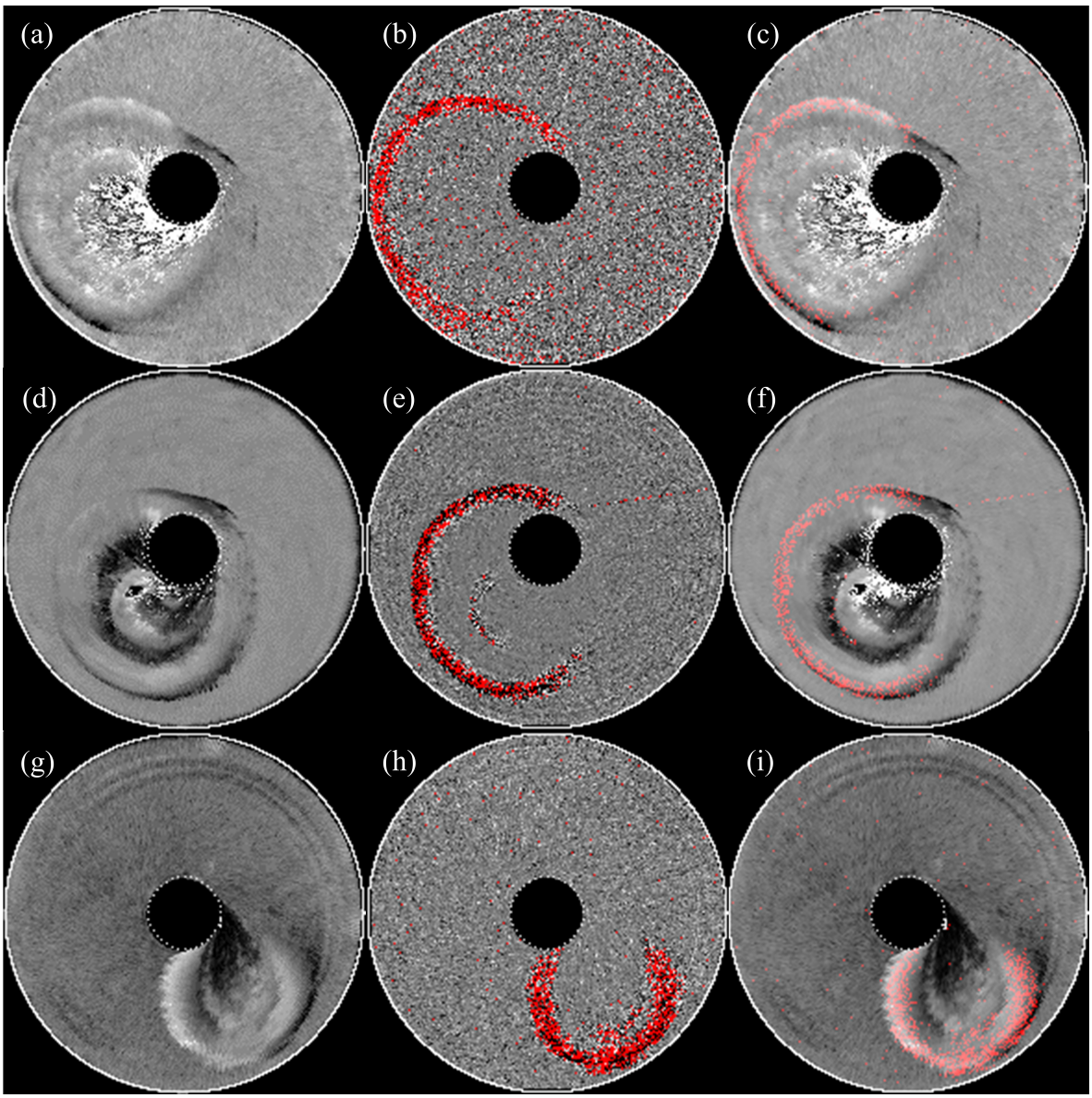


Figure A.11: Visualization results for each test material, (a)–(c) apple, (d)–(f) tomato, and (g)–(i) kiwi, where (a), (d), and (g) indicate Doppler velocity, (b), (e), and (h) indicate echo intensity, (c), (f), and (i) indicate composite view with the Doppler velocity and the region of high echo intensity represented by red dots.

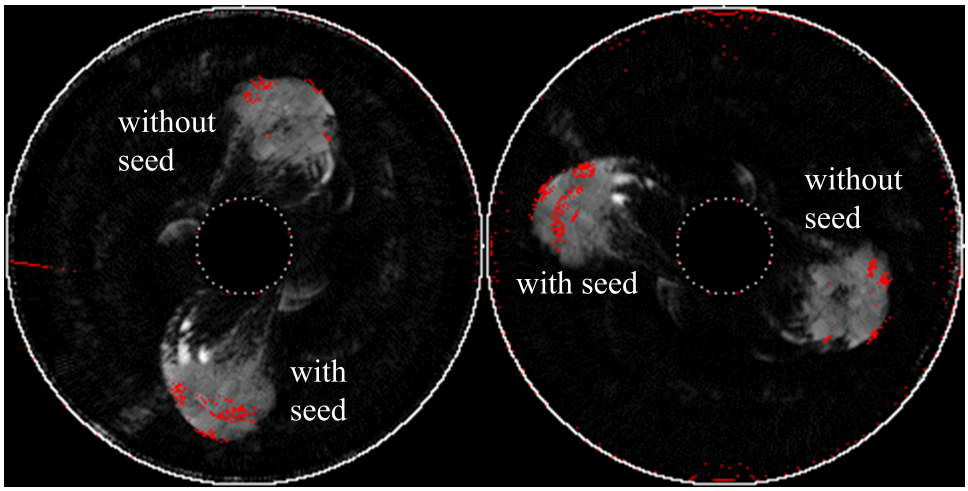


Figure A.12: Visualization results for syruped cherry indicating composite view with the Doppler velocity and the region of high echo intensity represented by red dots.

be overcome by considering the optimal design of ultrasonic transducer for better measurement.

As an another application of the visualization technique, inner seed detection for syruped cherries was examined (Fig. A.12). When the test cherry is seeded, the ultrasonic echo amplitude is weaker than the result with seed. Further, the Doppler velocity in the result without seed is also modulated compared to that in the result with seed. The reproducibility was ensured with twice experiments as shown in Fig. A.12. From the observation of experiments, it is speculated that the acoustic impedance of the syruped cherry matches better than the fresh fruit pulp because inner gas containing fruit pulp may be extracted during making the syruped fruits.

## A.4 Conclusion

We proposed a novel ultrasonic Doppler–echo visualization, which allows us to estimate the maturity and inner pulp structures of fresh fruit using a rotating cylinder system and information of the Doppler velocity and echo intensity. Conditions of the spatial resolution of the ultrasonic measurement and the number of scanning lines that form visualization images were investigated theoretically. The measurement systems including ambient fluids that hold test objects were optimized by considering basic acoustic characteristics. The feasibility of the present visualization method was evaluated through trial measurements of a rubber ball, fresh apple, and fresh tomato while considering the acoustic characteristics of the tissue and inner materials. Complementarily distributions of the Doppler velocity and echo intensity had different patterns reflecting the outline and inner structures of test objects including fresh fruit. In particular, the Doppler velocity distributions showed clearly that the interior medium of each test material had distinct effects of the Doppler-shifted frequency. Superposition of the distributions visualized details of the structures even though there were effects of multiple reflections of ultrasonic waves.

## References

[1] Y. Takeda, “Ultrasonic Doppler velocity profiler for fluid flow,” Springer, Tokyo (2012).
[2] M. Iima, Y. Tasaka, “Dynamics of flow structures and surface shapes in the surface switching of rotating fluid,” J. Fluid Mech. 789, 402–424 (2016).
[3] Y. Tasaka, M. Iima, “Flow transition in the surface switching of rotating fluid,” J. Fluid Mech. 636, 475–484 (2009).
[4] T. Vogt, I. Grants, S. Eckert, G. Gerbeth, “Spin-up of a magnetically driven tornado-like vortex,” J. Fluid Mech. 736, 641–662 (2013).
[5] K. Timmel, S. Eckert, G. Gerbeth, “Experimental investigation of the flow in a continuous-casting mold under the influence of a transverse, direct current magnetic field,” Metall Mater. Trans. B 42(1), 68–80 (2011).
[6] L. Cordovaa, N. Furuichib, T. Lederera, “Qualification of an ultrasonic flow meter as a transfer standard for measurements at Reynolds numbers up to $4 \times 10^6$ between NMIJ and PTB,” Flow Meas. Instrum. 45, 28–42 (2015).

[7] B. Ouriev, E. J. Windhab, "Rheological study of concentrated suspensions in pressure-driven shear flow using a novel in-line ultrasound Doppler method," Exp. Fluids 32(2), 204–211 (2002).
[8] B. Derakhshandeh, D. Vlassopoulos, "Thixotropy, yielding and ultrasonic Doppler velocimetry in pulp fiber suspensions," Rheol. Acta 51, 201–214 (2012).
[9] T. Yoshida, Y. Tasaka, Y. Murai, "Rheological evaluation of complex fluids using ultrasonic spinning rheometry in an open container," J. Rheol. 61(3), 537–549 (2017).
[10] Y. Murai, S. Ohta, A. Shigetomi, Y. Tasaka, Y. Takeda, "Development of an ultrasonic void fraction profiler," Meas. Sci. Technol. 20(11), 114003 (2009).
[11] Y. Murai, Y. Tasaka, Y. Nambu, Y. Takeda, S. R. Gonzalez, "Ultrasonic detection of moving interfaces in gas–liquid two phase flow," Flow Meas. Instrum. 21(3), 356–366 (2010).
[12] T. T. Nguyen, N. Tsuzuki, H. Murakawa, H. N. Duong, H. Kikura, "Measurement of the condensation rate in subcooled flow boiling by using two ultrasonic frequencies," Int. J. Heat. Mass Tran. 99, 159–169 (2016).
[13] C. J. Clarka, P. D. Hockings, D. C. Joyce, R. A. Mazucco, "Application of magnetic resonance imaging to pre- and post-harvest studies of fruits and vegetables," Postharvest Biol. Technol. 11(1), 1–21 (1997).
[14] M. E. Saltveit, "Determining tomato fruit maturity with nondestructive in vivo nuclear magnetic resonance imaging," Postharvest Biol. Technol. 1(2), 153–159 (1991).
[15] L. Zhang, J. M. Michael, "Measurement and evaluation of tomato maturity using magnetic resonance imaging," Postharvest Biol. Technol. 67, 37–43 (2012).
[16] C. R. Brodersen, E. F. Lee, B. Choat, S. Jansen, R. J. Phillips, K. A. Shackel, A. J. McElrone, M. A. Matthews, "Automated analysis of three-dimensional xylem networks using high-resolution computed tomography," New phytol. 191(4), 1168–1179 (2011).
[17] Y. M. Staedler, D. Masson, J. Schönenberger, "Plant tissues in 3D via X-ray tomography: simple contrasting methods allow high resolution imaging," PLoS One 8(9), e75295 (2013).
[18] C. Lee, S. Y. Lee, J. Y. Kim, H. Y. Jung, J. Kim, "Optical sensing method for screening disease in melon seeds by using optical coherence tomography," Sensors 11(10), 9467–9477 (2011).
[19] A. L. Oldenburg, X. Chenyang, S. A. Boppart, "Spectroscopic optical coherence tomography and microscopy," IEEE J. Sel. Top Quant. 113(6), 1629–1640 (2007).
[20] P. Verboven, A. Nemeth, M. K. Abera, E. Bongaers, D. Daelemans, P. Estrade, E. Herremans, M. Hertog, W. Saeys, E. Vanstreels, B. Verlinden, M. Leitner, B. Nicolai, "Optical coherence tomography visualizes microstructure of apple peel," Postharvest Biol. Technol. 78, 123–132 (2013).
[21] N. Hosoya, M. Mishima, I. Kajiwara, S. Maeda, "Non-destructive firmness assessment of apples using a non-contact laser excitation system based on a laser-induced plasma shock wave," Postharvest Biol. Tecnol. 128, 11–17 (2017).
[22] R. C. Chivers, H. Russell, L. W. Anson, "Ultrasonic studies of preserved peaches," Ultrasonics 33(1), 75–77 (1995).
[23] A. Mizrach, "Assessing plum fruit quality attributes with an ultrasonic method," Food Res. Int. 37(6), 627–631 (2004).
[24] A. Mizrach, "Nondestructive ultrasonic monitoring of tomato quality during shelf-life storage," Postharvest Biol. Technol. 46(3), 271–274 (2007).
[25] A. Mizrach, "Ultrasonic technology for quality evaluation of fresh fruit and vegetables in pre- and postharvest processes," Postharvest Biol. Technol. 48(3), 315–330 (2008).
[26] Y. Tasaka, T. Kimura, Y. Murai, "Estimating the effective viscosity of bubble suspension in oscillatory shear flows by means of ultrasonic spinning rheometry," Exp. Fluids 56(1), 1897 (2015).
[27] Y. Murai, H. Fujii, Y. Tasaka, Y. Takeda, "Turbulent bubbly channel flow investigated by ultrasound velocity profiler," J. Fluid Sci. Technol. 1(1), 12–23 (2006).
[28] H. J. Park, Y. Tasaka, Y. Murai, "Ultrasonic pulse echography for bubbles traveling in the proximity of a wall," Meas. Sci. Technol. 26(12), 125301 (2015).
[29] S. N. Jha, "Nondestructive evaluation of food quality," vol. 375, Springer, Heidelberg (2010).

Appendix B

# Supplemental information to upgrade USR

## Contents


**B.1 Noise evaluation in measured velocity . . . 169**
B.1.1 Statistical calculation for obtained velocity . . . 169
B.1.2 Production of artificial random noises with normal distribution . . . 170
**B.2 Accuracy and precision assessments . . . 170**
B.2.1 Phase lag averaging with short time DFT . . . 170
B.2.2 Spectral subtraction method utilizing periodic functionalized algorithm . . . 171
**B.3 Influence from radial gradient of viscosity profile in phase-lag analysis . . . 172**
**B.4 Summary . . . 174**
**References . . . 175**


## B.1 Noise evaluation in measured velocity

### B.1.1 Statistical calculation for obtained velocity

To obtain velocity fluctuations of unsteady shear flows in silicon oil ($\nu$ = 1000 mm$^2$/s), an ultrasonic transducer of resonance frequency 4 MHz and 5 mm effective element diameter was selected. Important parameters of UVP are temporal resolution $\Delta\tau$ = 50 ms, spatial resolution $\Delta\xi$ = 0.74 mm, and speed of sound $c$ = 980 m/s. Instantaneous spatiotemporal velocity $u_\xi$, cycle-averaged velocity $u_{\mathrm{ave}}$, and residual velocity $u_{\mathrm{err}}$ are shown in Fig. B.1(a)–(c), where the horizontal and vertical axes indicate cycle-period, $tf_{\mathrm{o}}$, and radial position normalized by the cylinder radius, $r/R$. The gray scale indicates velocity amplitude. $u_{\mathrm{ave}}$ and $u_{\mathrm{err}}$ were calculated by cycle average of $u_\xi$ for $N$ = 100 ($\Delta t$ = 1$s$) and $u_\xi - u_{\mathrm{ave}}$. The velocity fluctuations propagate according with phase-lag from the cylindrical wall, $r/R$ = 1.0 [Fig. B.1(a) and (b)], where the result of Fig. B.1(a) has more noisy profiles than that of Fig. B.1(b). From $u_{\mathrm{err}}$ distribution [Fig. B.1(c)], these noises increase with getting closer to the wall, because quality of velocity obtained by UVP may change depending on velocity magnitude.

To confirm factors in the generation of $u_{\mathrm{err}}$, instantaneous velocity was compared to the averaged velocity [Fig. B.2(a)], where differences between $u_\xi$ and uave were compared in all data of $r/R$ and $tf_{\mathrm{o}}$. Two significant findings were observed: (1) Deviations in the measured velocity increase as measurement target velocity increases. (2) Measured velocity profiles have the lowest noise level observed from low velocity in Fig. B.2(a). Moreover, the variance profile of $u_{\mathrm{err}}$ also indicates the deviation tendency of obtained instantaneous velocity [Fig. B.2(b)], where the horizontal and vertical axes show variance

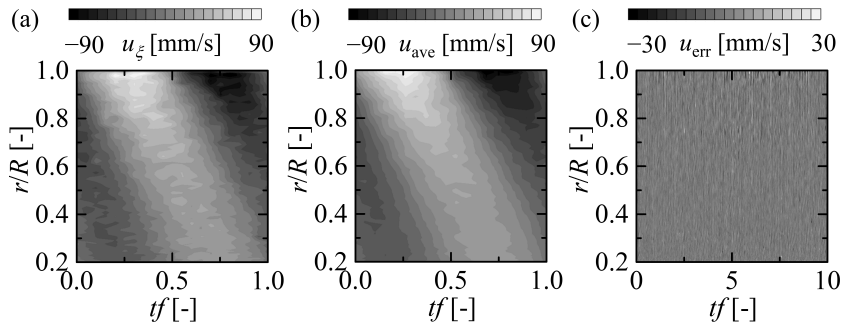


Figure B.1: (a) Instantaneous velocity distribution, $u_\xi$, in experiment, (b) averaged velocity distribution, $u_{\mathrm{ave}}$, with $N$ = 100, (c) relative error velocity subtracted $u_{\mathrm{ave}}$ from $u_\xi$

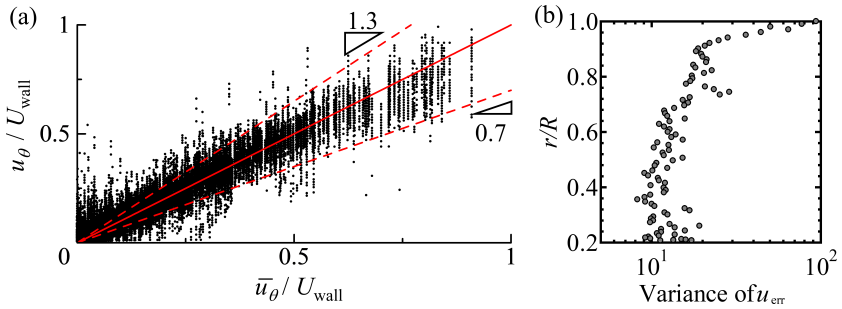


Figure B.2: (a) Comparison of instantaneous and averaged velocity, where a total number of plotted data is $2000 \times 96$, (b) variance profile of $u_{\text{err}}$ calculated from Fig. B.1(c)

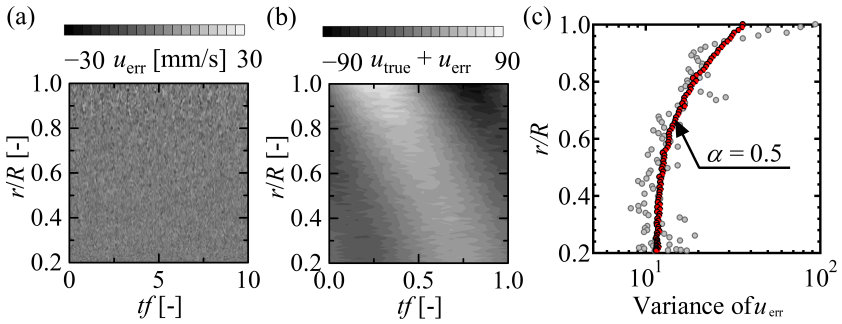


Figure B.3: (a) Produced artificial random noises at $\alpha = 0.5$, (b) velocity distribution with noise (a) to velocity calculated form numerical solution, (c) $u_{\text{err}}$ variance in noise amplitude $\alpha = 0.5$

and normalized radial position in the cylindrical container. The variance profiles converged to almost 10 $\text{mm}^2/\text{s}^2$ when $r/R$ get closer to the cylinder center. The reason for the significant increase in the variance near the wall is co-reflection of the ultrasound at the interface between acrylic resin the fluid media.

### B.1.2 Production of artificial random noises with normal distribution

Considering the tendency of noises estimated from $u_\xi$ [see Fig. B.2], artificial random noises assuming experimental conditions are created by a noise-model function using Box-Muller method [1] to create uniform random values with $(0, 1]$, which are generated by Mersenne Twister [2]. The noises are defined as $n(\mu, \sigma^2)$ with Gaussian distribution, where $\mu$ and $\sigma$ indicate average and standard deviation. The noise-model considered from the experimental result is given as

$$u_{\text{err}} = n_1\left(0, \alpha|u_\xi|\right) + n_2\left(0, \sigma^2_{\text{min}}\right), \tag{B.1}$$

where $\alpha$ and $\sigma^2_{\text{min}}$ indicate a noise amplitude coefficient and the lowest noise level. $n_1$ and $n_2$ are a Gaussian random function with normal distribution and are independent of each other. The noise amplitudes were determined by $\alpha$, included in a function, $n_1$. On the other hand, the standard deviation of $n_2$ was determined from the lowest noise level of the experimental result as shown in Fig. B.2(b). Produced noise at $\alpha = 0.5$ and velocity distribution with noises to the analytical solution are shown in Fig. B.3(a) and (b). The produced noises of Fig. B.3(b) are qualitatively agree with that of Fig. B.1(a). Variance profiles at the case of $\alpha = 0.5$ have good agreement with experimental result [Fig. B.3(c)], so these parameters were determined in the next section to evaluate the accuracy of the viscosity measurement algorithms.

## B.2 Accuracy and precision assessments

### B.2.1 Phase lag averaging with short time DFT

By utilizing the method to produce velocity distributions by numerical solution with artificial random noises as mentioned above, it is possible to evaluate the accuracy as a probability density distribution $P_{\text{vis}}(= M_{\text{count}}/M)$ by repetitive computing. $M_{\text{count}}$ and $M$ indicate the count number of how many values fall into each bin and number of trials. $P_{\text{vis}}$ is calculated by

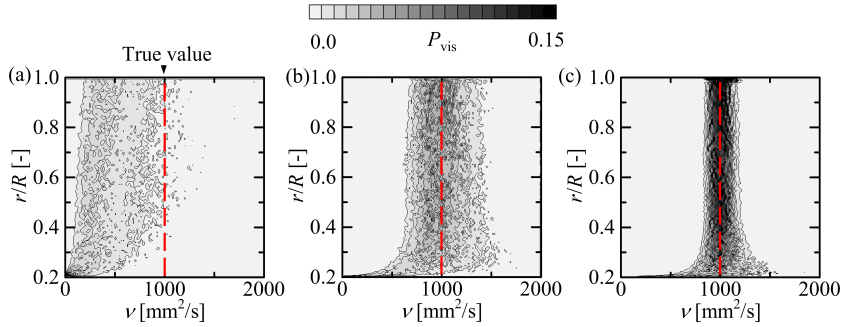


Figure B.4: Histogram in probability density distribution of the viscosity at cases (a) $N = 1$, (b) $N = 80$, (c) $N = 320$

numerical computation with $M = 2000$. Histograms of simulated results were calculated by counting $M_{\mathrm{count}}$ at every step of $\nu$ in 20 mm$^2$/s from 0 mm$^2$/s to 2000 mm$^2$/s. Probability density distribution of viscosity profiles was evaluated from simulated velocity distribution at cases of averaging cycle times, $N = 1, 80, 320$ [Fig. B.4]. The horizontal and vertical axes indicate kinematic viscosity and normalized radial position, where the true value of kinematic viscosity to solve the analytical solution is emphasized by the dashed line. The gray scale shows the probability of viscosity measurement using the phase-lag analysis. To evaluate the viscosity profiles, phase lag obtained from the velocity distribution is needed to calculate the differential. Noises in the phase lag influences viscosity measurements due to noise amplification of differential in phase-lag profiles. So, before the calculations are processed, noise reductions of phase-lag profiles are required to reduce viscosity scattering. When the phase-lag profiles are $N = 1$, the evaluated viscosity profiles are scattered with large difference from the true value [Fig. B.4(a)]. Since the noises in phase-lag profiles decreases by calculating arithmetic mean profiles in $N > 1$, histograms of the viscosity show higher accuracy and precision than that of $N = 1$ [Fig. B.4(b) and (c)].

At noise amplitudes in different $N$, mode value (highest probability density distribution), +25% summation of the distribution from the mode value, and −25% of that are summarized in Table B.1, where these results were averaged by $0.6 < r/R < 1.0$ and obtained from the viscosity. It indicates the accuracy of the viscosity depending on the averaging cycle times $N$. Arithmetic mean calculations are, however, limited when test fluids have constant rheological properties with changing shear rate (Newtonian fluid).

Table B.1: Mode, +25%, and −25% values calculated from histograms of the viscosity, which are averaged by $0.6 < r/R < 1.0$

| $N$ | 1 | 20 | 40 | 80 | 160 | 320 |
|---|---|---|---|---|---|---|
| Mode [mm$^2$/s] | 316 | 919 | 938 | 965 | 981 | 993 |
| +25% [mm$^2$/s] | 684 | 1122 | 1083 | 1051 | 1040 | 1032 |
| −25% [mm$^2$/s] | – | 695 | 754 | 818 | 919 | 952 |

### B.2.2 Spectral subtraction method utilizing periodic functionalized algorithm

Considering noise reductions in phase-lag profiles obtained from instantaneous velocity fluctuations, it is expected that spectral subtraction method utilizing periodic functionalized algorithm is efficient. A restricting condition in both ends of the phase-lag profiles was given to apply the DFT filtering for the phase-lag profiles. The condition is a periodic functionalized formula, $\varphi$, which is defined as following formula [schematic details in Fig. B.5(a)]:

$$\varphi(i) = \begin{cases} \phi_{X-i-1} & (\mathrm{I} : 0 \le i < X) \\ \phi_{i-X+1} & (\mathrm{II} : X \le i < 2X-1) \\ \phi_{3X-i-2} & (\mathrm{III} : 2X-1 \le i < 3X-2) \\ \phi_{i-3X+3} & (\mathrm{IV} : 3X-2 \le i < 4X-4) \end{cases} \tag{B.2}$$

$X$ indicates a total number of radial profiles. Power spectra in $\varphi(i)$ calculated by DFT have dominant Fourier components [Fig. B.5(b)], where the power smaller than $E_{\mathrm{thre}}(= 10^{-2})$ are regarded as additive noise components due to white noise characteristics. Removing the noise components on the spectra, the original phase-lag profiles $\phi(r)$ were filtered by inverse DFT. Comparing analytical solution with spatial gradients obtained from filtered phase-lag profiles $\phi_f(r)$ and $\phi(r)$, gradients

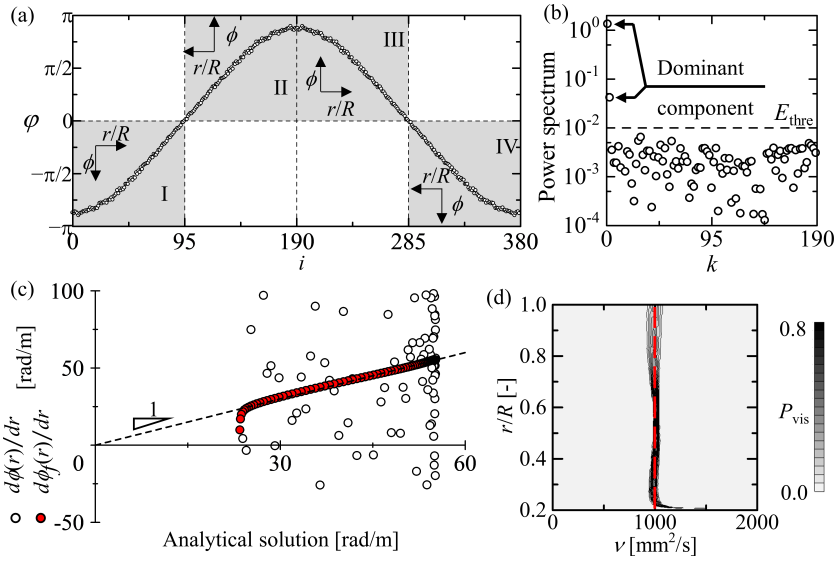


Figure B.5: (a) Periodic function defined in Eq. B.2, (b) power spectrum obtained from periodic function, (c) analytical solution versus spatial gradient of $\phi(r)$ and $\phi_f(r)$, (d) probability density distribution of the measurement from filtered phase-lag profiles

of the filtered profiles are better agreement with the analytical solution than that of original profiles [Fig. B.5(c)]. By using this filtering process, the probability density distributions[Fig. B.5(d)] indicate higher accuracy compared to the original histogram shown in Fig. B.4(a).

Actual measurement results (silicon oil: 1000 mm$^2$/s) were analyzed to confirm the applicability of this spectral subtraction method. $d\phi(r)/dr$ and $d\phi_f(r)/dr$ obtained from $N = 1$ were compared with $d\bar{\phi}(r)/dr$ [Fig. B.6(a)], where $\bar{\phi}(r)$ was averaged by $N = 500$ times of phase-lag profiles. $d\phi_f(r)/dr$ has a correlation with $d\bar{\phi}(r)/dr$ compared to $d\phi(r)/dr$, therefore this filtering method can reduce the noises equal to or greater than the arithmetic mean calculation. Probability density distributions of the kinematic viscosity obtained from $d\phi(r)/dr$ and $d\phi_f(r)/dr$ were evaluated as shown in Fig. B.6(b) and (c). The precision of viscosity measurement from $\phi_f(r)$ became higher than that of $\phi(r)$, although silicon oil may not be given accurate kinematic viscosity value due to fluid quality and temperature control.

## B.3 Influence from radial gradient of viscosity profile in phase-lag analysis

In this section, the methodology to estimate the effective viscosity using phase-lag analysis (Chapters 2 and 3) is ensured regarding the condition of radial gradient of viscosity. Considering conservation of the angular momentum, the fluid flows can be regarded as

$$\frac{\partial(\rho u_\theta r)}{\partial t} = \frac{1}{r}\frac{\partial\left(r^2\tau_\theta\right)}{\partial r}, \quad \text{s.t.} \quad \tau_\theta = \mu(r)\left(\frac{\partial u_\theta}{\partial r} - \frac{u_\theta}{r}\right), \tag{B.3}$$

where $\mu(r)$ denotes the radial function of viscosity. Eq. B.3 is transformed into

$$\underline{\frac{\partial u_\theta}{\partial t}}_{(A)} = \underline{\nu(r)\left(\frac{\partial^2 u_\theta}{\partial r^2} + \frac{1}{r}\frac{\partial u_\theta}{\partial r} - \frac{u_\theta}{r^2}\right)}_{(B)} + \underline{\frac{\partial \nu(r)}{\partial r}\left(\frac{\partial u_\theta}{\partial r} - \frac{u_\theta}{r}\right)}_{(C)}. \tag{B.4}$$

The relation, $(A) = (B)$, shown in the underlines of Eq. B.4, is the same with Eq. 2.3 in Chapter 2, and the underline $(C)$ indicates an additional term to describe radial gradient of viscosity. When the term $(C)$ is much smaller than the other terms, the viscosity can be regarded as constant. To calculate the value of each term by substituting the values of $u_\theta$ and $\nu(r)$ obtained from phase-lag analysis, the formula was modified by considering Fourier transformation as

$$i\omega\hat{u}_\theta = \nu(r)\left(\frac{\partial^2}{\partial r^2} + \frac{1}{r}\frac{\partial}{\partial r} - \frac{1}{r^2}\right)\hat{u}_\theta + \frac{\partial \nu(r)}{\partial r}\left(\frac{\partial}{\partial r} - \frac{1}{r}\right)\hat{u}_\theta. \tag{B.5}$$

When the unsteady flows have dominant frequency, $\omega = \omega_0$, the values, $\Re[\hat{u}_\theta]$, $\Im[\hat{u}_\theta]$, and $\nu(r)$, are described as one-

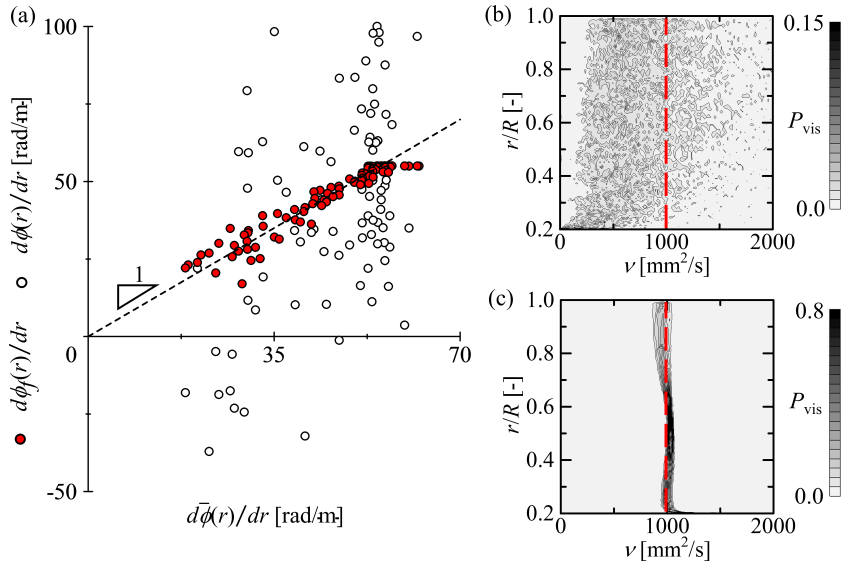


Figure B.6: (a) Spatial gradient of $\bar{\phi}(r)$ versus $\phi(r)$ and $\phi_f(r)$ at each radial position, and probability density distribution of viscosity measurement from (b) $\phi(r)$ and (c)$\phi_f(r)$ in $\Delta t$ = 1 s ($N$ = 500) of viscosity measurement

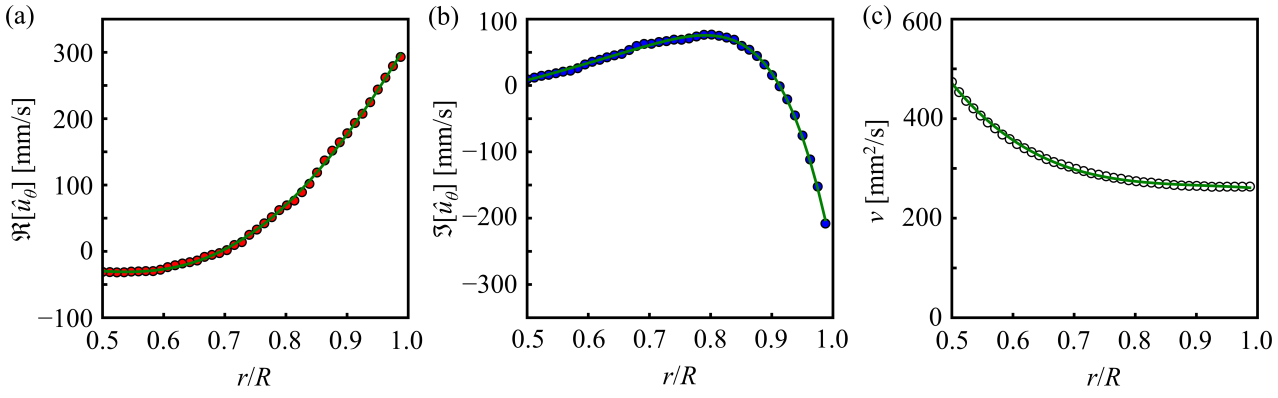


Figure B.7: Radial profiles of (a) $\Re[\hat{u}_\theta]$,(b) $\Im[\hat{u}_\theta]$, (c) $\nu$ obtained from experimental result of carboxymethyl cellulose solution, where the solid curves indicate profiles of polynomial approximation.

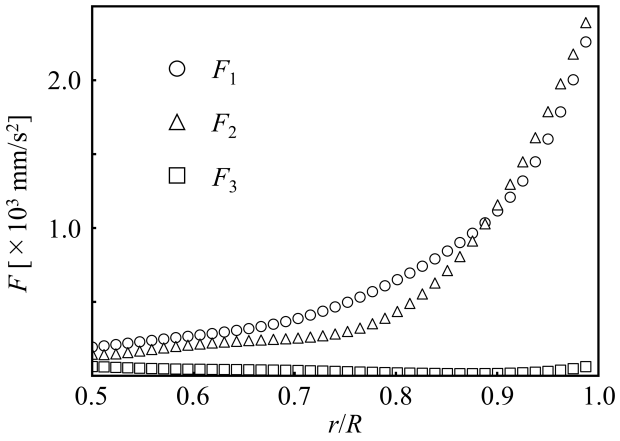


Figure B.8: Radial profiles of $F_1$, $F_2$, and $F_3$ calculated from Eqs. B.7–B.9.

dimensional profiles [Fig. B.7(a)–(c)]. The obtained profiles can be modified as polynomial function,

$$\Re[\hat{u}_\theta]_{\omega=\omega_o} = \sum_{k=0}^{N_1} a_k r^k, \quad \Im[\hat{u}_\theta]_{\omega=\omega_o} = \sum_{k=0}^{N_2} b_k r^k, \quad \nu(r) = \sum_{k=0}^{N_3} c_k r^k. \tag{B.6}$$

The results of polynomial fitting are shown in Fig. B.7(a)–(c), where the results were obtained by measuring carboxymethyl solution with 0.5 wt.% that is the same test fluid with Chapter 5.

To calculate each term in Eq. B.4, the norms were defined and quantified as follows:

$$F_1(r) \stackrel{\text{def}}{=\!=} |i\omega_o \hat{u}_\theta| = \omega_o \sqrt{\left(\sum_{k=0}^{N_1} a_k r^k\right)^2 + \left(\sum_{k=0}^{N_2} b_k r^k\right)^2}. \tag{B.7}$$

$$F_2(r) \stackrel{\text{def}}{=\!=} \left|\nu(r)\left(\frac{\partial^2}{\partial r^2} + \frac{1}{r}\frac{\partial}{\partial r} - \frac{1}{r^2}\right)\hat{u}_\theta\right| = \sum_{k=0}^{N_3} c_k r^k \sqrt{\left(\sum_{k=0}^{N_1} (k^2-1)\, a_k r^{k-2}\right)^2 + \left(\sum_{k=0}^{N_2} (k^2-1)\, b_k r^{k-2}\right)^2}. \tag{B.8}$$

$$F_3(r) \stackrel{\text{def}}{=\!=} \left|\frac{\partial \nu(r)}{\partial r}\left(\frac{\partial}{\partial r} - \frac{1}{r}\right)\hat{u}_\theta\right| = \sum_{k=0}^{N_3} k c_k r^{k-1} \sqrt{\left(\sum_{k=0}^{N_1} (k-1)\, a_k r^{k-1}\right)^2 + \left(\sum_{k=0}^{N_2} (k-1)\, b_k r^{k-1}\right)^2}. \tag{B.9}$$

Figure B.8 shows the radial profiles of norm calculation results in $F_1$, $F_2$, and $F_3$, substituting experimental results (Fig. B.7). The radial profile of $F_1$ has good accordance with that of $F_2$, whereas both profiles of $F_1$ and $F_2$ are much larger than the profile of $F_3$. This means the term $(C)$ in Eq. B.4 is negligible toward the result of carboxymethylcellulose solution, so there is no need for considering the radial gradient of viscosity in the phase-lag analysis.

## B.4 Summary

We estimated the accuracy of the rheological evaluation using phase-lag analysis. Artificial random noises with the normal distribution, which can represent actual velocity by estimating experimental noises in UVP, were produced. This production of artificial random noises can realize statistical evaluations from numerical calculations. Thus, it is possible to estimate the accuracy of the measurement system by iterative computing. The measurement noises of viscosity were caused by the noise of differential amplification in phase-lag profiles. To apply the spectral subtraction to the phase-lag profiles, the additive noises can be eliminated. These results were obtained from $N = 1$ ($\Delta t = 1$ s), so the filtering process is expected to be applied to complex fluids with instantaneously changeable rheological properties, such as polymer solutions, thixotropic fluids, and bubbly liquids. This can lead to highly accurate and real-time rheometry. As future prospects, the accuracy of another analytical procedure in USR will be validated by the iterative calculation using the artificial random noises assuming actual measurement errors.

## References

[1] G. E. Box, “A note on the generation of random normal deviates,” Ann. Math. Stat., 29, 610–611 (1958).
[2] M. Matsumoto, and T. Nishimura, “Mersenne twister: a 623-dimensionally equidistributed uniform pseudo-random number generator,” ACM Transactions on Modeling and Computer Simulation (TOMACS), 8(1), 3–30 (1998).

Appendix C

# Rheological evaluation of non-Newtonian effects on Newtonian fluid with localized bubble dispersions

## Contents


C.1 Introduction . . . 177
C.2 Experimental setup . . . 177
C.3 Statistics of viscoelastic analysis in the region of localized bubble dispersions . . . 178
C.4 Summary . . . 179
References . . . 180


## C.1 Introduction

Effective viscosity of fluid with dispersed multiphase media, such as bubbles or droplet, is difficult to evaluate by estimation of its volume fraction alone. It is due to complex effects of surface tension arising from the deformation of bubble/droplet. The effective viscosity of fluid with deformed bubbles is studied in the field of volcanology; To estimate the effective viscosity in the gas-liquid two-phase flow, Llwellin & Manga presented flow diagram under steady and unsteady flow condition [1]. There is, however, limitations in applicable range of the estimation of effective viscosity, so it is required to expand and universalize the applicability.

Utilizing ultrasonic velocity profiling technique [2], our research group has been established ultrasonic spinning rheometry [3] and Chapters 2–9. Tasaka *et al.* [3] evaluated the effective viscosity of fluid with homogeneously dispersed bubbles under unsteady shear deformation, and extended a part of the flow diagram presented by Llwellin & Manga [1]. There are still unexamined issues on the bubble rheology; because the deformed bubbles have relaxation time showing viscoelastic behavior, evaluating higher-ordered non-Newtonian effect and controlling the applied shear rate to dispersed bubbles are required. In this chapter, by constructing the system to realize the localized bubble dispersions, viscoelasticity arising from the bubble deformation is quantified utilizing liner viscoelastic analysis (Chapter 4).

## C.2 Experimental setup

The experimental setup was constructed by a simple open cylindrical container made of acrylic resin with the inner diameter $2R = 150$ mm, the height, 280 mm, from the bottom of cylinder to upper surface of test fluid as shown in Fig. C.1(a) and (b). The shear flow is propagated from the wall of container to the inner test fluids by oscillating the container centering on the center with amplitude $\Theta$ and frequency $f_o$. The measurement line of ultrasonic transducer with basic frequency, 4 MHz was set at 150 mm height from the needle for injecting bubbles, and the distance, $\Delta y = 15$ mm, from the center of cylindrical container.

The gray part shown in Fig. C.1(b) was fixed at outside water chamber to move independently from the cylinder rotation and oscillation. The needles with inner diameter 0.1 mm were set at $r/R = 0.85$ of the bottom disk in the cylindrical container, and the container rotated with a steady angular velocity in 10 rpm($f_r = 0.167$ Hz) [Fig. C.1(c)]. During this rotating process, the fine bubbles (the diameter; $d \approx 1$ mm) were generated with the volume of flow, 10 mm$^3$/s, approximately. By injecting bubbles in 10 times rotations, the bubbles were dispersed like curtain at $0.8 < r/R < 0.9$. After that, to obtain the velocity profiles, periodic oscillations were applied with frequency $f_o = 1$ Hz and oscillating amplitude $\Theta$. Using UVP,

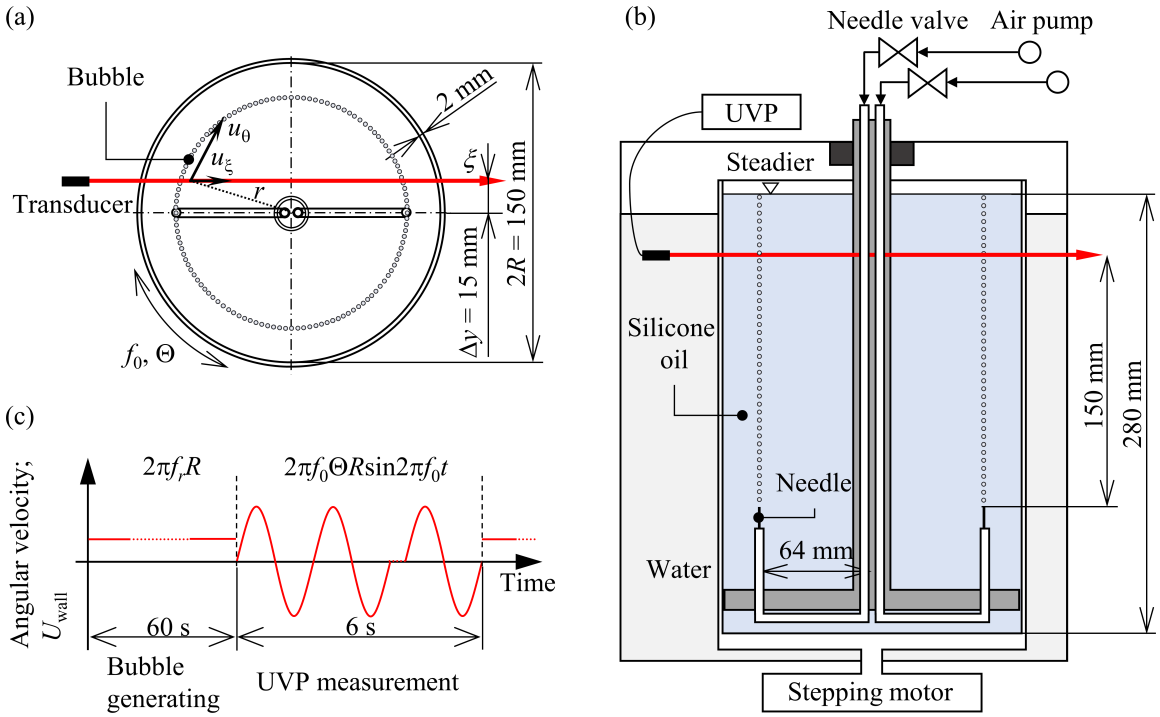


Figure C.1: Schematic of experimental apparatus from (a) top view and (b) side view, and (c) angular velocity in different control modes.

the flow velocity propagating inside the cylinder was measured as fluctuations of $u_\xi$ along the measurement line as shown in Fig. C.1(a). If the fluid flows in the container are one directional and axisymmetric, the fluid motion obeys Cauchy's equation of motion given as $\rho\partial u_\theta/\partial t = \partial\tau/\partial r + 2\tau/r$, where $\rho$ is the density of the test fluid, and $\tau$ represents the shear stress. By repeating the modes of steady rotation and periodic oscillation, the processes of bubble generation and measurement were examined 50 times as shown in Fig. C.1(c). From Stokes's law, the bubble raising speed in the diameter $d = O(1\text{ mm})$ is much less than shear amplitude of oscillating cylinder so as to be negligible.

Oscillating the cylinder with $f_o$ and Θ, azimuthal velocity $u_\theta$ is applied and satisfied the equation of motion, $\rho\partial u_\theta/\partial t = \partial\tau/\partial r + 2\tau/r$. To describe the relation between $u_\theta$ and $\tau$, Maxwell's model, $\tau + (\mu/E)(\partial\tau/\partial t) = \mu(\partial u_\theta/\partial r - u_\theta/r)$, is selected as the simplest expression for the linear viscoelastic characteristics, where $\mu$ and $E$ denote the viscosity and elasticity of the fluid. To determine the $\mu$ and $E$ satisfying the optimization problem, the cost function is given as $F(\mu, E; r) = |\rho\partial u_\theta/\partial t - \partial\tau/\partial r - 2\tau/r|^2$. The details of the basic concept about USR are conferred in Chapters 4 and 5.

## C.3 Statistics of viscoelastic analysis in the region of localized bubble dispersions

In the condition of $f_o = 1$ Hz and $\Theta = \pi/2$, the fluid flow propagates inside with constant phase-lag when the fluid viscosity is homogeneous as shown in Fig. C.2(a). However, in the condition that the bubbles are dispersed at $0.8 < r/R < 0.9$ [Fig. C.2(b)], the velocity profiles in the region with the bubbles are different from those in the case of single phase [Fig. C.2(a)]. This is considered as the velocity modulation arising from the bubble deformations; from observations of the deformed bubbles in the oscillation, the dispersed bubbles were deformed periodically as shown in Fig. C.2(c).

The power spectrum of the velocity fluctuation is calculated by the discrete Fourier transform with respect to time, and the frequency component, $f_o$, at the applied oscillation is the most dominant (97% compared to total energy of the power spectrum). Thus, the Fourier components of real and imaginary parts shown in Fig. C.3(a) and (b) fully represent the original information of the measured velocity fluctuation. In comparison of Fig. C.3(a) and (b), there is a clear difference in the existence of bubble dispersions. To determine the $\mu$ and $\delta$ minimizing the cost function value, $F(\mu, \delta; r)$ was calculated by substituting the real and imaginary parts, where phase difference $\delta$ was used as an indicator of viscoelasticity. The $\delta$ was defined as $\tan\delta = E/(2\pi f_o\mu); (0 < \delta < \pi/2)$, and it is physically interpreted that $\delta \to \pi/2$ means viscous characteristic, $0 < \delta < \pi/2$ means viscoelastic characteristic, and $\delta \to 0$ means elastic characteristic. as shown in Fig. C.3(c) Figure C.3(c) shows the calculated results of $F(\mu, \delta)$ integrated $0.84 < r/R < 0.86$ where is the region of bubble dispersions [Fig. C.3(b)];

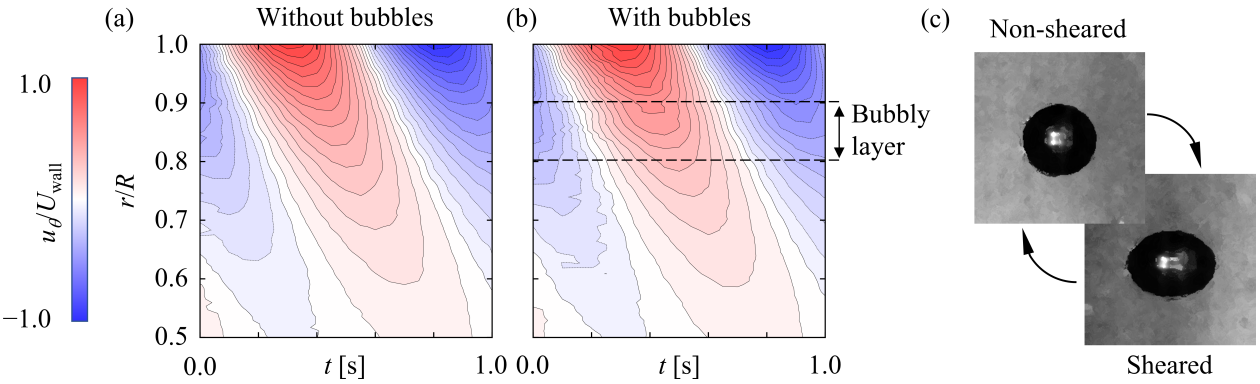


Figure C.2: Spatiotemporal velocity distribution (a) without bubbles and (b) with bubbles in $0.8 < r/R < 0.9$, and (c) photographies of bubble deformation in an oscillating cycle.

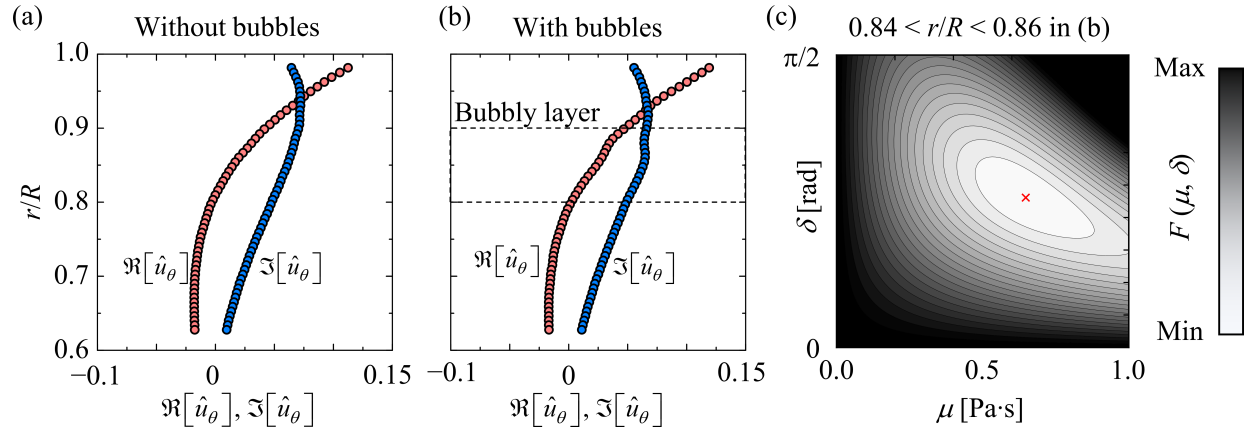


Figure C.3: Profiles of real and imaginary components of the most dominant Fourier component, $f_o$ (a) without bubbles and (b) with bubbles in $0.8 < r/R < 0.9$, and (c) $F(\mu, \delta)$ at $0.84 < r/R < 0.86$ in (b), where a red cross indicates the minimum value.

the distribution $F(\mu, \delta)$ has a minimal point at $\mu \approx 0.6$ Pa · s and $\delta \approx \pi/4$, showing viscoelastic characteristic.

To investigate the interrelationship between the bubble deformation and viscoelastic response, for the different oscillating amplitudes $\Theta(= \pi/4, \pi/2, 5\pi/6, \pi)$, the measurements and viscoelastic analyses were examined 50 times with the same procedure mentioned above. Because the maximum shear amplitude changes with respect to oscillating frequency $f_o$ and angle $\Theta$, the bubble deformations are closely related to them. To help the graphical understanding of the bubble deformation, the short and long axes, $a$ and $b$, of ellipse shaped bubbles at the maximum deformed state were quantified from the photography in each condition of $\Theta$. Using $a$ and $b$, the maximum flattening of the bubble, $\varepsilon_{\mathrm{Max}}(= 1 - a/b)$, can be illustrated as bottom of Fig. C.4. The vertical and horizontal axes indicate the obtained $\mu$ and $E$ with the standard deviation, and $\dot{\gamma}$ with the standard deviation. The dotted line in the Fig. C.4(a) indicates the catalog viscosity (0.49 Pa · s) of silicone oil at 25°C. In the case without bubble [black plots in the Fig. C.4(a)], the measured viscosity equals to the catalog viscosity 0.49 Pa · s, so the rheometry was ensured well. In the case of injected bubbles, the measured viscosity increases at the bubble regions regardless of $\Theta$. It is speculated that the effective viscosity increases because the momentum propagation is enhanced by functions of localized bubble dispersion. Further, the shear rate in the bubble region shows constant as shown in Fig. C.4(a). This is regarded as shear banding phenomena that the bubble deformation is localized shearing. Figure C.4(b) shows the measured elasticity $E$ calculated from $\delta$ and $\mu$; the $E$ decreases with increasing the shear rate for deforming the bubbles, as the surface tension effect of bubble is less with increasing deformation degree of the bubbles.

## C.4 Summary

The viscoelasticity of deformed bubbles under unsteady shear was investigated by ultrasonic spinning rheometry. To clarify the interrelationship between deformation of bubble and viscoelasticity, viscoelastic effects arising from the deformations

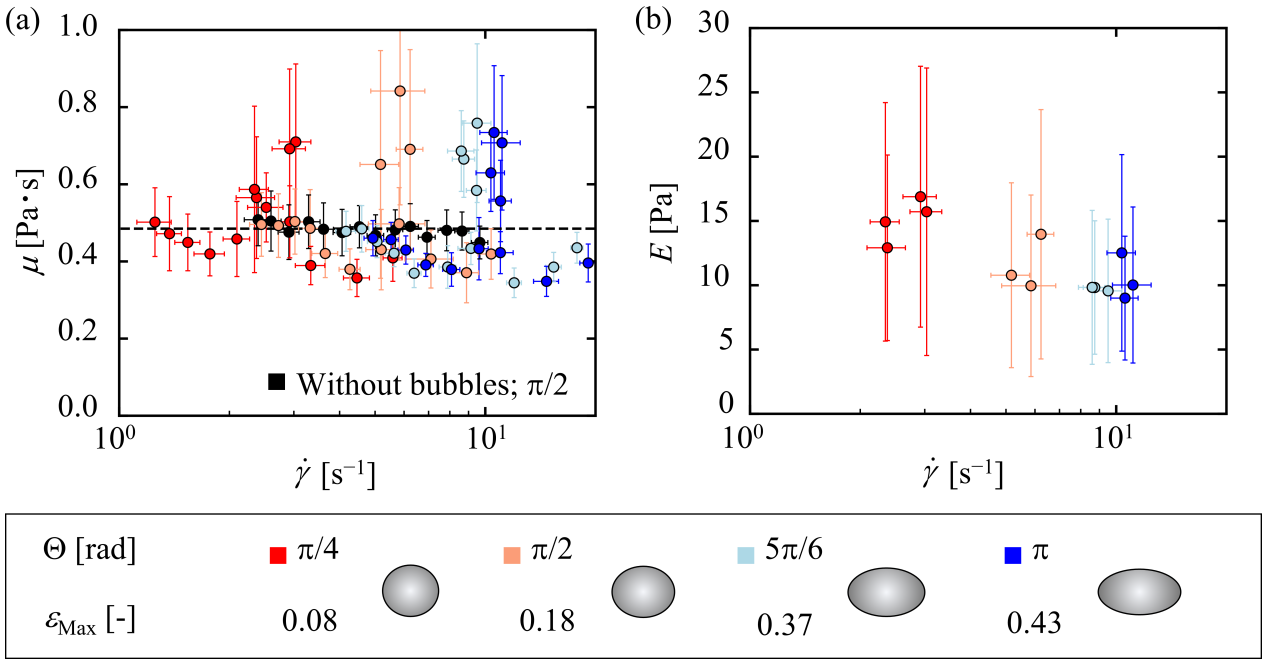


Figure C.4: (a) Viscosity $\mu$ and (b) elasticity $E$ evaluated by linear viscoelastic analysis for different oscillating amplitude $\Theta$.

were evaluated as statistical values by several-time measurements for curtained-like bubble dispersions inside the cylindrical container. As a result, the rheological effects in the deformed bubble can be separated into viscosity and elasticity. Noteworthy-experimental findings were as follows; (1) The effective viscosity with deformed bubble dispersions is modulated. (2) The elasticity with the deformed bubbles decreases with increasing shear amplitude.

## References

[1] E. W. Llewellin, and M. Manga, "Bubble suspension rheology and implications for conduit flow," Journal of Volcanology and Geothermal Research, 143(1-3), 205–217 (2005).

[2] *Ultrasonic Doppler Velocity Profiler for Fluid Flow*, Springer Science, edited by Y. Takeda (Springer, Tokyo, 2012).

[3] Y. Tasaka, T. Kimura, and Y. Murai, "Estimating the effective viscosity of bubble suspensions in oscillatory shear flows by means of ultrasonic spinning rheometry," Exp. Fluids 56, 1867 (2015).

# Curriculum Vitae


## Taiki YOSHIDA

Laboratory for Flow Control
Faculty of Engineering
Hokkaido University

Date of birth: May 12, 1992
Office: N13W8, Sapporo 060-8628, Japan
Phone: +81-(0)11-706-6373
E-mail: yoshida@ring-me.eng.hokudai.ac.jp

Google Scholar: https://scholar.google.com/citations?user=txl-C5cAAAAJ&hl=ja
Research map: https://researchmap.jp/taiki_yoshida_eng/
ResearchGate: https://www.researchgate.net/profile/Taiki_Yoshida2


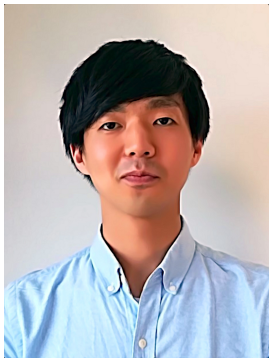

### Research interests

- ✓ Novel development of ultrasonic velocity-profiling rheometry
- ✓ Rheology of clay dispersion with thixotropy
- ✓ Rheological modulation by multi-phase dispersions in viscoelastic fluids
- ✓ Rheology of gelled food material
- ✓ Rheology of bubbly liquid with unsteady deformation
- ✓ In-line rheometry development for chemical and food engineering

### Career

| | |
|---|---|
| Apr. 2020 – Present | Research Fellow (PD), Japan Society for the Promotion of Science |
| Apr. 2019 – Jul. 2019 | Academic guest, ETH Zürich, Switzerland |
| Apr. 2018 – Mar. 2020 | Research Fellow (DC1), Japan Society for the Promotion of Science |
| Oct. 2017 – Mar. 2018 | Research assistant, Hokkaido University |
| Oct. 2016 – Dec. 2016 | Invited student, ETH Zürich, Switzerland |

### Education

| | |
|---|---|
| Oct. 2017 – Mar. 2020 | Ph. D. studies at the Laboratory for Flow Control, Hokkaido University, Sapporo, Japan<br>Dissertation title: Study on Kinematic Rheometry Utilizing Ultrasonic Velocity Profiling |
| Apr. 2016 – Sep. 2017 | Diploma studies of fluid mechanics at Hokkaido University, Sapporo, Japan<br>Diploma thesis: Development of Advanced Ultrasonic Spinning Rheometry for Complex Fluids |
| Apr. 2012 – Mar. 2016 | Basic studies at the Faculty of Engineering, Hokkaido University, Sapporo, Japan |

### Honors & Awards

1. Taiki Yoshida, Early Completion of the Doctor's Degree, Hokkaido University, 2020.
2. Taiki Yoshida, Yuji Tasaka, and Peter Fischer, Japanese press release in Hokkaido University: 流体力学の手法で食品の流動物性評価法を更新～食品の食べやすさ・食べ応えの普遍的評価法確立に期待～, 2019.
3. Taiki Yoshida, Yuji Tasaka, and Peter Fischer, Press release in AIP publishing: Century-Old Food Testing Method Updated to Include Complex Fluid Dynamics, 2019.

4. Taiki Yoshida, *et al.*, Journal's best in *Physics of Fluids*: Featured article (doi: 10.1063/1.5122874), 2019.
5. Taiki Yoshida, *et al.*, Journal's best in *Physics of Fluids*: Featured article (doi: 10.1063/1.5119335), 2019.
6. Taiki Yoshida, Yuji Tasaka, Hyun Jin Park, and Yuichi Murai, Technical Award: Category I, *The Visualization Society of Japan*, 2018.
7. Taiki Yoshida, Research Fellowship (DC1), Japan Society for the Promotion of Science (JSPS) (2018–2021).
8. Taiki Yoshida, Scholarship for Doctor's course student provided by Japan Student Services Organization (JASSO), 2018.
9. Taiki Yoshida, Early Completion of the Master's Degree, Hokkaido University, 2017.
10. Taiki Yoshida, Scholarship for Master's course student provided by Japan Student Services Organization (JASSO), 2017.

## Research Grants & Projects

1. Taiki Yoshida, **Project**: "Study on Intelligent Rheometry Designed by Ultrasonic Velocity Profiler," *Overseas Challenge Program for Young Researchers supported by Japan Society for the Promotion of Science*, Collaborative project with ETHZ, 1.4 MJPY, (2019).
2. Taiki Yoshida, **Project**: "Development of Intelligent Rheometry Designed by 2-D Ultrasonic Velocity Profiler," *Grant-in-Aid for Japan Society for the Promotion of Science Fellows*, 2.8 MJPY, (2018–2020).

## Specialized skills

- ◇ C language
- ◇ $C^{++}$
- ◇ LaTex
- ◇ Open MP
- ◇ C#
- ◇ Python 3
- ◇ LabVIEW
- ◇ Visual Basic
- ◇ ImageJ macro coding

# List of Publications

## Published Papers

1. Taiki Yoshida, Yuji Tasaka, and Peter Fischer, "Ultrasonic spinning rheometry test on rheology of gelled food for making better tasting desserts," *Physics of Fluids*, 31(11), p. 113101, (2019) [Selected as Featured Article and Press released in AIP Publishing].
2. Taiki Yoshida, Yuji Tasaka, and Yuichi Murai, "Effective viscoelasticity of non-Newtonian fluids modulated by large-spherical particles aligned under unsteady shear," *Physics of Fluids*, 31(10), p. 103304, (2019) [Selected as Featured Article].
3. Taiki Yoshida, Yuji Tasaka, and Yuichi Murai, "Efficacy assessments in ultrasonic spinning rheometry: Linear viscoelastic analysis on non-Newtonian fluids," *Journal of Rheology*, 63(4), pp. 503–517, (2019).
4. Taiki Yoshida, Yuji Tasaka, Shingo Tanaka, Hyun Jin Park, and Yuichi Murai, "Rheological properties of montmorillonite dispersions in dilute NaCl concentration investigated by ultrasonic spinning rheometry," *Applied Clay Science*, 161, pp. 513–523, (2018).
5. Yuji Tasaka, Taiki Yoshida, Richard Rapberger, Yuichi Murai, "Linear viscoelastic analysis using frequency-domain algorithm on oscillating circular shear flows for bubble suspensions," *Rheologica Acta*, 57(3), pp. 229–240, (2018).
6. Taiki Yoshida, Yuji Tasaka, Hyun Jin Park, Yuichi Murai, Hiroki Teramura, and Shigenobu Koseki, "Inner structure visualization of fresh fruits utilizing ultrasonic velocity profiler," *Journal of Visualization*, 21(2), pp. 253–265, (2018) [Prize-Awarded Article from *The Visualization Society of Japan*].
7. Taiki Yoshida, Yuji Tasaka, and Yuichi Murai, "Rheological evaluation of complex fluids using ultrasonic spinning rheometry in an open container," *Journal of Rheology*, 61(3), pp. 537–549, (2017).

## Proceedings (Peer reviewed)

1. Taiki Yoshida, Yuji Tasaka, Hyun Jin Park, and Yuichi Murai, "Accuracy and Robustness Evaluations on Algorithms of Ultrasonic Spinning Rheometry," *Proceedings of the 11th International Symposium on Ultrasonic Doppler Methods for Fluid Mechanics and Fluid Engineering*, pp. 67–70, (2018).
2. Yuji Tasaka, Taiki Yoshida, and Yuichi Murai, "A novel design of ultrasonic spinning rheometry," *Proceedings of the 10th International Symposium on Ultrasonic Doppler Methods for Fluid Mechanics and Fluid Engineering*, pp. 121–124, (2016).
3. Taiki Yoshida, Yuji Tasaka, and Yuichi Murai, "Quantitative evaluation of rheological properties for complex fluids using ultrasonic spinning rheometry," *Proceedings of the 10th International Symposium on Ultrasonic Doppler Methods for Fluid Mechanics and Fluid Engineering*, pp. 5–8, (2016).

## Presentations at International Conference

1. Taiki Yoshida*, Yuji Tasaka, and Yuichi Murai, "Is the macro-rheology of non-Newtonian fluid modulated by particle alignment?," *ICTAM 2020*, Milano, Italy, (2020), Oral.
2. Kohei Ohie*, Taiki Yoshida, Hyun Jin Park, Yuji Tasaka, and Yuichi Murai, "A novel multiple rheology mapping by ultrasonic spinning rheometry," *ICTAM 2020*, Milano, Italy, (2020), Oral.
3. Taiki Yoshida*, Yuji Tasaka, and Yuichi Murai, "Particle alignment under unsteady shear in non-Newtonian fluids causing modulations of effective viscoelasticity," *The DFD19 Meeting of the American Physical Society*, Seattle, The

US, (2019), Poster.

4. Yuji Tasaka*, Taiki Yoshida, and Yuichi Murai, "An idea to contactless in-line rheometry using ultrasonic velocity profiling," *8th ISFRS – The International Symposium on Food Rheology and Structure*, Zürich, Switzerland, (2019), Oral.
5. Taiki Yoshida*, Yuji Tasaka, and Yuichi Murai, "Rheological and inner structural assessments for complex materials using ultrasonic spinning rheometry," *8th ISFRS – The International Symposium on Food Rheology and Structure*, Zürich, Switzerland, (2019), Poster.
6. Taiki Yoshida*, Yuji Tasaka, and Yuichi Murai, "Rheological evaluations and capability assessments of ultrasonic spinning rheometry for non-Newtonian fluids," *AERC2019 – The Annual European Rheology Conference 2019*, Portorož, Slovenia, (2019), Oral.
7. Ruixue Li*, Taiki Yoshida, Yuji Tasaka, and Yuichi Murai, "Ultrasonic measurement of milk products flowing in stainless steel pipe," *8th AECoR Joint Meeting between ETHZ and Hokkaido University*, Sapporo, Japan, (2018), Oral.
8. Yuichi Murai*, Taiki Yoshida, Hyun Jin Park, and Yuji Tasaka, "Ultrasonic scan-imaging technology for visualizing internal structures," *8th AECoR Joint Meeting between ETHZ and Hokkaido University*, Sapporo, Japan, (2018), Oral.
9. Yuji Tasaka*, Taiki Yoshida, and Yuichi Murai, "Ultrasonic spinning rheometry – concept and algorithms –," *8th AECoR Joint Meeting between ETHZ and Hokkaido University*, Sapporo, Japan, (2018), Oral.
10. Taiki Yoshida*, Yuji Tasaka, and Yuichi Murai, "Capability assessments of ultrasonic spinning rheometry for non-Newtonian Fluid," *8th AECoR Joint Meeting between ETHZ and Hokkaido University*, Sapporo, Japan, (2018), Oral.
11. Taiki Yoshida*, Yuji Tasaka, Hyun Jin Park, and Yuichi Murai, "Accuracy and Robustness Evaluations on Algorithms of Ultrasonic Spinning Rheometry," *The 11th International Symposium on Ultrasonic Doppler Methods for Fluid Mechanics and Fluid Engineering*, Berlin, Germany, (2018), Oral.
12. Taiki Yoshida*, Yuji Tasaka, Yuichi Murai, Hyun Jin Park, Hiroki Teramura, and Shigenobu Koseki, "Visualization of the inner structure of fresh fruit using an ultrasonic velocity profiler," *7th AECoR Joint Meeting between ETHZ and Hokkaido University*, Zürich, Switzerland, (2017), Oral.
13. Shun Nomura*, De Cesare Giovanni, Yasushi Takeda, Taiki Yoshida, Yuji Tasaka, and Hide Sakaguchi, "Velocity Structure and Spatio-temporal Evolution in the Head Turbidity Currents based on Ultrasound Doppler Velocity Profiling," *European Geosciences Union General Assembly 2017*, Vienna, Austria, (2017), Poster.
14. Jumpei Hitomi*, Taiki Yoshida, Megumi Akashi, Hyun Jin Park, Yuji Tasaka, and Yuichi Murai, "Ultrasonic velocity profiler for three phase pipe flows," *6th AECoR Joint Meeting between ETHZ and Hokkaido University*, Sapporo, Japan, (2016), Oral.
15. Yuji Tasaka*, Taiki Yoshida, and Yuichi Murai, "A novel design of ultrasonic spinning rheometry," *The 10th International Symposium on Ultrasonic Doppler Methods for Fluid Mechanics and Fluid Engineering*,Tokyo, Japan, (2016), Oral.
16. Taiki Yoshida*, Yuji Tasaka, and Yuichi Murai, "Quantitative evaluation of rheological properties for complex fluids using ultrasonic spinning rheometry," *The 10th International Symposium on Ultrasonic Doppler Methods for Fluid Mechanics and Fluid Engineering*, Tokyo, Japan, (2016), Oral.

## 解説記事

1. 田坂 裕司, 芳田 泰基, 村井 祐一, "超音波流速分布計測を用いた複雑流体のレオロジー物性評価", ながれ (日本流体力学会誌), 38(4), pp. 283–290, (2019).
2. 田坂 裕司, 白鳥 貴久, 芳田 泰基, 村井 祐一, "超音波流速分布計を用いたレオメトリについて：流れ計測の重要性と課題 (特集 UVP による流体の可視化)," 可視化情報学会誌 (*Journal of the Visualization Society of Japan*), 36(142), pp. 103-107, (2016).

## 国内学会発表

1. 田坂裕司, 芳田泰基, 村井祐一, “超音波を用いた非侵襲インラインレオメータ,” 第 97 期流体工学部門講演会, 2019 年 11 月, ポスター.
2. 田坂裕司, 芳田泰基, 村井祐一, “剪断流における分散気泡を含む液体のレオロジー評価,” 混相流シンポジウム 2019, 2019 年 8 月, 口頭.
3. 田坂裕司, 芳田泰基, Hyun Jin Park, 村井祐一, “超音波スピニングレオメトリ,” 第 96 期流体工学部門講演会, 2018 年 11 月, ポスター.
4. 李瑞雪, 芳田 泰基, 人見純平, 澤田航希, Hyun Jin Park, 田坂裕司, 村井祐一, Stéphane Fischer, “ステンレス管内を流れる乳製品の超音波診断,” 第 96 期流体工学部門講演会, 2018 年 11 月, ポスター.
5. Neetu Tiwari, 芳田 泰基, Hyun Jin Park, 田坂裕司, 村井祐一, “Ultrasonic velocity profiler (UVP) based pressure estimation method: Vortex shedding downstream of cylinder,” 可視化情報学会 第 46 回, 2018 年 9 月, 口頭.
6. 芳田 泰基, 田坂 裕司, Hyun Jin Park, 村井 祐一, “ニュートン流体中の分散気泡が与える非ニュートン性評価,” 混相流シンポジウム 2018, 2018 年 8 月, 口頭.
7. 芳田 泰基, 田坂 裕司, Hyun Jin Park, 村井 祐一, “回転式超音波レオメトリを用いた粘土懸濁液のレオロジー評価,” 日本レオロジー学会第 45 年会 , 2018 年 5 月, 口頭.
8. 岩佐 耕節, 芳田 泰基, Hyun Jin Park, 田坂 裕司, 村井 祐一, “超音波スピニングレオメトリによるマイクロバブル懸濁液の乱流渦粘度の評価,” 混相流シンポジウム 2017, 2017 年 8 月, 口頭.
9. 村井 祐一, 芳田 泰基, Hyun Jin Park, 田坂 裕司, “液状食品の超音波非接触モニタリング技術,” 日本食品科学工学会北海道支部大会, 2017 年 2 月, 口頭, 招待講演.
10. 寺村 大輝, 芳田 泰基, 村井 祐一, 田坂 裕司, 川村 周三, 小関 成樹, “超音波ドップラー流速分布計を用いたキウイの非破壊果肉硬度測定,” 日本食品科学工学会北海道支部大会, 2017 年 2 月, 口頭.
11. 村井 祐一, 芳田 泰基, 田坂 裕司, “超音波ドップラー法によるレオロジー物性の空間分布の定量可視化,” 第 6 回ソフトマター研究会, 2016 年 10 月, 口頭.
12. 田坂 裕司, 芳田 泰基, 村井 祐一, “線形粘弾性解析による分散気泡液体のレオロジー評価,” 混相流シンポジウム 2016, 2016 年 8 月, 口頭.
13. 芳田 泰基, 田坂 裕司, 村井 祐一, “超音波を用いた食品流動の可視化とレオロジー評価,” 第 44 回可視化情報シンポジウム, 2016 年 7 月, 口頭.
14. 田坂 裕司, 木村 拓文, Richard Rapberger, 大石 義彦, 村井 祐一, 芳田 泰基, “超音波流速分布計を用いた分散混相流体の複素粘度診断,” 混相流シンポジウム 2015, 2015 年 8 月, 口頭.

## 特許

1. 特願 2019 – 056493, “非接触型レオロジー物性計測装置、システム、プログラムおよび方法,” 発明者 : 田坂 裕司, 芳田 泰基, 村井祐一 (2019 年 3 月)